Neutron Transport in Hexagonal Reactor Cores Modeled by Trigonal-Geometry Diffusion and Simplified P_3 Nodal Methods

Susan Duerigen

May 2013

This scientific-technical report with the number HZDR-035 includes the content and research results of the doctoral thesis by Susan Duerigen published by the Karlsruhe Institute of Technology (KIT), Department of Mechanical Engineering: http://digbib.ubka.uni-karlsruhe.de/volltexte/1000034870.

Contents

Acknowledgments

I would like to express my sincere appreciation to my advising professors, Professor Dr. Robert Stieglitz (Karlsruhe Institute of Technology (KIT), Germany) and Professor Dr. Kostadin N. Ivanov (Pennsylvania State University, USA), for their scientific support and valuable comments.

Especially, I owe my deep gratitude to Dr. Siegfried Mittag, who has spent countless hours with me discussing my work, for his abundance of patience, inspiring conversations, and substantial guidance.

I am indebted to the developers of the DYN3D code, Dr. Ulrich Grundmann and Dr. Ulrich Rohde, for their helpful remarks, Dr. Sören Kliem for his continuous support and motivation, Dr. Emil Fridman, Yuri Bilodid, and Evgeny Nikitin for their contributions relating to the reference codes as well as Dr. Roland Rzehak and Professor Dr. Udo Rindelhardt for their valuable advice.

Furthermore, I would like to thank my friends and, in particular, my family for their continuous encouragement, deep trust, and love.

Lastly, I should thank Dr. Hauschka for their eye care products, which made me look halfway presentable even after several resource-guzzling night shifts.

This work took place within the project "Development of a version of the reactor dynamics code DYN3D applicable for High Temperature Reactors" funded by the German Federal Ministry of Economics and Technology (BMWi) (project no. 1501358).

Danksagung

Meinen aufrichtigen Dank möchte ich meinen Referenten, Professor Dr. Robert Stieglitz (Karlsruher Institut für Technologie (KIT)) und Professor Dr. Kostadin N. Ivanov (Pennsylvania State University, USA), für ihre wissenschaftliche Unterstützung und wertvollen Anregungen aussprechen.

Dr. Siegfried Mittag, der zahllose Stunden in die Diskussion meiner Arbeit investierte und auf dessen Geduld ich immer zählen konnte, gebührt mein ganz besonderer Dank für anregende Gespräche und fachliche Führung (und einen ganz hervorragenden Karpfen blau).

Zu Dank verpflichtet bin ich weiterhin den DYN3D-Programmentwicklern, Dr. Ulrich Grundmann und Dr. Ulrich Rohde, für ihre hilfreichen Erläuterungen, Dr. Sören Kliem für seine stetige Unterstützung und Motivation, Dr. Emil Fridman, Yuri Bilodid und Evgeny Nikitin für ihre Zuarbeit bei der Referenzdatenerzeugung sowie Dr. Roland Rzehak und Professor Dr. Udo Rindelhardt, die mir mit wertvollem Rat zur Seite standen.

Nicht minder gilt mein herzlicher Dank meinen Freunden und insbesondere meine Familie für ihre unermüdliche Ermutigung, ihr tiefes Vertrauen und ihre Liebe.

Zuletzt sollte ich Dr. Hauschka für deren Augenpflegeprodukte danken, durch ich in Zeiten zehrender Nachtschichten halbwegs tageslichttauglich blieb.

Diese Arbeit wurde im Rahmen des Projekts "Entwicklung einer Version des Reaktordynamikcodes DYN3D für Hochtemperaturreaktoren" durchgeführt – gefördert vom Bundesministeriums für Wirtschaft und Technologie (BMWi) (Projektnummer 1501358).

Abstract

The superior advantage of a nodal method for reactor cores with hexagonal fuel assemblies discretized as cells consisting of equilateral triangles is its mesh refinement capability. In this thesis, a diffusion and a simplified P_3 (or SP_3) neutron transport nodal method are developed based on trigonal geometry. Both models are implemented in the reactor dynamics code DYN3D. As yet, no other well-established nodal core analysis code comprises an SP_3 transport theory model based on trigonal meshes. The development of two methods based on different neutron transport approximations but using identical underlying spatial trigonal discretization allows a profound comparative analysis of both methods with regard to their mathematical derivations, nodal expansion approaches, solution procedures, and their physical performance.

The developed nodal approaches can be regarded as a hybrid NEM/AFEN form. They are based on the transverse-integration procedure, which renders them computationally efficient, and they use a combination of polynomial and exponential functions to represent the neutron flux moments of the SP_3 and diffusion equations, which guarantees high accuracy.

The SP_3 equations are derived in within-group form thus being of diffusion type. On this basis, the conventional diffusion solver structure can be retained also for the solution of the SP_3 transport problem.

The verification analysis provides proof of the methodological reliability of both trigonal DYN3D models. By means of diverse hexagonal academic benchmark and realistic detailed-geometry full-transport-theory problems, the superiority of the SP_3 transport over the diffusion model is demonstrated in cases with pronounced anisotropy effects, which is, e.g., highly relevant to the modeling of fuel assemblies comprising absorber material.

Zusammenfassung

Die herausragende Eigenschaft eines nodalen Verfahrens, dem eine Dreiecksdiskretisierung zu Grunde liegt, ist, für Reaktorkerne mit hexagonaler Brennelementstruktur eine beliebige Gitterverfeinerung zu ermöglichen. Gegenstand dieser Arbeit ist die Entwicklung und Implementierung nodaler Diffusions- und SP_3-Transportverfahren basierend auf trigonaler Geometrie für das Reaktordynamikprogramm DYN3D. Bislang umfasst kein anderer weltweit etablierter Code zur Reaktorkernanalyse ein SP_3-Transportmodell für trigonale Geometrie. Die Entwicklung zweier Verfahren beruhend auf unterschiedlichen Neutronentransportnäherungen, jedoch mit identischer räumlicher Diskretisierung, ermöglicht eine fundierte vergleichende Analyse beider Methoden hinsichtlich ihrer mathematischen Ableitungen, ihrer nodalen Entwicklungsansätze, ihrer Lösungsverfahren sowie ihrer Vorhersagegenauigkeit in unterschiedlichen Anwendungen.

Die entwickelten nodalen Ansätze können als hybride NEM/AFEN-Methoden betrachtet werden. Sie beruhen auf dem Verfahren der transversalen Integration und einer Kombination aus Polynom- und Exponentialfunktionen zur Darstellung der Neutronenflussmomente, was sowohl numerische Effizienz als auch hohe Genauigkeit gewährleistet.

Die SP_3-Gleichungen werden in der "Within-Group"-Form abgeleitet und erhalten somit die Gestalt von Diffusionsgleichungen. Daher kann auch für die Behandlung des SP_3-Transportproblems die konventionelle Programmstruktur zur Lösung der Diffusionsgleichung beibehalten werden.

Die methodische Zuverlässigkeit beider DYN3D-Modelle wird umfassend verifiziert. Anhand hexagonaler akademischer Benchmarks sowie praxisbezogener, geometrisch detaillierter Transportprobleme wird die Überlegenheit des SP_3-Transportverfahrens gegenüber der Diffusionsmethode in Fällen mit ausgeprägten Anisotropieeffekten aufgezeigt. Dies ist insbesondere relevant für die Modellierung von Brennelementen, die Neutronenabsorber enthalten.

List of Figures

List of Tables

List of Algorithms

List of Abbreviations

Acronym	Description
ADF	**a**ssembly **d**iscontinuity **f**actor
AFEN	**a**nalytic **f**unction **e**xpansion **n**odal method
ANM	**a**nalytic **n**odal **m**ethod
BMWi	**B**undes**m**inisteriums für **Wi**rtschaft und Technologie
CDF	pin-**c**ell **d**iscontinuity **f**actor
CMFD	**c**oarse-**m**esh **f**inite-**d**ifference method
CP	**c**ollision **p**robability method
CR	**c**ontrol **r**od
DYN3D	3-**D** reactor **dyn**amics code
ENDF	**E**valuated **N**uclear **D**ata **F**ile
ET	**e**quivalence **t**heory
FA	**f**uel **a**ssembly
FD	**f**inite-**d**ifference method
FEM	**f**inite-**e**lement **m**ethod
FENM	**f**lux **e**xpansion **n**odal **m**ethod
GET	**g**eneralized **e**quivalence **t**heory
HEXNEM1	DYN3D **hex**agonal diffusion neutronic model (**NEM**/AFEN approach)
HEXNEM2	DYN3D advanced **hex**agonal diffusion neutronic model (**NEM**/AFEN approach)
HOPEN	**h**igher-**o**rder **p**olynomial **e**xpansion **n**odal method
HTGR	**h**igh-**t**emperature **g**as-cooled **r**eactor
HZDR	**H**elmholtz-**Z**entrum **D**resden-**R**ossendorf

IDF	**i**nterface **d**iscontinuity **f**actor
INEEL	**I**daho **N**ational **E**ngineering and **E**nvironmental **L**aboratory
KIT	**K**arlsruhe **I**nstitute of **T**echnology
LWR	**l**ight-**w**ater **r**eactor
MC	**M**onte **C**arlo method
MOC	**m**ethod **o**f **c**haracteristics
NEM	**n**odal **e**xpansion **m**ethod
NGFM	**n**odal **G**reen's **f**unction **m**ethod
NIM	**n**odal **i**ntegration **m**ethod
NGNP	**N**ext **G**eneration **N**uclear **P**lant
NURESIM	European **Re**ference **Sim**ulation Platform for **Nu**clear Reactors
PEN	**p**olynomial **e**xpansion **n**odal method
P_N	spherical harmonics method
PWR	**p**ressurised **w**ater **r**eactor
RDF	**r**eference **d**iscontinuity **f**actor
RHF	**r**eference **h**eterogeneity **f**actor
RMS	**r**oot **m**ean **s**quare
SANM	**s**emi-**a**nalytic **n**odal **m**ethod
SFR	**s**odium-cooled **f**ast **r**eactor
S_N	discrete ordinates method
SPH	**s**u**p**er**h**omogenization
SP_N	**s**implified P_N method
TPEN	**t**riangle-based **p**olynomial **e**xpansion **n**odal method
TRIDIF	DYN3D **tri**gonal **dif**fusion neutronic model (NEM/AFEN approach)
TRIPEN	**tri**angular **p**olynomial **e**xpansion **n**odal method
TRISP3	DYN3D **tri**gonal **s**implified P_3 neutronic model (NEM/AFEN approach)
VHTR	**v**ery-**h**igh-**t**emperature **r**eactor
VVER	Russian-type PWR (water-water power reactor)

B_4C	boron carbide
Gd_2O_3	gadolinium(III) oxide
H_2O	water
^{235}U	uranium-235
UO_2	uranium dioxide
Zr	zirconium

List of Symbols

Symbol	Description	Physical unit
A	area	cm^2
$A_{\triangle}$	trigonal area	cm^2
a_z	height of an prismatic node	cm
a	edge length of an equilateral triangular base	cm
B^2	buckling	cm^{-2}
D_n	diffusion coefficient	cm
E	neutron energy	eV
$\mathbf{e}_l$	outer normal unit vector of the lth trigonal nodal face	
$\mathbf{e}_{sl}$	outer normal unit vector of the lth hexagonal nodal face	
$\mathbf{e}_{cl}$	outer normal unit vector of the lth hexagonal nodal vertex	
G	number of energy groups	
g	energy group index	
h_k	orthonormal polynomial of maximum order two	
I	number of spatial intervals or volumes	
i	spatial index	
$J^+_{n,g}$	partial outward neutron current (multi-group)	$\mathrm{cm}^{-2}\ \mathrm{s}^{-1}$
$J^-_{n,g}$	partial inward neutron current (multi-group)	$\mathrm{cm}^{-2}\ \mathrm{s}^{-1}$
$J^{(\mathrm{net})}_{n,g}$	neutron net current (multi-group)	$\mathrm{cm}^{-2}\ \mathrm{s}^{-1}$
k_{eff}	effective multiplication factor	
k_{inf}	infinite multiplication factor	

$L_{n,g}$	transverse neutron leakage (multi-group)	$\mathrm{cm}^{-3}\ \mathrm{s}^{-1}$
$\max_{in}$	maximum number of inner iterations	
N	angular neutron density	$\mathrm{cm}^{-3}\ \mathrm{sr}^{-1}\ \mathrm{eV}^{-1}$
N	approximation order (index)	
$\mathbb{N}$	set of the natural numbers including 0	
$\mathbf{n}$	outer normal unit vector of a volume V	
P	thermal power density	$\mathrm{W}\ \mathrm{cm}^{-3}$
p_n	nth Legendre polynomial	
$\mathbf{r}$	spatial vector	cm
r	radial distance	cm
S	neutron source	$\mathrm{cm}^{-3}\ \mathrm{sr}^{-1}\ \mathrm{eV}^{-1}\ \mathrm{s}^{-1}$
S_g	neutron source (angle-independent, multi-group)	$\mathrm{cm}^{-3}\ \mathrm{s}^{-1}$
S_{ext}	external neutron source	$\mathrm{cm}^{-3}\ \mathrm{sr}^{-1}\ \mathrm{eV}^{-1}\ \mathrm{s}^{-1}$
S_f	neutron fission source	$\mathrm{cm}^{-3}\ \mathrm{sr}^{-1}\ \mathrm{eV}^{-1}\ \mathrm{s}^{-1}$
S_s	neutron scattering source	$\mathrm{cm}^{-3}\ \mathrm{sr}^{-1}\ \mathrm{eV}^{-1}\ \mathrm{s}^{-1}$
$S_{s,g}$	neutron scattering source (angle-independent, multi-group)	$\mathrm{cm}^{-3}\ \mathrm{s}^{-1}$
$S_{sd,g}$	neutron downscattering source (angle-independent, multi-group)	$\mathrm{cm}^{-3}\ \mathrm{s}^{-1}$
$S_{su,g}$	neutron upscattering source (angle-independent, multi-group)	$\mathrm{cm}^{-3}\ \mathrm{s}^{-1}$
t	time	s
V	volume	cm^3
$\mathbf{v}$	neutron velocity vector	$\mathrm{cm}\ \mathrm{s}^{-1}$
v	scalar magnitude of $\mathbf{v}$	$\mathrm{cm}\ \mathrm{s}^{-1}$
x	spatial coordinate	cm
y	spatial coordinate	cm
z	spatial coordinate	cm

δ_{nm}	Kronecker delta	
ϵ_f	outer iteration tolerance criterion for the fission source	
ϵ_k	outer iteration tolerance criterion for the effective multiplication factor k_{eff}	
ϵ_{nj}	weighting factor of exponential flux ansatz	
θ	polar angle of the direction of neutron motion	rad
κ	usable energy produced per fission event	W s
μ	cosine of the polar angle θ	
ν	average number of neutrons released per fission	
$\bar{\mu}_0$	average cosine of the scattering angle	
Σ_a	macroscopic absorption cross section	cm^{-1}
Σ_f	macroscopic fission cross section	cm^{-1}
Σ_{rn}	nth moment of the macroscopic removal cross section	cm^{-1}
Σ_s	macroscopic scattering cross section	cm^{-1}
$\Sigma_{sn,gg'}$	nth moment of the macroscopic scattering cross section from energy group g' to energy group g	cm^{-1}
Σ_t	total macroscopic interaction cross section	cm^{-1}
Σ_{tr}	macroscopic transport cross section	cm^{-1}
τ_n	albedo function	
$\Phi_{n,g}$	nth neutron flux moment (multi-group)	$\text{cm}^{-2}\ \text{s}^{-1}$
φ	azimuthal angle of the direction of neutron motion	rad
χ	fission spectrum	
Ψ	angular neutron flux	$\text{cm}^{-2}\ \text{sr}^{-1}\ \text{eV}^{-1}\ \text{s}^{-1}$
Ψ_g	angular neutron flux (μ-dependent, multi-group)	$\text{cm}^{-2}\ \text{s}^{-1}$
$\mathbf{\Omega}$	unit vector in direction of neutron motion	sr

1 Introduction

In order to ensure the inherent safety and economic operation of nuclear reactors by an efficient reactor design and to estimate and limit the detrimental consequences of potential accidents, operational and incident scenarios have to be modeled by adequate simulation tools. The reliable safe operation of a nuclear reactor is highly dependent on the ability to precisely predict the neutron flux, which is needed to derive criticality, power shapes, temperature distributions, and feedback coefficients of reactivity.

1.1 Reactor physics calculations

The discipline of reactor physics studies the interactions between neutrons and matter in a nuclear reactor. Such an interaction occurs when a neutron collides with the nucleus of a specific nuclide. Two phenomena are responsible for the complexity of reactor physics. A nuclear reactor is generally a complicated three-dimensional assembly of components with different geometries made of a variety of materials, and many materials have interaction characteristics which vary strongly with neutron energy [72, c. 1].

The neutron flux in a reactor core can be obtained as the solution of the neutron transport equation. Whole-core transport calculations, however, would lead to enormous calculation times. Therefore, reactor calculations for the detailed heterogeneous geometry and the complex energy-dependent interaction characteristics are typically performed using the following three main steps, as depicted in Figure 1.1:

- the cross-section calculation [38],
- the lattice calculation [138], and
- the full-core reactor calculation [3, 159].

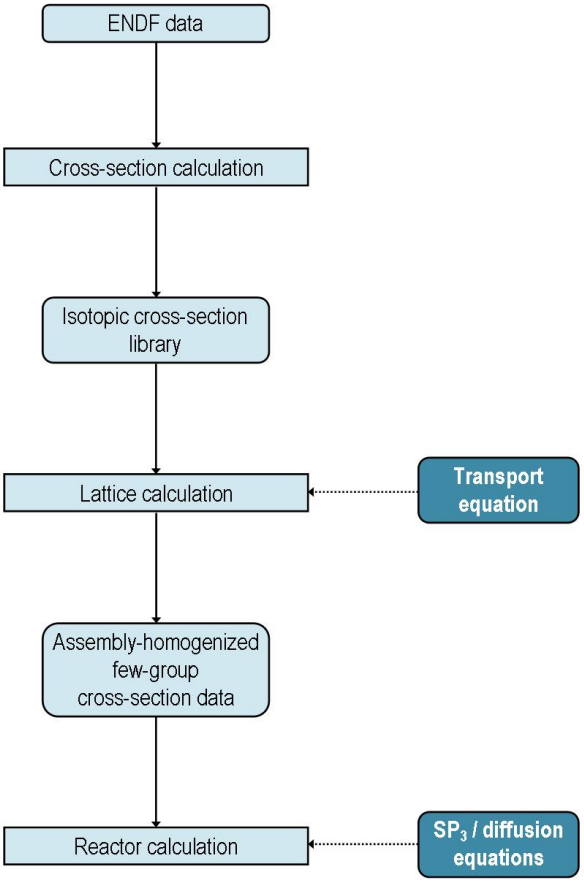

FIGURE 1.1: Data flow for reactor physics calculations (according to [72, fig. 2.29]).

Nuclear data are edited, e.g., in the Evaluated Nuclear Data File (ENDF) format [79] containing categorized information, e.g., about resonance parameters, cross-sections, energetic and angular distributions of secondary neutrons, and radioactive decay (more details are given in [72, s. 2.9]). These data are used in the cross-section calculation to produce the isotopic cross-section library [147, c. III] for the lattice code consistent with the type of transport equation solution, i.e., in multi-group structure for deterministic approaches or in continuous-energy form for Monte Carlo methods. Lattice calculations are performed for a small component of the reactor, e.g., a pin cell or an assembly, usually in a fine energy group structure and taking heterogeneous material compositions and properties into account. The operating conditions outside the small component are generally not considered (infinite two-dimensional lattice). The neutron flux obtained from the lattice calculation is used to produce cell- or assembly-homogenized flux- and volume-weighted cross sections, which are then collapsed in a coarse energy group structure. The reactor core calculation utilizes the average cross sections generated in the previous step for polygonal prisms (applying an appropriate axial core subdivision). However, even after the aforementioned cell heterogeneity is replaced by a homogenized representation, a reactor core remains a heterogeneous object because of its intra- and inter-assembly material composition. On

the scale of a full core, the neutron transport equation is generally replaced by a simplified form, e.g., the diffusion or simplified P_3 approximation (abbreviated as SP_3 approximation), which is the main focus of the present work.

1.2 The reactor dynamics code DYN3D

DYN3D is a three-dimensional nodal code for steady-state and transient analysis of nuclear reactor cores applicable to both square and hexagonal fuel assembly geometries, which has been developed at the Helmholtz-Zentrum Dresden-Rossendorf (HZDR) and its predecessor organizations since the 1980s. The code allows the simulation of the neutronic and thermal-hydraulic core response to reactivity changes caused by control-rod movements or variations of the core coolant inlet conditions, the boron acid concentration, the core pressure, or the total mass-flow rates. Burn-up and reactor-poison-dynamics calculations can also be performed [66, 67, 68].

The code is undergoing continuous development with respect to the improvement of the physical models and the numerical methods. Originally, it was developed for Russian VVERs with hexagonal-geometry fuel assemblies, applying a two-group nodal neutron diffusion method [65], and then extended to square-geometry western-type light-water reactors (LWRs) [66]. A multi-group approach was introduced [61] in order to improve the description of spectral effects, which are increasingly important for mixed-oxide LWR loadings, but also for innovative nuclear reactor designs [53, 94, 133, 136]. Furthermore, the SP_3 approximation of the multi-group transport equation was implemented on the basis of Cartesian geometries [9].

DYN3D is one of the deterministic reference core codes of the European reactor simulation platform NURESIM [26, 27, 137].

1.3 Research objectives

The commonly used and most widely accepted approximation to the transport equation for performing full-core reactor calculations is the diffusion equation. This approach does not include the direction-of-motion variables and, therefore, requires low computational effort. Physically, it places the following rather stringent restrictions:

- The neutron migration process must be dominated by scattering interactions, i.e., the material must be highly scattering and weakly absorbing for neutrons.

- The neutron migration process must be sufficiently far removed from material where large gradients in the neutron density may occur.

However, quoting Alcouffe and O'Dell [3]: "[...] diffusion theory has been [...] found to perform better [in practice] than it theoretically has any right to."

Although the diffusion approach provides a sufficiently accurate prediction of the neutron flux in a wide spectrum of reactor problems without resolving the complexities of the directional neutron transport, a simplified transport method, such as the SP_3 method, is able to capture anisotropic transport effects without a drastic increase in computational resources.

Besides VVERs, innovative reactor concepts like the sodium-cooled fast reactor (SFR) [1] and the block-type high-temperature gas-cooled reactor (HTGR) (or very-high-temperature reactor (VHTR)) [2] are based on hexagonal fuel assembly geometries. As a hexagon can not be subdivided into hexagons of smaller size, hexagonal-geometry reactor problems are effectively discretized as cells consisting of equilateral triangles. Hence, there has been the necessity of developing both a diffusion and an SP_3 model based on trigonal geometry for the code DYN3D to enable advanced hexagonal reactor core analysis including the capability of mesh refinement.

The important innovative aspects of the trigonal DYN3D models developed here are the following:

- As yet, none of the worldwide well-established core analysis codes comprises a multi-group SP_3 transport theory model based on nodal triangular meshes and, therefore, combines the advantage of the capability to capture anisotropic transport effects with the possibility of mesh refinement for hexagonal fuel assembly geometries.
- The specific approach used to approximate the neutron flux within the trigonal prisms is unique for both the diffusion and the SP_3 transport theory. It combines the so-called transverse-integration procedure, leading to a computationally efficient numerical method, with a sophisticated flux expansion ansatz based on polynomial and exponential functions, which provides high performance.

The development of two methods based on different approximations of the transport equation but using identical underlying spatial discretization allows a profound comparative analysis of both methods with regard to their mathematical derivations, nodal expansion approaches, solution procedures, and especially their physical performance, but also with regard to aspects of the respective computational outlay.

Apart from the necessary technical development to equip the code with trigonal mesh capability, this thesis provides an answer to the following question:

> Which degree of improvement can be achieved by the trigonal nodal DYN3D SP_3 transport method in comparison to the respective diffusion method?

1.4 Thesis outline

The main part of this thesis addresses the theoretical examination and derivation of the nodal diffusion and SP_3 solution approaches to the neutron transport equation based on trigonal geometry.

In Chapter 2, an introduction to the neutron transport equation is given. Different solution approaches are briefly described. A particular focus, however, is put on the simplified P_N (or SP_N) transport method, which provides a basis for both the SP_3 and the diffusion approaches. The respective equations are derived including boundary conditions.

In Chapter 3, the concept of nodal methods is outlined comprising a comprehensive literature review. The characteristics of a method based on trigonal geometry are identified. The transverse-leakage procedure is introduced and the specific expansion ansatzes of the unknown functions are derived in trigonal geometry. Additionally, the hitherto existing DYN3D expansion approaches in Cartesian and hexagonal geometries are outlined.

Chapter 4 of this thesis is concerned with the rigorous development of the numerical solution procedure for the SP_3 transport and diffusion equations in trigonal geometry. The response-matrix equations are derived leading to an iterative procedure involving inner and outer iteration cycles by which finally the core neutron flux distribution can be computed.

In Chapter 5, a numerical analysis of the performance of the trigonal SP_3 transport and diffusion methods developed in the previous chapters is demonstrated with particular regard to mesh refinement analyses. Several hexagonal benchmark and test problems with different material compositions are studied. The respective computation times are evaluated.

In Chapter 6, finally, the conclusions are presented and suggestions for future work are given.

2 Neutron Transport Methods

The behavior of a nuclear reactor is governed by the transport of neutrons and the interactions between neutrons and matter.

An introduction to the neutron transport equation and its solution approaches is given in Sections 2.1 and 2.2 with particular regard to the simplified P_N (or SP_N) transport method in Section 2.3. In Sections 2.4 and 2.5, the SP_3 and diffusion equations are derived including interface and boundary conditions.

The following facts will become evident by the end of this chapter:

- Both the SP_3 transport and diffusion approach represent efficient solution techniques capable to perform whole-core reactor calculations.
- The SP_3 equations in within-group form are of diffusion type, which allows the use of very similar solution strategies for both approaches.
- In contrast to diffusion theory, the SP_3 approach takes higher-order neutron flux moments into account, which enables the description of anisotropic neutron migration processes.

2.1 The neutron transport equation

Regarding a neutron as a point particle, it has a position $\mathbf{r}$ and a velocity $\mathbf{v} = v\mathbf{\Omega}$, where v denotes the scalar magnitude of the velocity and $\mathbf{\Omega}(\mu, \varphi)$ is the unit vector in the direction of neutron motion. In a polar coordinate system, $\mu \in [-1, 1]$ describes the cosine of the polar angle θ and $\varphi \in [0, 2\pi]$ specifies the azimuthal angle as shown in Figure 2.1.

The distribution of neutrons in a reactor core is defined by the angular neutron density function $N(\mathbf{r}, \mathbf{\Omega}, E, t)$, which represents the expected number of neutrons at the position $\mathbf{r}$

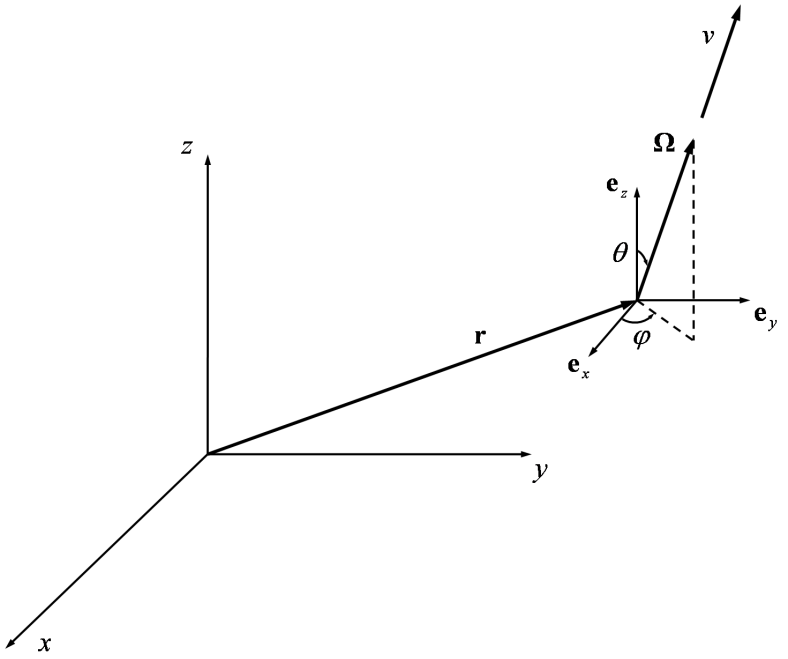

FIGURE 2.1: Position and direction variables characterizing a neutron (according to [45, fig. 4-2]).

with direction $\mathbf{\Omega}$ and energy E at a time t per unit volume per unit solid angle per unit energy. The product of the neutron speed v and the angular neutron density is called the angular neutron flux:

$$vN(\mathbf{r}, \mathbf{\Omega}, E, t) \equiv \Psi(\mathbf{r}, \mathbf{\Omega}, E, t)$$

[12, s. 1.1]. Referring to the derivations, e.g., by Duderstadt and Hamilton [45, c. 4] or Stacey [146, s. 9.1], an equation for $\Psi(\mathbf{r}, \mathbf{\Omega}, E, t)$ can be derived by balancing the mechanisms by which neutrons, that are traveling in a specific direction $\mathbf{\Omega}$ and that are characterized by a specific energy E, can be gained or lost from a differential volume element $\mathrm{d}V$ at the position $\mathbf{r}$. The time rate of change of $N(\mathbf{r}, \mathbf{\Omega}, E, t)$ within this volume equals

- the rate at which neutrons within the solid angle interval $\mathrm{d}\mathbf{\Omega}$ about $\mathbf{\Omega}$ and of the energy interval $\mathrm{d}E$ about E are streaming into the volume $\mathrm{d}V$ ①
- less the rate at which neutrons of $\mathbf{\Omega}, E$ are streaming out of the volume ②,
- plus the rate at which neutrons of $\mathbf{\Omega}, E$ are being introduced into the volume by scattering of neutrons within the volume from different directions $\mathbf{\Omega}'$ and different energies E' ③,
- plus the rate at which neutrons of $\mathbf{\Omega}, E$ are being generated within the volume by fission ④,

- plus the rate at which neutrons of $\mathbf{\Omega}, E$ are being introduced into the volume by an external source ⑤,
- minus the rate at which neutrons of $\mathbf{\Omega}, E$ within the volume are being absorbed ⑥,
- minus the rate at which neutrons of $\mathbf{\Omega}, E$ within the volume are being scattered into a different direction $\mathbf{\Omega}'$ or different energy E' ⑦.

Hence, we have

$$\frac{1}{v}\frac{\partial}{\partial t}\Psi(\mathbf{r},\mathbf{\Omega},E,t) = S(\mathbf{r},\mathbf{\Omega},E,t) - \underbrace{\mathbf{\Omega}\cdot\nabla\Psi(\mathbf{r},\mathbf{\Omega},E,t)}_{②\text{-}①} - \underbrace{\Sigma_t(\mathbf{r},E,t)\Psi(\mathbf{r},\mathbf{\Omega},E,t)}_{⑥+⑦} \tag{2.1}$$

with the source term

$$S(\mathbf{r},\mathbf{\Omega},E,t) = \underbrace{S_s(\mathbf{r},\mathbf{\Omega},E,t)}_{③} + \underbrace{S_f(\mathbf{r},\mathbf{\Omega},E,t)}_{④} + \underbrace{S_{\text{ext}}(\mathbf{r},\mathbf{\Omega},E,t)}_{⑤}. \tag{2.2}$$

The balance relation (2.1) is known as the neutron transport equation and provides an exact description of the neutron distribution within a reactor. Σ_t denotes the total macroscopic interaction cross section. The macroscopic absorption cross section $\Sigma_a = \Sigma_t - \Sigma_s$ is defined to characterize any other event than scattering [45, c. 2].

In the steady-state case, the neutron transport equation (2.1) with (2.2) reduces to

$$\mathbf{\Omega}\cdot\nabla\Psi(\mathbf{r},\mathbf{\Omega},E) + \Sigma_t(\mathbf{r},E)\Psi(\mathbf{r},\mathbf{\Omega},E) = S_s(\mathbf{r},\mathbf{\Omega},E) + S_f(\mathbf{r},\mathbf{\Omega},E) + S_{\text{ext}}(\mathbf{r},\mathbf{\Omega},E). \tag{2.3}$$

Applying the normalization

$$\int \mathrm{d}\mathbf{\Omega} = 1,$$

the scattering and fission sources are integral functions of the angular neutron flux, i.e.,

$$S_s(\mathbf{r},\mathbf{\Omega},E) = \iint_0^\infty \Sigma_s(\mathbf{r},\mathbf{\Omega}'\to\mathbf{\Omega},E'\to E)\Psi(\mathbf{r},\mathbf{\Omega}',E')\mathrm{d}E'\mathrm{d}\mathbf{\Omega}',$$
$$S_f(\mathbf{r},\mathbf{\Omega},E) \equiv S_f(\mathbf{r},E) = \chi(\mathbf{r},E)\iint_0^\infty \nu\Sigma_f(\mathbf{r},E')\Psi(\mathbf{r},\mathbf{\Omega}',E')\mathrm{d}E'\mathrm{d}\mathbf{\Omega}',$$

where Σ_s denotes the macroscopic scattering cross section. χ describes the fission spectrum, ν the average number of neutrons released per fission, and Σ_f the macroscopic fission cross section. Therefore, the transport equations stated above are integro-differential equations.

Even without considering time dependence, there are six independent variables, three for the space, two describing a direction on the unit sphere, and one for energy, which makes the solution of transport problems a difficult task.

2.2 Solution methods for the neutron transport equation

Different approaches can be used to solve the neutron transport equation. The most accurate and most expensive technique is the Monte Carlo method. The second class of neutron transport methods comprises deterministic solution techniques, which are based on approximations related to energetic and spatial discretizations and the limitation of the angular representation. Numerical analysis methods have to be applied to the transport equation [72, c. 3].

2.2.1 Monte Carlo methods

The Monte Carlo (MC) method simulates a neutron population on the basis of a stochastic process. The life of a single neutron is traced from its initial emission (or birth) until its death by capture or leakage out of the system using a sequence of random numbers to simulate the random physical events according to cross-section and collision laws. In a Monte Carlo calculation, the criticality source iteration (eigenvalue problem in steady state) is run in cycles and the source distribution of each cycle is formed by the fission reaction distribution of the previous cycle, while the number of source neutrons per cycle is fixed. Before starting to collect the results, inactive cycles are run in order to allow the initial fission source distribution to converge. The statistical accuracy of the results depends on the total number of active neutron histories run, which is determined by the neutron population size per cycle and the total number of active cycles [110]. The Monte Carlo method is exact, as far as the geometry and the interactions are correctly represented and as far as the number of neutron histories is sufficiently large. Therefore, the Monte Carlo result can be a detailed simulation of the steady-state neutron transport process [72, s. 3.11].

Monte Carlo methods are mostly used to study difficult and nonstandard situations, such as complex geometries, and to validate deterministic results. Their disadvantage is the high computational cost. See also [111, c. 7] for further discussion.

2.2.2 Deterministic methods

Treating the energy variable E in the neutron transport equation as not being continuous but dividing the neutron energy spectrum into a number of discrete intervals, called energy groups, leads to the use of multi-group methods [12, c. 4].

The collision probability (CP) approach is a deterministic multi-group method treating general unstructured meshes. It applies a specialized "ray-tracing" routine to span a sufficiently large number of neutron trajectories over the spatial domains in the given geometry. These trajectories are then used to generate the appropriate collision probability matrices in the number of required energy groups. The collision matrices are dense, so that the method may involve high computational costs. Therefore, collision probability methods are mainly used for two-dimensional cell and assembly transport problems [72, s. 3.8].

The method of characteristics (MOC) solves the multi-group transport equation along straight paths of the neutron, called characteristics, as it moves across the complete system. This approach is based on an iterative calculation of the neutron flux. It applies to discrete directions and arbitrary spatial domains with nuclear properties assumed to be constant. The methodology allows for an accurate treatment of highly heterogeneous systems and is preferred to the collision probability method in cases where the number of regions exceeds a few hundreds [72, s. 3.10]. Since the method of characteristics accounts for uncollided neutron trajectories inside a cell, it is more suitable for problems in which streaming dominates scattering [139]. It is routinely used for two-dimensional cell and assembly transport calculations.

A method applicable to three-dimensional core calculations is the discrete ordinates (or S_N) method. The essential basis of this method is the treatment of the angular variable $\mathbf{\Omega}$ as a set of N discrete directions in the multi-group neutron transport equation. Each direction is characterized by a direction cosine, which is chosen to integrate the appropriate quadrature ansatz functions with maximum accuracy. Different quadrature sets are used depending on the type of geometry. In the limit of $N \to \infty$, the S_N solution converges to the true transport solution. However, this is subject to the limitations of the computing resources [72, s. 3.9]. Furthermore, the discrete ordinates method may suffer from anomalies in the neutron flux distribution, called ray effects [111, s. 4-6].

Another approach for solving the multi-group neutron transport equation is the spherical harmonics (or P_N) method. It is based on the expansion of the directional dependence $\mathbf{\Omega}$ of the angular flux Ψ in spherical harmonics. Truncating this series after a finite number of terms, i.e., $N + 1$, leads to the P_N approximation [72, s. 3.7]. This method is characterized by the following properties [100]:

- As the order N of the approximation increases to infinity, the exact transport solution is obtained.
- The P_N equations are free from ray effects.
- In three-dimensional geometries, the number of P_N equations grows like $(N+1)^2$. In one-dimensional planar geometry, the number of P_N equations is only $N+1$.

Although it is possible to consider full three-dimensional P_N core calculations, they significantly strain computing resources. A closely related approximation to the P_N method, based on the solution of the simplified P_N equations, leads to a more efficient solution technique that can be used for full-core calculations as will be discussed in detail in the following.

2.3 Theoretical aspects of the simplified P_N method

The spherical harmonics equations in multi-dimensional geometries are complicated. In addition to a large number of equations, the complexity arises from the fact that both components μ and φ of the angular variable $\mathbf{\Omega}$ are inherent in the spherical harmonics expansion. The complex coupling involves not only the angular moments but also complicated cross-derivative terms [14, 57, 119]. However, limiting the calculation to $N = 1$, which leads to the diffusion approximation, can turn out to be insufficient [73, 114].

About half a century ago, Gelbard [54, 55, 56] proposed a simplification of the P_N equations, the simplified P_N (or SP_N) equations. This approximation evolves from the planar-geometry P_N equations, which are relatively simple, and involves an ad hoc substitution of the one-dimensional second-order derivatives by the three-dimensional Laplacian operator. Hence, the SP_N equations can be considered a multi-dimensional generalization of the planar-geometry P_N equations. Compared to the full spherical harmonics approximation, this simplification substantially reduces the number of unknowns and avoids the complexities thereof.

Two facts should be noted comparing the SP_N with the P_N method [72, s. 3.7.4]:

- The SP_1 method is equivalent to the P_1 method in multi-dimensional geometries.
- For all values of N, the SP_N method is equivalent to the P_N method in one-dimensional geometry.

The SP_N method is based on an expansion of the angular flux Ψ in an incomplete basis of orthogonal functions. In two- and three-dimensional cases, this does not guarantee the

convergence of the numerical results as N increases. However, SP_N results have proven to be more accurate than P_1 solutions in many reactor problems. It is a common assertion based on experience and numerical experimentation that the maximum potential accuracy is obtained around SP_5 or SP_7 [119].

The SP_N equations can be derived by different approaches. Gelbard's [54] original idea yields only a formal derivation involving an ad hoc substitution of the multivariable differential operators, which is only a weak theoretical basis of the simplified P_N approximation. Larsen et al. [99, 100, 101] as well as Pomraning [130] used asymptotic analysis and independently provided theoretical foundation for the numerical accuracy of the SP_N method. However, neither of these asymptotic derivations includes boundary conditions. The SP_N equations can also be derived using variational analysis [12, s. 6.4]. On the basis of variational methods, Tomašević and Larsen [155, 157] derived the simplified P_2 equations, whereas Brantley and Larsen [15, 16] accordingly established the theoretical foundation of the SP_3 method. The variational analysis is also able to provide interface and boundary conditions for the SP_N equations.

This work focuses on the SP_3 approximation, where the number of second-order equations to be solved equals two. This is significantly less than with the multi-dimensional P_3 equations. Therefore, the SP_3 method is conceived a compromise between calculation precision and cost.

2.4 Derivation of the steady-state simplified P_N equations

With the awareness of the theoretical foundation of the simplified P_N method via asymptotic or variational analysis, we focus on the derivation of the SP_N equations by Gelbard's [54] formal procedure (cf. [10] or any well-known reactor physics textbook, e.g., [146, s. 9.6]). We begin by considering the planar-geometry P_N approximation in Section 2.4.1 deriving in particular the one-dimensional P_3 and P_1 equations. The three-dimensional generalization for the P_3 equations with full anisotropic scattering is given in Section 2.4.2, its modification allowing only within-group higher-order anisotropic scattering in Section 2.4.3. Finally, the diffusion approximation is derived from the P_1 equations in Section 2.4.4.

2.4.1 The planar-geometry P_N equations

While the spherical harmonics equations in multi-dimensional geometries are complicated, the P_N equations in one-dimensional planar geometry are relatively simple.

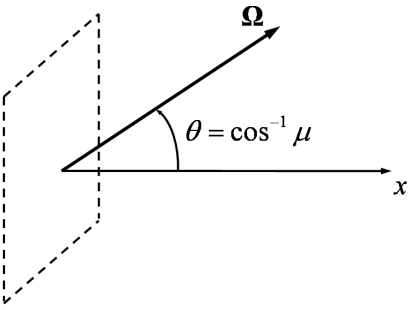

FIGURE 2.2: Planar-geometry coordinates (according to [45, fig. 4-9]).

Let the steady-state neutron transport equation of (2.3) in one-dimensional geometry

$$\mu \frac{\partial}{\partial x} \Psi(x, \mu, E) + \Sigma_t(x, E) \Psi(x, \mu, E) = S_s(x, \mu, E) + S_f(x, E) + S_{\text{ext}}(x, \mu, E) \tag{2.4}$$

be the starting point for the following derivation of the planar-geometry P_N equations. For convenience, the angular coordinate system is chosen with its polar coordinate axis in the x-direction. The assumption of planar geometry implies that there is no dependence on the azimuthal angle φ. Hence, in equation (2.4), the occurring angular dependent neutron flux Ψ, the total macroscopic cross section Σ_t, the neutron scattering source S_s, the fission source S_f, and the external source S_{ext} only depend on a single spatial coordinate x and the cosine of the polar angle $\mu = \cos\theta$ with θ being the direction of neutron motion as depicted in Figure 2.2. Discretizations in space and energy are introduced and constant cross sections are assumed for the resulting spatial intervals with the indices $i \in (1, \ldots, I)$ and energy groups $g \in (1, \ldots, G)$, where $g = 1$ denotes the fastest group. The macroscopic cross sections used in the subsequent equations are averaged values over space and energy and determined via flux-volume weighting of the heterogeneous cross sections applying the flux obtained from the lattice calculation (cf. Figure 1.1). Assuming furthermore the absence of an external source, the following multi-group form of the above neutron transport equation holds:

$$\mu \frac{\partial}{\partial x} \Psi_g^i(x, \mu) + \Sigma_{t,g}^i \Psi_g^i(x, \mu) = S_{s,g}^i(x, \mu) + S_{f,g}^i(x) \tag{2.5}$$

with $x \in [x_{i-1}, x_i]$ and x_{i-1}, x_i being the respective lower and upper interval bounds. The angular dependence of the flux and source functions in equation (2.5) can be approximated by a truncated series expansion. Therefore, the Legendre polynomials $p_n(\mu)$ are introduced representing the one-dimensional equivalents of the spherical harmonics, the

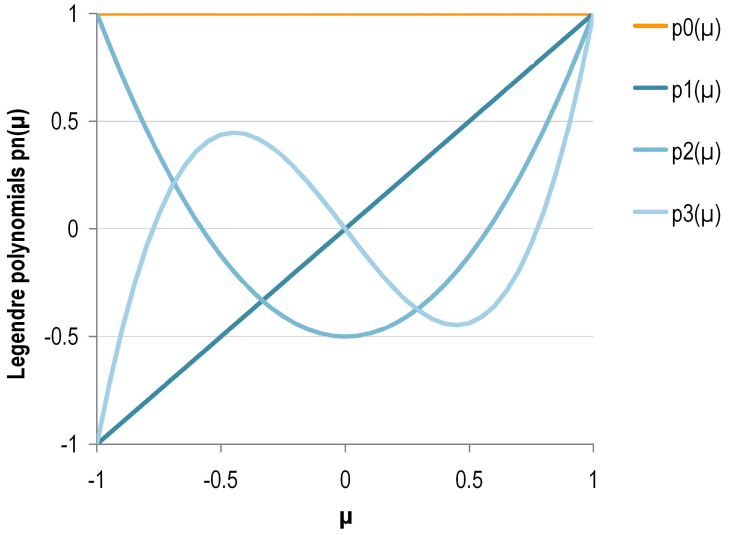

FIGURE 2.3: Graphs of the Legendre polynomials p_n up to $n = 3$.

expansion functions of the P_N equations. Like the spherical harmonic functions, the Legendre polynomials

$$\begin{aligned} p_0(\mu) &= 1, \\ p_1(\mu) &= \mu, \\ p_2(\mu) &= \frac{1}{2}(3\mu^2 - 1), \\ p_3(\mu) &= \frac{1}{2}(5\mu^3 - 3\mu), \\ &\vdots \end{aligned}$$

(see Figure 2.3) form an orthogonal system with the properties

$$\int_{-1}^{1} p_n(\mu) p_m(\mu) \mathrm{d}\mu = \frac{2}{2n+1} \delta_{nm} \tag{2.6}$$

and

$$\mu p_n(\mu) = \frac{n}{2n+1} p_{n-1}(\mu) + \frac{n+1}{2n+1} p_{n+1}(\mu), \qquad n \geq 1, \tag{2.7}$$

where δ_{nm} denotes the Kronecker delta. According to this, the angular neutron flux Ψ and

the angle-dependent scattering term S_s are expanded into Legendre series as follows:

$$\begin{aligned}\Psi^i_g(x,\mu) &= \sum_{n=0}^{\infty}(2n+1)p_n(\mu)\Phi^i_{n,g}(x)\\ &\approx \sum_{n=0}^{N}(2n+1)p_n(\mu)\Phi^i_{n,g}(x), \qquad (2.8)\\ S^i_{s,g}(x,\mu) &= \sum_{n=0}^{\infty}(2n+1)p_n(\mu)\sum_{g'=1}^{G}\Sigma^i_{sn,gg'}\Phi^i_{n,g'}(x)\\ &\approx \sum_{n=0}^{N}(2n+1)p_n(\mu)\sum_{g'=1}^{G}\Sigma^i_{sn,gg'}\Phi^i_{n,g'}(x) \qquad (2.9)\end{aligned}$$

with finite order of truncation $N \in \mathbb{N}$. The quantity

$$\Phi^i_{n,g}(x) \equiv \frac{1}{2}\int_{-1}^{1} p_n(\mu)\Psi^i_g(x,\mu)\mathrm{d}\mu \qquad (2.10)$$

is the nth Legendre-weighted moment of the neutron flux increasing its directional variation with n. $\Sigma^i_{sn,gg'}$ denotes the nth moment of the macroscopic scattering cross section from energy group g' to energy group g. Inserting the expansions (2.8)–(2.9) into the transport equation (2.5) and applying the recursion formula (2.7) gives

$$\begin{aligned}&\sum_{n=0}^{N}\big(np_{n-1}(\mu)+(n+1)p_{n+1}(\mu)\big)\frac{\partial}{\partial x}\Phi^i_{n,g}(x)+\sum_{n=0}^{N}(2n+1)p_n(\mu)\Sigma^i_{t,g}\Phi^i_{n,g}(x)\\ &\quad=\sum_{n=0}^{N}(2n+1)p_n(\mu)\sum_{g'=1}^{G}\Sigma^i_{sn,gg'}\Phi^i_{n,g'}(x)+S^i_{f,g}(x).\end{aligned}$$

Multiplying these equations with $p_m(\mu)$ for $m = 0, \ldots, N$ and integrating over $\mu \in [-1, 1]$ by taking the orthogonality condition (2.6) into account and assuming $\Phi^i_{-1,g}(x) = \Phi^i_{N+1,g}(x) \equiv 0$, the following $N+1$ steady-state P_N equations for the $N+1$ unknown flux moments $\Phi^i_{n,g}$ are obtained in planar geometry:

$$\frac{n}{2n+1}\frac{\mathrm{d}}{\mathrm{d}x}\Phi^i_{n-1,g}(x)+\frac{n+1}{2n+1}\frac{\mathrm{d}}{\mathrm{d}x}\Phi^i_{n+1,g}(x)+\Sigma^i_{t,g}\Phi^i_{n,g}(x)=\sum_{g'=1}^{G}\Sigma^i_{sn,gg'}\Phi^i_{n,g'}(x)+\check{S}^i_{n,g}(x),$$
$$n = 0, \ldots, N.$$

The occurring isotropic source term

$$\begin{aligned}\check{S}^i_{0,g}(x) &= \frac{1}{k_{\mathrm{eff}}}S^i_{f,g}(x)\\ &= \frac{1}{k_{\mathrm{eff}}}\chi^i_g\sum_{g'=1}^{G}\nu\Sigma^i_{f,g'}\Phi^i_{0,g'}(x)\end{aligned}$$

comprises the fission source S_f and the effective multiplication factor k_{eff} to create an eigenvalue problem, whereas

$$\check{S}^i_{n,g}(x) = 0, \qquad n > 0.$$

Truncating the series expansions of (2.8)–(2.9) after the fourth term, i.e., $N = 3$, the four first-order linear differential equations

$$\frac{\mathrm{d}}{\mathrm{d}x}\Phi^i_{1,g}(x) \; + \Sigma^i_{t,g}\Phi^i_{0,g}(x) = \sum_{g'=1}^{G} \Sigma^i_{s0,gg'}\Phi^i_{0,g'}(x) + \check{S}^i_{0,g}(x), \tag{2.11}$$

$$\frac{1}{3}\frac{\mathrm{d}}{\mathrm{d}x}\Phi^i_{0,g}(x) + \frac{2}{3}\frac{\mathrm{d}}{\mathrm{d}x}\Phi^i_{2,g}(x) + \Sigma^i_{t,g}\Phi^i_{1,g}(x) = \sum_{g'=1}^{G} \Sigma^i_{s1,gg'}\Phi^i_{1,g'}(x), \tag{2.12}$$

$$\frac{2}{5}\frac{\mathrm{d}}{\mathrm{d}x}\Phi^i_{1,g}(x) + \frac{3}{5}\frac{\mathrm{d}}{\mathrm{d}x}\Phi^i_{3,g}(x) + \Sigma^i_{t,g}\Phi^i_{2,g}(x) = \sum_{g'=1}^{G} \Sigma^i_{s2,gg'}\Phi^i_{2,g'}(x), \tag{2.13}$$

$$\frac{3}{7}\frac{\mathrm{d}}{\mathrm{d}x}\Phi^i_{2,g}(x) + \qquad\qquad \Sigma^i_{t,g}\Phi^i_{3,g}(x) = \sum_{g'=1}^{G} \Sigma^i_{s3,gg'}\Phi^i_{3,g'}(x) \tag{2.14}$$

represent the one-dimensional P_3 equations for the energy group g with full anisotropic scattering. Describing the angular dependence of Ψ and S_s only linearly anisotropic, i.e., up to $N = 1$, the system above reduces to the well-known one-dimensional P_1 equations

$$\frac{\mathrm{d}}{\mathrm{d}x}\Phi^i_{1,g}(x) + \Sigma^i_{t,g}\Phi^i_{0,g}(x) = \sum_{g'=1}^{G} \Sigma^i_{s0,gg'}\Phi^i_{0,g'}(x) + \check{S}^i_{0,g}(x), \tag{2.15}$$

$$\frac{1}{3}\frac{\mathrm{d}}{\mathrm{d}x}\Phi^i_{0,g}(x) + \Sigma^i_{t,g}\Phi^i_{1,g}(x) = \sum_{g'=1}^{G} \Sigma^i_{s1,gg'}\Phi^i_{1,g'}(x). \tag{2.16}$$

The above systems of P_3 and P_1 equations show that the consideration of full anisotropic scattering – from energy group to energy group and within the particular groups – results in a coupling of the equations over all energy groups.

2.4.2 The SP_3 equations with full anisotropic scattering

Defining the vector functions

$$\boldsymbol{\Phi}^i_n(x) = \begin{pmatrix} \Phi^i_{n,1}(x) \\ \Phi^i_{n,2}(x) \\ \vdots \\ \Phi^i_{n,G}(x) \end{pmatrix} \qquad \text{and} \qquad \check{\mathbf{S}}^i_0(x) = \begin{pmatrix} \check{S}^i_{0,1}(x) \\ \check{S}^i_{0,2}(x) \\ \vdots \\ \check{S}^i_{0,G}(x) \end{pmatrix}$$

with[1]

$$\check{S}^i_{0,g}(x) = \frac{1}{k_{\text{eff}}}\chi^i_g\left\langle \boldsymbol{\Sigma}^i_{vf}, \boldsymbol{\Phi}^i_0(x)\right\rangle \qquad \text{and} \qquad \boldsymbol{\Sigma}^i_{vf} = \begin{pmatrix} \nu\Sigma^i_{f,1} \\ \nu\Sigma^i_{f,2} \\ \vdots \\ \nu\Sigma^i_{f,G} \end{pmatrix}$$

as well as the matrices

$$\boldsymbol{\Sigma}^i_n = \begin{pmatrix} \Sigma^i_{t,1} - \Sigma^i_{sn,11} & -\Sigma^i_{sn,12} & \cdots & -\Sigma^i_{sn,1G} \\ -\Sigma^i_{sn,21} & \Sigma^i_{t,2} - \Sigma^i_{sn,22} & \ddots & \vdots \\ \vdots & \ddots & \ddots & -\Sigma^i_{sn,G-1G} \\ -\Sigma^i_{sn,G1} & \cdots & -\Sigma^i_{sn,GG-1} & \Sigma^i_{t,G} - \Sigma^i_{sn,GG} \end{pmatrix}, \qquad n = 0, ..., 3,$$

the equations (2.11)–(2.14) can be rewritten in the following matrix form:

$$\frac{\mathrm{d}}{\mathrm{d}x}\boldsymbol{\Phi}^i_1(x) \; + \boldsymbol{\Sigma}^i_0\boldsymbol{\Phi}^i_0(x) = \check{\mathbf{S}}^i_0(x), \tag{2.17}$$

$$\frac{1}{3}\frac{\mathrm{d}}{\mathrm{d}x}\boldsymbol{\Phi}^i_0(x) + \frac{2}{3}\frac{\mathrm{d}}{\mathrm{d}x}\boldsymbol{\Phi}^i_2(x) + \boldsymbol{\Sigma}^i_1\boldsymbol{\Phi}^i_1(x) = 0, \tag{2.18}$$

$$\frac{2}{5}\frac{\mathrm{d}}{\mathrm{d}x}\boldsymbol{\Phi}^i_1(x) + \frac{3}{5}\frac{\mathrm{d}}{\mathrm{d}x}\boldsymbol{\Phi}^i_3(x) + \boldsymbol{\Sigma}^i_2\boldsymbol{\Phi}^i_2(x) = 0, \tag{2.19}$$

$$\frac{3}{7}\frac{\mathrm{d}}{\mathrm{d}x}\boldsymbol{\Phi}^i_2(x) + \qquad\qquad \boldsymbol{\Sigma}^i_3\boldsymbol{\Phi}^i_3(x) = 0. \tag{2.20}$$

The equations (2.18) and (2.20) yield the expressions

$$\boldsymbol{\Phi}^i_1(x) = -\frac{1}{3}(\boldsymbol{\Sigma}^i_1)^{-1}\frac{\mathrm{d}}{\mathrm{d}x}\left(\boldsymbol{\Phi}^i_0(x) + 2\boldsymbol{\Phi}^i_2(x)\right),$$
$$\boldsymbol{\Phi}^i_3(x) = -\frac{3}{7}(\boldsymbol{\Sigma}^i_3)^{-1}\frac{\mathrm{d}}{\mathrm{d}x}\boldsymbol{\Phi}^i_2(x)$$

for the odd-order flux moments. Hence, $\boldsymbol{\Phi}^i_1$ and $\boldsymbol{\Phi}^i_3$ can be eliminated from (2.17) and (2.19). With

$$\frac{\mathrm{d}}{\mathrm{d}x}\boldsymbol{\Phi}^i_1(x) = -\boldsymbol{\Sigma}^i_0\boldsymbol{\Phi}^i_0(x) + \check{\mathbf{S}}^i_0(x)$$

from (2.17), we obtain the following second-order differential system of equations:

$$-\frac{1}{3}(\boldsymbol{\Sigma}^i_1)^{-1}\frac{\mathrm{d}^2}{\mathrm{d}x^2}\left(\boldsymbol{\Phi}^i_0(x) + 2\boldsymbol{\Phi}^i_2(x)\right) + \boldsymbol{\Sigma}^i_0\boldsymbol{\Phi}^i_0(x) = \check{\mathbf{S}}^i_0(x), \tag{2.21}$$

$$-\frac{9}{35}(\boldsymbol{\Sigma}^i_3)^{-1}\frac{\mathrm{d}^2}{\mathrm{d}x^2}\boldsymbol{\Phi}^i_2(x) - \frac{2}{5}\boldsymbol{\Sigma}^i_0\boldsymbol{\Phi}^i_0(x) + \boldsymbol{\Sigma}^i_2\boldsymbol{\Phi}^i_2(x) = -\frac{2}{5}\check{\mathbf{S}}^i_0(x). \tag{2.22}$$

[1]The inner product $\langle\cdot,\cdot\rangle : \mathbb{R}^G \times \mathbb{R}^G \to \mathbb{R}$ denotes a generalized scalar product over the vector space $\mathbb{R}^G$. Note that the geometrical scalar product is designated by the centered dot '$\cdot$' in this document.

Introducing the diagonal matrices

$$\boldsymbol{\Sigma}^i_{\mathrm{diag},n} = \begin{pmatrix} \Sigma^i_{t,1} - \Sigma^i_{sn,11} & 0 & \dots & 0 \\ 0 & \Sigma^i_{t,2} - \Sigma^i_{sn,22} & \ddots & \vdots \\ \vdots & \ddots & \ddots & 0 \\ 0 & \dots & 0 & \Sigma^i_{t,G} - \Sigma^i_{sn,GG} \end{pmatrix}, \qquad n = 0, ..., 3,$$

the matrix diffusion coefficients can be defined as

$$\mathbf{D}^i_0 := \frac{1}{3}(\boldsymbol{\Sigma}^i_{\mathrm{diag},1})^{-1} = \frac{1}{3} \begin{pmatrix} \frac{1}{\Sigma^i_{t,1} - \Sigma^i_{s1,11}} & 0 & \dots & 0 \\ 0 & \frac{1}{\Sigma^i_{t,2} - \Sigma^i_{s1,22}} & \ddots & \vdots \\ \vdots & \ddots & \ddots & 0 \\ 0 & \dots & 0 & \frac{1}{\Sigma^i_{t,G} - \Sigma^i_{s1,GG}} \end{pmatrix}$$

and, respectively,

$$\mathbf{D}^i_2 := \frac{9}{35}(\boldsymbol{\Sigma}^i_{\mathrm{diag},3})^{-1} = \frac{9}{35} \begin{pmatrix} \frac{1}{\Sigma^i_{t,1} - \Sigma^i_{s3,11}} & 0 & \dots & 0 \\ 0 & \frac{1}{\Sigma^i_{t,2} - \Sigma^i_{s3,22}} & \ddots & \vdots \\ \vdots & \ddots & \ddots & 0 \\ 0 & \dots & 0 & \frac{1}{\Sigma^i_{t,G} - \Sigma^i_{s3,GG}} \end{pmatrix}.$$

So, the system (2.21)–(2.22) can be written as

$$\begin{aligned} -\mathbf{D}^i_0 \boldsymbol{\Sigma}^i_{\mathrm{diag},1} (\boldsymbol{\Sigma}^i_1)^{-1} \frac{\mathrm{d}^2}{\mathrm{d}x^2} \left(\boldsymbol{\Phi}^i_0(x) + 2\boldsymbol{\Phi}^i_2(x) \right) + \boldsymbol{\Sigma}^i_0 \boldsymbol{\Phi}^i_0(x) &= \check{\mathbf{S}}^i_0(x), \\ -\mathbf{D}^i_2 \boldsymbol{\Sigma}^i_{\mathrm{diag},3} (\boldsymbol{\Sigma}^i_3)^{-1} \frac{\mathrm{d}^2}{\mathrm{d}x^2} \boldsymbol{\Phi}^i_2(x) - \frac{2}{5} \boldsymbol{\Sigma}^i_0 \boldsymbol{\Phi}^i_0(x) + \boldsymbol{\Sigma}^i_2 \boldsymbol{\Phi}^i_2(x) &= -\frac{2}{5} \check{\mathbf{S}}^i_0(x). \end{aligned}$$

Defining now the modified neutron flux moment vectors

$$\begin{aligned} \hat{\boldsymbol{\Phi}}^i_0(x) &:= \boldsymbol{\Sigma}^i_{\mathrm{diag},1} (\boldsymbol{\Sigma}^i_1)^{-1} \left(\boldsymbol{\Phi}^i_0(x) + 2\boldsymbol{\Phi}^i_2(x) \right), \\ \hat{\boldsymbol{\Phi}}^i_2(x) &:= \boldsymbol{\Sigma}^i_{\mathrm{diag},3} (\boldsymbol{\Sigma}^i_3)^{-1} \boldsymbol{\Phi}^i_2(x), \end{aligned}$$

the above system results in the system of second-order differential equations

$$-\mathbf{D}^i_0 \frac{\mathrm{d}^2}{\mathrm{d}x^2} \hat{\boldsymbol{\Phi}}^i_0(x) + \boldsymbol{\Sigma}^i_{01} \hat{\boldsymbol{\Phi}}^i_0(x) - 2\boldsymbol{\Sigma}^i_{03} \hat{\boldsymbol{\Phi}}^i_2(x) = \check{\mathbf{S}}^i_0(x), \tag{2.23}$$

$$-\mathbf{D}^i_2 \frac{\mathrm{d}^2}{\mathrm{d}x^2} \hat{\boldsymbol{\Phi}}^i_2(x) - \frac{2}{5} \boldsymbol{\Sigma}^i_{01} \hat{\boldsymbol{\Phi}}^i_0(x) + \left(\frac{4}{5} \boldsymbol{\Sigma}^i_{03} + \boldsymbol{\Sigma}^i_{23} \right) \hat{\boldsymbol{\Phi}}^i_2(x) = -\frac{2}{5} \check{\mathbf{S}}^i_0(x) \tag{2.24}$$

with the matrices

$$\mathbf{\Sigma}^i_{01} = \mathbf{\Sigma}^i_0 \mathbf{\Sigma}^i_1 (\mathbf{\Sigma}^i_{\text{diag},1})^{-1}, \tag{2.25}$$

$$\mathbf{\Sigma}^i_{03} = \mathbf{\Sigma}^i_0 \mathbf{\Sigma}^i_3 (\mathbf{\Sigma}^i_{\text{diag},3})^{-1}, \tag{2.26}$$

$$\mathbf{\Sigma}^i_{23} = \mathbf{\Sigma}^i_2 \mathbf{\Sigma}^i_3 (\mathbf{\Sigma}^i_{\text{diag},3})^{-1}. \tag{2.27}$$

As mentioned before, the SP_3 concept has evolved from the idea of a multi-dimensional generalization of the one-dimensional P_3 equations. Thus, the ad hoc replacement of the second derivatives in (2.23)–(2.24) by the general Laplacian operators yields the following equations in three-dimensional form:

$$-\mathbf{D}^i_0 \Delta \hat{\mathbf{\Phi}}^i_0(\mathbf{r}) + \mathbf{\Sigma}^i_{01} \hat{\mathbf{\Phi}}^i_0(\mathbf{r}) - 2\mathbf{\Sigma}^i_{03} \hat{\mathbf{\Phi}}^i_2(\mathbf{r}) = \check{\mathbf{S}}^i_0(\mathbf{r}), \tag{2.28}$$

$$-\mathbf{D}^i_2 \Delta \hat{\mathbf{\Phi}}^i_2(\mathbf{r}) - \frac{2}{5}\mathbf{\Sigma}^i_{01} \hat{\mathbf{\Phi}}^i_0(\mathbf{r}) + \left(\frac{4}{5}\mathbf{\Sigma}^i_{03} + \mathbf{\Sigma}^i_{23}\right) \hat{\mathbf{\Phi}}^i_2(\mathbf{r}) = -\frac{2}{5}\check{\mathbf{S}}^i_0(\mathbf{r}) \tag{2.29}$$

with the gth component

$$\begin{aligned} \check{S}^i_{0,g}(\mathbf{r}) &= \frac{1}{k_{\text{eff}}} \chi^i_g \left\langle \mathbf{\Sigma}^i_{\nu f}, \mathbf{\Phi}^i_0(\mathbf{r}) \right\rangle \\ &= \frac{1}{k_{\text{eff}}} \chi^i_g \left\langle \mathbf{\Sigma}^i_{\nu f}, \mathbf{\Sigma}^i_1 (\mathbf{\Sigma}^i_{\text{diag},1})^{-1} \hat{\mathbf{\Phi}}^i_0(\mathbf{r}) - 2\mathbf{\Sigma}^i_3 (\mathbf{\Sigma}^i_{\text{diag},3})^{-1} \hat{\mathbf{\Phi}}^i_2(\mathbf{r}) \right\rangle, \end{aligned}$$

$g = 1, \ldots, G$, of the source term vector function $\check{\mathbf{S}}^i_0(\mathbf{r})$.

Since the above system of second-order differential equations (2.28)–(2.29) takes the full anisotropic scattering into account, the coefficient matrices $\mathbf{\Sigma}^i_{01}$, $\mathbf{\Sigma}^i_{03}$, and $\mathbf{\Sigma}^i_{23}$ in (2.25)–(2.27) are dense. Consequently, the SP_3 equations are coupled over all energy groups $g = 1, \ldots, G$. For a sufficiently large G, solving $2G$ coupled equations implies an extensive numerical effort. Therefore, the anisotropic group-to-group scattering is neglected in the following applying the so-called within-group approximation.

2.4.3 The SP_3 equations in within-group form

Let the one-dimensional P_3 equations in first-order form (2.11)–(2.14) be the starting point. Brantley and Larsen [16] as well as Beckert and Grundmann [10] described the SP_3 equations in the so-called within-group form. The approximation involved assumes only isotropic neutron scattering between different energy groups, i.e.,

$$\Sigma^i_{sn,gg'} = 0 \qquad \text{for} \qquad g' \neq g \qquad \text{and} \qquad n \geq 1. \tag{2.30}$$

With this assumption, the P_3 equations (2.11)–(2.14) become merely coupled via the isotropic scattering source. Taking the definition of the removal cross sections

$$\Sigma^i_{rn,g} := \Sigma^i_{t,g} - \Sigma^i_{sn,gg}, \qquad n = 0, ..., 3, \tag{2.31}$$

into account, they can be written as

$$\frac{\mathrm{d}}{\mathrm{d}x}\Phi^i_{1,g}(x) \; + \Sigma^i_{r0,g}\Phi^i_{0,g}(x) = \sum_{\substack{g'=1\\g'\neq g}}^{G} \Sigma^i_{s0,gg'}\Phi^i_{0,g'}(x) + \check{S}^i_{0,g}(x), \tag{2.32}$$

$$\frac{1}{3}\frac{\mathrm{d}}{\mathrm{d}x}\Phi^i_{0,g}(x) + \frac{2}{3}\frac{\mathrm{d}}{\mathrm{d}x}\Phi^i_{2,g}(x) + \Sigma^i_{r1,g}\Phi^i_{1,g}(x) = 0, \tag{2.33}$$

$$\frac{2}{5}\frac{\mathrm{d}}{\mathrm{d}x}\Phi^i_{1,g}(x) + \frac{3}{5}\frac{\mathrm{d}}{\mathrm{d}x}\Phi^i_{3,g}(x) + \Sigma^i_{r2,g}\Phi^i_{2,g}(x) = 0, \tag{2.34}$$

$$\frac{3}{7}\frac{\mathrm{d}}{\mathrm{d}x}\Phi^i_{2,g}(x) + \qquad\qquad \Sigma^i_{r3,g}\Phi^i_{3,g}(x) = 0. \tag{2.35}$$

By dint of the equations (2.33) and (2.35), the odd-order flux moments $\Phi^i_{1,g}$ and $\Phi^i_{3,g}$ can be eliminated from the equations (2.32) and (2.34) also in this case. Hence,

$$\Phi^i_{1,g}(x) = -\frac{1}{3\Sigma^i_{r1,g}}\frac{\mathrm{d}}{\mathrm{d}x}\left(\Phi^i_{0,g}(x) + 2\Phi^i_{2,g}(x)\right) \tag{2.36}$$

and

$$\Phi^i_{3,g}(x) = -\frac{3}{7\Sigma^i_{r3,g}}\frac{\mathrm{d}}{\mathrm{d}x}\Phi^i_{2,g}(x) \tag{2.37}$$

as well as the diffusion coefficients defined as

$$D^i_{0,g} := \frac{1}{3\Sigma^i_{r1,g}} \qquad \text{and} \qquad D^i_{2,g} := \frac{9}{35\Sigma^i_{r3,g}} \tag{2.38}$$

give the system of second-order ordinary differential equations

$$-D^i_{0,g}\frac{\mathrm{d}^2}{\mathrm{d}x^2}\left(\Phi^i_{0,g}(x) + 2\Phi^i_{2,g}(x)\right) + \Sigma^i_{r0,g}\Phi^i_{0,g}(x) = \sum_{\substack{g'=1\\g'\neq g}}^{G} \Sigma^i_{s0,gg'}\Phi^i_{0,g'}(x) + \check{S}^i_{0,g}(x), \tag{2.39}$$

$$-\frac{2}{5}D^i_{0,g}\frac{\mathrm{d}^2}{\mathrm{d}x^2}\left(\Phi^i_{0,g}(x) + 2\Phi^i_{2,g}(x)\right) - D^i_{2,g}\frac{\mathrm{d}^2}{\mathrm{d}x^2}\Phi^i_{2,g}(x) + \Sigma^i_{r2,g}\Phi^i_{2,g}(x) = 0 \tag{2.40}$$

and, accordingly,

$$-D^i_{0,g}\frac{\mathrm{d}^2}{\mathrm{d}x^2}\widetilde{\Phi}^i_{0,g}(x) + \Sigma^i_{r0,g}\widetilde{\Phi}^i_{0,g}(x) - 2\Sigma^i_{r0,g}\widetilde{\Phi}^i_{2,g}(x) = S^i_{0,g}(x), \tag{2.41}$$

$$-D^i_{2,g}\frac{\mathrm{d}^2}{\mathrm{d}x^2}\widetilde{\Phi}^i_{2,g}(x) - \frac{2}{5}\Sigma^i_{r0,g}\widetilde{\Phi}^i_{0,g}(x) + \left(\frac{4}{5}\Sigma^i_{r0,g} + \Sigma^i_{r2,g}\right)\widetilde{\Phi}^i_{2,g}(x) = -\frac{2}{5}S^i_{0,g}(x) \tag{2.42}$$

with the new source term

$$\begin{aligned}\widetilde{S}^i_{0,g}(x) &= \sum_{\substack{g'=1\\g'\neq g}}^{G} \Sigma^i_{s0,gg'}\left(\widetilde{\Phi}^i_{0,g'}(x) - 2\widetilde{\Phi}^i_{2,g'}(x)\right) + \check{S}^i_{0,g}(x) \\ &= \sum_{\substack{g'=1\\g'\neq g}}^{G} \Sigma^i_{s0,gg'}\left(\widetilde{\Phi}^i_{0,g'}(x) - 2\widetilde{\Phi}^i_{2,g'}(x)\right) + \frac{1}{k_{\text{eff}}}\chi^i_g \sum_{g'=1}^{G} \nu\Sigma^i_{f,g'}\left(\widetilde{\Phi}^i_{0,g'}(x) - 2\widetilde{\Phi}^i_{2,g'}(x)\right)\end{aligned}$$

and the modified neutron flux moments

$$\widetilde{\Phi}^i_{0,g}(x) := \Phi^i_{0,g}(x) + 2\Phi^i_{2,g}(x), \tag{2.43}$$

$$\widetilde{\Phi}^i_{2,g}(x) := \Phi^i_{2,g}(x). \tag{2.44}$$

The substitutional expressions (2.43)–(2.44) are introduced to manipulate the second-order form P_3 equations (2.39)–(2.40) into a form (2.41)–(2.42) that resembles a set of diffusion-like equations. The subsequently described nodal expansion method treats the quantities $\widetilde{\Phi}^i_{0,g}$ and $\widetilde{\Phi}^i_{2,g}$. The actual flux moments $\Phi^i_{0,g}$ and $\Phi^i_{2,g}$ are only recalculated at the very end of the calculation procedure.

In analogous manner to the previous subsection, the three-dimensional form of the SP_3 equations is obtained by substituting the one-dimensional second derivatives in (2.41)–(2.42) by the general Laplacian operators. Hence, we obtain the following system of second-order elliptic partial differential equations, the SP_3 equations

$$-D^i_{0,g}\Delta\widetilde{\Phi}^i_{0,g}(\mathbf{r}) + \Sigma^i_{r0,g}\widetilde{\Phi}^i_{0,g}(\mathbf{r}) - 2\Sigma^i_{r0,g}\widetilde{\Phi}^i_{2,g}(\mathbf{r}) = \widetilde{S}^i_{0,g}(\mathbf{r}), \tag{2.45}$$

$$-D^i_{2,g}\Delta\widetilde{\Phi}^i_{2,g}(\mathbf{r}) - \frac{2}{5}\Sigma^i_{r0,g}\widetilde{\Phi}^i_{0,g}(\mathbf{r}) + \left(\frac{4}{5}\Sigma^i_{r0,g} + \Sigma^i_{r2,g}\right)\widetilde{\Phi}^i_{2,g}(\mathbf{r}) = -\frac{2}{5}\widetilde{S}^i_{0,g}(\mathbf{r}) \tag{2.46}$$

with

$$\widetilde{S}^i_{0,g}(\mathbf{r}) = \sum_{\substack{g'=1\\g'\neq g}}^{G} \Sigma^i_{s0,gg'}\left(\widetilde{\Phi}^i_{0,g'}(\mathbf{r}) - 2\widetilde{\Phi}^i_{2,g'}(\mathbf{r})\right) + \frac{1}{k_{\text{eff}}}\chi^i_g \sum_{g'=1}^{G} \nu\Sigma^i_{f,g'}\left(\widetilde{\Phi}^i_{0,g'}(\mathbf{r}) - 2\widetilde{\Phi}^i_{2,g'}(\mathbf{r})\right) \tag{2.47}$$

and the unknowns $\widetilde{\Phi}^i_{0,g}$ and $\widetilde{\Phi}^i_{2,g}$ being now dependent on the three-dimensional position vector $\mathbf{r}$. The index i now indicates a volume element with spatially constant cross sections.

The derivation above is based on the consideration of only isotropic scattering between different energy groups. However, also a linearly anisotropic angular dependence of the group-to-group scattering can be included allowing for a further approximation discussed in the following. We now assume

$$\Sigma^i_{sn,gg'} = 0, \qquad g' \neq g, \qquad \text{only for} \qquad n \geq 2$$

(compare (2.30)) and, consequently, the P_3 equations (2.11)–(2.14) reduce to

$$\begin{aligned}
\frac{\mathrm{d}}{\mathrm{d}x}\Phi^i_{1,g}(x) \;+\Sigma^i_{r0,g}\Phi^i_{0,g}(x) &= \sum_{\substack{g'=1\\g'\neq g}}^{G}\Sigma^i_{s0,gg'}\Phi^i_{0,g'}(x)+\check{S}^i_{0,g}(x),\\
\frac{1}{3}\frac{\mathrm{d}}{\mathrm{d}x}\Phi^i_{0,g}(x)+\frac{2}{3}\frac{\mathrm{d}}{\mathrm{d}x}\Phi^i_{2,g}(x)+\Sigma^i_{r1,g}\Phi^i_{1,g}(x) &= \sum_{\substack{g'=1\\g'\neq g}}^{G}\Sigma^i_{s1,gg'}\Phi^i_{1,g'}(x),\\
\frac{2}{5}\frac{\mathrm{d}}{\mathrm{d}x}\Phi^i_{1,g}(x)+\frac{3}{5}\frac{\mathrm{d}}{\mathrm{d}x}\Phi^i_{3,g}(x)+\Sigma^i_{r2,g}\Phi^i_{2,g}(x) &= 0,\\
\frac{3}{7}\frac{\mathrm{d}}{\mathrm{d}x}\Phi^i_{2,g}(x)+\qquad\qquad\Sigma^i_{r3,g}\Phi^i_{3,g}(x) &= 0
\end{aligned}$$

with the linearly anisotropic scattering term $\Sigma^i_{s1,gg'}\Phi^i_{1,g'}$. The derivation of the SP_3 equations can be continued in the aforementioned manner, however, with the exception that the diffusion coefficient now obtains the artificial form

$$D^i_{0,g}(x) := \frac{1}{3\left(\Sigma^i_{r1,g}-\sum_{\substack{g'=1\\g'\neq g}}^{G}\Sigma^i_{s1,gg'}\frac{\Phi^i_{1,g'}(x)}{\Phi^i_{1,g}(x)}\right)} = \frac{1}{3\left(\Sigma^i_{t,g}-\sum_{g'=1}^{G}\Sigma^i_{s1,gg'}\frac{\Phi^i_{1,g'}(x)}{\Phi^i_{1,g}(x)}\right)}, \tag{2.48}$$

which depends on the neutron flux $\Phi^i_{1,g}$. A common procedure for avoiding this difficulty is to take account of the heuristic argument that the contribution from the slowing down of neutrons from energy groups $g' > g$ is assumed almost the same as the slowing down from g to lower energy groups [12, s. 4.2d]. Thus, the assumption

$$\sum_{g'=1}^{G}\Sigma^i_{s1,gg'}\Phi^i_{1,g'}(x) \approx \sum_{g'=1}^{G}\Sigma^i_{s1,g'g}\Phi^i_{1,g}(x) \tag{2.49}$$

simplifies the diffusion coefficient (2.48) to

$$D^i_{0,g} \approx \frac{1}{3\left(\Sigma^i_{t,g}-\sum_{g'=1}^{G}\Sigma^i_{s1,g'g}\right)} = \frac{1}{3\left(\Sigma^i_{t,g}-\bar{\mu}_{0,g}\sum_{g'=1}^{G}\Sigma^i_{s0,g'g}\right)} =: \frac{1}{3\Sigma^i_{tr,g}} \tag{2.50}$$

with the average cosine of the scattering angle $\bar{\mu}_{0,g}$ and the transport cross section $\Sigma^i_{tr,g}$. The approximation (2.49) is also considered by Beckert and Grundmann [10].

In principle, the SP_3 equations (2.45)–(2.46) in within-group form are of the same structure as the SP_3 equations (2.28)–(2.29) considering full anisotropic scattering. However, approximating the linearly anisotropic group-to-group scattering by using the transport cross section and allowing only anisotropic within-group scattering, the respective system of equations is merely coupled via the isotropic group-to-group scattering, which is treated as a source term in the following. It is shown in Chapter 4 that, in the so-called inner iteration procedure, only one pair of coupled equations has to be solved separately for

each energy group g (instead of $2G$ coupled equations in the full anisotropic scattering case). This provides a reasonable compromise to obtain an efficient numerical solution as previous works [8, 9, 16, 91, 123, 140] have shown.

2.4.4 The diffusion equation with transport correction

In the previous section, two second-order differential equations are obtained from four first-order differential equations. Considering now the P_1 equations of (2.15)–(2.16), a single second-order differential equation is derived in the following. With the aid of assumption (2.49), the odd-order flux moment $\Phi^i_{1,g}$ can be eliminated from equation (2.16) via

$$\Phi^i_{1,g}(x) = -D^i_{0,g}\frac{\mathrm{d}}{\mathrm{d}x}\Phi^i_{0,g}(x), \tag{2.51}$$

where $D^i_{0,g}$ denotes the transport-corrected diffusion coefficient of (2.50). Hence, applying (2.51) to the first P_1 equation (2.15), the planar-geometry diffusion equation

$$-D^i_{0,g}\frac{\mathrm{d}^2}{\mathrm{d}x^2}\Phi^i_{0,g}(x) + \Sigma^i_{r0,g}\Phi^i_{0,g}(x) = \sum_{\substack{g'=1\\g'\neq g}}^{G}\Sigma^i_{s0,gg'}\Phi^i_{0,g'}(x) + \check{S}^i_{0,g}(x)$$

is obtained with the removal cross section

$$\Sigma^i_{r0,g} := \Sigma^i_{t,g} - \Sigma^i_{s0,gg}.$$

It is seen that the planar P_1 equations lead to diffusion theory in which the contribution of the anisotropic scattering to the energy transfer is approximated.

In three dimensions, the same is true if also the spatial derivatives of higher flux moments $\Phi^i_{2,g}$ and anisotropic neutron sources $\check{S}^i_{n,g}$, $n > 0$, can be neglected [146, s. 9.7]. We accordingly have the three-dimensional steady-state diffusion equation

$$-D^i_{0,g}\Delta\Phi^i_{0,g}(\mathbf{r}) + \Sigma^i_{r0,g}\Phi^i_{0,g}(\mathbf{r}) = S^i_{0,g}(\mathbf{r}) \tag{2.52}$$

with the modified source term

$$\begin{aligned} S^i_{0,g}(\mathbf{r}) &= \sum_{\substack{g'=1\\g'\neq g}}^{G}\Sigma^i_{s0,gg'}\Phi^i_{0,g'}(\mathbf{r}) + \check{S}^i_{0,g}(\mathbf{r}) \\ &= \sum_{\substack{g'=1\\g'\neq g}}^{G}\Sigma^i_{s0,gg'}\Phi^i_{0,g'}(\mathbf{r}) + \frac{1}{k_{\mathrm{eff}}}\chi^i_g\sum_{g'=1}^{G}\nu\Sigma^i_{f,g'}\Phi^i_{0,g'}(\mathbf{r}). \end{aligned}$$

2.5 Interface and exterior boundary conditions

To obtain solutions to the SP_3 and diffusion equations, boundary conditions have to be defined. As these equations are furthermore not defined at interfaces where cross sections are discontinuous, also interface conditions are required. Assuming again a one-dimensional geometry for the beginning, the true boundary conditions

$$\Psi_g^i(x_i, \mu) = \Psi_g^{i+1}(x_i, \mu) \tag{2.53}$$

at a nodal interface x_i and

$$\Psi_g^i(x_b, \mu) = \Psi_g^b(x_b, \mu), \qquad \mu < 0, \tag{2.54}$$

at an outer boundary x_b, respectively, where Ψ_g^b represents a known incident angular flux at the exterior position x_b in the incoming direction μ, can not be satisfied exactly by the finite angular flux approximation (2.8). Therefore, approximate boundary conditions have to be developed. The most obvious way is to substitute (2.8) into the exact boundary conditions of (2.53) and (2.54), respectively.

Hence, for arbitrary material interfaces and $N = 3$, we trivially obtain

$$\begin{aligned}
\Phi_{0,g}^i(x_i) &= \Phi_{0,g}^{i+1}(x_i),\\
\Phi_{1,g}^i(x_i) &= \Phi_{1,g}^{i+1}(x_i),\\
\Phi_{2,g}^i(x_i) &= \Phi_{2,g}^{i+1}(x_i),\\
\Phi_{3,g}^i(x_i) &= \Phi_{3,g}^{i+1}(x_i).
\end{aligned}$$

Taking the relations (2.36)–(2.37) and the definitions (2.38), (2.50), and (2.43)–(2.44) into account, the above conditions can be rewritten involving only the modified flux moments of zeroth and second order:

$$\begin{aligned}
\widetilde{\Phi}_{0,g}^i(x_i) &= \widetilde{\Phi}_{0,g}^{i+1}(x_i),\\
D_{0,g}^i \frac{\mathrm{d}}{\mathrm{d}x}\widetilde{\Phi}_{0,g}^i(x_i) &= D_{0,g}^{i+1} \frac{\mathrm{d}}{\mathrm{d}x}\widetilde{\Phi}_{0,g}^{i+1}(x_i),\\
\widetilde{\Phi}_{2,g}^i(x_i) &= \widetilde{\Phi}_{2,g}^{i+1}(x_i),\\
D_{2,g}^i \frac{\mathrm{d}}{\mathrm{d}x}\widetilde{\Phi}_{2,g}^i(x_i) &= D_{2,g}^{i+1} \frac{\mathrm{d}}{\mathrm{d}x}\widetilde{\Phi}_{2,g}^{i+1}(x_i).
\end{aligned}$$

Generalizing to three dimensions, the interface conditions

$$\widetilde{\Phi}_{n,g}^i(\mathbf{r}) = \widetilde{\Phi}_{n,g}^j(\mathbf{r}), \tag{2.55}$$

$$D_{n,g}^i\, \mathbf{n}_i \cdot \nabla\widetilde{\Phi}_{n,g}^i(\mathbf{r}) = D_{n,g}^j\, \mathbf{n}_i \cdot \nabla\widetilde{\Phi}_{n,g}^j(\mathbf{r}), \qquad \mathbf{r} \in \partial V^{ij}, \qquad n = 0, 2, \tag{2.56}$$

hold, where $\partial V^{ij} = \partial V^i \cap \partial V^j = V^i \cap V^j$ indicates the interface between two nonoverlapping volumes V^i and V^j with their boundaries ∂V^i and ∂V^j, respectively, and $\mathbf{n}_i$ denotes the unit outer normal vector of V^i directed towards V^j.

In case of an outer boundary, we substitute (2.8) for $N = 3$ into (2.54), multiply by the Legendre polynomial $p_m(|\mu|)$ and the factor $\frac{1}{2}$, integrate over $\mu < 0$, and obtain the two Marshak boundary conditions [146, p. 333f.]

$$\frac{1}{2}\int_{-1}^{0} p_m(|\mu|)\sum_{n=0}^{3}(2n+1)p_n(\mu)\Phi^i_{n,g}(x_b)\mathrm{d}\mu = \frac{1}{2}\int_{-1}^{0} p_m(|\mu|)\Psi^b_g(x_b,\mu)\mathrm{d}\mu, \qquad m = 1,3. \tag{2.57}$$

As the odd Legendre polynomials represent directionality, only those are taken into account as weighting functions. Thus, using $p_1(|\mu|) = -\mu$, $\mu < 0$, gives

$$\frac{1}{4}\Phi^i_{0,g}(x_b) - \frac{1}{2}\Phi^i_{1,g}(x_b) + \frac{5}{16}\Phi^i_{2,g}(x_b) = \frac{1}{2}\int_{-1}^{0}|\mu|\Psi^b_g(x_b,\mu)\mathrm{d}\mu.$$

With the polynomial $p_3(|\mu|) = -\frac{1}{2}(5\mu^3 - 3\mu)$, $\mu < 0$, and an additional factor $\frac{3}{5}$, we have

$$-\frac{3}{80}\Phi^i_{0,g}(x_b) + \frac{3}{16}\Phi^i_{2,g}(x_b) - \frac{3}{10}\Phi^i_{3,g}(x_b) = \frac{3}{5}\frac{1}{2}\int_{-1}^{0} p_3(|\mu|)\Psi^b_g(x_b,\mu)\mathrm{d}\mu.$$

Applying also here (2.36)–(2.37), (2.38), (2.50), and (2.43)–(2.44), and generalizing to multidimensional geometries, we finally get the Marshak-like boundary conditions

$$\frac{1}{4}\widetilde{\Phi}^i_{0,g}(\mathbf{r}) + \frac{1}{2}D^i_{0,g}\,\mathbf{n}_i\cdot\nabla\widetilde{\Phi}^i_{0,g}(\mathbf{r}) - \frac{3}{16}\widetilde{\Phi}^i_{2,g}(\mathbf{r}) = \frac{1}{4\pi}\int_0^{2\pi}\int_{-1}^{0}|\mu|\Psi^b_g(\mathbf{r},\mu,\varphi)\mathrm{d}\mu\mathrm{d}\varphi, \tag{2.58}$$

$$-\frac{3}{80}\widetilde{\Phi}^i_{0,g}(\mathbf{r}) + \frac{21}{80}\widetilde{\Phi}^i_{2,g}(\mathbf{r}) + \frac{1}{2}D^i_{2,g}\,\mathbf{n}_i\cdot\nabla\widetilde{\Phi}^i_{2,g}(\mathbf{r}) = \frac{3}{5}\frac{1}{4\pi}\int_0^{2\pi}\int_{-1}^{0} p_3(|\mu|)\Psi^b_g(\mathbf{r},\mu,\varphi)\mathrm{d}\mu\mathrm{d}\varphi, \tag{2.59}$$

$\mathbf{r} \in \partial V^{i_{\mathrm{ext}}} \subset \partial V^i$, with the exterior boundary $\partial V^{i_{\mathrm{ext}}} = V^i \cap \partial\bigcup_{i=1}^{I} V^i$ of the volume V^i and the azimuthal angle φ (see Figure 2.1). The factor $\frac{1}{4\pi}$ arises from the normalization of the integral

$$\int \mathrm{d}\mathbf{\Omega} \equiv \frac{1}{2\pi}\int_0^{2\pi}\mathrm{d}\varphi\ \frac{1}{2}\int_{-1}^{1}\mathrm{d}\mu = 1.$$

The boundary conditions (2.58)–(2.59) are called 'Marshak-like' since the Marshak boundary conditions (2.57) are traditionally defined only in one-dimensional geometries.

The derivations above are based again on Gelbard's formal approach of simply replacing the one-dimensional parameters by multivariable terms. However, Brantley [14] derived

the material interface conditions (2.55)–(2.56) and the Marshak-like boundary conditions (2.58)–(2.59) using a complex variational analysis and established a theoretical basis also of the interface and boundary conditions of SP_3 transport approximation.

With regard to diffusion theory, the interface conditions

$$\Phi^i_{0,g}(\mathbf{r}) = \Phi^j_{0,g}(\mathbf{r}), \tag{2.60}$$

$$D^i_{0,g}\,\mathbf{n}_i \cdot \nabla\Phi^i_{0,g}(\mathbf{r}) = D^j_{0,g}\,\mathbf{n}_i \cdot \nabla\Phi^j_{0,g}(\mathbf{r}), \qquad \mathbf{r} \in \partial V^{ij}, \tag{2.61}$$

and the Marshak-like boundary conditions

$$\frac{1}{4}\Phi^i_{0,g}(\mathbf{r}) + \frac{1}{2}D^i_{0,g}\,\mathbf{n}_i \cdot \nabla\Phi^i_{0,g}(\mathbf{r}) = \frac{1}{4\pi}\int_0^{2\pi}\int_{-1}^{0} |\mu|\Psi^b_g(\mathbf{r},\mu,\varphi)\mathrm{d}\mu\mathrm{d}\varphi, \qquad \mathbf{r} \in \partial V^{i_{\text{ext}}} \subset \partial V^i, \tag{2.62}$$

hold according to (2.55)–(2.56) and (2.58), respectively.

3 Nodal Reactor Analysis Methods

A reactor is a complex object in terms of its geometry, its composition, and the involved nuclear data, which renders whole-core transport calculations practically impossible. As outlined in Section 1.1, problem-specific modeling is essential to perform such calculations in practice. The determination of the full-core neutron flux is generally a result of a computational procedure based on three levels: the isotopic-cross-section calculation, the deterministic or Monte-Carlo-based lattice neutron transport calculation, and the full-core calculation. A scheme for determining the three-dimensional core flux distribution, which avoids high computational costs, is provided by nodal methods.

In Section 3.1, a brief introduction to the difficulties associated with spatial homogenization is provided to better assess the concept of nodal methods, which is described in Section 3.2. In Section 3.3, the characteristics of a method based on trigonal geometry are identified. Two key techniques of the nodal DYN3D approach are derived in Sections 3.4 and 3.5: the transverse-leakage approximation and the specific expansion of the unknown functions in trigonal geometry. In Section 3.6, the DYN3D expansion approaches in Cartesian and hexagonal geometries are presented.

The following facts will become evident by the end of this chapter:

- The superior advantage of a nodal method for reactor cores with hexagonal fuel assemblies based on trigonal geometries is its mesh refinement capability.
- The nodal approaches implemented in DYN3D are based on the transverse-integration procedure, which renders them computationally efficient. They furthermore use a combination of polynomial and exponential functions to expand the unknown neutron flux moments of the SP_3 and diffusion equations, which guarantees high accuracy.

- In both the SP_3 and the diffusion approach, the intra-nodal unknown functions are finitely represented in terms of only a small number of unknown parameters, so that the equations can be numerically processed.

3.1 Remarks on homogenization theory

As any matter, also neutrons are submerged to an equilibration process. Hence, neutrons are transported from a domain with high population density towards a reduced one. This process formulates the following heuristic relation between the neutron current and the gradient of the neutron flux, known as Fick's law [72, s. 5.1.1]:

$$\mathbf{J}(\mathbf{r}) = -D\nabla\Phi(\mathbf{r}). \tag{3.1}$$

This relation is a generalization of (2.51) and based on the assumptions of the neutron migration process being sufficiently slow varying in space and scattering dominated [146, c. 3].

Referring to Section 1.1, reactor core calculation procedures, such as nodal methods, utilize cell- or assembly-homogenized cross sections. The difficulty associated with the homogenization process is to define heterogeneous reactor properties which should be reproduced when the homogeneous problem is solved. To obtain a global power distribution with a homogenized reactor representation identical to the heterogeneous representation, the interaction between adjacent regions has to be described in an equivalent manner. To account for the influence of adjacent regions, considering local and spectral interaction, the integral reaction rates and neutron fluxes in every homogenized volume as well as the integral net currents and fluxes at the interfaces between adjacent volumes should be preserved [87].

Evaluating ideal homogenized parameters, obtained via flux-volume weighting of the heterogeneous cross sections, implies the a-priori knowledge of the solution to the heterogeneous reactor problem, which creates a practical difficulty. An additional dilemma exists in the determination of a spatially constant diffusion coefficient, which is, taking Fick's law (3.1) into account, strictly defined as the negative ratio of the heterogeneous surface current and the gradient of the homogeneous surface flux. Imposing the continuity of the interface net currents and fluxes, the values of the diffusion coefficients would be different on each surface of the homogenized volume [145].

Consequently, approximations have to be applied and some of the constraints of the homogenization theory have to be relaxed. In the framework of Koebke's equivalence theory

(ET) [87, 88] of heterogeneous and homogeneous regions, the integral reaction rates and net currents at interfaces between adjacent volumes are preserved. The flux continuity between adjacent homogenized regions, however, is no longer postulated.

To reproduce the reference heterogeneous solution, Koebke [87] introduced reference heterogeneity factors (RHFs). In Koebke's ET method, the determination of the diffusion coefficients is constrained such that the RHFs are identical on opposite volume surfaces. Using the conventional flux-volume-weighted diffusion coefficients, Smith [145] proposed the application of reference discontinuity factors (RDFs) in the framework of his generalized equivalence theory (GET). The RDF $f_{l,g}^{i}$ at a surface l of the volume V^{i} is defined for every energy group g as

$$f_{l,g}^{i} = \frac{\overline{\Phi}_{0,g}^{i,\text{het}}}{\overline{\Phi}_{0,g}^{i,\text{hom}}}, \tag{3.2}$$

where $\overline{\Phi}_{0,g}^{i,\text{het}}$ is the surface-averaged flux calculated in detailed heterogeneous geometry, and $\overline{\Phi}_{0,g}^{i,\text{hom}}$ denotes the surface-averaged flux calculated in homogenized diffusion theory. Smith [145] furthermore defined assembly discontinuity factors (ADFs) adapted to fuel assemblies, which can be computed directly from the information available in standard assembly calculations. ADFs are simply ratios of the node-surface-averaged fluxes to the node-averaged fluxes in the heterogeneous assembly calculation with zero-current boundary conditions. Tahara et al. [152] and Mittag et al. [121] derived discontinuity factors applicable to control absorbers and reflector assemblies.

For rather homogeneous assembly configurations, the ratio of (3.2) is approximately one and, hence, the use of discontinuity factors is dispensable. However, if the assembly has significant heterogeneities in the vicinity of its boundary, e.g., due to absorber pins, the effect of discontinuity factors may be relevant.

Discontinuity factors, however, have been solely defined for diffusion theory. The SP_N theory formulations, obtained from asymptotic or variational analysis, do not provide an explicit and readily evaluated representation for the corresponding angular flux solution. This makes it impossible to calculate the necessary surface discontinuity factors to force consistency between the SP_N and the transport solution. Recently, Chao and Yamamoto [25] presented a different SP_N formulation that provides the angular flux solution. However, a practical approach in order to calculate SP_N discontinuity factors is not provided.

Due to the lack of the definition of discontinuity factors for the SP_3 transport theory, the use of discontinuity factors is generally not considered in this thesis.

Spatial-homogenization methods can not only be applied to assembly-size volumes but also at the pin-cell level. Pin-cell homogenization approaches [164], such as superhomogenization (SPH) factors [64, 76, 77, 82], interface discontinuity factors (IDFs) [5, 17, 80], and pin-cell discontinuity factors (CDFs) [92, 93, 126] are also based on the well-established ET and GET described above. In the present work, however, pin-cell homogenization methods are excluded.

3.2 Characteristics of nodal methods

Realistic reactor models may contain hundreds or several thousand different homogenized regions, even after the local cell-level homogenization has been imposed. There are different numerical techniques to solve the diffusion or simplified neutron transport equations.

In the finite-difference (FD) method [50, 102], the continuous spatial dependence of the neutron flux is replaced by a finite number of flux values at discrete spatial locations. Furthermore, the occurring flux derivatives are approximated by quotients of finite differences. Accordingly, the mesh spacing should be smaller than the neutron diffusion length [146, s. 3.10]. This constraint reveals a limitation of the conventional finite-difference method since the high cost of solving core dynamics problems forces the use of methods based on coarse mesh elements. E.g., coarse-mesh finite-difference (CMFD) methods [20, 78] overcome this constraint.

In the finite-element method (FEM) [74, 103, 112, 123], the system is also cut up into finite mesh elements. The neutron flux, however, is represented by a sum of polynomial test functions in each element. Therefore, the finite-element method, particularly in an approximation higher than linear, is far more efficient than the conventional finite-difference method as the mesh elements may be an order of magnitude wider [134, s. 6.2.4].

Nodal methods also allow a reactor core to be handled with large volume elements, so-called nodes. The approach is similar to finite elements in terms of the intra-nodal flux representation by only a small number of parameters. However, the neutron currents at the nodal faces are additionally taken into consideration. Once the flux-current relationships are specified, equations with a simple structure can be constructed. On this account, nodal methods have been widely accepted for multi-dimensional reactor calculations already for a very long time [4, 48, 104, 142].

Most common nodal methods are based on transverse integration of the multi-dimensional diffusion (or diffusion-like) equations and on the transverse-leakage approximation. The idea behind a transversely integrated nodal method is to reduce a multi-dimensional transport problem to a coupled set of typically one-dimensional problems and, therefore, reduce

the computational effort. The expansion coefficients of the transverse leakage are calculated by assuming that the (usually quadratic) polynomials extend over the adjacent node surfaces. There are different classes of transversely integrated nodal methods. The analytic nodal method (ANM) [69, 71, 144] and the nodal integration method (NIM) [49], a modification of ANM, solve the one-dimensional transversely integrated equations analytically without any other approximation than the transverse leakage. However, the resulting formulation is complex making a multi-group generalization difficult. The nodal expansion method (NEM) [36, 48, 89, 132] is based on a local polynomial flux expansion which is used to determine a relationship between the mean interface partial currents and the node-averaged fluxes. Also the nodal Green's function method (NGFM) [105] is based on polynomial expansions. Furthermore, combinations of ANM and NEM were proposed, such as the semi-analytic nodal method (SANM) [47] and the hybrid ANM/NEM [42]. Using the transverse-integration procedure, however, causes limitations. The transverse-leakage term must be appropriately approximated; quadratic polynomials may not handle well large flux gradients near nodal interfaces of strong material discontinuity. Furthermore, the transverse leakage defined for nonrectangular nodes, e.g., hexagonal, triangular, or cylindrical, becomes complicated due to the occurrence of nonphysical singular terms [19, 125].

An approach for avoiding such singularities is the technique of conformal mapping, in which a polygonal or cylindrical node is conformally mapped to a rectangular node. Then traditional Cartesian-geometry nodal methods are applied, i.e., ANM [24, 131, 156] or NEM [166].

To entirely overcome the limitations of the transverse-integration procedure, Langenbuch [96, 97, 98] developed a flux expansion method in which the neutron flux is locally expanded in polynomials with coefficients determined by the weighted residual technique (similar to the finite-element method). In the interface flux nodal method developed by Chao [23], only node-interface fluxes are involved as unknown quantities. The interior fluxes are subsequently determined from the interface fluxes. Further approaches which do not use transverse integration are the analytic function expansion nodal (AFEN) method [33, 35, 81, 125] and the flux expansion nodal method (FENM) [163]. Here, the intra-nodal flux is expanded in terms of nonseparable multi-dimensional analytic basis functions satisfying the neutron diffusion or SP_3 transport equations at any point of the node. To improve the convergence property, polynomials are used instead of analytic basis functions to represent the intra-nodal flux distribution in the polynomial expansion nodal (PEN) method [31] and the higher-order polynomial expansion nodal (HOPEN) method [32].

The approach implemented in DYN3D can be regarded as a hybrid NEM/AFEN form, which was similarly used by Wagner [160] (one-dimensional NEM/AFEN approach) and Kim et al. [83] (one-dimensional NEM/AFEN approach based on conformal mapping).

Core analysis code	Nodal Method	Geometries	References
ARTEMIS	NEM	Cartesian	[129, 158]
COREDAX	AFEN	Cartesian hexagonal (only diffusion)	[29, 34, 108]
DYN3D	hybrid NEM/AFEN	Cartesian hexagonal (only diffusion) trigonal	[11, 46, 68]
PARCS	ANM, NEM	Cartesian trigonal (only diffusion)	[41, 86, 107]
SCOPE2	hybrid ANM/CMFD	Cartesian	[148, 153, 165]
SIMULATE	SANM	Cartesian	[6, 7, 47]
SUBARU	hybrid ANM/CMFD	Cartesian	[149, 150, 151]

TABLE 3.1: Summary of nodal core analysis codes comprising multi-group diffusion and SP_3 transport models.

DYN3D is a transversely integrated nodal method leading to one- or two-dimensional equations, which are to be solved. It uses local polynomial expansion ansatzes according to NEM. However, the neutron flux is additionally represented by analytic basis functions similar to the AFEN approach. In this manner, DYN3D encompasses the advantages of both methods: the efficiency of the NEM and the improved accuracy of the AFEN method.

Without any claim of completeness, a review of the worldwide well-established core analysis codes comprising both multi-group diffusion and SP_3 transport theory models is given in Table 3.1 (see also [141]).

3.3 Advantages of trigonal geometries

The obvious advantage in developing a nodal method for reactor cores with hexagonal fuel assembly geometry on a trigonal basis is the capability of mesh refinement, as a hexagon can not be subdivided into hexagons of smaller size. A further field of application is the modeling of asymmetric hexagonal fuel assemblies, which can be performed with considerably more precision in trigonal than in hexagonal geometries.

Compared to Cartesian and hexagonal geometries, triangular meshes have attracted rather scant attention in reactor core analyses. However, there are finite-difference [85, 95, 116] and finite-element [58, 59, 122] approaches in trigonal geometry. In several publications [117, 128, 161, 162], e.g., trigonal nodal methods are applied to solve the discrete ordinates form of the neutron transport equation. With regard to nodal diffusion methods,

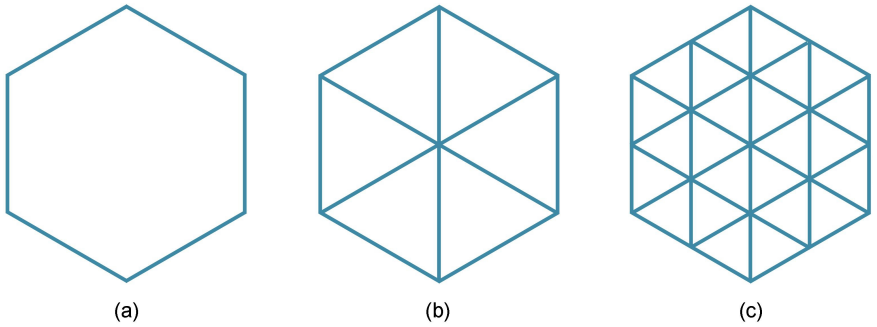

FIGURE 3.1: Hexagonal fuel assembly (a) with triangular subdivision ($m = 0$) (b) and one subsequent refinement level ($m = 1$) (c).

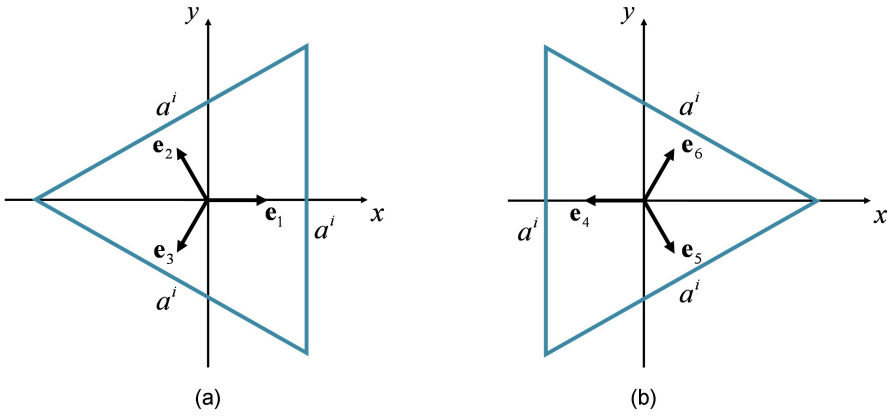

FIGURE 3.2: Nodal orientations A (a) and B (b) with indication of the local coordinate systems.

the triangle-based polynomial expansion nodal (TPEN) method [30, 44] as well as the triangular polynomial expansion nodal (TRIPEN) method [86] combine the NEM and the HOPEN method employing two transversely integrated diffusion equations, one for the radial and one for the axial direction. Also an AFEN-like method [113, 127] as well as the PEN [31] and the HOPEN methods [32] were applied to trigonal geometries. Moreover, Li et al. [113] use an AFEN-like method to solve the SP_3 equations in two-dimensional unstructured triangular geometries.

In this work, a volume element with a hexagonal radial area can be uniformly subdivided into $6 \cdot 4^m, m \in \mathbb{N}$, equilateral trigonal nodes. In Figure 3.1, the refinement mode is schematically illustrated for the first two trigonal levels ($m = 0, 1$). There are two nodal orientations to be taken into account, as depicted in Figure 3.2, with the origin of the local coordinate system in the center of the triangle. Figure 3.3 shows a prismatic node V^i with the height a_z^i and the edge length a^i of the triangular base, which is the subject of the subsequent analysis. In contrast to the Cartesian-geometry approach, the node boundaries do not coincide with the coordinate axes on either side. This fact increases the complexity of the problem.

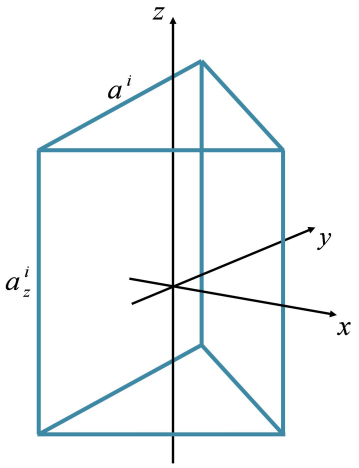

FIGURE 3.3: Prismatic node with equilateral triangular base. Indication of the local coordinate system.

3.4 PROCEDURE OF TRANSVERSE INTEGRATION

The DYN3D nodal method is based on transverse integration to scale down the volume of the numerical calculations. In trigonal geometries, the transverse-integration procedure leads to a two-dimensional radial and a one-dimensional axial set of equations as shown as follows.

Assuming the absence of an external source, let the SP_3 equations (2.45)–(2.47) in within-group form

$$-D^i_{0,g}\Delta\widetilde{\Phi}^i_{0,g}(\mathbf{r}) + \Sigma^i_{r0,g}\widetilde{\Phi}^i_{0,g}(\mathbf{r}) - 2\Sigma^i_{r0,g}\widetilde{\Phi}^i_{2,g}(\mathbf{r}) = \widetilde{S}^i_{0,g}(\mathbf{r}), \tag{3.3}$$

$$-D^i_{2,g}\Delta\widetilde{\Phi}^i_{2,g}(\mathbf{r}) - \frac{2}{5}\Sigma^i_{r0,g}\widetilde{\Phi}^i_{0,g}(\mathbf{r}) + \left(\frac{4}{5}\Sigma^i_{r0,g} + \Sigma^i_{r2,g}\right)\widetilde{\Phi}^i_{2,g}(\mathbf{r}) = -\frac{2}{5}\widetilde{S}^i_{0,g}(\mathbf{r}) \tag{3.4}$$

with the source term

$$\widetilde{S}^i_{0,g}(\mathbf{r}) = \sum_{\substack{g'=1\\g'\neq g}}^{G}\Sigma^i_{s0,gg'}\left(\widetilde{\Phi}^i_{0,g'}(\mathbf{r}) - 2\widetilde{\Phi}^i_{2,g'}(\mathbf{r})\right) + \frac{1}{k_{\text{eff}}}\chi^i_g\sum_{g'=1}^{G}\nu\Sigma^i_{f,g'}\left(\widetilde{\Phi}^i_{0,g'}(\mathbf{r}) - 2\widetilde{\Phi}^i_{2,g'}(\mathbf{r})\right) \tag{3.5}$$

and the diffusion equation (2.52)

$$-D^i_{0,g}\Delta\Phi^i_{0,g}(\mathbf{r}) + \Sigma^i_{r0,g}\Phi^i_{0,g}(\mathbf{r}) = S^i_{0,g}(\mathbf{r}) \tag{3.6}$$

with the respective source term

$$S^i_{0,g}(\mathbf{r}) = \sum_{\substack{g'=1\\g'\neq g}}^{G}\Sigma^i_{s0,gg'}\Phi^i_{0,g'}(\mathbf{r}) + \frac{1}{k_{\text{eff}}}\chi^i_g\sum_{g'=1}^{G}\nu\Sigma^i_{f,g'}\Phi^i_{0,g'}(\mathbf{r}), \qquad \mathbf{r} = (x, y, z), \tag{3.7}$$

be the starting points of the following operation. By transverse integration of (3.3)–(3.4) and (3.6), respectively, we decouple the three-dimensional equations into radial and axial components as follows.

SP_3 METHOD – RADIAL TREATMENT: Integrating over the axial height a_z^i of the node V^i leads to the two-dimensional system of SP_3 equations

$$\begin{aligned} &-D_{0,g}^i\Big(\frac{\partial^2}{\partial x^2}+\frac{\partial^2}{\partial y^2}\Big)\widetilde{\Phi}_{0,g}^{r,i}(x,y)+\Sigma_{r0,g}^i\widetilde{\Phi}_{0,g}^{r,i}(x,y)-2\Sigma_{r0,g}^i\widetilde{\Phi}_{2,g}^{r,i}(x,y)\\ &\quad=\widetilde{S}_{0,g}^{r,i}(x,y)-\widetilde{L}_{0,g}^{r,i}(x,y), \qquad (3.8)\\ &-D_{2,g}^i\Big(\frac{\partial^2}{\partial x^2}+\frac{\partial^2}{\partial y^2}\Big)\widetilde{\Phi}_{2,g}^{r,i}(x,y)-\frac{2}{5}\Sigma_{r0,g}^i\widetilde{\Phi}_{0,g}^{r,i}(x,y)+\Big(\frac{4}{5}\Sigma_{r0,g}^i+\Sigma_{r2,g}^i\Big)\widetilde{\Phi}_{2,g}^{r,i}(x,y)\\ &\quad=-\frac{2}{5}\widetilde{S}_{0,g}^{r,i}(x,y)-\widetilde{L}_{2,g}^{r,i}(x,y) \qquad (3.9)\end{aligned}$$

with the radial neutron flux moments

$$\widetilde{\Phi}_{n,g}^{r,i}(x,y)=\frac{1}{a_z^i}\int_{-\frac{a_z^i}{2}}^{\frac{a_z^i}{2}}\widetilde{\Phi}_{n,g}^i(x,y,z)\mathrm{d}z$$

as well as the radial neutron source

$$\begin{aligned}\widetilde{S}_{0,g}^{r,i}(x,y)=&\sum_{\substack{g'=1\\g'\neq g}}^{G}\Sigma_{s0,gg'}^i\big(\widetilde{\Phi}_{0,g'}^{r,i}(x,y)-2\widetilde{\Phi}_{2,g'}^{r,i}(x,y)\big)\\ &+\frac{1}{k_{\mathrm{eff}}}\chi_g^i\sum_{g'=1}^{G}\nu\Sigma_{f,g'}^i\big(\widetilde{\Phi}_{0,g'}^{r,i}(x,y)-2\widetilde{\Phi}_{2,g'}^{r,i}(x,y)\big) \qquad (3.10)\end{aligned}$$

and the term

$$\widetilde{L}_{n,g}^{r,i}(x,y)=-\frac{D_{n,g}^i}{a_z^i}\int_{-\frac{a_z^i}{2}}^{\frac{a_z^i}{2}}\frac{\partial^2}{\partial z^2}\widetilde{\Phi}_{n,g}^i(x,y,z)\mathrm{d}z,\qquad n=0,2, \qquad (3.11)$$

representing the neutron leakage into the axial direction.

SP_3 METHOD – AXIAL TREATMENT: On the other hand, integrating over the trigonal area $A_{\triangle}^i$ of the nodal element V^i gives the one-dimensional system of SP_3 equations

$$\begin{aligned}&-D_{0,g}^i\frac{\mathrm{d}^2}{\mathrm{d}z^2}\widetilde{\Phi}_{0,g}^{z,i}(z)+\Sigma_{r0,g}^i\widetilde{\Phi}_{0,g}^{z,i}(z)-2\Sigma_{r0,g}^i\widetilde{\Phi}_{2,g}^{z,i}(z)=\widetilde{S}_{0,g}^{z,i}(z)-\widetilde{L}_{0,g}^{z,i}(z), \qquad (3.12)\\ &-D_{2,g}^i\frac{\mathrm{d}^2}{\mathrm{d}z^2}\widetilde{\Phi}_{2,g}^{z,i}(z)-\frac{2}{5}\Sigma_{r0,g}^i\widetilde{\Phi}_{0,g}^{z,i}(z)+\Big(\frac{4}{5}\Sigma_{r0,g}^i+\Sigma_{r2,g}^i\Big)\widetilde{\Phi}_{2,g}^{z,i}(z)=-\frac{2}{5}\widetilde{S}_{0,g}^{z,i}(z)-\widetilde{L}_{2,g}^{z,i}(z) \qquad (3.13)\end{aligned}$$

with the axial flux moments

$$\widetilde{\Phi}^{z,i}_{n,g}(z) = \frac{4\sqrt{3}}{3(a^i)^2} \iint_{A^i_\triangle} \widetilde{\Phi}^i_{n,g}(x,y,z)\mathrm{d}A,$$

the axial source

$$\widetilde{S}^{z,i}_{0,g}(z) = \sum_{\substack{g'=1\\g'\neq g}}^{G} \Sigma^i_{s0,gg'}\big(\widetilde{\Phi}^{z,i}_{0,g'}(z) - 2\widetilde{\Phi}^{z,i}_{2,g'}(z)\big) + \frac{1}{k_{\mathrm{eff}}}\chi^i_g \sum_{g'=1}^{G} \nu\Sigma^i_{f,g'}\big(\widetilde{\Phi}^{z,i}_{0,g'}(z) - 2\widetilde{\Phi}^{z,i}_{2,g'}(z)\big),$$

and the transverse-leakage term

$$\widetilde{L}^{z,i}_{n,g}(z) = -\frac{4\sqrt{3}D^i_{n,g}}{3(a^i)^2} \iint_{A^i_\triangle} \Big(\frac{\partial^2}{\partial x^2} + \frac{\partial^2}{\partial y^2}\Big)\widetilde{\Phi}^i_{n,g}(x,y,z)\mathrm{d}A, \qquad n = 0,2, \tag{3.14}$$

describing the neutron leakage at height z into the radial directions.

The radial and the axial SP_3 equations given above are merely coupled via the transverse-leakage terms (3.11) and (3.14), which are formally treated as source terms.

Diffusion method: With respect to the three-dimensional diffusion equation (3.6) and its source term (3.7), we accordingly obtain the radial diffusion equation

$$-D^i_{0,g}\Big(\frac{\partial^2}{\partial x^2} + \frac{\partial^2}{\partial y^2}\Big)\Phi^{r,i}_{0,g}(x,y) + \Sigma^i_{r0,g}\Phi^{r,i}_{0,g}(x,y) = S^{r,i}_{0,g}(x,y) - L^{r,i}_{0,g}(x,y)$$

with the isotropic source

$$S^{r,i}_{0,g}(x,y) = \sum_{\substack{g'=1\\g'\neq g}}^{G} \Sigma^i_{s0,gg'}\Phi^{r,i}_{0,g'}(x,y) + \frac{1}{k_{\mathrm{eff}}}\chi^i_g \sum_{g'=1}^{G} \nu\Sigma^i_{f,g'}\Phi^{r,i}_{0,g'}(x,y)$$

and the transverse-leakage term

$$L^{r,i}_{0,g}(x,y) = -\frac{D^i_{0,g}}{a^i_z}\int_{-\frac{a^i_z}{2}}^{\frac{a^i_z}{2}} \frac{\partial^2}{\partial z^2}\Phi^i_{0,g}(x,y,z)\mathrm{d}z. \tag{3.15}$$

In axial direction, we analogously have the one-dimensional expression

$$-D^i_{0,g}\frac{\mathrm{d}^2}{\mathrm{d}z^2}\Phi^{z,i}_{0,g}(z) + \Sigma^i_{r0,g}\Phi^{z,i}_{0,g}(z) = S^{z,i}_{0,g}(z) - L^{z,i}_{0,g}(z)$$

with

$$S_{0,g}^{z,i}(z) = \sum_{\substack{g'=1 \\ g'\neq g}}^{G} \Sigma_{s0,gg'}^{i} \Phi_{0,g'}^{z,i}(z) + \frac{1}{k_{\text{eff}}} \chi_g^i \sum_{g'=1}^{G} \nu\Sigma_{f,g'}^{i} \Phi_{0,g'}^{z,i}(z),$$

$$L_{0,g}^{z,i}(z) = -\frac{4\sqrt{3}D_{0,g}^{i}}{3(a^i)^2} \iint_{A_{\triangle}^{i}} \Big(\frac{\partial^2}{\partial x^2} + \frac{\partial^2}{\partial y^2} \Big) \Phi_{0,g}^{i}(x, y, z) \mathrm{d}A. \tag{3.16}$$

For the sake of simplification, the node index i and the energy group index g are omitted in the following as far as possible.

3.5 Expansion of neutron flux, source, and transverse leakage in trigonal geometry

In this section, the neutron flux, source, and transverse-leakage terms are locally approximated, which is necessary to determine relationships between the interface partial currents and the fluxes in a further stage.

The unknown intra-nodal flux moments $\widetilde{\Phi}_n^r$ and $\widetilde{\Phi}_n^z$, $n = 0, 2$, are represented by the sum of a particular solution of the inhomogeneous equations and the general solution of their complementary equations, i.e., the respective homogeneous equations (according to [8, 10, 63]). Therefore, consider first the following homogeneous three-dimensional SP_3 equations:

$$-D_0 \Delta\widetilde{\Phi}_0(\mathbf{r}) + \Sigma_{r0}\widetilde{\Phi}_0(\mathbf{r}) - 2\Sigma_{r0}\widetilde{\Phi}_2(\mathbf{r}) = 0, \tag{3.17}$$

$$-D_2 \Delta\widetilde{\Phi}_2(\mathbf{r}) - \frac{2}{5}\Sigma_{r0}\widetilde{\Phi}_0(\mathbf{r}) + \Big(\frac{4}{5}\Sigma_{r0} + \Sigma_{r2} \Big) \widetilde{\Phi}_2(\mathbf{r}) = 0. \tag{3.18}$$

The general solution of the system above is obtained by means of the exponential ansatz

$$\widetilde{\Phi}_n(\mathbf{r}) = \epsilon_n \exp(B\,\mathbf{n} \cdot \mathbf{r}), \qquad \mathbf{r} = (x, y, z)^T,$$

with the buckling B^2 and the arbitrary unit vector $\mathbf{n} = (n_x, n_y, n_z)^T$. Inserting this solution approach into (3.17)–(3.18), we get

$$\Big(- D_0\epsilon_0 B^2 (n_x^2 + n_y^2 + n_z^2) + \Sigma_{r0}\epsilon_0 - 2\Sigma_{r0}\epsilon_2 \Big) \exp(B\,\mathbf{n} \cdot \mathbf{r}) = 0,$$

$$\Big(- D_2\epsilon_2 B^2 \underbrace{(n_x^2 + n_y^2 + n_z^2)}_{\equiv 1} - \frac{2}{5}\Sigma_{r0}\epsilon_0 + \Big(\frac{4}{5}\Sigma_{r0} + \Sigma_{r2} \Big) \epsilon_2 \Big) \underbrace{\exp(B\,\mathbf{n} \cdot \mathbf{r})}_{\neq 0} = 0,$$

which consequently gives the fourth-order equation for B

$$B^4 - \frac{1}{5}\Big(\frac{5\Sigma_{r0}}{D_0} + \frac{4\Sigma_{r0}}{D_2} + \frac{5\Sigma_{r2}}{D_2}\Big)B^2 + \frac{\Sigma_{r0}\Sigma_{r2}}{D_0 D_2} = 0$$

with

$$\epsilon_{0j} = 1 \qquad \text{and} \qquad \epsilon_{2j} = \frac{\Sigma_{r0} - D_0 B_j^2}{2\Sigma_{r0}}, \qquad j = 1, 2,$$

arbitrarily chosen. Hence, we obtain the two positive solutions

$$B_{1/2} = \sqrt{\frac{1}{10}\Big(\frac{5\Sigma_{r0}}{D_0} + \frac{4\Sigma_{r0}}{D_2} + \frac{5\Sigma_{r2}}{D_2}\Big) \pm \sqrt{\frac{1}{100}\Big(\frac{5\Sigma_{r0}}{D_0} + \frac{4\Sigma_{r0}}{D_2} + \frac{5\Sigma_{r2}}{D_2}\Big)^2 - \frac{\Sigma_{r0}\Sigma_{r2}}{D_0 D_2}}}.$$

SP_3 METHOD – RADIAL TREATMENT: To specify the general solution of the homogeneous equations (3.8)–(3.9), the outer normal unit vectors of the trigonal nodal faces are used (cf. Figure 3.2), i.e.,

$$\mathbf{e}_1 = \begin{pmatrix} 1 \\ 0 \end{pmatrix}, \qquad \mathbf{e}_2 = \begin{pmatrix} -\frac{1}{2} \\ \frac{\sqrt{3}}{2} \end{pmatrix}, \qquad \mathbf{e}_3 = \begin{pmatrix} -\frac{1}{2} \\ -\frac{\sqrt{3}}{2} \end{pmatrix} \tag{3.19}$$

and

$$\mathbf{e}_4 = \begin{pmatrix} -1 \\ 0 \end{pmatrix}, \qquad \mathbf{e}_5 = \begin{pmatrix} \frac{1}{2} \\ -\frac{\sqrt{3}}{2} \end{pmatrix}, \qquad \mathbf{e}_6 = \begin{pmatrix} \frac{1}{2} \\ \frac{\sqrt{3}}{2} \end{pmatrix}. \tag{3.20}$$

For the particular solution of the inhomogeneous equations (3.8)–(3.9), a polynomial ansatz is deemed appropriate. Therefore, the orthogonal polynomials of maximum order two

$$\begin{aligned} h_0^{\mathtt{A}}(x,y) &= N_0, \\ h_1^{\mathtt{A}}(x,y) &= N_1 \frac{x}{a}, \\ h_2^{\mathtt{A}}(x,y) &= -N_2 \frac{y}{a}, \\ h_3^{\mathtt{A}}(x,y) &= N_3\Big(\frac{x^2}{a^2} + \frac{y^2}{a^2}\Big) - N_4 \end{aligned} \tag{3.21}$$

and

$$\begin{aligned} h_0^{\mathtt{B}}(x,y) &= N_0, \\ h_1^{\mathtt{B}}(x,y) &= -N_1 \frac{x}{a}, \\ h_2^{\mathtt{B}}(x,y) &= N_2 \frac{y}{a}, \\ h_3^{\mathtt{B}}(x,y) &= N_3\Big(\frac{x^2}{a^2} + \frac{y^2}{a^2}\Big) - N_4 \end{aligned} \tag{3.22}$$

are chosen according to the nodal orientations A and B. With the normalization factors

$$\begin{aligned} N_0 &= 1, \\ N_1 &= 2\sqrt{6}, \\ N_2 &= 2\sqrt{6}, \\ N_3 &= 4\sqrt{15}, \\ N_4 &= \frac{1}{3}\sqrt{15}, \end{aligned}$$

they become orthonormal, i.e.,

$$\begin{aligned} &\frac{4\sqrt{3}}{3a^2} \int_{-\frac{\sqrt{3}}{3}a}^{\frac{\sqrt{3}}{6}a} \int_{-\frac{\sqrt{3}}{3}x-\frac{1}{3}a}^{\frac{\sqrt{3}}{3}x+\frac{1}{3}a} h_k^{\mathtt{A}}(x,y) h_l^{\mathtt{A}}(x,y) \mathrm{d}y \, \mathrm{d}x \\ &\quad = \frac{4\sqrt{3}}{3a^2} \int_{-\frac{\sqrt{3}}{6}a}^{\frac{\sqrt{3}}{3}a} \int_{\frac{\sqrt{3}}{3}x-\frac{1}{3}a}^{-\frac{\sqrt{3}}{3}x+\frac{1}{3}a} h_k^{\mathtt{B}}(x,y) h_l^{\mathtt{B}}(x,y) \mathrm{d}y \, \mathrm{d}x = \delta_{kl}, \qquad k,l = 0,\ldots,3, \end{aligned}$$

with δ_{kl} denoting the Kronecker delta. Hence, the radial neutron flux expansion approaches

$$\widetilde{\Phi}_n^{\mathtt{A}\,r}(x,y) = \sum_{k=0}^{3} c_{nk} h_k^{\mathtt{A}}(x,y) + \sum_{j=1}^{2} \epsilon_{nj} \sum_{l=1}^{3} d_{jl} \exp(B_j \mathbf{e}_l \cdot \mathbf{r}), \tag{3.23}$$

$$\widetilde{\Phi}_n^{\mathtt{B}\,r}(x,y) = \sum_{k=0}^{3} c_{nk} h_k^{\mathtt{B}}(x,y) + \sum_{j=1}^{2} \epsilon_{nj} \sum_{l=1}^{3} d_{jl} \exp(B_j \mathbf{e}_{l+3} \cdot \mathbf{r}), \qquad n = 0,2, \tag{3.24}$$

hold with $\mathbf{r} = (x,y)^T$ for the trigonal nodal orientations A and B.

The use of exponential functions in addition to the polynomial representation is important to sufficiently describe the neutron flux especially at interfaces between nodes with differing material properties. For the radial neutron source and the corresponding transverse-leakage terms, the following purely polynomial approximation is sufficient:

$$\widetilde{S}_0^{\mathtt{A/B}\,r}(x,y) = \sum_{k=0}^{3} s_{0k} h_k^{\mathtt{A/B}}(x,y), \tag{3.25}$$

$$\widetilde{L}_n^{\mathtt{A/B}\,r}(x,y) = \sum_{k=0}^{3} l_{nk} h_k^{\mathtt{A/B}}(x,y), \qquad n = 0,2. \tag{3.26}$$

Note that the same polynomial bases (3.21) and (3.22) are used here.

SP_3 METHOD – AXIAL TREATMENT: Analogous ansatzes are applied in axial direction. With the orthonormal polynomials

$$\begin{aligned} h_0^z(z) &= 1, \\ h_1^z(z) &= 2\sqrt{3}\frac{z}{a_z}, \\ h_2^z(z) &= \frac{\sqrt{5}}{2}\Big(12\frac{z^2}{a_z^2} - 1\Big), \end{aligned} \tag{3.27}$$

the neutron flux, the neutron source, and the transverse neutron leakage of (3.12)–(3.13) are represented as follows:

$$\widetilde{\Phi}_n^z(z) = \sum_{k=0}^{2} c_{nk}^z h_k^z(z) + \sum_{j=1}^{2} \epsilon_{nj}\big(d_{j+}^z \exp(B_j z) + d_{j-}^z \exp(-B_j z)\big), \tag{3.28}$$

$$\widetilde{S}_0^z(z) = \sum_{k=0}^{2} s_{0k}^z h_k^z(z), \tag{3.29}$$

$$\widetilde{L}_n^z(z) = \sum_{k=0}^{2} l_{nk}^z h_k^z(z), \qquad n = 0, 2. \tag{3.30}$$

DIFFUSION METHOD: Considering the homogeneous three-dimensional diffusion equation

$$-D_0 \Delta \Phi_0(\mathbf{r}) + \Sigma_{r0}\Phi_0(\mathbf{r}) = 0,$$

with $\epsilon_{01} = 1$ and $\epsilon_{02} = 0$, the buckling simplifies to one positive solution

$$B_1 = \sqrt{\frac{\Sigma_{r0}}{D_0}}.$$

Hence, we have the flux expansion approaches

$$\Phi_0^{\mathtt{A}\,r}(x,y) = \sum_{k=0}^{3} c_{0k} h_k^{\mathtt{A}}(x,y) + \sum_{l=1}^{3} d_{1l} \exp(B_1 \mathbf{e}_l \cdot \mathbf{r}), \tag{3.31}$$

$$\Phi_0^{\mathtt{B}\,r}(x,y) = \sum_{k=0}^{3} c_{0k} h_k^{\mathtt{B}}(x,y) + \sum_{l=1}^{3} d_{1l} \exp(B_1 \mathbf{e}_{l+3} \cdot \mathbf{r}), \tag{3.32}$$

$$\Phi_0^z(z) = \sum_{k=0}^{2} c_{0k}^z h_k^z(z) + \big(d_{1+}^z \exp(B_1 z) + d_{1-}^z \exp(-B_1 z)\big). \tag{3.33}$$

For the sources $S_0^{\mathtt{A/B}\,r}$ and the leakages transversal to the radial plane $L_0^{\mathtt{A/B}\,r}$ as well as for the respective axial functions S_0^z and L_0^z, identical expansion ansatzes are used, i.e., (3.25)–(3.26) and (3.29)–(3.30).

As a result, in both the SP_3 and the diffusion method, the intra-nodal neutron flux, source, and transverse leakage are finitely represented in terms of only a small number of unknown parameters, the coefficients c_{nk}, d_{jl}, s_{0k}, l_{nk}, and c^z_{nk}, $d^z_{j\pm}$, s^z_{0k}, l^z_{nk}. Thus, a numerical procedure can be applied to solve the equations.

3.6 Previous nodal DYN3D models

Besides the newly developed trigonal methods, the reactor code DYN3D introduced in Section 1.2 comprises the hitherto existing neutronic models based on Cartesian and hexagonal geometries. Different nodal expansion approaches are available for both geometry options [66, 67, 68].

3.6.1 The Cartesian-geometry DYN3D nodal expansion approaches

For reactor cores with square-geometry fuel assemblies, DYN3D offers both an SP_3 transport and a diffusion option [9, 10, 11].

Due to the fact that all nodal edges are parallel to the Cartesian coordinate axes, a separate treatment of all directions is easily manageable. Considering volume elements of the radial size of a fuel assembly, such a purely one-dimensional ansatz is more accurate than a two-dimensional treatment of the radial plane, since the transverse leakage is described less precisely in the latter case. This effect diminishes with a reduction of the node size to pin-cell level [62]. In the diffusion model, only the one-dimensional ansatz is implemented, while both the one-dimensional and the two-dimensional approaches are available for the Cartesian SP_3 method.

The transverse-leakage approximation in the purely one-dimensional approach is realized for every coordinate direction in a similar manner to the axial treatment derived in Section 3.4, so that three one-dimensional systems of SP_3 equations or three one-dimensional diffusion equations have to be solved. Using the polynomials of (3.27)

$$\begin{aligned} h^u_0(u) &= 1, \\ h^u_1(u) &= 2\sqrt{3}\frac{u}{a_u}, \\ h^u_2(u) &= \frac{\sqrt{5}}{2}\left(12\frac{u^2}{a_u^2} - 1\right), \end{aligned} \tag{3.34}$$

the neutron flux, source, and transverse leakage are represented as follows:

$$\Phi_n^u(u) = \sum_{k=0}^{2} c_{nk}^u h_k^u(u) + \sum_{j=1}^{2} \epsilon_{nj} \left(d_{j+}^u \exp(B_j u) + d_{j-}^u \exp(-B_j u) \right), \tag{3.35}$$

$$S_0^u(u) = \sum_{k=0}^{2} s_{0k}^u h_k^u(u), \tag{3.36}$$

$$L_n^u(u) = \sum_{k=0}^{2} l_{nk}^u h_k^u(u), \tag{3.37}$$

where $n = 0, 2$ in case of SP_3 (tilde omitted) and $n = 0$ in case of diffusion. $u \in \{x, y, z\}$ denotes the respective coordinate direction. B_j and ϵ_{nj} apply analogously to Section 3.5.

In the two-dimensional approach, the one-dimensional ansatzes are simply combined for the radial plane:

$$\Phi_n^r(x, y) = \sum_{u=x,y} \left(\sum_{k=0}^{2} c_{nk}^u h_k^u(u) + \sum_{j=1}^{2} \epsilon_{nj} \left(d_{j+}^u \exp(B_j u) + d_{j-}^u \exp(-B_j u) \right) \right),$$

$$S_0^r(x, y) = \sum_{u=x,y} \left(\sum_{k=0}^{2} s_{0k}^u h_k^u(u) \right),$$

$$L_n^r(x, y) = \sum_{u=x,y} \left(\sum_{k=0}^{2} l_{nk}^u h_k^u(u) \right).$$

The axial treatment remains identical to the above approach.

3.6.2 The hexagonal-geometry DYN3D nodal expansion approaches

DYN3D comprises two hexagonal nodal expansion methods based on diffusion theory – the models HEXNEM1 and HEXNEM2 [60, 63]. Similarly to the trigonal approach, the radial plane is not one-dimensionally separated to avoid the occurrence of singularities, so that a two-dimensional and a one-dimensional diffusion equation have to be solved.

In the radial plane, the outer normal unit vectors of the hexagonal nodal faces are

$$\mathbf{e}_{s1} = \begin{pmatrix} 1 \\ 0 \end{pmatrix}, \qquad \mathbf{e}_{s2} = \begin{pmatrix} \frac{1}{2} \\ \frac{\sqrt{3}}{2} \end{pmatrix}, \qquad \mathbf{e}_{s3} = \begin{pmatrix} -\frac{1}{2} \\ \frac{\sqrt{3}}{2} \end{pmatrix},$$

$$\mathbf{e}_{s4} = \begin{pmatrix} -1 \\ 0 \end{pmatrix}, \qquad \mathbf{e}_{s5} = \begin{pmatrix} -\frac{1}{2} \\ -\frac{\sqrt{3}}{2} \end{pmatrix}, \qquad \mathbf{e}_{s6} = \begin{pmatrix} \frac{1}{2} \\ -\frac{\sqrt{3}}{2} \end{pmatrix}$$

as illustrated in Figure 3.4. With the orthonormal ansatz polynomials

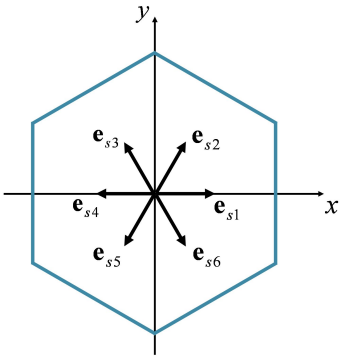

FIGURE 3.4: Hexagon with normal vectors of the six nodal faces.

$$
\begin{aligned}
h_0(x,y) &= \hat{N}_0,\\
h_1(x,y) &= \hat{N}_1\frac{x}{a},\\
h_2(x,y) &= \hat{N}_2\frac{y}{a},\\
h_3(x,y) &= \hat{N}_3\left(\frac{x^2}{a^2}+\frac{y^2}{a^2}\right)-\hat{N}_4,\\
h_4(x,y) &= \hat{N}_5\left(\frac{x^2}{a^2}-\frac{y^2}{a^2}\right),\\
h_5(x,y) &= \hat{N}_6\frac{xy}{a^2}
\end{aligned}
$$

and the appropriate normalization factors $\hat{N}_k$, $k = 0,\ldots,6$, the following expansion approaches hold for the HEXNEM1 method:

$$
\begin{aligned}
\Phi_0^r(x,y) &= \sum_{k=0}^{5} c_{0k}h_k(x,y)+\sum_{l=1}^{6} d_{sl}\exp(B_1\mathbf{e}_{sl}\cdot\mathbf{r}), \qquad \mathbf{r}=(x,y)^T,\\
S_0^r(x,y) &= \sum_{k=0}^{5} s_{0k}h_k(x,y),\\
L_0^r(x,y) &= \sum_{k=0}^{5} l_{0k}h_k(x,y).
\end{aligned}
$$

The nodal coupling, however, can be realized not only via the neutron currents at the nodal faces but also additionally via the hexagonal vertices. This extension leads to the HEXNEM2 method, which achieves higher accuracy than HEXNEM1. Hence, we have

$$
\Phi_0^r(x,y) = \sum_{k=0}^{5} c_{0k}h_k(x,y)+\sum_{l=1}^{6} d_{sl}\exp(B_1\mathbf{e}_{sl}\cdot\mathbf{r})+\sum_{l=1}^{6} d_{cl}\exp(B_1\mathbf{e}_{cl}\cdot\mathbf{r}), \qquad \mathbf{r}=(x,y)^T,
$$

with the outer normal unit vectors of the hexagonal nodal vertices

$$\mathbf{e}_{c1} = \begin{pmatrix} \frac{\sqrt{3}}{2} \\ \frac{1}{2} \end{pmatrix}, \qquad \mathbf{e}_{c2} = \begin{pmatrix} 0 \\ 1 \end{pmatrix}, \qquad \mathbf{e}_{c3} = \begin{pmatrix} -\frac{\sqrt{3}}{2} \\ \frac{1}{2} \end{pmatrix},$$
$$\mathbf{e}_{c4} = \begin{pmatrix} -\frac{\sqrt{3}}{2} \\ -\frac{1}{2} \end{pmatrix}, \qquad \mathbf{e}_{c5} = \begin{pmatrix} 0 \\ -1 \end{pmatrix}, \qquad \mathbf{e}_{c6} = \begin{pmatrix} \frac{\sqrt{3}}{2} \\ -\frac{1}{2} \end{pmatrix}.$$

The axial direction of both methods is processed with the same expansion approaches as used for both the trigonal and the Cartesian geometry. Using the polynomials (3.34), the neutron flux, source, and transverse leakage are approximated via (3.35)–(3.37), where $u = z$, $n = 0$, and B_j, ϵ_{0j} as specified in Section 3.5.

A variation of the HEXNEM methods introducing tangentially weighted exponential basis functions was recently described by Christoskov and Petkov [37].

4

Solution of the SP_3 Transport and Diffusion Equations in Trigonal Geometry

In the previous chapters, the physical phenomena of the neutron transport are identified and translated into mathematical entities. A trigonal nodal scheme is proposed using the transverse-integration procedure, which converts the original three-dimensional neutron SP_3 transport and diffusion equations into two-dimensional radial and one-dimensional axial sets of equations. All intra-nodal unknown functions are finitely represented in terms of only a small number of unknown parameters.

This chapter focuses on a rigorous analysis of the mathematical interrelations. The principle unknowns of the problem are the outgoing neutron partial currents at the faces of the nodal elements. Subject to the Legendre moments of the neutron flux, the outgoing partial currents are determined in Section 4.1. For each homogeneous node, the local response-matrix equations are derived in Section 4.2 allowing to calculate the moments of the node-interface outgoing partial currents in terms of the flux coefficients and the incoming partial currents. As the incoming partial currents are the outgoing partial currents of the adjacent nodes (shown in Section 4.3), the discrete representation of the equations leads naturally to an iterative procedure, the inner iteration, which is performed for each energy group $g = 1, ..., G$ to solve the steady-state multi-group SP_3 transport or diffusion problem for a given source distribution. The calculation of the upward and downward neutron scattering as well as of the neutron fission source is discussed in Section 4.4. The transverse neutron leakage is also treated as a source. It is shown in Section 4.5, how the transverse leakage of a node is calculated involving its adjacent nodal elements. Eventually, in Section 4.6, the node-averaged flux is deduced from the neutron balance equations. The standard power method, called outer iteration, is used to compute successive estimates of the effective multiplication factor k_{eff}. Finally, the nodal thermal power densities P^i are determined

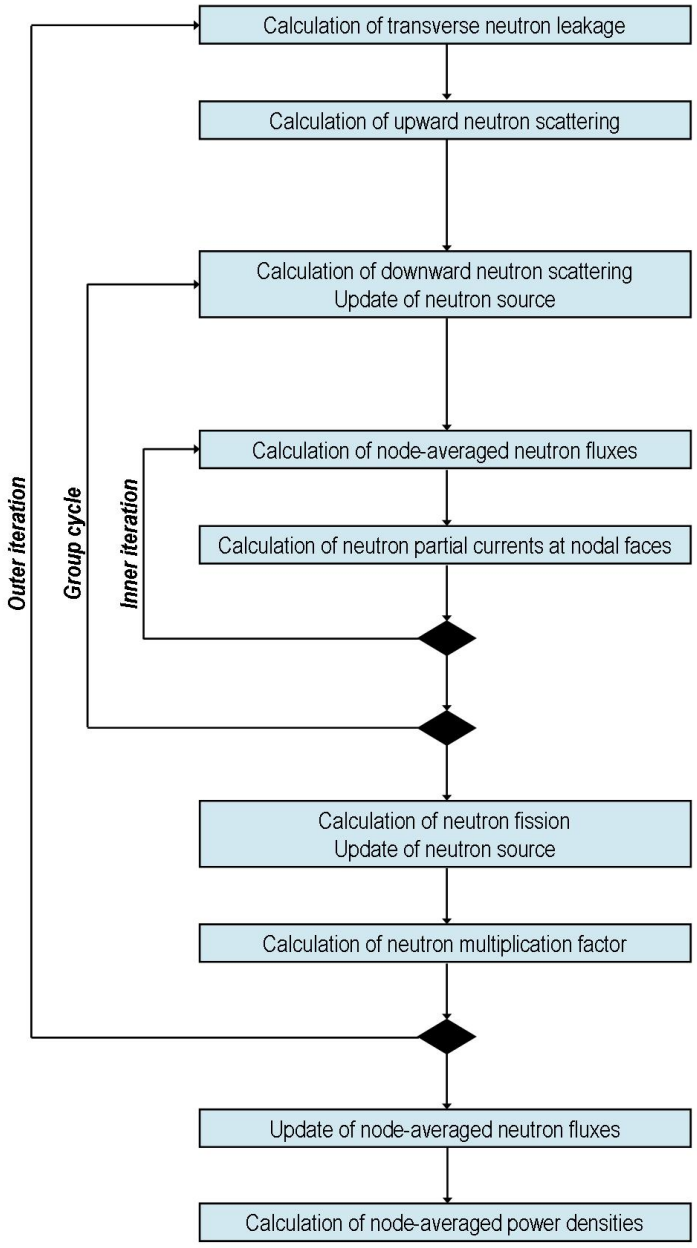

FIGURE 4.1: Block diagram of the inner and outer iteration scheme.

from the node-averaged neutron fluxes $\overline{\Phi}^i_{0,g}$ via

$$P^i = \sum_{g=1}^{G} \kappa^i_g \Sigma^i_{f,g} \overline{\Phi}^i_{0,g}, \tag{4.1}$$

where κ^i_g and $\Sigma^i_{f,g}$ denote the usable energy produced per fission event and the macroscopic fission cross section, respectively. The total power generated by the core is the sum of the power densities over all nodes V^i. The block diagram in Figure 4.1 visualizes the inner and outer iteration scheme outlined above.

In Section 4.7, specific simplifications in terms of the implementation are explained. Section 4.8 summarizes the implementation of the inner and outer iteration schemes in a compact algorithmic form.

The following facts will become evident by the end of this chapter:

- As the SP_3 equations in within-group form are of diffusion type, the conventional diffusion solver structure can be retained also for the solution of the SP_3 transport problem.
- The inter-nodal neutron exchange ("coupling") is realized via the nodal face-averaged partial currents.
- To simplify the input structure of the cross-section sets, higher-order scattering cross sections are not included in the present SP_3 implementation. Identical cross-section data are used in the DYN3D trigonal SP_3 and diffusion models.
- Although only node-averaged neutron fluxes are finally used to determine relevant reaction rates, the accuracy of these node-averaged fluxes is strongly impacted by the intra-nodal flux representation, which contains higher-order flux moments in the SP_3 approach.

4.1 Derivation of the neutron partial currents at nodal faces

In this section, expressions for the face-averaged partial currents of the trigonal nodes are derived. These partial currents are of particular importance since they realize the nodal coupling and, therefore, contribute significantly to the inter-nodal neutron balance.

At first, we recall Fick's law (3.1) and introduce the net current

$$J(\mathbf{r}) := \mathbf{n} \cdot \mathbf{J}(\mathbf{r}) = J^+(\mathbf{r}) - J^-(\mathbf{r}) \tag{4.2}$$

which is defined as the sum of the partial outward current J^+ and the negative partial inward current J^-. The unit vector $\mathbf{n}$ denotes the outer normal of the considered node. Hence, from (2.10) and (2.36)–(2.38), (2.50), we obtain the one-dimensional relations

$$\begin{aligned}\widetilde{J}_0(x) &= -D_0 \frac{\mathrm{d}}{\mathrm{d}x}\widetilde{\Phi}_0(x) = \Phi_1(x) = \frac{1}{2}\int_{-1}^{1} p_1(\mu)\Psi(x,\mu)\mathrm{d}\mu \\ &= \underbrace{-\frac{1}{2}\int_{-1}^{0} |\mu|\Psi(x,\mu)\mathrm{d}\mu}_{=:\widetilde{J}_0^-(x)} + \underbrace{\frac{1}{2}\int_{0}^{1} \mu\Psi(x,\mu)\mathrm{d}\mu}_{=:\widetilde{J}_0^+(x)}\end{aligned}$$

and

$$\begin{aligned}\widetilde{J}_2(x) &= -D_2\frac{\mathrm{d}}{\mathrm{d}x}\widetilde{\Phi}_2(x) = \frac{3}{5}\Phi_3(x) = \frac{3}{5}\frac{1}{2}\int_{-1}^{1} p_3(\mu)\Psi(x,\mu)\mathrm{d}\mu \\ &= \underbrace{-\frac{3}{10}\int_{-1}^{0} p_3(|\mu|)\Psi(x,\mu)\mathrm{d}\mu}_{=:\widetilde{J}_2^-(x)} + \underbrace{\frac{3}{10}\int_{0}^{1} p_3(\mu)\Psi(x,\mu)\mathrm{d}\mu}_{=:\widetilde{J}_2^+(x)}.\end{aligned}$$

Note that the currents $\widetilde{J}_n$, $\widetilde{J}_n^-$, and $\widetilde{J}_n^+$ are denoted with a tilde since they refer to the modified fluxes $\widetilde{\Phi}_n$, $n = 0, 2$, of the SP_3 approach. Using the angular neutron flux expansion (2.8) for $N = 3$ and the definitions of the modified flux moments (2.43)–(2.44), the one-dimensional outwardly and inwardly directed partial currents can be approximated by

$$\begin{aligned}\widetilde{J}_0^+(x) &= \frac{1}{2}\int_0^1 \mu\Psi(x,\mu)\mathrm{d}\mu \\ &= \frac{1}{4}\widetilde{\Phi}_0(x) - \frac{1}{2}D_0\frac{\mathrm{d}}{\mathrm{d}x}\widetilde{\Phi}_0(x) - \frac{3}{16}\widetilde{\Phi}_2(x), \\ \widetilde{J}_0^-(x) &= \frac{1}{2}\int_{-1}^0 |\mu|\Psi(x,\mu)\mathrm{d}\mu = \frac{1}{2}\int_{-1}^0 -\mu\Psi(x,\mu)\mathrm{d}\mu = \frac{1}{2}\int_0^1 \mu\Psi(x,-\mu)\mathrm{d}\mu \\ &= \frac{1}{4}\widetilde{\Phi}_0(x) + \frac{1}{2}D_0\frac{\mathrm{d}}{\mathrm{d}x}\widetilde{\Phi}_0(x) - \frac{3}{16}\widetilde{\Phi}_2(x), \\ \widetilde{J}_2^+(x) &= \frac{3}{10}\int_0^1 p_3(\mu)\Psi(x,\mu)\mathrm{d}\mu = \frac{3}{20}\int_0^1 (5\mu^3 - 3\mu)\Psi(x,\mu)\mathrm{d}\mu \\ &= -\frac{3}{80}\widetilde{\Phi}_0(x) + \frac{21}{80}\widetilde{\Phi}_2(x) - \frac{1}{2}D_2\frac{\mathrm{d}}{\mathrm{d}x}\widetilde{\Phi}_2(x), \\ \widetilde{J}_2^-(x) &= \frac{3}{10}\int_{-1}^0 p_3(|\mu|)\Psi(x,\mu)\mathrm{d}\mu = \frac{3}{10}\int_{-1}^0 -p_3(\mu)\Psi(x,\mu)\mathrm{d}\mu \\ &= \frac{3}{10}\int_0^1 p_3(\mu)\Psi(x,-\mu)\mathrm{d}\mu = \frac{3}{20}\int_0^1 (5\mu^3 - 3\mu)\Psi(x,-\mu)\mathrm{d}\mu \\ &= -\frac{3}{80}\widetilde{\Phi}_0(x) + \frac{21}{80}\widetilde{\Phi}_2(x) + \frac{1}{2}D_2\frac{\mathrm{d}}{\mathrm{d}x}\widetilde{\Phi}_2(x).\end{aligned}$$

Generalization to multi-dimensional geometries gives

$$\widetilde{J}_0^{\pm}(\mathbf{r}) = \frac{1}{4\pi}\int_0^{2\pi}\int_0^1 \mu\Psi(\mathbf{r},\pm\mu,\varphi)\mathrm{d}\mu\mathrm{d}\varphi = \frac{1}{4}\widetilde{\Phi}_0(\mathbf{r}) \mp \frac{1}{2}D_0\,\mathbf{n}\cdot\nabla\widetilde{\Phi}_0(\mathbf{r}) - \frac{3}{16}\widetilde{\Phi}_2(\mathbf{r}), \tag{4.3}$$

$$\widetilde{J}_2^{\pm}(\mathbf{r}) = \frac{3}{20\pi}\int_0^{2\pi}\int_0^1 p_3(\mu)\Psi(\mathbf{r},\pm\mu,\varphi)\mathrm{d}\mu\mathrm{d}\varphi = -\frac{3}{80}\widetilde{\Phi}_0(\mathbf{r}) + \frac{21}{80}\widetilde{\Phi}_2(\mathbf{r}) \mp \frac{1}{2}D_2\,\mathbf{n}\cdot\nabla\widetilde{\Phi}_2(x). \tag{4.4}$$

SP_3 METHOD – RADIAL TREATMENT: To average the incoming and outgoing partial currents over the nodal faces perpendicular to the radial plane (recall Figure 3.3), line integrals

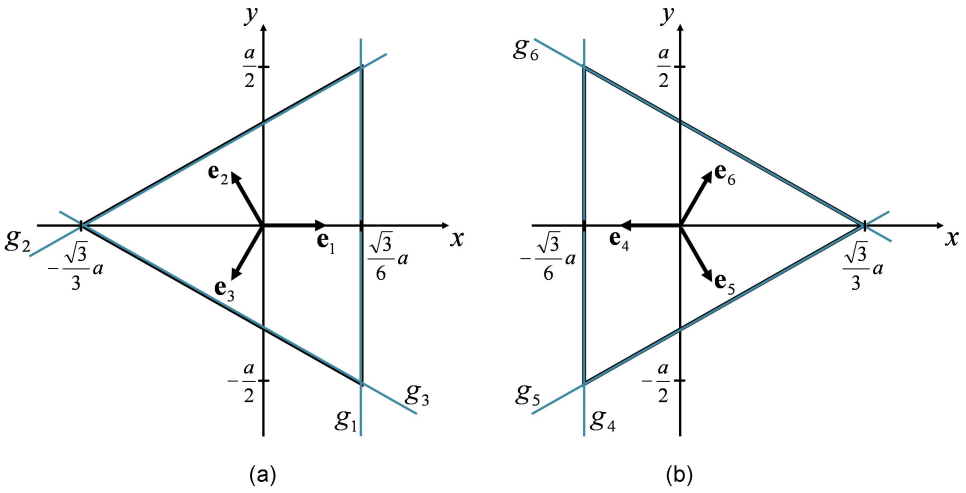

FIGURE 4.2: Location of the linear functions g_l describing the radial faces $l = 1, 2, 3$ of node A (a) and $l = 4, 5, 6$ of node B (b).

along the linear functions

$$g_2(x) = \frac{\sqrt{3}}{3}x + \frac{1}{3}a, \tag{4.5}$$

$$g_3(x) = -\frac{\sqrt{3}}{3}x - \frac{1}{3}a, \tag{4.6}$$

$$g_5(x) = \frac{\sqrt{3}}{3}x - \frac{1}{3}a, \tag{4.7}$$

$$g_6(x) = -\frac{\sqrt{3}}{3}x + \frac{1}{3}a \tag{4.8}$$

describing the respective faces $l = 2, 3, 5, 6$ have to be solved. Figure 4.2 shows the location of the sides $l = 1, ..., 6$ of the nodes A and B. Now, let

$$\widetilde{J}^{\pm}_{0l}(x,y) = \frac{1}{4}\widetilde{\Phi}^{\mathrm{A/B}\,r}_0(x,y) \mp \frac{1}{2}D_0\,\mathbf{e}_l \cdot \nabla\widetilde{\Phi}^{\mathrm{A/B}\,r}_0(x,y) - \frac{3}{16}\widetilde{\Phi}^{\mathrm{A/B}\,r}_2(x,y),$$
$$\widetilde{J}^{\pm}_{2l}(x,y) = -\frac{3}{80}\widetilde{\Phi}^{\mathrm{A/B}\,r}_0(x,y) + \frac{21}{80}\widetilde{\Phi}^{\mathrm{A/B}\,r}_2(x,y) \mp \frac{1}{2}D_2\,\mathbf{e}_l \cdot \nabla\widetilde{\Phi}^{\mathrm{A/B}\,r}_0(x,y), \qquad l = 1, ..., 6$$

be the two-dimensional partial currents at the trigonal nodal faces with their particular unit outer vectors $\mathbf{e}_l$ of (3.19) and (3.20), respectively. Hence, the radial face-averaged

zeroth moment partial currents are given by

$$\begin{aligned}
\overline{\widetilde{J}^{\pm}_{01}} &= \frac{1}{a\,a_z}\int_{-\frac{a_z}{2}}^{\frac{a_z}{2}}\int_{-\frac{a}{2}}^{\frac{a}{2}} \widetilde{J}^{\pm}_{01}(\frac{\sqrt{3}}{6}a, y)\mathrm{d}y\,\mathrm{d}z \\
&= \frac{1}{a}\int_{-\frac{a}{2}}^{\frac{a}{2}} \frac{1}{4}\widetilde{\Phi}^{\mathtt{A}\,r}_0(\frac{\sqrt{3}}{6}a, y) \mp \frac{1}{2}D_0\frac{\partial}{\partial x}\widetilde{\Phi}^{\mathtt{A}\,r}_0(x, y)\Big|_{x=\frac{\sqrt{3}}{6}a} - \frac{3}{16}\widetilde{\Phi}^{\mathtt{A}\,r}_2(\frac{\sqrt{3}}{6}a, y)\mathrm{d}y, \qquad (4.9)\\
\overline{\widetilde{J}^{\pm}_{02}} &= \frac{1}{a\,a_z}\int_{-\frac{a_z}{2}}^{\frac{a_z}{2}}\int_{-\frac{\sqrt{3}}{3}a}^{\frac{\sqrt{3}}{6}a} \widetilde{J}^{\pm}_{02}(x, g_2(x))\sqrt{1+\left(\frac{\mathrm{d}}{\mathrm{d}x}g_2(x)\right)^2}\mathrm{d}x\,\mathrm{d}z \\
&= \frac{2\sqrt{3}}{3a}\int_{-\frac{\sqrt{3}}{3}a}^{\frac{\sqrt{3}}{6}a} \frac{1}{4}\widetilde{\Phi}^{\mathtt{A}\,r}_0(x, g_2(x)) \pm \frac{1}{4}D_0\frac{\partial}{\partial x}\widetilde{\Phi}^{\mathtt{A}\,r}_0(x, y)\Big|_{y=g_2(x)} \\
&\qquad \mp \frac{\sqrt{3}}{4}D_0\frac{\partial}{\partial y}\widetilde{\Phi}^{\mathtt{A}\,r}_0(x, y)\Big|_{y=g_2(x)} - \frac{3}{16}\widetilde{\Phi}^{\mathtt{A}\,r}_2(x, g_2(x))\mathrm{d}x, \qquad (4.10)\\
\overline{\widetilde{J}^{\pm}_{03}} &= \frac{1}{a\,a_z}\int_{-\frac{a_z}{2}}^{\frac{a_z}{2}}\int_{-\frac{\sqrt{3}}{3}a}^{\frac{\sqrt{3}}{6}a} \widetilde{J}^{\pm}_{03}(x, g_3(x))\sqrt{1+\left(\frac{\mathrm{d}}{\mathrm{d}x}g_3(x)\right)^2}\mathrm{d}x\,\mathrm{d}z \\
&= \frac{2\sqrt{3}}{3a}\int_{-\frac{\sqrt{3}}{3}a}^{\frac{\sqrt{3}}{6}a} \frac{1}{4}\widetilde{\Phi}^{\mathtt{A}\,r}_0(x, g_3(x)) \pm \frac{1}{4}D_0\frac{\partial}{\partial x}\widetilde{\Phi}^{\mathtt{A}\,r}_0(x, y)\Big|_{y=g_3(x)} \\
&\qquad \pm \frac{\sqrt{3}}{4}D_0\frac{\partial}{\partial y}\widetilde{\Phi}^{\mathtt{A}\,r}_0(x, y)\Big|_{y=g_3(x)} - \frac{3}{16}\widetilde{\Phi}^{\mathtt{A}\,r}_2(x, g_3(x))\mathrm{d}x, \qquad (4.11)
\end{aligned}$$

and

$$\begin{aligned}
\overline{\widetilde{J}^{\pm}_{04}} &= \frac{1}{a\,a_z}\int_{-\frac{a_z}{2}}^{\frac{a_z}{2}}\int_{-\frac{a}{2}}^{\frac{a}{2}} \widetilde{J}^{\pm}_{04}(-\frac{\sqrt{3}}{6}a, y)\mathrm{d}y\,\mathrm{d}z \\
&= \frac{1}{a}\int_{-\frac{a}{2}}^{\frac{a}{2}} \frac{1}{4}\widetilde{\Phi}^{\mathtt{B}\,r}_0(-\frac{\sqrt{3}}{6}a, y) \pm \frac{1}{2}D_0\frac{\partial}{\partial x}\widetilde{\Phi}^{\mathtt{B}\,r}_0(x, y)\Big|_{x=-\frac{\sqrt{3}}{6}a} - \frac{3}{16}\widetilde{\Phi}^{\mathtt{B}\,r}_2(-\frac{\sqrt{3}}{6}a, y)\mathrm{d}y, \qquad (4.12)\\
\overline{\widetilde{J}^{\pm}_{05}} &= \frac{1}{a\,a_z}\int_{-\frac{a_z}{2}}^{\frac{a_z}{2}}\int_{-\frac{\sqrt{3}}{6}a}^{\frac{\sqrt{3}}{3}a} \widetilde{J}^{\pm}_{05}(x, g_5(x))\sqrt{1+\left(\frac{\mathrm{d}}{\mathrm{d}x}g_5(x)\right)^2}\mathrm{d}x\,\mathrm{d}z \\
&= \frac{2\sqrt{3}}{3a}\int_{-\frac{\sqrt{3}}{6}a}^{\frac{\sqrt{3}}{3}a} \frac{1}{4}\widetilde{\Phi}^{\mathtt{B}\,r}_0(x, g_5(x)) \mp \frac{1}{4}D_0\frac{\partial}{\partial x}\widetilde{\Phi}^{\mathtt{B}\,r}_0(x, y)\Big|_{y=g_5(x)} \\
&\qquad \pm \frac{\sqrt{3}}{4}D_0\frac{\partial}{\partial y}\widetilde{\Phi}^{\mathtt{B}\,r}_0(x, y)\Big|_{y=g_5(x)} - \frac{3}{16}\widetilde{\Phi}^{\mathtt{B}\,r}_2(x, g_5(x))\mathrm{d}x, \qquad (4.13)\\
\overline{\widetilde{J}^{\pm}_{06}} &= \frac{1}{a\,a_z}\int_{-\frac{a_z}{2}}^{\frac{a_z}{2}}\int_{-\frac{\sqrt{3}}{6}a}^{\frac{\sqrt{3}}{3}a} \widetilde{J}^{\pm}_{06}(x, g_6(x))\sqrt{1+\left(\frac{\mathrm{d}}{\mathrm{d}x}g_6(x)\right)^2}\mathrm{d}x\,\mathrm{d}z \\
&= \frac{2\sqrt{3}}{3a}\int_{-\frac{\sqrt{3}}{6}a}^{\frac{\sqrt{3}}{3}a} \frac{1}{4}\widetilde{\Phi}^{\mathtt{B}\,r}_0(x, g_6(x)) \mp \frac{1}{4}D_0\frac{\partial}{\partial x}\widetilde{\Phi}^{\mathtt{B}\,r}_0(x, y)\Big|_{y=g_6(x)} \\
&\qquad \mp \frac{\sqrt{3}}{4}D_0\frac{\partial}{\partial y}\widetilde{\Phi}^{\mathtt{B}\,r}_0(x, y)\Big|_{y=g_6(x)} - \frac{3}{16}\widetilde{\Phi}^{\mathtt{B}\,r}_2(x, g_6(x))\mathrm{d}x. \qquad (4.14)
\end{aligned}$$

Similarly, the face-averaged second moment partial currents are obtained:

$$\widetilde{\overline{J_{21}^{\pm}}} = \frac{1}{a}\int_{-\frac{a}{2}}^{\frac{a}{2}} -\frac{3}{80}\widetilde{\Phi}_0^{\mathtt{A}\,r}(\frac{\sqrt{3}}{6}a,y) + \frac{21}{80}\widetilde{\Phi}_2^{\mathtt{A}\,r}(\frac{\sqrt{3}}{6}a,y) \mp \frac{1}{2}D_0\frac{\partial}{\partial x}\widetilde{\Phi}_2^{\mathtt{A}\,r}(x,y)\Big|_{x=\frac{\sqrt{3}}{6}a}\mathrm{d}y, \tag{4.15}$$

$$\begin{aligned}\widetilde{\overline{J_{22}^{\pm}}} = \frac{2\sqrt{3}}{3a}\int_{-\frac{\sqrt{3}}{3}a}^{\frac{\sqrt{3}}{6}a} &-\frac{3}{80}\widetilde{\Phi}_0^{\mathtt{A}\,r}(x,g_2(x)) + \frac{21}{80}\widetilde{\Phi}_2^{\mathtt{A}\,r}(x,g_2(x))\\ &\pm\frac{1}{4}D_0\frac{\partial}{\partial x}\widetilde{\Phi}_2^{\mathtt{A}\,r}(x,y)\Big|_{y=g_2(x)} \mp \frac{\sqrt{3}}{4}D_0\frac{\partial}{\partial y}\widetilde{\Phi}_2^{\mathtt{A}\,r}(x,y)\Big|_{y=g_2(x)}\mathrm{d}x,\end{aligned} \tag{4.16}$$

$$\begin{aligned}\widetilde{\overline{J_{23}^{\pm}}} = \frac{2\sqrt{3}}{3a}\int_{-\frac{\sqrt{3}}{3}a}^{\frac{\sqrt{3}}{6}a} &-\frac{3}{80}\widetilde{\Phi}_0^{\mathtt{A}\,r}(x,g_3(x)) + \frac{21}{80}\widetilde{\Phi}_2^{\mathtt{A}\,r}(x,g_3(x))\\ &\pm\frac{1}{4}D_0\frac{\partial}{\partial x}\widetilde{\Phi}_2^{\mathtt{A}\,r}(x,y)\Big|_{y=g_3(x)} \pm \frac{\sqrt{3}}{4}D_0\frac{\partial}{\partial y}\widetilde{\Phi}_2^{\mathtt{A}\,r}(x,y)\Big|_{y=g_3(x)}\mathrm{d}x,\end{aligned} \tag{4.17}$$

$$\widetilde{\overline{J_{24}^{\pm}}} = \frac{1}{a}\int_{-\frac{a}{2}}^{\frac{a}{2}} -\frac{3}{80}\widetilde{\Phi}_0^{\mathtt{B}\,r}(\frac{\sqrt{3}}{6}a,y) + \frac{21}{80}\widetilde{\Phi}_2^{\mathtt{B}\,r}(\frac{\sqrt{3}}{6}a,y) \pm \frac{1}{2}D_0\frac{\partial}{\partial x}\widetilde{\Phi}_2^{\mathtt{B}\,r}(x,y)\Big|_{x=\frac{\sqrt{3}}{6}a}\mathrm{d}y, \tag{4.18}$$

$$\begin{aligned}\widetilde{\overline{J_{25}^{\pm}}} = \frac{2\sqrt{3}}{3a}\int_{-\frac{\sqrt{3}}{6}a}^{\frac{\sqrt{3}}{3}a} &-\frac{3}{80}\widetilde{\Phi}_0^{\mathtt{B}\,r}(x,g_5(x)) + \frac{21}{80}\widetilde{\Phi}_2^{\mathtt{B}\,r}(x,g_5(x))\\ &\mp\frac{1}{4}D_0\frac{\partial}{\partial x}\widetilde{\Phi}_2^{\mathtt{B}\,r}(x,y)\Big|_{y=g_5(x)} \pm \frac{\sqrt{3}}{4}D_0\frac{\partial}{\partial y}\widetilde{\Phi}_2^{\mathtt{B}\,r}(x,y)\Big|_{y=g_5(x)}\mathrm{d}x,\end{aligned} \tag{4.19}$$

$$\begin{aligned}\widetilde{\overline{J_{26}^{\pm}}} = \frac{2\sqrt{3}}{3a}\int_{-\frac{\sqrt{3}}{6}a}^{\frac{\sqrt{3}}{3}a} &-\frac{3}{80}\widetilde{\Phi}_0^{\mathtt{B}\,r}(x,g_6(x)) + \frac{21}{80}\widetilde{\Phi}_2^{\mathtt{B}\,r}(x,g_6(x))\\ &\mp\frac{1}{4}D_0\frac{\partial}{\partial x}\widetilde{\Phi}_2^{\mathtt{B}\,r}(x,y)\Big|_{y=g_6(x)} \mp \frac{\sqrt{3}}{4}D_0\frac{\partial}{\partial y}\widetilde{\Phi}_2^{\mathtt{B}\,r}(x,y)\Big|_{y=g_6(x)}\mathrm{d}x.\end{aligned} \tag{4.20}$$

SP_3 method – axial treatment: For the nodal faces parallel to the radial plane (see again Figure 3.3), the axial averaged partial inward (superscript –) and outward (superscript +) currents are determined in the conventional way. Accordingly, we have

$$\widetilde{\overline{J_{0+}^{z\pm}}} := J_{0,z=\frac{a_z}{2}}^{\pm} = \frac{1}{4}\widetilde{\Phi}_0^z(a_z/2) \mp \frac{1}{2}D_0\frac{\mathrm{d}}{\mathrm{d}z}\widetilde{\Phi}_0^z(z)\Big|_{z=\frac{a_z}{2}} - \frac{3}{16}\widetilde{\Phi}_2^z(a_z/2), \tag{4.21}$$

$$\widetilde{\overline{J_{0-}^{z\pm}}} := J_{0,z=-\frac{a_z}{2}}^{\pm} = \frac{1}{4}\widetilde{\Phi}_0^z(-a_z/2) \pm \frac{1}{2}D_0\frac{\mathrm{d}}{\mathrm{d}z}\widetilde{\Phi}_0^z(z)\Big|_{z=-\frac{a_z}{2}} - \frac{3}{16}\widetilde{\Phi}_2^z(-a_z/2), \tag{4.22}$$

$$\widetilde{\overline{J_{2+}^{z\pm}}} := J_{2,z=\frac{a_z}{2}}^{\pm} = -\frac{3}{80}\widetilde{\Phi}_0^z(a_z/2) + \frac{21}{80}\widetilde{\Phi}_2^z(a_z/2) \mp \frac{1}{2}D_2\frac{\mathrm{d}}{\mathrm{d}z}\widetilde{\Phi}_2^z(z)\Big|_{z=\frac{a_z}{2}}, \tag{4.23}$$

$$\widetilde{\overline{J_{2-}^{z\pm}}} := J_{2,z=-\frac{a_z}{2}}^{\pm} = -\frac{3}{80}\widetilde{\Phi}_0^z(-a_z/2) + \frac{21}{80}\widetilde{\Phi}_2^z(-a_z/2) \pm \frac{1}{2}D_2\frac{\mathrm{d}}{\mathrm{d}z}\widetilde{\Phi}_2^z(z)\Big|_{z=-\frac{a_z}{2}}. \tag{4.24}$$

Diffusion method: With respect to diffusion theory, an analogous relation holds for the net current

$$J_0(x) = -D_0\frac{\mathrm{d}}{\mathrm{d}x}\Phi_0(x) = \Phi_1(x) = J_0^+(x) - J_0^-(x)$$

with the incoming and outgoing partial currents

$$J_0^{\pm}(x) = \frac{1}{4}\Phi_0(x) \mp \frac{1}{2}D_0\frac{\mathrm{d}}{\mathrm{d}x}\Phi_0(x),$$

which finally gives the same expressions for the radial and axial face-averaged partial currents (4.9)–(4.14) and (4.21)–(4.22) by just assuming the terms comprising the second flux moment $\widetilde{\Phi}_2$ zero.

In the following, the overbar and the tilde on the face-averaged partial currents are omitted, i.e.,

$$\begin{aligned} J_{nl}^{\pm} &:= \overline{\widetilde{J}_{nl}^{\pm}}, \\ J_{n\pm}^{z\pm} &:= \overline{\widetilde{J}_{n\pm}^{z\pm}}, \qquad n = 0, 2, \qquad l = 1, ..., 6. \end{aligned}$$

4.2 Response-matrix representation of the neutron partial currents

SP_3 method – radial treatment: Let

$$\mathbf{J}_n^{\mathtt{A}\pm} = \begin{pmatrix} J_{n1}^{\pm} \\ J_{n2}^{\pm} \\ J_{n3}^{\pm} \end{pmatrix} \qquad \text{and} \qquad \mathbf{J}_n^{\mathtt{B}\pm} = \begin{pmatrix} J_{n4}^{\pm} \\ J_{n5}^{\pm} \\ J_{n6}^{\pm} \end{pmatrix}, \qquad n = 0, 2, \tag{4.25}$$

be the vectors of the face-averaged partial currents (4.9)–(4.20) of the previous section for the respective trigonal nodal orientations A and B in the radial plane. Applying the flux expansion approaches (3.23) and (3.24) for $\widetilde{\Phi}_n^{\mathtt{A/B}\,r}$ to the relations (4.9)–(4.20) results in the independence of the averaged partial currents on the nodal orientation. By the use of the particular polynomial bases (3.21) and (3.22), the local coordinate system is simply rotated. Thus, we define

$$\mathbf{J}_n^{\pm} := \mathbf{J}_n^{\mathtt{A}\pm} \equiv \mathbf{J}_n^{\mathtt{B}\pm}. \tag{4.26}$$

Writing the flux expansion coefficients in the vector forms

$$\mathbf{c}_n = \begin{pmatrix} c_{n0} \\ c_{n1} \\ c_{n2} \\ c_{n3} \end{pmatrix}, \qquad n = 0, 2, \qquad \text{and} \qquad \mathbf{d}_j = \begin{pmatrix} d_{j1} \\ d_{j2} \\ d_{j3} \end{pmatrix}, \qquad j = 1, 2,$$

the linear algebraic system of equations

$$\mathbf{J}_n^{\pm} = \mathbf{P}_{n0}^{\pm}\mathbf{c}_0 + \mathbf{P}_{n2}^{\pm}\mathbf{c}_2 + \mathbf{Q}_{n1}^{\pm}\mathbf{d}_1 + \mathbf{Q}_{n2}^{\pm}\mathbf{d}_2, \qquad n = 0, 2, \tag{4.27}$$

is obtained for the SP_3 approach with the matrices

$$\mathbf{P}_{nm}^{\pm} = \begin{pmatrix} p_{nm,0} & 2p_{nm,1}^{\pm} & 0 & p_{nm,3}^{\pm} \\ p_{nm,0} & -p_{nm,1}^{\pm} & -p_{nm,2}^{\pm} & p_{nm,3}^{\pm} \\ p_{nm,0} & -p_{nm,1}^{\pm} & p_{nm,2}^{\pm} & p_{nm,3}^{\pm} \end{pmatrix}, \tag{4.28}$$

$$\mathbf{Q}_{nj}^{\pm} = \begin{pmatrix} q_{nj,1}^{\pm} & q_{nj,2}^{\pm} & q_{nj,2}^{\pm} \\ q_{nj,2}^{\pm} & q_{nj,1}^{\pm} & q_{nj,2}^{\pm} \\ q_{nj,2}^{\pm} & q_{nj,2}^{\pm} & q_{nj,1}^{\pm} \end{pmatrix}, \qquad n, m = 0, 2, \qquad j = 1, 2, \tag{4.29}$$

and their respective entries

$$\begin{aligned}
p_{nm,0} &= N_0\eta_{nm} = \eta_{nm}, \\
p_{nm,1}^{\pm} &= \frac{\sqrt{3}}{12}N_1\left(\eta_{nm} \mp \delta_{nm}\frac{\sqrt{3}D_n}{a}\right) = \frac{\sqrt{2}}{2}\left(\eta_{nm} \mp \delta_{nm}\frac{\sqrt{3}D_n}{a}\right), \\
p_{nm,2}^{\pm} &= \frac{1}{4}N_2\left(\eta_{nm} \mp \delta_{nm}\frac{\sqrt{3}D_n}{a}\right) = \frac{\sqrt{6}}{2}\left(\eta_{nm} \mp \delta_{nm}\frac{\sqrt{3}D_n}{a}\right), \\
p_{nm,3}^{\pm} &= \frac{1}{6}N_3\left(\eta_{nm} \mp \delta_{nm}\frac{\sqrt{3}D_n}{a}\right) - N_4\eta_{nm} = \frac{2\sqrt{15}}{3}\left(\eta_{nm} \mp \delta_{nm}\frac{\sqrt{3}D_n}{a}\right) - \frac{\sqrt{15}}{3}\eta_{nm}
\end{aligned}$$

and

$$\begin{aligned}
q_{nj,1}^{\pm} &= \left(\eta_{n0}\,\epsilon_{0j} + \eta_{n2}\,\epsilon_{2j} \mp \frac{1}{2}\epsilon_{nj}D_nB_j\right)\exp\left(\frac{\sqrt{3}}{6}aB_j\right), \\
q_{nj,2}^{\pm} &= \frac{2\sqrt{3}}{3aB_j}\left(\eta_{n0}\,\epsilon_{0j} + \eta_{n2}\,\epsilon_{2j} \pm \frac{1}{4}\epsilon_{nj}D_nB_j\right)\left(\exp\left(\frac{\sqrt{3}}{6}aB_j\right) - \exp\left(-\frac{\sqrt{3}}{3}aB_j\right)\right)
\end{aligned}$$

with

$$\eta_{00} = \frac{1}{4}, \qquad \eta_{02} = -\frac{3}{16}, \qquad \eta_{20} = -\frac{3}{80}, \qquad \eta_{22} = \frac{21}{80}. \tag{4.30}$$

Note that $\mathbf{P}_{nm}^{+} \equiv \mathbf{P}_{nm}^{-}$ for $n \neq m$.

In the system of equations (4.27), the vectors $\mathbf{d}_j$ can be eliminated. Considering the equations only for the inwardly directed partial currents, the exponential terms comprising $\mathbf{d}_j$ can be expressed by $\mathbf{J}_n^{-}$ and the polynomial terms, i.e.,

$$\mathbf{Q}_{n1}^{-}\mathbf{d}_1 + \mathbf{Q}_{n2}^{-}\mathbf{d}_2 = \mathbf{J}_n^{-} - \mathbf{P}_{n0}^{-}\mathbf{c}_0 - \mathbf{P}_{n2}^{-}\mathbf{c}_2 =: \mathbf{R}_n, \qquad n = 0, 2.$$

Thus, we have

$$\begin{pmatrix} \mathbf{d}_1 \\ \mathbf{d}_2 \end{pmatrix} = \begin{pmatrix} \mathbf{Q}_{01}^- & \mathbf{Q}_{02}^- \\ \mathbf{Q}_{21}^- & \mathbf{Q}_{22}^- \end{pmatrix}^{-1} \begin{pmatrix} \mathbf{R}_0 \\ \mathbf{R}_2 \end{pmatrix}. \tag{4.31}$$

The matrices $\mathbf{Q}_{nj}^{\pm}$ are nonsingular, symmetric, real, and circulant. Circulant matrices of the same size have the property of multiplicative commutativity. In addition, the product of circulant matrices is circulant [39, s. 3.3]. By means of these matrix properties, the inversion of the block matrix in (4.31) can be simplified as follows:

$$\begin{aligned} \begin{pmatrix} \mathbf{Q}_{01}^- & \mathbf{Q}_{02}^- \\ \mathbf{Q}_{21}^- & \mathbf{Q}_{22}^- \end{pmatrix}^{-1} &\overset{\text{gen.}}{=} \begin{pmatrix} {\mathbf{Q}_{01}^-}^{-1} + {\mathbf{Q}_{01}^-}^{-1}\mathbf{Q}_{02}^-\mathbf{S}_S^{-1}\mathbf{Q}_{21}^-{\mathbf{Q}_{01}^-}^{-1} & -{\mathbf{Q}_{01}^-}^{-1}\mathbf{Q}_{02}^-\mathbf{S}_S^{-1} \\ -\mathbf{S}_S^{-1}\mathbf{Q}_{21}^-{\mathbf{Q}_{01}^-}^{-1} & \mathbf{S}_S^{-1} \end{pmatrix} \\ &\overset{\substack{\mathbf{Q}_{nj}^- \\ \text{circul.}}}{=} \begin{pmatrix} \mathbf{Q}_{22}^-\mathbf{S}^{-1} & -\mathbf{Q}_{02}^-\mathbf{S}^{-1} \\ -\mathbf{Q}_{21}^-\mathbf{S}^{-1} & \mathbf{Q}_{01}^-\mathbf{S}^{-1} \end{pmatrix} \\ &=: \begin{pmatrix} \mathbf{Q}_{01}^I & \mathbf{Q}_{02}^I \\ \mathbf{Q}_{21}^I & \mathbf{Q}_{22}^I \end{pmatrix} \end{aligned}$$

with the so-called Schur complement

$$\mathbf{S}_S := \mathbf{Q}_{22}^- - \mathbf{Q}_{21}^-{\mathbf{Q}_{01}^-}^{-1}\mathbf{Q}_{02}^-$$

and the circulant matrix

$$\mathbf{S} := \mathbf{Q}_{01}^-\mathbf{Q}_{22}^- - \mathbf{Q}_{02}^-\mathbf{Q}_{21}^-.$$

Hence, we get

$$\mathbf{d}_1 = \mathbf{Q}_{01}^I(\mathbf{J}_0^- - \mathbf{P}_{00}^-\mathbf{c}_0 - \mathbf{P}_{02}^-\mathbf{c}_2) + \mathbf{Q}_{02}^I(\mathbf{J}_2^- - \mathbf{P}_{20}^-\mathbf{c}_0 - \mathbf{P}_{22}^-\mathbf{c}_2), \tag{4.32}$$

$$\mathbf{d}_2 = \mathbf{Q}_{21}^I(\mathbf{J}_0^- - \mathbf{P}_{00}^-\mathbf{c}_0 - \mathbf{P}_{02}^-\mathbf{c}_2) + \mathbf{Q}_{22}^I(\mathbf{J}_2^- - \mathbf{P}_{20}^-\mathbf{c}_0 - \mathbf{P}_{22}^-\mathbf{c}_2). \tag{4.33}$$

Accordingly, the matrices

$$\mathbf{S} = \begin{pmatrix} s_1 & s_2 & s_2 \\ s_2 & s_1 & s_2 \\ s_2 & s_2 & s_1 \end{pmatrix}, \qquad \mathbf{S}^{-1} = \begin{pmatrix} \breve{s}_1 & \breve{s}_2 & \breve{s}_2 \\ \breve{s}_2 & \breve{s}_1 & \breve{s}_2 \\ \breve{s}_2 & \breve{s}_2 & \breve{s}_1 \end{pmatrix},$$

and

$$\mathbf{Q}_{nj}^I = \begin{pmatrix} q_{nj,1}^I & q_{nj,2}^I & q_{nj,2}^I \\ q_{nj,2}^I & q_{nj,1}^I & q_{nj,2}^I \\ q_{nj,2}^I & q_{nj,2}^I & q_{nj,1}^I \end{pmatrix} \tag{4.34}$$

contain the entries

$$
\begin{aligned}
s_1 &= q^-_{01,1}q^-_{22,1} + 2q^-_{01,2}q^-_{22,2} - q^-_{02,1}q^-_{21,1} - 2q^-_{02,2}q^-_{21,2},\\
s_2 &= q^-_{01,1}q^-_{22,2} + q^-_{01,2}(q^-_{22,1} + q^-_{22,2}) - q^-_{02,1}q^-_{21,2} - q^-_{02,2}(q^-_{21,1} + q^-_{21,2}),\\
\check{s}_1 &= \frac{s_1 + s_2}{s_1^2 + s_1 s_2 - 2s_2^2},\\
\check{s}_2 &= \frac{-s_2}{s_1^2 + s_1 s_2 - 2s_2^2},\\
q^l_{nj,1} &= (-1)^{(\frac{n}{2}+j-1)}\big(q^-_{n'j',1}\check{s}_1 + 2q^-_{n'j',2}\check{s}_2\big),\\
q^l_{nj,2} &= (-1)^{(\frac{n}{2}+j-1)}\big(q^-_{n'j',1}\check{s}_2 + q^-_{n'j',2}(\check{s}_1 + \check{s}_2)\big),
\end{aligned}
$$

where

$$
n, n' = 0, 2, \qquad j, j' = 1, 2 \qquad \text{with} \qquad \begin{cases} n' = n, \;\; j' = j & \text{if } \mathrm{mod}(\frac{n}{2} + j, 2) = 0 \\ n' \neq n, \;\; j' \neq j, & \text{otherwise} \end{cases}.
$$

By the use of (4.32)–(4.33), the partial outward currents $\mathbf{J}^+_n$ can eventually be expressed as functions of the partial inward currents $\mathbf{J}^-_n$. Hence, the algebraic system of radial response-matrix equations

$$
\begin{aligned}
\mathbf{J}^+_n &= \mathbf{P}^+_{n0}\mathbf{c}_0 + \mathbf{P}^+_{n2}\mathbf{c}_2 + \mathbf{Q}^+_{n1}\mathbf{d}_1 + \mathbf{Q}^+_{n2}\mathbf{d}_2\\
&= \mathbf{V}_{n0}\mathbf{c}_0 + \mathbf{V}_{n2}\mathbf{c}_2 + \mathbf{W}_{n1}\mathbf{J}^-_0 + \mathbf{W}_{n2}\mathbf{J}^-_2
\end{aligned} \tag{4.35}
$$

holds with the matrices

$$
\mathbf{W}_{nj} := \mathbf{Q}^+_{n1}\mathbf{Q}^l_{0j} + \mathbf{Q}^+_{n2}\mathbf{Q}^l_{2j}, \tag{4.36}
$$

$$
\mathbf{V}_{nm} := \mathbf{P}^+_{nm} - \mathbf{W}_{n1}\mathbf{P}^-_{0m} - \mathbf{W}_{n2}\mathbf{P}^-_{2m}, \qquad n, m = 0, 2, \qquad j = 1, 2. \tag{4.37}
$$

The neutron current formulation based on the response-matrix method is a common technique in nodal approaches (see, e.g., [143, 150, 154, 160]).

SP_3 METHOD – AXIAL TREATMENT: The axial partial currents are proceeded in the same manner. Inserting the flux expansion approach (3.28) into the relations (4.21)–(4.24) gives the linear algebraic systems of equations

$$
\mathbf{J}^{z\pm}_n = \mathbf{P}^{z\pm}_{n0}\mathbf{c}^z_0 + \mathbf{P}^{z\pm}_{n2}\mathbf{c}^z_2 + \mathbf{Q}^{z\pm}_{n1}\mathbf{d}^z_1 + \mathbf{Q}^{z\pm}_{n2}\mathbf{d}^z_2
$$

and, eliminating $\mathbf{d}^z_j$, the response-matrix equations

$$
\mathbf{J}^{z+}_n = \mathbf{V}^z_{n0}\mathbf{c}^z_0 + \mathbf{V}^z_{n2}\mathbf{c}^z_2 + \mathbf{W}^z_{n1}\mathbf{J}^{z-}_0 + \mathbf{W}^z_{n2}\mathbf{J}^{z-}_2, \qquad n = 0, 2, \tag{4.38}
$$

with the vectors

$$\mathbf{J}_n^{z\pm} = \begin{pmatrix} J_{n+}^{z\pm} \\ J_{n-}^{z\pm} \end{pmatrix} \tag{4.39}$$

and

$$\mathbf{c}_n^z = \begin{pmatrix} c_{n0}^z \\ c_{n1}^z \\ c_{n2}^z \end{pmatrix}, \qquad \mathbf{d}_j^z = \begin{pmatrix} d_{j+}^z \\ d_{j-}^z \end{pmatrix}$$

as well as the matrices

$$\mathbf{P}_{nm}^{z\pm} = \begin{pmatrix} p_{nm,0}^z & p_{nm,1}^{z\pm} & p_{nm,2}^{z\pm} \\ p_{nm,0}^z & -p_{nm,1}^{z\pm} & p_{nm,2}^{z\pm} \end{pmatrix}, \tag{4.40}$$

$$\mathbf{Q}_{nj}^{z\pm} = \begin{pmatrix} q_{nj,1}^{z\pm} & q_{nj,2}^{z\pm} \\ q_{nj,2}^{z\pm} & q_{nj,1}^{z\pm} \end{pmatrix}, \tag{4.41}$$

$$\mathbf{Q}_{nj}^{zl} = \begin{pmatrix} q_{nj,1}^{zl} & q_{nj,2}^{zl} \\ q_{nj,2}^{zl} & q_{nj,1}^{zl} \end{pmatrix}, \qquad \text{where} \qquad \begin{pmatrix} \mathbf{Q}_{01}^{zl} & \mathbf{Q}_{02}^{zl} \\ \mathbf{Q}_{21}^{zl} & \mathbf{Q}_{22}^{zl} \end{pmatrix} := \begin{pmatrix} \mathbf{Q}_{01}^{z-} & \mathbf{Q}_{02}^{z-} \\ \mathbf{Q}_{21}^{z-} & \mathbf{Q}_{22}^{z-} \end{pmatrix}^{-1}, \tag{4.42}$$

and

$$\mathbf{W}_{nj}^z := \mathbf{Q}_{n1}^{z+}\mathbf{Q}_{0j}^{zl} + \mathbf{Q}_{n2}^{z+}\mathbf{Q}_{2j}^{zl}, \tag{4.43}$$

$$\mathbf{V}_{nm}^z := \mathbf{P}_{nm}^{z+} - \mathbf{W}_{n1}^z\mathbf{P}_{0m}^{z-} - \mathbf{W}_{n2}^z\mathbf{P}_{2m}^{z-}, \qquad n,m = 0,2, \qquad j = 1,2, \tag{4.44}$$

where

$$\begin{aligned}
p_{nm,0}^z &= \eta_{nm}, \\
p_{nm,1}^{z\pm} &= \sqrt{3}\Big(\eta_{nm} \mp \delta_{nm}\frac{D_n}{a_z}\Big), \\
p_{nm,2}^{z\pm} &= \sqrt{5}\Big(\eta_{nm} \mp \delta_{nm}\frac{3D_n}{a_z}\Big),
\end{aligned}$$

$$\begin{aligned}
q_{nj,1}^{z\pm} &= \Big(\eta_{n0}\,\epsilon_{0j} + \eta_{n2}\,\epsilon_{2j} \mp \frac{1}{2}\epsilon_{nj}D_nB_j\Big)\exp\Big(\frac{1}{2}a_zB_j\Big), \\
q_{nj,2}^{z\pm} &= \Big(\eta_{n0}\,\epsilon_{0j} + \eta_{n2}\,\epsilon_{2j} \pm \frac{1}{2}\epsilon_{nj}D_nB_j\Big)\exp\Big(-\frac{1}{2}a_zB_j\Big),
\end{aligned}$$

$$\begin{aligned}
s_1^z &= q_{01,1}^{z-}q_{22,1}^{z-} + q_{01,2}^{z-}q_{22,2}^{z-} - q_{02,1}^{z-}q_{21,1}^{z-} - q_{02,2}^{z-}q_{21,2}^{z-}, \\
s_2^z &= q_{01,1}^{z-}q_{22,2}^{z-} + q_{01,2}^{z-}q_{22,1}^{z-} - q_{02,1}^{z-}q_{21,2}^{z-} - q_{02,2}^{z-}q_{21,1}^{z-},
\end{aligned}$$

$$\check{s}_1^z = \frac{s_1^z}{s_1^{z\,2} - s_2^{z\,2}},$$
$$\check{s}_2^z = \frac{-s_2^z}{s_1^{z\,2} - s_2^{z\,2}},$$
$$q_{nj,1}^{zl} = (-1)^{(\frac{n}{2}+j-1)}\left(q_{n'j',1}^{z-}\check{s}_1^z + q_{n'j',2}^{z-}\check{s}_2^z\right),$$
$$q_{nj,2}^{zl} = (-1)^{(\frac{n}{2}+j-1)}\left(q_{n'j',1}^{z-}\check{s}_2^z + q_{n'j',2}^{z-}\check{s}_1^z\right)$$

with η_{nm} from (4.30) and again

$$n, n' = 0, 2, \qquad j, j' = 1, 2 \qquad \text{with} \qquad \begin{cases} n' = n, \;\; j' = j & \text{if } \mathrm{mod}(\frac{n}{2} + j, 2) = 0 \\ n' \neq n, \;\; j' \neq j, & \text{otherwise} \end{cases}.$$

Diffusion method: Considering the diffusion theory approach and inserting the radial flux expansion ansatzes (3.31)–(3.32) for $\Phi_0^{\mathbb{A}/\mathbb{B}\,r}$ into the relations (4.9)–(4.14) for the respective diffusion modification and, accordingly, (3.33) for Φ_0^z into (4.21)–(4.22), we obtain the reduced linear algebraic system of equations

$$\mathbf{J}_0^{(z)\pm} = \mathbf{P}_{00}^{(z)\pm}\mathbf{c}_0^{(z)} + \mathbf{Q}_{01}^{(z)\pm}\mathbf{d}_1^{(z)}$$

with the matrices $\mathbf{P}_{00}^{(z)\pm}$ and $\mathbf{Q}_{01}^{(z)}$ of (4.28)–(4.29) and (4.40)–(4.41), respectively. Expressing the partial outward currents $\mathbf{J}_0^{(z)+}$ by the partial inward currents $\mathbf{J}_0^{(z)-}$, we get

$$\begin{aligned} \mathbf{J}_0^{(z)+} &= \mathbf{P}_{00}^{(z)+}\mathbf{c}_0^{(z)} + \mathbf{Q}_{01}^{(z)+}\mathbf{d}_1^{(z)} \\ &= \mathbf{V}_{00}^{(z)}\mathbf{c}_0^{(z)} + \mathbf{W}_{01}^{(z)}\mathbf{J}_0^{(z)-} \end{aligned} \tag{4.45}$$

with the matrices

$$\mathbf{W}_{01}^{(z)} := \mathbf{Q}_{01}^{(z)+}\mathbf{Q}_{0j}^{(z)-\,-1},$$
$$\mathbf{V}_{00}^{(z)} := \mathbf{P}_{00}^{(z)+} - \mathbf{W}_{01}^{(z)}\mathbf{P}_{00}^{(z)-},$$

where

$$\mathbf{Q}_{0j}^{-\,-1} = \begin{pmatrix} \check{q}_{01,1} & \check{q}_{01,2} & \check{q}_{01,2} \\ \check{q}_{01,2} & \check{q}_{01,1} & \check{q}_{01,2} \\ \check{q}_{01,2} & \check{q}_{01,2} & \check{q}_{01,1} \end{pmatrix} \tag{4.46}$$

with

$$\breve{q}_{01,1} = \frac{q_{01,1} + q_{01,2}}{q_{01,1}^2 + q_{01,1}q_{01,2} - 2q_{01,2}^2},$$
$$\breve{q}_{01,2} = \frac{-q_{01,2}}{q_{01,1}^2 + q_{01,1}q_{01,2} - 2q_{01,2}^2}$$

and

$$\mathbf{Q}_{0j}^{z\,-1} = \begin{pmatrix} \breve{q}_{01,1}^z & \breve{q}_{01,2}^z \\ \breve{q}_{01,2}^z & \breve{q}_{01,1}^z \end{pmatrix} \tag{4.47}$$

with

$$\breve{q}_{01,1}^z = \frac{q_{01,1}^z}{{q_{01,1}^z}^2 - {q_{01,2}^z}^2},$$
$$\breve{q}_{01,2}^z = \frac{-q_{01,2}^z}{{q_{01,1}^z}^2 - {q_{01,2}^z}^2}.$$

4.3 Nodal boundary conditions

So far, expressions are derived to determine the nodal partial currents in terms of the flux expansion coefficients. By means of these averaged inwardly and outwardly directed partial currents, information between one trigonal prismatic element and its five neighboring nodes is exchanged ("nodal coupling"). We, therefore, recall Section 2.5, in which the approximate boundary conditions for the SP_3 and the diffusion approach are derived.

Conferring the deficiencies of homogenization theory outlined in Section 3.1, the interaction between adjacent regions has to be described in an equivalent manner to obtain a global power distribution with a homogenized reactor representation identical to the corresponding heterogeneous representation. Without the use of discontinuity factors, this equivalence may not be guarantied. However, in consequence of the lack of adequate discontinuity factors for the SP_3 transport theory, continuous surface-averaged neutron fluxes are assumed leading to continuous partial currents at nodal interfaces.

Let V^j be an adjacent node of V^i, then the interface condition (2.56) together with Fick's law (3.1) give the continuity of the nth moment neutron currents

$$\mathbf{n}_i \cdot \nabla \mathbf{J}_n^i(\mathbf{r}) = \mathbf{n}_i \cdot \nabla \mathbf{J}_n^j(\mathbf{r}), \qquad \mathbf{r} \in \partial V^{ij} = V^i \cap V^j, \qquad n = 0, 2, \tag{4.48}$$

with respect to the SP_3 approach. The unit outer normal vector $\mathbf{n}_i$ of the node V^i is directed towards V^j.

In the case that a boundary of a node V^i is part of the outer core boundary, the Marshak-like boundary conditions (2.58)–(2.59) have to be applied. With the SP_3 approximation of the partial currents (4.3)–(4.4), the incoming partial currents at the exterior boundary $\partial V^{i_{\text{ext}}}$ can be expressed as

$$\widetilde{J}_0^{-,i}(\mathbf{r}) = \frac{1}{4\pi}\int_0^{2\pi}\int_{-1}^{0} |\mu|\Psi^b(\mathbf{r},\mu,\varphi)\mathrm{d}\mu\mathrm{d}\varphi, \tag{4.49}$$

$$\widetilde{J}_2^{-,i}(\mathbf{r}) = \frac{3}{20\pi}\int_0^{2\pi}\int_{-1}^{0} p_3(|\mu|)\Psi^b(\mathbf{r},\mu,\varphi)\mathrm{d}\mu\mathrm{d}\varphi, \qquad \mathbf{r}\in\partial V^{i_{\text{ext}}}. \tag{4.50}$$

Assuming the particular class of the incident angular flux at the boundary

$$\Psi^b(\mathbf{r},\mathbf{\Omega}) = \tau(\mathbf{r})\Psi^i(\mathbf{r},-\mathbf{\Omega}), \qquad \mathbf{r}\in\partial V^{i_{\text{ext}}}, \qquad \mathbf{n_i}\cdot\mathbf{\Omega}<0, \tag{4.51}$$

with an arbitrary albedo function τ, and $\mathbf{n_i}$ denoting the outer unit normal vector of V^i at $\partial V^{i_{\text{ext}}}$, the above conditions (4.49)–(4.50) can be rewritten as

$$\widetilde{J}_0^{-,i}(\mathbf{r}) = \frac{1}{4\pi}\int_0^{2\pi}\tau_0(\mathbf{r})\int_0^{1}\mu\Psi^i(\mathbf{r},\mu,\varphi)\mathrm{d}\mu\mathrm{d}\varphi,$$

$$\widetilde{J}_2^{-,i}(\mathbf{r}) = \frac{3}{20\pi}\int_0^{2\pi}\tau_2(\mathbf{r})\int_0^{1}p_3(\mu)\Psi^i(\mathbf{r},\mu,\varphi)\mathrm{d}\mu\mathrm{d}\varphi.$$

Note that τ_n can optionally be chosen unequally for different moments $n=0,2$. Thus, taking again (4.3)–(4.4) into account, the incoming neutron currents at an exterior boundary $\partial V^{i_{\text{ext}}}$ of the node V^i can be determined via the outgoing partial currents of the same node, i.e.,

$$\widetilde{J}_n^{-,i}(\mathbf{r}) = \tau_n(\mathbf{r})\widetilde{J}_n^{+,i}(\mathbf{r}), \qquad \mathbf{r}\in\partial V^{i_{\text{ext}}}, \qquad n=0,2. \tag{4.52}$$

This relation can also be expressed in terms of the neutron flux. Hence, applying (4.3)–(4.4) to (4.52), the outer boundary conditions

$$\frac{1}{2}\big(1+\tau_0^i\big)D_0^i\,\mathbf{n}_i\cdot\nabla\widetilde{\Phi}_0^i(\mathbf{r}) = \big(1-\tau_0^i\big)\Big(-\frac{1}{4}\widetilde{\Phi}_0^i(\mathbf{r})+\frac{3}{16}\widetilde{\Phi}_2^i(\mathbf{r})\Big), \tag{4.53}$$

$$\frac{1}{2}\big(1+\tau_2^i\big)D_2^i\,\mathbf{n}_i\cdot\nabla\widetilde{\Phi}_2^i(\mathbf{r}) = \big(1-\tau_2^i\big)\Big(\frac{3}{80}\widetilde{\Phi}_0^i(\mathbf{r})-\frac{21}{80}\widetilde{\Phi}_2^i(\mathbf{r})\Big), \qquad \mathbf{r}\in\partial V^{i_{\text{ext}}}, \tag{4.54}$$

are obtained.

SP_3 METHOD – RADIAL TREATMENT: Considering the radial currents, let V^{i_l} be the adjacent node of V^i which is located in radial direction $\mathbf{e}_l$ referring to the vectors (3.19)–(3.20), $l=1,\ldots,6$. The above interface condition (4.48) can be rewritten to describe the continuity

of the radial neutron currents as follows:

$$\mathbf{e}_l \cdot \nabla \mathbf{J}_n^i(x,y) = \mathbf{e}_l \cdot \nabla \mathbf{J}_n^{i_l}(x,y), \qquad (x,y) \in \partial V^{ii_l}.$$

Hence, with (4.2) and particularly regarding the face-averaged incoming partial currents, we obtain

$$J_{nl}^{-,i} = J_{n\,l\pm3}^{+,i_l},$$

where $l = 1,2,3$ and $l = 4,5,6$, respectively. Hence, with the vector notation (4.25)–(4.26), the above continuity of the radially incoming and outgoing partial currents can be expressed via

$$\mathbf{J}_n^{-,i} = \mathbf{J}_n^{+,i_l}, \qquad n = 0,2. \tag{4.55}$$

With regard to the outer boundary, the albedo function τ_n of (4.52) is now assumed constant on each exterior nodal face $\partial V^{i_{\text{ext}}}$ for all V^i, which means that τ_n is to be a stepwise constant function along the outer core boundary. Thus, with

$$\tau_n^i := \tau_n(\mathbf{r}), \qquad \mathbf{r} \in \partial V^{i_{\text{ext}}},$$

the condition

$$\mathbf{J}_n^{-,i} = \tau_n^i \mathbf{J}_n^{+,i}, \qquad n = 0,2, \tag{4.56}$$

holds for the face-averaged radial partial currents. Particularly, we have

$$\tau_n^i = \begin{cases} 1, & \text{for reflective boundary conditions} \\ 0, & \text{for vacuum boundary conditions} \\ -1, & \text{for zero-flux boundary conditions} \end{cases} \tag{4.57}$$

for every nodal element V^i and every energy group g, whose index is omitted here.

SP_3 METHOD – AXIAL TREATMENT: Analogously, for an axial upper adjacent node V^{i_a} and a lower adjacent node V^{i_b}, the interface conditions

$$J_{n\pm}^{z-,i} = J_{n\mp}^{z+,i_{a/b}} \tag{4.58}$$

and the outer boundary conditions

$$J_{n\pm}^{z-,i} = \tau_n^i J_{n\mp}^{z+,i} \tag{4.59}$$

are obtained for the axial partial currents defined in (4.39), where $n = 0, 2$.

Diffusion method: Considering only the zeroth moment $n = 0$, both the interface conditions (4.55), (4.58) and the exterior boundary conditions (4.56), (4.59) also hold for the partial currents $\mathbf{J}_0^{(z)\pm,i}$ derived from diffusion theory when applying the conditions (2.61) and (2.62), respectively. The expressions (4.53)–(4.54) accordingly reduce to the outer boundary condition

$$\frac{1}{2}\big(1+\tau_0^i\big)D_0^i\,\mathbf{n}_i\cdot\nabla\Phi_0^i(\mathbf{r}) = -\frac{1}{4}\big(1-\tau_0^i\big)\Phi_0^i(\mathbf{r}), \qquad \mathbf{r}\in\partial V^{i_{\text{ext}}}.$$

4.4 Determination of the nodal neutron source

Consider the general neutron source (3.5) of the SP_3 equations (3.3)–(3.4) in within-group form

$$\begin{aligned}\widetilde{S}_{0,g}(\mathbf{r}) = &\sum_{g'<g}\Sigma_{s0,gg'}\big(\widetilde{\Phi}_{0,g'}(\mathbf{r})-2\widetilde{\Phi}_{2,g'}(\mathbf{r})\big)+\sum_{g'>g}\Sigma_{s0,gg'}\big(\widetilde{\Phi}_{0,g'}(\mathbf{r})-2\widetilde{\Phi}_{2,g'}(\mathbf{r})\big)\\ &+\frac{1}{k_{\text{eff}}}\chi_g\sum_{g'=1}^{G}\nu\Sigma_{f,g'}\big(\widetilde{\Phi}_{0,g'}(\mathbf{r})-2\widetilde{\Phi}_{2,g'}(\mathbf{r})\big)\end{aligned} \tag{4.60}$$

comprising a downward and an upward scattering term as wells as a term describing the neutron fission. In the course of the iteration process, the particular neutron source terms averaged over the nodal volumes have to be calculated. Let, therefore,

$$\overline{\widetilde{\Phi}}_{n,g} = \frac{1}{V}\iiint_V\widetilde{\Phi}_{n,g}(\mathbf{r})\mathrm{d}V = \frac{1}{A_\triangle}\iint_{A_\triangle}\widetilde{\Phi}_{n,g}^{\mathtt{A/B}\,r}(x,y)\mathrm{d}A = \frac{1}{a_z}\int_{-\frac{a_z}{2}}^{\frac{a_z}{2}}\widetilde{\Phi}_{n,g}^{z}(z)\mathrm{d}z, \tag{4.61}$$

$$\overline{\widetilde{S}}_{0,g} = \frac{1}{V}\iiint_V\widetilde{S}_{0,g}(\mathbf{r})\mathrm{d}V = \frac{1}{A_\triangle}\iint_{A_\triangle}\widetilde{S}_{0,g}^{\mathtt{A/B}\,r}(x,y)\mathrm{d}A = \frac{1}{a_z}\int_{-\frac{a_z}{2}}^{\frac{a_z}{2}}\widetilde{S}_{0,g}^{z}(z)\mathrm{d}z \tag{4.62}$$

be the formal definitions of the node-averaged neutron flux and source, $n = 0, 2$, with the nodal height a_z, the trigonal node area $A_\triangle = \frac{\sqrt{3}a^2}{4}$, and the nodal volume $V = A_\triangle a_z$. According to the source representation of (4.60), the average neutron source

$$\overline{\widetilde{S}}_{0,g} = \overline{\widetilde{S}}_{sd,g} + \overline{\widetilde{S}}_{su,g} + \frac{1}{k_{\text{eff}}}\chi_g\overline{\widetilde{S}}_f \tag{4.63}$$

is split into the respective averaged downscattering term

$$\overline{\widetilde{S}}_{sd,g} := \sum_{g'<g}\Sigma_{s0,gg'}(\overline{\widetilde{\Phi}}_{0,g'}-2\overline{\widetilde{\Phi}}_{2,g'}), \tag{4.64}$$

the upscattering term

$$\overline{\widetilde{S}}_{su,g} := \sum_{g'>g} \Sigma_{s0,gg'}(\overline{\widetilde{\Phi}}_{0,g'} - 2\overline{\widetilde{\Phi}}_{2,g'}), \tag{4.65}$$

and the fission source term

$$\overline{\widetilde{S}}_{f} := \sum_{g'=1}^{G} \nu\Sigma_{f,g'}(\overline{\widetilde{\Phi}}_{0,g'} - 2\overline{\widetilde{\Phi}}_{2,g'}), \tag{4.66}$$

which are determined via the average neutron flux moments $\overline{\widetilde{\Phi}}_{0,g}$ and $\overline{\widetilde{\Phi}}_{2,g}$.

SP_3 METHOD – RADIAL TREATMENT: In addition to the average neutron source, the coefficients of the source expansions have to be determined. Let, therefore,

$$\mathbf{s}_{0,g} = \begin{pmatrix} s_{00,g} \\ s_{01,g} \\ s_{02,g} \\ s_{03,g} \end{pmatrix}$$

be the coefficient vector of the radial polynomial source representation (3.25). Applying (3.25) to the radial neutron source (3.10), multiplying by the polynomials $h_k^{\mathtt{A/B}}$ of (3.21)–(3.22), and integrating over the respective trigonal area yields expressions for the source coefficients in relation to the neutron flux coefficients $\mathbf{c}_{n,g}$ of (3.23)–(3.24), $n = 0, 2$. Using the property of orthogonality of $h_k^{\mathtt{A/B}}$, we obtain

$$\mathbf{s}_{0,g} = \mathbf{s}_{sd,g} + \mathbf{s}_{su,g} + \frac{1}{k_{\text{eff}}}\chi_g \mathbf{s}_f \tag{4.67}$$

with

$$\mathbf{s}_{sd,g} := \sum_{g'<g} \Sigma_{s0,gg'}(\mathbf{c}_{0,g'} - 2\mathbf{c}_{2,g'}), \tag{4.68}$$

$$\mathbf{s}_{su,g} := \sum_{g'>g} \Sigma_{s0,gg'}(\mathbf{c}_{0,g'} - 2\mathbf{c}_{2,g'}), \tag{4.69}$$

$$\mathbf{s}_{f} := \sum_{g'=1}^{G} \nu\Sigma_{f,g'}(\mathbf{c}_{0,g'} - 2\mathbf{c}_{2,g'}). \tag{4.70}$$

SP_3 METHOD – AXIAL TREATMENT: In z direction, the coefficients

$$\mathbf{s}^z_{0,g} = \begin{pmatrix} s^z_{00,g} \\ s^z_{01,g} \\ s^z_{02,g} \end{pmatrix}$$

of the respective axial source expansion (3.29) are related to the axial flux coefficients $\mathbf{c}^z_{n,g}$ of (3.28) as follows:

$$\mathbf{s}^z_{0,g} = \mathbf{s}^z_{sd,g} + \mathbf{s}^z_{su,g} + \frac{1}{k_{\text{eff}}}\chi_g \mathbf{s}^z_f, \tag{4.71}$$

where

$$\mathbf{s}^z_{sd,g} := \sum_{g'<g} \Sigma_{s0,gg'}(\mathbf{c}^z_{0,g'} - 2\mathbf{c}^z_{2,g'}), \tag{4.72}$$

$$\mathbf{s}^z_{su,g} := \sum_{g'>g} \Sigma_{s0,gg'}(\mathbf{c}^z_{0,g'} - 2\mathbf{c}^z_{2,g'}), \tag{4.73}$$

$$\mathbf{s}^z_{f} := \sum_{g'=1}^{G} \nu\Sigma_{f,g'}(\mathbf{c}^z_{0,g'} - 2\mathbf{c}^z_{2,g'}). \tag{4.74}$$

Diffusion method: Considering the neutron source (3.7) of the diffusion equation (3.6)

$$S_{0,g}(\mathbf{r}) = \sum_{g'<g} \Sigma_{s0,gg'}\Phi_{0,g'}(\mathbf{r}) + \sum_{g'>g} \Sigma_{s0,gg'}\Phi_{0,g'}(\mathbf{r}) + \frac{1}{k_{\text{eff}}}\chi_g \sum_{g'=1}^{G} \nu\Sigma_{f,g'}\Phi_{0,g'}(\mathbf{r}),$$

we have

$$\overline{S}_{0,g} = \underbrace{\sum_{g'<g} \Sigma_{s0,gg'}\overline{\Phi}_{0,g'}}_{=:\overline{S}_{sd,g}} + \underbrace{\sum_{g'>g} \Sigma_{s0,gg'}\overline{\Phi}_{0,g'}}_{=:\overline{S}_{su,g}} + \frac{1}{k_{\text{eff}}}\chi_g \underbrace{\sum_{g'=1}^{G} \nu\Sigma_{f,g'}\overline{\Phi}_{0,g'}}_{=:\overline{S}_f}. \tag{4.75}$$

for the respective average source. According to the derivation above, the polynomial diffusion theory source coefficients are approximated as follows:

$$\mathbf{s}^{(z)}_{0,g} = \underbrace{\sum_{g'<g} \Sigma_{s0,gg'}\mathbf{c}^{(z)}_{0,g'}}_{=:\mathbf{s}^{(z)}_{sd,g}} + \underbrace{\sum_{g'>g} \Sigma_{s0,gg'}\mathbf{c}^{(z)}_{0,g'}}_{=:\mathbf{s}^{(z)}_{su,g}} + \frac{1}{k_{\text{eff}}}\chi_g \underbrace{\sum_{g'=1}^{G} \nu\Sigma_{f,g'}\mathbf{c}^{(z)}_{0,g'}}_{=:\mathbf{s}^{(z)}_{f}}. \tag{4.76}$$

4.5 Determination of the nodal transverse neutron leakage

In consequence of the decoupling of the solution space of the DYN3D SP_3 transport and diffusion method into the radial plane and the axial direction by transverse integration, the neutron leakage in the respective transverse direction or plane is described by the SP_3 transverse leakages (3.11) and (3.14) as well as the terms (3.15) and (3.16) in case of the diffusion approach. In addition to the scattering and fission terms of Section 4.4, these nodal transverse leakages are formally treated as neutron sources as well.

In Section 3.5, equations (3.26) and (3.30), the axial and radial neutron leakages are approximated by polynomials of maximum order two. It is shown in the following that the polynomial coefficients can be determined by the average transverse leakages of the considered node and its respective radial and axial nodal neighbors. These average transverse leakages can then be represented in terms of face-averaged partial currents, which play a central role in the DYN3D inner-iteration algorithm.

SP_3 METHOD – RADIAL TREATMENT: Hence, considering the SP_3 approach, the averaged neutron leakage of the node V^i transverse to the radial plane is obtained by integrating $\widetilde{L}_n^{r,i}$ of (3.11) over the trigonal area $A_\triangle^i$ of the node. Applying the divergence theorem to the vector field $\mathbf{F}_z := \begin{pmatrix} 0 \\ 0 \\ \frac{\partial}{\partial z}\widetilde{\Phi}_n^i \end{pmatrix}$ and Fick's law (3.1) yields

$$
\begin{aligned}
\overline{\widetilde{L}}_n^{r,i} &= \frac{4\sqrt{3}}{3(a^i)^2} \iint_{A_\triangle^i} \widetilde{L}_n^{r,i}(x,y)\mathrm{d}A \\
&\overset{\text{def. (3.11)}}{=} -\frac{4\sqrt{3}D_n^i}{3(a^i)^2 a_z^i} \iiint_{V^i} \frac{\partial^2}{\partial z^2}\widetilde{\Phi}_n^i(x,y,z)\mathrm{d}V \\
&= -\frac{4\sqrt{3}D_n^i}{3(a^i)^2 a_z^i} \iiint_{V^i} \nabla\cdot\mathbf{F}_z\,\mathrm{d}V \\
&\overset{\text{div. thm.}}{=} -\frac{4\sqrt{3}D_n^i}{3(a^i)^2 a_z^i} \oiint_{\partial V^i} \mathbf{F}_z\cdot\mathbf{n}\,\mathrm{d}S \\
&= -\frac{4\sqrt{3}D_n^i}{3(a^i)^2 a_z^i} \left(\iint_{A_\triangle^i, z=\frac{a_z^i}{2}} + \iint_{A_\triangle^i, z=-\frac{a_z^i}{2}} \right) \frac{\partial}{\partial z}\widetilde{\Phi}_n^i(x,y,z)\mathrm{d}A \\
&\overset{\text{Fick's law (3.1)}}{=} \frac{4\sqrt{3}}{3(a^i)^2 a_z^i} \left(\iint_{A_\triangle^i, z=\frac{a_z^i}{2}} + \iint_{A_\triangle^i, z=-\frac{a_z^i}{2}} \right) \widetilde{J}_n^{z,i}(x,y,z)\mathrm{d}A \\
&= \frac{1}{a_z^i}\left(J_{n+}^{z+,i} - J_{n+}^{z-,i} + J_{n-}^{z+,i} - J_{n-}^{z-,i}\right) \\
&= \frac{1}{a_z^i}\sum_{l=1}^{2}(\mathbf{J}_n^{z+,i} - \mathbf{J}_n^{z-,i})_l, \qquad n = 0,2,
\end{aligned}
\tag{4.77}
$$

where $\widetilde{J}_n^{z,i}(\mathbf{r}) = \begin{pmatrix} 0 \\ 0 \\ 1 \end{pmatrix} \cdot \widetilde{\mathbf{J}}_n^i(\mathbf{r})$. Evidently, like the partial currents $J_{n\pm}^{z\pm,i}$ of (4.21)–(4.24), the average transverse leakages $\overline{\widetilde{L}}_n^{r,i}$ are independent of the nodal orientations A/B. Next, consider a node V^i and its in direction $\mathbf{e}_l$ adjacent node V^{i_l}. In Figure 4.3, the locations of the respective radial nodal faces l are illustrated in consideration of the different nodal orientations A and B. See further the vectors given in (3.19)–(3.20) to recall the unit outer normals $\mathbf{e}_l$ of the faces l. Assuming the same continuity requirements at material interfaces

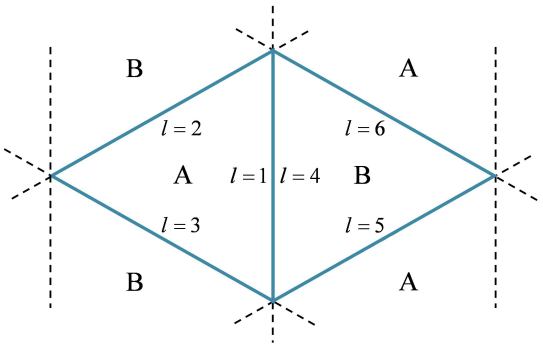

FIGURE 4.3: Location of the nodal faces l of adjacent nodes with the respective orientations A and B.

for the second derivative of the flux with respect to the coordinate z as for the flux itself, the general relations

$$\frac{\partial^2}{\partial z^2}\widetilde{\Phi}_n^i(\mathbf{r}) = \frac{\partial^2}{\partial z^2}\widetilde{\Phi}_n^{i_l}(\mathbf{r}), \tag{4.78}$$

$$D_n^i\,\mathbf{n}_i \cdot \nabla\left(\frac{\partial^2}{\partial z^2}\widetilde{\Phi}_n^i(\mathbf{r})\right) = D_n^{i_l}\,\mathbf{n}_i \cdot \nabla\left(\frac{\partial^2}{\partial z^2}\widetilde{\Phi}_n^{i_l}(\mathbf{r})\right), \qquad \mathbf{r} = (x,y,z) \in \partial V^{ii_l}, \tag{4.79}$$

hold according to the flux interface conditions (2.55) and (2.56) for $n = 0, 2$. Hence, with (3.11) and the assumption of an identical node height $a_z^i = a_z^{i_l}$, the interface conditions

$$\frac{1}{D_n^i}\widetilde{L}_{nl}^{r,i}(x,y) = \frac{1}{D_n^{i_l}}\widetilde{L}_{n\,l\pm3}^{r,i_l}(x,y), \tag{4.80}$$

$$\mathbf{e}_l \cdot \nabla\widetilde{L}_{nl}^{r,i}(x,y) = -\mathbf{e}_{l\pm3} \cdot \nabla\widetilde{L}_{n\,l\pm3}^{r,i_l}(x,y), \qquad (x,y) \in \partial V^{ii_l}, \qquad n = 0,2, \tag{4.81}$$

result from the above relations (4.78)–(4.79) for the transverse leakages $\widetilde{L}_{nl}^{r,i}$ at the interfaces l between two adjacent nodal elements V^i and V^{i_l}, $l = 1,2,3$ and $l = 4,5,6$, respectively. Let now the point with the coordinates (x_l, y_l) be the center of the nodal face l, then the occurring derivatives can be approximated by the respective difference quotients

$$\mathbf{e}_l \cdot \nabla\widetilde{L}_{nl}^{r,i}(x,y)\Big|_{(x,y)=(x_l,y_l)} \approx \frac{\bar{\widetilde{L}}_{nl}^{r,i} - \bar{\widetilde{L}}_{n}^{r,i}}{\frac{\sqrt{3}}{6}a^i}, \tag{4.82}$$

where $\bar{\widetilde{L}}_{nl}^{r,i}$ denotes the mean transverse leakage of the faces l. From (4.81) and (4.82), we consequently get

$$\bar{\widetilde{L}}_{nl}^{r,i} - \bar{\widetilde{L}}_{n}^{r,i} = -\left(\bar{\widetilde{L}}_{n\,l\pm3}^{r,i_l} - \bar{\widetilde{L}}_{n}^{r,i_l}\right)$$

and, with (4.80) eventually,

$$\bar{\tilde{L}}^{r,i}_{nl} = \frac{D^i_n}{D^i_n + D^{i_l}_n}\big(\bar{\tilde{L}}^{r,i}_n + \bar{\tilde{L}}^{r,i_l}_n\big), \qquad l = 1,\dots,6, \qquad n = 0,2. \tag{4.83}$$

In case the nodal boundary $\partial V^{i_{\text{ext}}}$ coincides the exterior boundary, the Marshak-like boundary conditions (2.58)–(2.59) are considered taking the particular class (4.51) of the incident flux into account. Assuming again the same conditions for the second derivative of the flux $\frac{\partial^2}{\partial z^2}\widetilde{\Phi}^i_n$ as for the flux itself, the outer boundary conditions (4.53)–(4.54) can be rewritten with respect to the transverse leakages in an analogous manner to the aforementioned interface conditions. Thus, for a point $(x,y) \in \partial V^{i_{\text{ext}}}$ on the nodal face l at the exterior boundary, the following outer boundary transverse-leakage conditions hold:

$$\begin{aligned}
\frac{1}{2}(1+\tau^i_0)\,\mathbf{e}_l \cdot \nabla \widetilde{L}^{r,i}_{0l}(x,y) &= (1-\tau^i_0)\Big(-\frac{1}{4D^i_0}\widetilde{L}^{r,i}_{0l}(x,y) + \frac{3}{16D^i_2}\widetilde{L}^{r,i}_{2l}(x,y)\Big),\\
\frac{1}{2}(1+\tau^i_2)\,\mathbf{e}_l \cdot \nabla \widetilde{L}^{r,i}_{2l}(x,y) &= (1-\tau^i_2)\Big(\frac{3}{80D^i_0}\widetilde{L}^{r,i}_{0l}(x,y) - \frac{21}{80D^i_2}\widetilde{L}^{r,i}_{2l}(x,y)\Big).
\end{aligned}$$

According to (4.82), the occurring derivatives are approximated, and we get

$$\begin{aligned}
\frac{\sqrt{3}}{a^i}(1+\tau^i_0)(\bar{\tilde{L}}^{r,i}_{0l} - \bar{\tilde{L}}^{r,i}_0) &= (1-\tau^i_0)\Big(-\frac{1}{4D^i_0}\bar{\tilde{L}}^{r,i}_{0l} + \frac{3}{16D^i_2}\bar{\tilde{L}}^{r,i}_{2l}\Big),\\
\frac{\sqrt{3}}{a^i}(1+\tau^i_2)(\bar{\tilde{L}}^{r,i}_{2l} - \bar{\tilde{L}}^{r,i}_2) &= (1-\tau^i_2)\Big(\frac{3}{80D^i_0}\bar{\tilde{L}}^{r,i}_{0l} - \frac{21}{80D^i_2}\bar{\tilde{L}}^{r,i}_{2l}\Big).
\end{aligned}$$

With

$$\begin{aligned}
\alpha^i_n &:= \frac{\sqrt{3}}{a^i}(1+\tau^i_n),\\
\beta^i_{kn} &:= \frac{1}{4D^i_k}(1-\tau^i_n),\\
\gamma^i &:= \alpha^i_0\alpha^i_2 + \frac{21}{20}\alpha^i_0\beta^i_{22} + \alpha^i_2\beta^i_{00} + \frac{15}{16}\beta^i_{00}\beta^i_{22},
\end{aligned}$$

the average transverse leakage from an exterior nodal face l can eventually be determined via

$$\bar{\tilde{L}}^{r,i}_{0l} = \frac{1}{\gamma^i}\Big(\alpha^i_0(\alpha^i_2 + \frac{21}{20}\beta^i_{22})\bar{\tilde{L}}^{r,i}_0 + \frac{3}{4}\alpha^i_2\beta^i_{20}\bar{\tilde{L}}^{r,i}_2\Big), \tag{4.84}$$

$$\bar{\tilde{L}}^{r,i}_{2l} = \frac{1}{\gamma^i}\Big(\frac{3}{20}\alpha^i_0\beta^i_{02}\bar{\tilde{L}}^{r,i}_0 + \alpha^i_2(\alpha^i_0 + \beta^i_{00})\bar{\tilde{L}}^{r,i}_2\Big). \tag{4.85}$$

As stated initially in this section, the leakage transversal to the radial plane is represented by the polynomial expansion approach (3.26). Hence, four polynomial leakage coefficients l^i_{nk}, $k = 0,\dots,3$, have to be determined for both moment indices $n = 0,2$. For a node with

the orientation A or B, we have

$$\begin{aligned}
\tilde{\bar{L}}_n^{r,i} &= \frac{4\sqrt{3}}{3(a^i)^2}\sum_{k=0}^{3} l_{nk}^i \int_{-\frac{\sqrt{3}}{3}a^i}^{\frac{\sqrt{3}}{6}a^i}\int_{-\frac{\sqrt{3}}{3}x-\frac{1}{3}a^i}^{\frac{\sqrt{3}}{3}x+\frac{1}{3}a^i} h_k^{\mathtt{A}}(x,y)\mathrm{d}y\,\mathrm{d}x \\
&= \frac{4\sqrt{3}}{3(a^i)^2}\sum_{k=0}^{3} l_{nk}^i \int_{-\frac{\sqrt{3}}{6}a^i}^{\frac{\sqrt{3}}{3}a^i}\int_{\frac{\sqrt{3}}{3}x-\frac{1}{3}a^i}^{-\frac{\sqrt{3}}{3}x+\frac{1}{3}a^i} h_k^{\mathtt{B}}(x,y)\mathrm{d}y\,\mathrm{d}x, \\
\tilde{\bar{L}}_{n1}^{r,i} &= \frac{1}{a^i}\sum_{k=0}^{3} l_{nk}^i \int_{-\frac{a^i}{2}}^{\frac{a^i}{2}} h_k^{\mathtt{A}}(\frac{\sqrt{3}}{6}a,y)\mathrm{d}y, \\
\tilde{\bar{L}}_{n\,2/3}^{r,i} &= \frac{1}{a^i}\sum_{k=0}^{3} l_{nk}^i \int_{-\frac{\sqrt{3}}{3}a^i}^{\frac{\sqrt{3}}{6}a^i} h_k^{\mathtt{A}}(x,g_{2/3}(x))\sqrt{1+\left(\frac{\mathrm{d}}{\mathrm{d}x}g_{2/3}(x)\right)^2}\mathrm{d}x, \\
\tilde{\bar{L}}_{n4}^{r,i} &= \frac{1}{a^i}\sum_{k=0}^{3} l_{nk}^i \int_{-\frac{a^i}{2}}^{\frac{a^i}{2}} h_k^{\mathtt{B}}(-\frac{\sqrt{3}}{6}a,y)\mathrm{d}y, \\
\tilde{\bar{L}}_{n\,5/6}^{r,i} &= \frac{1}{a^i}\sum_{k=0}^{3} l_{nk}^i \int_{-\frac{\sqrt{3}}{6}a^i}^{\frac{\sqrt{3}}{3}a^i} h_k^{\mathtt{B}}(x,g_{5/6}(x))\sqrt{1+\left(\frac{\mathrm{d}}{\mathrm{d}x}g_{5/6}(x)\right)^2}\mathrm{d}x,
\end{aligned}$$

where $g_l(x)$, $l = 2,3,5,6$, refers to the linear functions describing the radial faces l (see equations (4.5)–(4.8)). Analogously to the neutron currents, the transverse neutron leakages can be expressed independently of the nodal orientation A/B. With the vectors

$$\tilde{\bar{\mathbf{L}}}_n^{r,i} := \begin{pmatrix} \tilde{\bar{L}}_n^{r,i} \\ \tilde{\bar{L}}_{n1}^{r,i} \\ \tilde{\bar{L}}_{n2}^{r,i} \\ \tilde{\bar{L}}_{n3}^{r,i} \end{pmatrix} \equiv \begin{pmatrix} \tilde{\bar{L}}_n^{r,i} \\ \tilde{\bar{L}}_{n4}^{r,i} \\ \tilde{\bar{L}}_{n5}^{r,i} \\ \tilde{\bar{L}}_{n6}^{r,i} \end{pmatrix}$$

and

$$\mathbf{l}_n^i = \begin{pmatrix} l_{n0}^i \\ l_{n1}^i \\ l_{n2}^i \\ l_{n3}^i \end{pmatrix},$$

the linear system of equations

$$\begin{pmatrix} N_0 & 0 & 0 & 0 \\ N_0 & \frac{\sqrt{3}}{6}N_1 & 0 & \frac{1}{6}N_3 - N_4 \\ N_0 & -\frac{\sqrt{3}}{12}N_1 & -\frac{1}{4}N_2 & \frac{1}{6}N_3 - N_4 \\ N_0 & -\frac{\sqrt{3}}{12}N_1 & \frac{1}{4}N_2 & \frac{1}{6}N_3 - N_4 \end{pmatrix} \mathbf{l}_n^i = \begin{pmatrix} 1 & 0 & 0 & 0 \\ 1 & \sqrt{2} & 0 & \frac{\sqrt{15}}{3} \\ 1 & -\frac{\sqrt{2}}{2} & -\frac{\sqrt{6}}{2} & \frac{\sqrt{15}}{3} \\ 1 & -\frac{\sqrt{2}}{2} & \frac{\sqrt{6}}{2} & \frac{\sqrt{15}}{3} \end{pmatrix} \mathbf{l}_n^i = \tilde{\bar{\mathbf{L}}}_n^{r,i}$$

holds for $n = 0, 2$. Thus,

$$\mathfrak{l}_n^i = \begin{pmatrix} \frac{1}{N_0}\overline{\widetilde{L}}_n^{r,i} \\ \frac{2\sqrt{3}}{3N_1}(2\overline{\widetilde{L}}_{n1}^{r,i} - \overline{\widetilde{L}}_{n2}^{r,i} - \overline{\widetilde{L}}_{n3}^{r,i}) \\ \frac{2}{N_2}(\overline{\widetilde{L}}_{n3}^{r,i} - \overline{\widetilde{L}}_{n2}^{r,i}) \\ \frac{1}{3(\frac{1}{6}N_3 - N_4)}(\overline{\widetilde{L}}_{n1}^{r,i} + \overline{\widetilde{L}}_{n2}^{r,i} + \overline{\widetilde{L}}_{n3}^{r,i} - 3\overline{\widetilde{L}}_n^{r,i}) \end{pmatrix} = \begin{pmatrix} \overline{\widetilde{L}}_n^{r,i} \\ \frac{\sqrt{2}}{6}(2\overline{\widetilde{L}}_{n1}^{r,i} - \overline{\widetilde{L}}_{n2}^{r,i} - \overline{\widetilde{L}}_{n3}^{r,i}) \\ \frac{\sqrt{6}}{6}(\overline{\widetilde{L}}_{n3}^{r,i} - \overline{\widetilde{L}}_{n2}^{r,i}) \\ \frac{\sqrt{15}}{15}(\overline{\widetilde{L}}_{n1}^{r,i} + \overline{\widetilde{L}}_{n2}^{r,i} + \overline{\widetilde{L}}_{n3}^{r,i} - 3\overline{\widetilde{L}}_n^{r,i}) \end{pmatrix}. \tag{4.86}$$

In summary, taking $\overline{\widetilde{L}}_n^{r,i}$ of (4.77) as well as $\overline{\widetilde{L}}_{nl}^{r,i}$ of (4.83) in case of an interfacial boundary or (4.84)–(4.85) in case of an exterior into account, we see from (4.86) that the transverse leakage of a node V^i can be approximated by the axially incoming and outgoing partial currents of the element itself together with those of the respective radially adjacent nodes.

SP_3 METHOD – AXIAL TREATMENT: For the z direction, the neutron leakage into the radial plane is to be considered. With $\widetilde{L}_n^{z,i}$ of (3.14), the average leakage perpendicular to the axial direction is obtained in an analogous manner to the derivation of (4.77) as follows:

$$\begin{aligned}
\overline{\widetilde{L}}_n^{z,i} &= \frac{1}{a_z^i}\int_{-\frac{a_z^i}{2}}^{\frac{a_z^i}{2}} \widetilde{L}_n^{z,i}(z)\mathrm{d}z \\
&\overset{\text{def. (3.14)}}{=} -\frac{4\sqrt{3}D_n^i}{3(a^i)^2 a_z^i}\iiint_{V^i}\Big(\frac{\partial^2}{\partial x^2} + \frac{\partial^2}{\partial y^2}\Big)\widetilde{\Phi}_n^i(x,y,z)\mathrm{d}V \\
&\overset{\text{div. thm.}}{=} -\frac{4\sqrt{3}D_n^i}{3(a^i)^2 a_z^i}\oiint_{\partial V^i}(\mathbf{F}_x + \mathbf{F}_y)\cdot\mathbf{n}\,\mathrm{d}S \\
&\overset{\text{Fick's law (3.1)}}{=} \frac{4\sqrt{3}}{3(a^i)^2 a_z^i}\Big(\iint_{A_1^i} + \iint_{A_2^i} + \iint_{A_3^i}\Big)\Big(\widetilde{J}_n^{x,i}(x,y,z) + \widetilde{J}_n^{y,i}(x,y,z)\Big)\mathrm{d}A \\
&= \frac{4\sqrt{3}}{3a^i}\sum_{l=1}^{3}\big(J_{nl}^{+,i} - J_{nl}^{-,i}\big) \\
&= \frac{4\sqrt{3}}{3a^i}\sum_{l=1}^{3}(\mathbf{J}_n^{+,i} - \mathbf{J}_n^{-,i})_l, \qquad n = 0, 2,
\end{aligned} \tag{4.87}$$

where $\mathbf{F}_x := \begin{pmatrix} \frac{\partial}{\partial x}\widetilde{\Phi}_n^i \\ 0 \\ 0 \end{pmatrix}$, $\mathbf{F}_y := \begin{pmatrix} 0 \\ \frac{\partial}{\partial y}\widetilde{\Phi}_n^i \\ 0 \end{pmatrix}$ as well as $\widetilde{J}_n^{x,i}(\mathbf{r}) = \begin{pmatrix} 1 \\ 0 \\ 0 \end{pmatrix}\cdot\widetilde{\mathbf{J}}_n^i(\mathbf{r})$ and $\widetilde{J}_n^{y,i}(\mathbf{r}) = \begin{pmatrix} 0 \\ 1 \\ 0 \end{pmatrix}\cdot\widetilde{\mathbf{J}}_n^i(\mathbf{r})$. The denotation A_l^i, $l = 1, 2, 3$, generally refers to the three surface areas of the node V^i parallelly aligned to the z coordinate axis (recall Figure 3.3). By reason of the equivalence relation of the radial partial currents (4.26), also $\overline{\widetilde{L}}_n^{z,i}$ is independent of the nodal orientation. We now define again an axial upper adjacent node V^{i_a} and a

lower adjacent node V^{i_b} relative to the considered node V^i. Assuming also here the same continuity conditions at axial interfaces for the second derivatives of the flux as for the flux itself, the relations

$$\Big(\frac{\partial^2}{\partial x^2}+\frac{\partial^2}{\partial y^2}\Big)\widetilde{\Phi}_n^i(\mathbf{r}) = \Big(\frac{\partial^2}{\partial x^2}+\frac{\partial^2}{\partial y^2}\Big)\widetilde{\Phi}_n^{i_{a/b}}(\mathbf{r}),$$

$$D_n^i\,\mathbf{n}_i\cdot\nabla\Big(\frac{\partial^2}{\partial x^2}+\frac{\partial^2}{\partial y^2}\Big)\widetilde{\Phi}_n^i(\mathbf{r}) = D_n^{i_{a/b}}\,\mathbf{n}_i\cdot\nabla\Big(\frac{\partial^2}{\partial x^2}+\frac{\partial^2}{\partial y^2}\Big)\widetilde{\Phi}_n^{i_{a/b}}(\mathbf{r}), \qquad \mathbf{r}=(x,y,z)\in\partial V^{ii_{a/b}},$$

and consequently, with (3.14) and the assumption $a^i = a^{i_{a/b}}$,

$$\frac{1}{D_n^i}\overline{\widetilde{L}}_{n\,a/b}^{z,i} = \frac{1}{D_n^{i_{a/b}}}\overline{\widetilde{L}}_{n\,b/a}^{z,i_{a/b}}, \tag{4.88}$$

$$\frac{\mathrm{d}}{\mathrm{d}z}\widetilde{L}_n^{z,i}(z)\Big|_{z=\pm\frac{a_z^i}{2}} = \frac{\mathrm{d}}{\mathrm{d}z}\widetilde{L}_n^{z,i_{a/b}}(z)\Big|_{z=\mp\frac{a_z^{i_{a/b}}}{2}} \tag{4.89}$$

are obtained according to (2.55)–(2.56) for $n=0,2$, where

$$\overline{\widetilde{L}}_{n\,a/b}^{z,i} := \widetilde{L}_n^{z,i}(\pm\frac{a_z^i}{2}) \tag{4.90}$$

denotes the mean transverse leakage at the upper (a) and lower (b) nodal interface. With the approximation of the occurring derivative

$$\frac{\mathrm{d}}{\mathrm{d}z}\widetilde{L}_n^{z,i}(z)\Big|_{z=\pm\frac{a_z^i}{2}} \approx \frac{\overline{\widetilde{L}}_{n\,a/b}^{z,i}-\overline{\widetilde{L}}_n^{z,i}}{\pm\frac{a_z^i}{2}}, \tag{4.91}$$

we get

$$\overline{\widetilde{L}}_{n\,a/b}^{z,i}-\overline{\widetilde{L}}_n^{z,i} = -\big(\overline{\widetilde{L}}_{n\,b/a}^{z,i_{a/b}}-\overline{\widetilde{L}}_n^{z,i_{a/b}}\big)$$

from (4.89) and eventually, with (4.88),

$$\overline{\widetilde{L}}_{n\,a/b}^{z,i} = \frac{D_n^i}{D_n^i+D_n^{i_{a/b}}}\big(\overline{\widetilde{L}}_n^{z,i}+\overline{\widetilde{L}}_n^{z,i_{a/b}}\big), \qquad n=0,2. \tag{4.92}$$

In the case that the upper or lower nodal boundary $\partial V^{i_{\mathrm{ext}}}$ is part of the exterior boundary, the relations (4.53)–(4.54) derived from the Marshak-like boundary conditions have to be applied analogously to the lateral case. With the aforementioned assumptions, the outer boundary transverse-leakage conditions

$$\frac{1}{2}(1+\tau_0^i)\Big(\pm\frac{\mathrm{d}}{\mathrm{d}z}\widetilde{L}_0^{z,i}(z)\Big)\Big|_{z=\pm\frac{a_z^i}{2}} = (1-\tau_0^i)\Big(-\frac{1}{4D_0^i}\widetilde{L}_0^{z,i}(\pm\frac{a_z^i}{2})+\frac{3}{16D_2^i}\widetilde{L}_2^{z,i}(\pm\frac{a_z^i}{2})\Big),$$

$$\frac{1}{2}(1+\tau_2^i)\Big(\pm\frac{\mathrm{d}}{\mathrm{d}z}\widetilde{L}_2^{z,i}(z)\Big)\Big|_{z=\pm\frac{a_z^i}{2}} = (1-\tau_2^i)\Big(\frac{3}{80D_0^i}\widetilde{L}_0^{z,i}(\pm\frac{a_z^i}{2})-\frac{21}{80D_2^i}\widetilde{L}_2^{z,i}(\pm\frac{a_z^i}{2})\Big)$$

hold with a stepwise constant albedo function τ_n^i. Hence, using (4.90) and the approximation (4.91), we obtain

$$\frac{1}{a_z^i}(1+\tau_0^i)(\bar{\bar{L}}_{0\,a/b}^{z,i} - \bar{\bar{L}}_0^{z,i}) = (1-\tau_0^i)\Big(-\frac{1}{4D_0^i}\bar{\bar{L}}_{0\,a/b}^{z,i} + \frac{3}{16D_2^i}\bar{\bar{L}}_{2\,a/b}^{z,i}\Big),$$
$$\frac{1}{a_z^i}(1+\tau_2^i)(\bar{\bar{L}}_{2\,a/b}^{z,i} - \bar{\bar{L}}_2^{z,i}) = (1-\tau_2^i)\Big(\frac{3}{80D_0^i}\bar{\bar{L}}_{0\,a/b}^{z,i} - \frac{21}{80D_2^i}\bar{\bar{L}}_{2\,a/b}^{z,i}\Big).$$

Finally, with

$$\alpha_n^{z,i} := \frac{1}{a_z^i}(1+\tau_n^i),$$
$$\beta_{kn}^i := \frac{1}{4D_k^i}(1-\tau_n^i),$$
$$\gamma^{z,i} := \alpha_0^{z,i}\alpha_2^{z,i} + \frac{21}{20}\alpha_0^{z,i}\beta_{22}^i + \alpha_2^{z,i}\beta_{00}^i + \frac{15}{16}\beta_{00}^i\beta_{22}^i,$$

the average transverse leakage of an axial outer node boundary is determined via

$$\bar{\bar{L}}_{0\,a/b}^{z,i} = \frac{1}{\gamma^{z,i}}\Big(\alpha_0^{z,i}(\alpha_2^{z,i} + \frac{21}{20}\beta_{22}^i)\bar{\bar{L}}_0^{z,i} + \frac{3}{4}\alpha_2^{z,i}\beta_{20}^i\bar{\bar{L}}_2^{z,i}\Big), \tag{4.93}$$
$$\bar{\bar{L}}_{2\,a/b}^{z,i} = \frac{1}{\gamma^{z,i}}\Big(\frac{3}{20}\alpha_0^{z,i}\beta_{02}^i\bar{\bar{L}}_0^{z,i} + \alpha_2^{z,i}(\alpha_0^{z,i} + \beta_{00}^i)\bar{\bar{L}}_2^{z,i}\Big). \tag{4.94}$$

The leakage transversal to the axial direction is approximated by the polynomial approach (3.30). Considering

$$\bar{\bar{L}}_n^{z,i} = \frac{1}{a_z^i}\sum_{k=0}^{2} l_{nk}^{z,i}\int_{-\frac{a_z^i}{2}}^{\frac{a_z^i}{2}} h_k^z(z)\mathrm{d}z,$$

the occurring leakage coefficients

$$\mathbf{l}_n^{z,i} = \begin{pmatrix} l_{n0}^{z,i} \\ l_{n1}^{z,i} \\ l_{n2}^{z,i} \end{pmatrix}$$

are obtained from the simple linear system of equations

$$\begin{pmatrix} 1 & 0 & 0 \\ 1 & \sqrt{3} & \sqrt{5} \\ 1 & -\sqrt{3} & \sqrt{5} \end{pmatrix}\mathbf{l}_n^{z,i} = \begin{pmatrix} \bar{\bar{L}}_n^{z,i} \\ \bar{\bar{L}}_{na}^{z,i} \\ \bar{\bar{L}}_{nb}^{z,i} \end{pmatrix},$$

which yields the relations

$$\mathbf{l}_n^{z,i} = \begin{pmatrix} \widetilde{\overline{L}}_n^{z,i} \\ \frac{\sqrt{3}}{6}(\widetilde{\overline{L}}_{na}^{z,i} - \widetilde{\overline{L}}_{nb}^{z,i}) \\ \frac{\sqrt{5}}{10}(\widetilde{\overline{L}}_{na}^{z,i} + \widetilde{\overline{L}}_{nb}^{z,i} - 2\widetilde{\overline{L}}_n^{z,i}) \end{pmatrix}, \qquad n = 0, 2. \tag{4.95}$$

Hence, the coefficients of the transverse leakage of a node V^i with respect to the z direction can be expressed by the terms (4.92) and (4.93)–(4.94) in case of a nodal interface and an exterior boundary, respectively. Finally, with (4.87), the leakage transversal to the axial direction is approximated by the incoming and outgoing radial partial currents of the element itself and its upper and lower adjacent nodes.

Diffusion method: Taking the diffusion theory instead of the SP_3 approach into consideration, the polynomial transverse-leakage coefficients $\mathbf{l}_0^{(z),i}$ can be determined from the same relations (4.86) and (4.95), respectively. The average nodal transverse leakages $\overline{L}_0^{r,i}$ and $\overline{L}_0^{z,i}$ are calculated from the perpendicular partial currents via (4.77) and (4.87), whereas the average transverse leakages at nodal interfaces $\overline{L}_{0l}^{r,i}$, $l = 1, 2, 3$, and $\overline{L}_{0\,a/b}^{z,i}$ are obtained from (4.83) and (4.92). However, the expressions for the average transverse leakages from exterior boundaries simplify to

$$\overline{L}_{0l}^{r,i} = \frac{\alpha_0^i}{\alpha_0^i + \beta_{00}^i} \overline{L}_0^{r,i},$$
$$\overline{L}_{0\,a/b}^{z,i} = \frac{\alpha_0^{z,i}}{\alpha_0^{z,i} + \beta_{00}^i} \overline{L}_0^{z,i}$$

with

$$\alpha_0^i := \frac{\sqrt{3}}{a^i}(1 + \tau_0^i),$$
$$\alpha_0^{z,i} := \frac{1}{a_z^i}(1 + \tau_0^i),$$
$$\beta_{00}^i := \frac{1}{4D_0^i}(1 - \tau_0^i).$$

4.6 Determination of the nodal neutron flux

To compute the nodal power distribution within the reactor core in the end of the neutronic calculation via equation (4.1), the node-averaged fluxes $\overline{\Phi}_0$ have to be known for each node and each energy group. Regarding the SP_3 transport method, this means that the modified

nodal flux moments $\overline{\overline{\Phi}}_n$, $n = 0, 2$, have to be determined as we have

$$\overline{\Phi}_0 = \overline{\overline{\Phi}}_0 - 2\overline{\overline{\Phi}}_2. \tag{4.96}$$

4.6.1 Formal derivation of the node-averaged flux and the polynomial flux coefficients

Consider, therefore, the three-dimensional system of SP_3 equations (3.3)–(3.4), which has to be integrated over the node volume V. Applying the divergence theorem, we get

$$\begin{aligned}
&-D_0 \oiint_{\partial V} \mathbf{n} \cdot \nabla \widetilde{\Phi}_0(\mathbf{r}) \mathrm{d}S + \Sigma_{r0} \iiint_V \widetilde{\Phi}_0(\mathbf{r}) \mathrm{d}V - 2\Sigma_{r0} \iiint_V \widetilde{\Phi}_2(\mathbf{r}) \mathrm{d}V = \iiint_V \widetilde{S}_0(\mathbf{r}) \mathrm{d}V, \\
&-D_2 \oiint_{\partial V} \mathbf{n} \cdot \nabla \widetilde{\Phi}_2(\mathbf{r}) \mathrm{d}S - \frac{2}{5}\Sigma_{r0} \iiint_V \widetilde{\Phi}_0(\mathbf{r}) \mathrm{d}V + \Big(\frac{4}{5}\Sigma_{r0} + \Sigma_{r2}\Big) \iiint_V \widetilde{\Phi}_2(\mathbf{r}) \mathrm{d}V \\
&\quad = -\frac{2}{5} \iiint_V \widetilde{S}_0(\mathbf{r}) \mathrm{d}V.
\end{aligned}$$

With the node-averaged terms $\overline{\overline{\Phi}}_n$ of (4.61) and $\overline{\overline{S}}_0$ of (4.62) as well as by the use of Fick's law (3.1), the relations

$$\begin{aligned}
\frac{1}{V} \oiint_{\partial V} \mathbf{n} \cdot \widetilde{\mathbf{J}}_0(\mathbf{r}) \mathrm{d}S + \Sigma_{r0}\overline{\overline{\Phi}}_0 - 2\Sigma_{r0}\overline{\overline{\Phi}}_2 &= \overline{\overline{S}}_0, \\
\frac{1}{V} \oiint_{\partial V} \mathbf{n} \cdot \widetilde{\mathbf{J}}_2(\mathbf{r}) \mathrm{d}S - \frac{2}{5}\Sigma_{r0}\overline{\overline{\Phi}}_0 + \Big(\frac{4}{5}\Sigma_{r0} + \Sigma_{r2}\Big)\overline{\overline{\Phi}}_2 &= -\frac{2}{5}\overline{\overline{S}}_0
\end{aligned}$$

are obtained. The occurring surface integrals can be expressed in terms of the averaged values of the partial inward and outward currents at the nodal faces (cf. (4.9)–(4.24) with the overbar and tilde omitted). Thus, we have

$$\begin{aligned}
\frac{1}{V} \oiint_{\partial V} \mathbf{n} \cdot \widetilde{\mathbf{J}}_n(\mathbf{r}) \mathrm{d}S &= \frac{4\sqrt{3}}{3a^2 a_z} \Big(a a_z \sum_{l=1}^{3} (J_{nl}^{+} - J_{nl}^{-}) + \frac{\sqrt{3}}{4} a^2 \big((J_{n+}^{z+} - J_{n+}^{z-}) + (J_{n-}^{z+} - J_{n-}^{z-}) \big) \Big) \\
&= \frac{4\sqrt{3}}{3a} \sum_{l=1}^{3} (\mathbf{J}_n^{+} - \mathbf{J}_n^{-})_l + \frac{1}{a_z} \sum_{l=1}^{2} (\mathbf{J}_n^{z+} - \mathbf{J}_n^{z-})_l, \qquad n = 0, 2,
\end{aligned}$$

which yields the integral balance equations

$$\frac{4\sqrt{3}}{3a} \sum_{l=1}^{3} (\mathbf{J}_0^{\mathrm{net}})_l + \frac{1}{a_z} \sum_{l=1}^{2} (\mathbf{J}_0^{z\,\mathrm{net}})_l + \Sigma_{r0}\overline{\overline{\Phi}}_0 - 2\Sigma_{r0}\overline{\overline{\Phi}}_2 = \overline{\overline{S}}_0, \tag{4.97}$$

$$\frac{4\sqrt{3}}{3a} \sum_{l=1}^{3} (\mathbf{J}_2^{\mathrm{net}})_l + \frac{1}{a_z} \sum_{l=1}^{2} (\mathbf{J}_2^{z\,\mathrm{net}})_l - \frac{2}{5}\Sigma_{r0}\overline{\overline{\Phi}}_0 + \Big(\frac{4}{5}\Sigma_{r0} + \Sigma_{r2}\Big)\overline{\overline{\Phi}}_2 = -\frac{2}{5}\overline{\overline{S}}_0. \tag{4.98}$$

Conferring (4.2) and using the algebraic expressions (4.35) and (4.38), the net currents in the above equations (4.97)–(4.98) are given via

$$\mathbf{J}_0^{\text{net}} = \mathbf{J}_0^+ - \mathbf{J}_0^- = \mathbf{V}_{00}\mathbf{c}_0 + \mathbf{V}_{02}\mathbf{c}_2 + (\mathbf{W}_{01} - I)\mathbf{J}_0^- + \mathbf{W}_{02}\mathbf{J}_2^-, \tag{4.99}$$

$$\mathbf{J}_2^{\text{net}} = \mathbf{J}_2^+ - \mathbf{J}_2^- = \mathbf{V}_{20}\mathbf{c}_0 + \mathbf{V}_{22}\mathbf{c}_2 + \mathbf{W}_{21}\mathbf{J}_0^- + (\mathbf{W}_{22} - I)\mathbf{J}_2^- \tag{4.100}$$

and

$$\mathbf{J}_0^{z\,\text{net}} = \mathbf{J}_0^{z+} - \mathbf{J}_0^{z-} = \mathbf{V}_{00}^z\mathbf{c}_0^z + \mathbf{V}_{02}^z\mathbf{c}_2^z + (\mathbf{W}_{01}^z - I)\mathbf{J}_0^{z-} + \mathbf{W}_{02}^z\mathbf{J}_2^{z-}, \tag{4.101}$$

$$\mathbf{J}_2^{z\,\text{net}} = \mathbf{J}_2^{z+} - \mathbf{J}_2^{z-} = \mathbf{V}_{20}^z\mathbf{c}_0^z + \mathbf{V}_{22}^z\mathbf{c}_2^z + \mathbf{W}_{21}^z\mathbf{J}_0^{z-} + (\mathbf{W}_{22}^z - I)\mathbf{J}_2^{z-}, \tag{4.102}$$

where I denotes the corresponding identity matrix. Hence, integrating equations (3.3)–(3.4) over the node volume yields the nodal neutron balance equations

$$\begin{pmatrix} \overline{\widetilde{\Phi}}_0 \\ \overline{\widetilde{\Phi}}_2 \end{pmatrix} = \frac{1}{\Sigma_{r0}\Sigma_{r2}} \begin{pmatrix} \frac{4}{5}\Sigma_{r0} + \Sigma_{r2} & 2\Sigma_{r0} \\ \frac{2}{5}\Sigma_{r0} & \Sigma_{r0} \end{pmatrix} \times \begin{pmatrix} \overline{\widetilde{S}}_0 - \frac{4\sqrt{3}}{3a}\sum_{l=1}^{3}(\mathbf{J}_0^{\text{net}})_l - \frac{1}{a_z}\sum_{l=1}^{2}(\mathbf{J}_0^{z\,\text{net}})_l \\ -\frac{2}{5}\overline{\widetilde{S}}_0 - \frac{4\sqrt{3}}{3a}\sum_{l=1}^{3}(\mathbf{J}_2^{\text{net}})_l - \frac{1}{a_z}\sum_{l=1}^{2}(\mathbf{J}_2^{z\,\text{net}})_l \end{pmatrix}, \tag{4.103}$$

where the node-averaged flux moments $\overline{\widetilde{\Phi}}_n$ can be determined from the flux coefficients $\mathbf{c}_n$ and $\mathbf{c}_n^z$, the incoming currents $\mathbf{J}_n^-$ and $\mathbf{J}_n^{z-}$ as well as from the node-averaged neutron source $\overline{\widetilde{S}}_0$.

SP_3 METHOD – RADIAL TREATMENT: Besides the average neutron flux moments, also the coefficients of the series expansions of the neutron flux have to be determined. Consider therefore the radial plane at first. Applying the expansion approaches of the flux (3.23), (3.24), the source (3.25), and the transverse-leakage terms (3.26) to the inhomogeneous system of SP_3 equations (3.8)–(3.9), multiplying by $h_k^{\mathbb{A}/\mathbb{B}}$ of (3.21) and (3.22), and integrating over the respective trigonal node area, relations between the flux coefficients c_{nk}, the source coefficients s_{0k}, and the transverse-leakage coefficients l_{nk}, $n = 0, 2$, $k = 0, \ldots, 3$, are obtained. Using the property of orthogonality of the polynomials $h_k^{\mathbb{A}/\mathbb{B}}$, we have

$$\begin{aligned} \Sigma_{r0}(c_{0k} - 2c_{2k}) &= s_{0k} - l_{0k} + \delta_{0k}\frac{4D_0}{a^2}\frac{N_3}{N_0}c_{03} \\ &= s_{0k} - l_{0k} + \delta_{0k}\frac{16\sqrt{15}D_0}{a^2}c_{03}, \\ -\frac{2}{5}\Sigma_{r0}c_{0k} + \left(\frac{4}{5}\Sigma_{r0} + \Sigma_{r2}\right)c_{2k} &= -\frac{2}{5}s_{0k} - l_{2k} + \delta_{0k}\frac{4D_2}{a^2}\frac{N_3}{N_0}c_{23} \\ &= -\frac{2}{5}s_{0k} - l_{2k} + \delta_{0k}\frac{16\sqrt{15}D_2}{a^2}c_{23}, \end{aligned}$$

where δ_{0k} denotes the Kronecker delta. Hence, the radial flux coefficients can be determined via

$$\begin{pmatrix} c_{0k} \\ c_{2k} \end{pmatrix} = \frac{1}{\Sigma_{r0}\Sigma_{r2}} \begin{pmatrix} \frac{4}{5}\Sigma_{r0} + \Sigma_{r2} & 2\Sigma_{r0} \\ \frac{2}{5}\Sigma_{r0} & \Sigma_{r0} \end{pmatrix} \begin{pmatrix} s_{0k} - l_{0k} + \delta_{0k}\frac{16\sqrt{15}D_0}{a^2}c_{03} \\ -\frac{2}{5}s_{0k} - l_{2k} + \delta_{0k}\frac{16\sqrt{15}D_0}{a^2}c_{23} \end{pmatrix}, \quad k = 0, ..., 3. \tag{4.104}$$

SP_3 method – axial treatment: Accordingly, we obtain the coefficients

$$\begin{pmatrix} c^z_{0k} \\ c^z_{2k} \end{pmatrix} = \frac{1}{\Sigma_{r0}\Sigma_{r2}} \begin{pmatrix} \frac{4}{5}\Sigma_{r0} + \Sigma_{r2} & 2\Sigma_{r0} \\ \frac{2}{5}\Sigma_{r0} & \Sigma_{r0} \end{pmatrix} \begin{pmatrix} s^z_{0k} - l^z_{0k} + \delta_{0k}\frac{12\sqrt{5}D_0}{a_z^2}c^z_{02} \\ -\frac{2}{5}s^z_{0k} - l^z_{2k} + \delta_{0k}\frac{12\sqrt{5}D_2}{a_z^2}c^z_{22} \end{pmatrix}, \quad k = 0, 1, 2, \tag{4.105}$$

for the axial series expansion of the neutron flux (3.28).

Diffusion method: With regard to diffusion theory, the three-dimensional diffusion equation (3.6) integrated over the node volume V gives an integral balance relation, which can be rearranged to the equation for the node-averaged neutron flux

$$\overline{\Phi}_0 = \frac{1}{\Sigma_{r0}}\left(\overline{S}_0 - \frac{4\sqrt{3}}{3a}\sum_{l=1}^{3}(\mathbf{J}_0^{\text{net}})_l - \frac{1}{a_z}\sum_{l=1}^{2}(\mathbf{J}_0^{z\,\text{net}})_l\right), \tag{4.106}$$

representing the diffusion-theory equivalent to (4.103), with the net currents

$$\mathbf{J}_0^{(z)\,\text{net}} := \mathbf{J}_0^{(z)+} - \mathbf{J}_0^{(z)-} = \mathbf{V}_{00}^{(z)}\mathbf{c}_0^{(z)} + (\mathbf{W}_{01}^{(z)} - I)\mathbf{J}_0^{(z)-}.$$

Note that the identity matrices I have different sizes for the above radial and axial equations. For the flux expansion coefficients, the following relations hold:

$$c_{0k} = \frac{1}{\Sigma_{r0}}\left(s_{0k} - l_{0k} + \delta_{0k}\frac{16\sqrt{15}D_0}{a^2}c_{03}\right), \qquad k = 0, ..., 3, \tag{4.107}$$

$$c^z_{0k} = \frac{1}{\Sigma_{r0}}\left(s^z_{0k} - l^z_{0k} + \delta_{0k}\frac{12\sqrt{5}D_0}{a_z^2}c^z_{02}\right), \qquad k = 0, 1, 2. \tag{4.108}$$

4.6.2 Exponential weighting of the polynomial flux coefficients

From Section 4.4, we infer that the calculation of the average neutron source $\overline{\overline{S}}_{0,g}$ of (4.63) via (4.64)–(4.66) is based on the node-average fluxes $\overline{\overline{\Phi}}_{n,g}$, which means that the exponential functions of the flux expansions (3.23), (3.24), and (3.28) are indirectly considered. However, the determination of the neutron source coefficients $\mathbf{s}_{0,g}$ of (4.67) and $\mathbf{s}^z_{0,g}$ of (4.71) via

(4.68)–(4.70) and (4.72)–(4.74) solely takes the polynomial part, i.e., only the coefficients $\mathbf{c}_{n,g}$ and $\mathbf{c}^z_{n,g}$ of the flux expansion, into account.

SP_3 METHOD – RADIAL TREATMENT: To overcome this limitation, the radial flux coefficients $\mathbf{c}_{n,g}$ are additionally updated involving the exponential impact as follows:

$$\begin{aligned} c^*_{nk} &= \frac{4\sqrt{3}}{3a^2}\int_{-\frac{\sqrt{3}}{3}a}^{\frac{\sqrt{3}}{6}a}\int_{-\frac{\sqrt{3}}{3}x-\frac{1}{3}a}^{\frac{\sqrt{3}}{3}x+\frac{1}{3}a} h^{\mathtt{A}}_k(x,y)\widetilde{\Phi}^{\mathtt{A}\,r}_n(x,y)\mathrm{d}y\,\mathrm{d}x \\ &= \frac{4\sqrt{3}}{3a^2}\int_{-\frac{\sqrt{3}}{6}a}^{\frac{\sqrt{3}}{3}a}\int_{\frac{\sqrt{3}}{3}x-\frac{1}{3}a}^{-\frac{\sqrt{3}}{3}x+\frac{1}{3}a} h^{\mathtt{B}}_k(x,y)\widetilde{\Phi}^{\mathtt{B}\,r}_n(x,y)\mathrm{d}y\,\mathrm{d}x, \qquad k=0,\ldots,3. \end{aligned} \tag{4.109}$$

Hence, applying (4.32)–(4.33), the matrix equation

$$\begin{aligned} \mathbf{c}^*_n &= \mathbf{c}_n + \mathbf{M}^T_{n1}\mathbf{d}_1 + \mathbf{M}^T_{n2}\mathbf{d}_2 \\ &= \mathbf{c}_n - \mathbf{T}_{n0}\mathbf{c}_0 - \mathbf{T}_{n2}\mathbf{c}_2 + \mathbf{U}_{n1}\mathbf{J}^-_0 + \mathbf{U}_{n2}\mathbf{J}^-_2 \end{aligned} \tag{4.110}$$

is obtained with

$$\begin{aligned} \mathbf{U}_{nj} &:= \mathbf{M}^T_{n1}\mathbf{Q}^I_{0j} + \mathbf{M}^T_{n2}\mathbf{Q}^I_{2j}, \\ \mathbf{T}_{nm} &:= \mathbf{U}_{n1}\mathbf{P}^-_{0m} + \mathbf{U}_{n2}\mathbf{P}^-_{2m}, \qquad n,m=0,2, \qquad j=1,2, \end{aligned} \tag{4.111}$$

and

$$\mathbf{M}_{nj} = \begin{pmatrix} m_{nj,0} & 2m_{nj,1} & 0 & m_{nj,3} \\ m_{nj,0} & -m_{nj,1} & -m_{nj,2} & m_{nj,3} \\ m_{nj,0} & -m_{nj,1} & m_{nj,2} & m_{nj,3} \end{pmatrix}, \tag{4.112}$$

where

$$\begin{aligned} m_{nj,0} &= \frac{4\sqrt{3}}{3}N_0\epsilon_{nj}(\omega_{j,1}-\omega_{j,21}) = \frac{4\sqrt{3}}{3}\epsilon_{nj}(\omega_{j,1}-\omega_{j,21}), \\ m_{nj,1} &= \frac{4\sqrt{3}}{3}\frac{\sqrt{3}}{12}N_1\epsilon_{nj}(\omega_{j,1}-\omega_{j,22}+\omega_{j,31}) = \frac{2\sqrt{6}}{3}\epsilon_{nj}(\omega_{j,1}-\omega_{j,22}+\omega_{j,31}), \\ m_{nj,2} &= \frac{4\sqrt{3}}{3}\frac{1}{4}N_2\epsilon_{nj}(\omega_{j,1}-\omega_{j,22}+\omega_{j,31}) = 2\sqrt{2}\epsilon_{nj}(\omega_{j,1}-\omega_{j,22}+\omega_{j,31}), \\ m_{nj,3} &= \frac{4\sqrt{3}}{3}\epsilon_{nj}\Big(\frac{1}{6}N_3(\omega_{j,1}-\omega_{j,23}+\omega_{j,32}-5\omega_{j,4}) - N_4(\omega_{j,1}-\omega_{j,21})\Big) \\ &= \frac{4\sqrt{5}}{3}\epsilon_{nj}\Big(2(\omega_{j,1}-\omega_{j,23}+\omega_{j,32}-5\omega_{j,4}) - (\omega_{j,1}-\omega_{j,21})\Big) \end{aligned} \tag{4.113}$$

holds with the exponential terms

$$\begin{aligned}
\omega_{j,1} &= \frac{1}{aB_j}\exp\left(\frac{\sqrt{3}}{6}aB_j\right),\\
\omega_{j,21} &= \frac{2\sqrt{3}}{3a^2B_j^2}\left(\exp\left(\frac{\sqrt{3}}{6}aB_j\right)-\exp\left(-\frac{\sqrt{3}}{3}aB_j\right)\right),\\
\omega_{j,22} &= \frac{4\sqrt{3}}{3a^2B_j^2}\left(2\exp\left(\frac{\sqrt{3}}{6}aB_j\right)+\exp\left(-\frac{\sqrt{3}}{3}aB_j\right)\right),\\
\omega_{j,23} &= \frac{2\sqrt{3}}{3a^2B_j^2}\left(5\exp\left(\frac{\sqrt{3}}{6}aB_j\right)-2\exp\left(-\frac{\sqrt{3}}{3}aB_j\right)\right),\\
\omega_{j,31} &= \frac{8}{a^3B_j^3}\left(\exp\left(\frac{\sqrt{3}}{6}aB_j\right)-\exp\left(-\frac{\sqrt{3}}{3}aB_j\right)\right),\\
\omega_{j,32} &= \frac{8}{a^3B_j^3}\left(3\exp\left(\frac{\sqrt{3}}{6}aB_j\right)+2\exp\left(-\frac{\sqrt{3}}{3}aB_j\right)\right),\\
\omega_{j,4} &= \frac{16\sqrt{3}}{3a^4B_j^4}\left(\exp\left(\frac{\sqrt{3}}{6}aB_j\right)-\exp\left(-\frac{\sqrt{3}}{3}aB_j\right)\right).
\end{aligned}$$

Note that the structural composition of the matrices $\mathbf{M}_{nj}$ is identical to the matrix compositions of $\mathbf{P}^{\pm}_{nm}$ by reason of the polynomial structure of $h_k^{\mathtt{A/B}}$ (compare (3.21), (3.22)).

SP_3 METHOD – AXIAL TREATMENT: In axial direction, the update of the polynomial flux coefficients $\mathbf{c}^z_{n,g}$ is analogously realized via

$$c^{z*}_{nk} = \frac{1}{a_z}\int_{-\frac{a_z}{2}}^{\frac{a_z}{2}} h^z_k(z)\widetilde{\Phi}^z_n(z)\mathrm{d}z, \qquad k=0,1,2. \tag{4.114}$$

Hence, we have

$$\mathbf{c}^{z*}_n = \mathbf{c}^z_n - \mathbf{T}^z_{n0}\mathbf{c}^z_0 - \mathbf{T}^z_{n2}\mathbf{c}^z_2 + \mathbf{U}^z_{n1}\mathbf{J}^{z-}_0 + \mathbf{U}^z_{n2}\mathbf{J}^{z-}_2 \tag{4.115}$$

with the respective matrices

$$\begin{aligned}
\mathbf{U}^z_{nj} &:= \mathbf{M}^{z\,T}_{n1}\mathbf{Q}^{zl}_{0j} + \mathbf{M}^{z\,T}_{n2}\mathbf{Q}^{zl}_{2j}, \qquad (4.116)\\
\mathbf{T}^z_{nm} &:= \mathbf{U}^z_{n1}\mathbf{P}^{z-}_{0m} + \mathbf{U}^z_{n2}\mathbf{P}^{z-}_{2m}, \qquad n,m=0,2, \qquad j=1,2,
\end{aligned}$$

and

$$\mathbf{M}^z_{nj} = \begin{pmatrix} m^z_{nj,0} & m^z_{nj,1} & m^z_{nj,2} \\ m^z_{nj,0} & -m^z_{nj,1} & m^z_{nj,2} \end{pmatrix}, \tag{4.117}$$

where

$$
\begin{aligned}
m^z_{nj,0} &= \epsilon_{nj}\omega^z_{j,11}, \\
m^z_{nj,1} &= \sqrt{3}\epsilon_{nj}(\omega^z_{j,12} - \omega^z_{j,21}), \\
m^z_{nj,2} &= \sqrt{5}\epsilon_{nj}(\omega^z_{j,11} - \omega^z_{j,22} + \omega^z_{j,3}),
\end{aligned}
\tag{4.118}
$$

and

$$
\begin{aligned}
\omega^z_{j,11} &= \frac{1}{a_z B_j}\left(\exp\left(\frac{1}{2}a_z B_j\right) - \exp\left(-\frac{1}{2}a_z B_j\right)\right), \\
\omega^z_{j,12} &= \frac{1}{a_z B_j}\left(\exp\left(\frac{1}{2}a_z B_j\right) + \exp\left(-\frac{1}{2}a_z B_j\right)\right), \\
\omega^z_{j,21} &= \frac{2}{a_z^2 B_j^2}\left(\exp\left(\frac{1}{2}a_z B_j\right) - \exp\left(-\frac{1}{2}a_z B_j\right)\right), \\
\omega^z_{j,22} &= \frac{6}{a_z^2 B_j^2}\left(\exp\left(\frac{1}{2}a_z B_j\right) + \exp\left(-\frac{1}{2}a_z B_j\right)\right), \\
\omega^z_{j,3} &= \frac{12}{a_z^3 B_j^3}\left(\exp\left(\frac{1}{2}a_z B_j\right) - \exp\left(-\frac{1}{2}a_z B_j\right)\right).
\end{aligned}
$$

Diffusion method: With respect to diffusion theory, the exponentially weighted update of the polynomial flux coefficients reduces to

$$
\mathbf{c}_0^{(z)*} = \mathbf{c}_0^{(z)} - \mathsf{T}_{00}^{(z)}\mathbf{c}_0^{(z)} + \mathsf{U}_{01}^{(z)}\mathbf{J}_0^{(z)-}, \tag{4.119}
$$

where the occurring matrices are defined as

$$
\begin{aligned}
\mathsf{U}_{01}^{(z)} &:= \mathsf{M}_{01}^{(z)\,T}\mathsf{Q}_{0j}^{(z)I}, \\
\mathsf{T}_{00}^{(z)} &:= \mathsf{U}_{01}^{(z)}\mathsf{P}_{00}^{(z)-}
\end{aligned}
$$

with $\mathsf{M}_{01}^{(z)}$ of (4.112), (4.117) and its components $m_{01,k}^{(z)}$ recalling that $\epsilon_{01} = 1$.

4.6.3 Explicit formulation of the node-averaged flux

A closer inspection of the relations (4.61) and (4.109), (4.114) for $k = 0$ reveals the identities

$$
c^*_{n0} \equiv c^{z*}_{n0} \equiv \overline{\overline{\Phi}}_n, \qquad n = 0, 2,
$$

based on the fact that $h_0^{\mathtt{A}/\mathtt{B}}(x, y) = h_0(z) = 1$. From this it follows that the expression (4.103) derived to calculate the average neutron flux moments $\overline{\overline{\Phi}}_0$ and $\overline{\overline{\Phi}}_2$ represents only an implicit formula since the determination of the neutron net currents $\mathbf{J}_0^{\text{net}}$ and $\mathbf{J}_0^{z\,\text{net}}$ requires the zeroth flux coefficients c_{n0} and c^z_{n0} (compare (4.99)–(4.102)). In the following, a respective explicit

computation approach is derived, which significantly improves the convergence behavior of the iterative procedure and reduces the computation time. However, the clear matrix equation structure has to be broken.

SP_3 METHOD – RADIAL TREATMENT: Substituting $\overline{\widetilde{\Phi}}_0 = c^*_{00}$ and $\overline{\widetilde{\Phi}}_2 = c^*_{20}$ in (4.110) gives

$$\begin{aligned}\overline{\widetilde{\Phi}}_0 = c_{00} &+ m_{01,0}\Big(- r_{00,0}c_{00} - r_{00,3}c_{03} - r_{02,0}c_{20} - r_{02,3}c_{23} + \hat{q}_{01}\sum_{l=1}^{3} J^-_{0l} + \hat{q}_{02}\sum_{l=1}^{3} J^-_{2l}\Big) \\ &+ m_{02,0}\Big(- r_{20,0}c_{00} - r_{20,3}c_{03} - r_{22,0}c_{20} - r_{22,3}c_{23} + \hat{q}_{21}\sum_{l=1}^{3} J^-_{0l} + \hat{q}_{22}\sum_{l=1}^{3} J^-_{2l}\Big),\end{aligned} \tag{4.120}$$

$$\begin{aligned}\overline{\widetilde{\Phi}}_2 = c_{20} &+ m_{21,0}\Big(- r_{00,0}c_{00} - r_{00,3}c_{03} - r_{02,0}c_{20} - r_{02,3}c_{23} + \hat{q}_{01}\sum_{l=1}^{3} J^-_{0l} + \hat{q}_{02}\sum_{l=1}^{3} J^-_{2l}\Big) \\ &+ m_{22,0}\Big(- r_{20,0}c_{00} - r_{20,3}c_{03} - r_{22,0}c_{20} - r_{22,3}c_{23} + \hat{q}_{21}\sum_{l=1}^{3} J^-_{0l} + \hat{q}_{22}\sum_{l=1}^{3} J^-_{2l}\Big)\end{aligned} \tag{4.121}$$

with $m_{nj,0}$ of (4.113) and

$$\begin{aligned}\hat{q}_{nj} &:= q^l_{nj,1} + 2q^l_{nj,2}, \\ r_{nm,0} &:= 3(\hat{q}_{n1}p_{0m,0} + \hat{q}_{n2}p_{2m,0}), \\ r_{nm,3} &:= 3(\hat{q}_{n1}p^-_{0m,3} + \hat{q}_{n2}p^-_{2m,3}), \qquad n,m = 0,2, \qquad j = 1,2,\end{aligned}$$

where $p_{nm,0}$, $p^-_{nm,3}$, $q^l_{nj,1}$, and $q^l_{nj,2}$ are entries of the matrices $\mathbf{P}^-_{nm}$ of (4.28) and $\mathbf{Q}^l_{nj}$ of (4.34). Note that only the first and the last components of the respective flux coefficient vectors $\mathbf{c}_n$ appear in the above equations, which can be traced back to the fact that the structure of the matrices $\mathbf{Q}^l_{n'j}\mathbf{P}^-_{nm}$ is identical to the matrix structures of $\mathbf{P}^{\pm}_{nm}$ with vanishing sums of the middle columns (see (4.28)). With the matrix

$$\mathbf{R} = \begin{pmatrix} 1 - m_{01,0}r_{00,0} - m_{02,0}r_{20,0} & -m_{01,0}r_{02,0} - m_{02,0}r_{22,0} \\ -m_{21,0}r_{00,0} - m_{22,0}r_{20,0} & 1 - m_{21,0}r_{02,0} - m_{22,0}r_{22,0} \end{pmatrix}$$

and its determinant

$$\begin{aligned}\det\mathbf{R} = &(1 - m_{01,0}r_{00,0} - m_{02,0}r_{20,0})(1 - m_{21,0}r_{02,0} - m_{22,0}r_{22,0}) \\ &- (m_{01,0}r_{02,0} + m_{02,0}r_{22,0})(m_{21,0}r_{00,0} + m_{22,0}r_{20,0}),\end{aligned}$$

the coefficients c_{00} and c_{20} can be extracted from (4.120)–(4.121) as follows:

$$\begin{pmatrix} c_{00} \\ c_{20} \end{pmatrix} = \frac{1}{\det \mathbf{R}} \mathbf{R}^{-1} \begin{pmatrix} \overline{\widetilde{\Phi}}_0 - m_{01,0} b_0 - m_{02,0} b_2 \\ \overline{\widetilde{\Phi}}_2 - m_{21,0} b_0 - m_{22,0} b_2 \end{pmatrix},$$

where

$$b_0 := -r_{00,3} c_{03} - r_{02,3} c_{23} + \hat{q}_{01} \sum_{l=1}^{3} J_{0l}^{-} + \hat{q}_{02} \sum_{l=1}^{3} J_{2l}^{-},$$
$$b_2 := -r_{20,3} c_{03} - r_{22,3} c_{23} + \hat{q}_{21} \sum_{l=1}^{3} J_{0l}^{-} + \hat{q}_{22} \sum_{l=1}^{3} J_{2l}^{-}.$$

Finally, with δ_{nk} denoting the Kronecker delta, we obtain

$$c_{n0} = \hat{m}_{n00} \overline{\widetilde{\Phi}}_0 + \hat{m}_{n20} \overline{\widetilde{\Phi}}_2 + \sum_{k=0,2} \Big(\hat{m}_{nk3} c_{k3} + \hat{h}_{nk} \sum_{l=1}^{3} J_{kl}^{-} \Big), \qquad n = 0, 2, \tag{4.122}$$

with

$$\hat{m}_{nk0} := \frac{1}{\det \mathbf{R}} \big(\delta_{nk} + (-1)^{\delta_{nk}} (m_{n'1,0} r_{0k',0} + m_{n'2,0} r_{2k',0}) \big),$$

where

$$n, n', k, k' = 0, 2 \qquad \text{with} \qquad \begin{cases} n' = n, \;\; k' = k, & \text{if } \; n = k \\ n' \neq n, \;\; k' \neq k, & \text{otherwise} \end{cases} \tag{4.123}$$

and

$$\hat{m}_{nk3} := \hat{m}_{n00} (m_{01,0} r_{0k,3} + m_{02,0} r_{2k,3}) + \hat{m}_{n20} (m_{21,0} r_{0k,3} + m_{22,0} r_{2k,3}),$$
$$\hat{h}_{nk} := -\hat{m}_{n00} (m_{01,0} \hat{q}_{0k} + m_{02,0} \hat{q}_{2k}) - \hat{m}_{n20} (m_{21,0} \hat{q}_{0k} + m_{22,0} \hat{q}_{2k}).$$

SP_3 METHOD – AXIAL TREATMENT: Analogously, the relation

$$\begin{pmatrix} c_{00}^z \\ c_{20}^z \end{pmatrix} = \frac{1}{\det \mathbf{R}^z} \mathbf{R}^{z\,-1} \begin{pmatrix} \overline{\widetilde{\Phi}}_0 - m_{01,0}^z b_0^z - m_{02,0}^z b_2^z \\ \overline{\widetilde{\Phi}}_2 - m_{21,0}^z b_0^z - m_{22,0}^z b_2^z \end{pmatrix}$$

describing the respective axial case can be derived, which gives the expression

$$c_{n0}^z = \hat{m}_{n00}^z \overline{\widetilde{\Phi}}_0 + \hat{m}_{n20}^z \overline{\widetilde{\Phi}}_2 + \sum_{k=0,2} \Big(\hat{m}_{nk2}^z c_{k2}^z + \hat{h}_{nk}^z (J_{k+}^{z-} + J_{k-}^{z-}) \Big), \qquad n = 0, 2, \tag{4.124}$$

for the axial zeroth flux coefficients. Here, we have

$$\mathbf{R}^z = \begin{pmatrix} 1 - m^z_{01,0} r^z_{00,0} - m^z_{02,0} r^z_{20,0} & -m^z_{01,0} r^z_{02,0} - m^z_{02,0} r^z_{22,0} \\ -m^z_{21,0} r^z_{00,0} - m^z_{22,0} r^z_{20,0} & 1 - m^z_{21,0} r^z_{02,0} - m^z_{22,0} r^z_{22,0} \end{pmatrix},$$

$$\begin{aligned} b^z_0 &:= -r^z_{00,2} c^z_{02} - r^z_{02,2} c^z_{22} + \hat{q}^z_{01}(J^{z-}_{0+} + J^{z-}_{0-}) + \hat{q}^z_{02}(J^{z-}_{2+} + J^{z-}_{2-}), \\ b^z_2 &:= -r^z_{20,2} c^z_{02} - r^z_{22,2} c^z_{22} + \hat{q}^z_{21}(J^{z-}_{0+} + J^{z-}_{0-}) + \hat{q}^z_{22}(J^{z-}_{2+} + J^{z-}_{2-}), \end{aligned}$$

and

$$\begin{aligned} \hat{q}^z_{nj} &:= q^{zl}_{nj,1} + q^{zl}_{nj,2}, \\ r^z_{nm,0} &:= 2(\hat{q}^z_{n1} p^z_{0m,0} + \hat{q}^z_{n2} p^z_{2m,0}), \\ r^z_{nm,2} &:= 2(\hat{q}^z_{n1} p^{z-}_{0m,2} + \hat{q}^z_{n2} p^{z-}_{2m,2}), \qquad n, m = 0, 2, \qquad j = 1, 2, \end{aligned}$$

with $p^z_{nm,0}$ and $p^{z-}_{nm,2}$ of (4.40), $q^{zl}_{nj,1}$ and $q^{zl}_{nj,2}$ of (4.42), and $m^z_{nj,0}$ of (4.118), as well as

$$\hat{m}^z_{nk0} := \frac{1}{\det \mathbf{R}^z} \left(\delta_{nk} + (-1)^{\delta_{nk}} (m^z_{n'1,0} r^z_{0k',0} + m^z_{n'2,0} r^z_{2k',0}) \right)$$

allowing for (4.123), and

$$\begin{aligned} \hat{m}^z_{nk2} &:= \hat{m}^z_{n00}(m^z_{01,0} r^z_{0k,2} + m^z_{02,0} r^z_{2k,2}) + \hat{m}^z_{n20}(m^z_{21,0} r^z_{0k,2} + m^z_{22,0} r^z_{2k,2}), \\ \hat{h}^z_{nk} &:= -\hat{m}^z_{n00}(m^z_{01,0} \hat{q}^z_{0k} + m^z_{02,0} \hat{q}^z_{2k}) - \hat{m}^z_{n20}(m^z_{21,0} \hat{q}^z_{0k} + m^z_{22,0} \hat{q}^z_{2k}). \end{aligned}$$

Radial/axial combination: Considering now all net currents (4.99)–(4.102), with

$$\begin{aligned} g_{nkj} &:= 3 v_{nk,j}, && j = 0, 3, \\ \hat{w}_{nk} &:= (w_{nk,1} + 2 w_{nk,2}) - \delta_{nk}, \\ g^z_{nkj} &:= 2 v^z_{nk,j}, && j = 0, 2, \\ \hat{w}^z_{nk} &:= (w^z_{nk,1} + w^z_{nk,2}) - \delta_{nk}, \end{aligned}$$

the sums of the radial and axial net currents can now be expressed as

$$\sum_{l=1}^{3} (\mathbf{J}^{\mathrm{net}}_n)_l = \sum_{k=0,2} \left(g_{nk0} c_{k0} + g_{nk3} c_{k3} + \hat{w}_{nk} \sum_{l=1}^{3} J^-_{kl} \right), \tag{4.125}$$

$$\sum_{l=1}^{2} (\mathbf{J}^{z\,\mathrm{net}}_n)_l = \sum_{k=0,2} \left(g^z_{nk0} c^z_{k0} + g^z_{nk2} c^z_{k2} + \hat{w}^z_{nk} (J^{z-}_{k+} + J^{z-}_{k-}) \right), \qquad n = 0, 2, \tag{4.126}$$

where $v_{nk,0}$, $v_{nk,3}$, $v^z_{nk,0}$, $v^z_{nk,2}$ and $w_{nk,1}$, $w_{nk,2}$, $w^z_{nk,1}$, $w^z_{nk,2}$ denote entries of the first and last columns of the matrices $\mathbf{V}_{nk}$, $\mathbf{V}^z_{nk}$ and $\mathbf{W}_{nj}$, $\mathbf{W}^z_{nj}$ (compare (4.36), (4.37), (4.43), (4.44)).

Note the partly modified indexing: $j = 1$ corresponds to $k = 0$ and $j = 2$ corresponds to $k = 2$. Like the matrices $\mathbf{Q}^{+}_{nj}$, $\mathbf{Q}^{z+}_{nj}$ and $\mathbf{Q}^{l}_{nj}$, $\mathbf{Q}^{zl}_{nj}$ of (4.29), (4.34), (4.41), (4.42), the matrices $\mathbf{W}_{nj}$ and $\mathbf{W}^{z}_{nj}$ are circulant. Furthermore, the matrices $\mathbf{V}_{nk}$ and $\mathbf{V}^{z}_{nk}$ feature the structure of the respective matrices $\mathbf{P}^{\pm}_{nk}$ and $\mathbf{P}^{z\pm}_{nk}$ of (4.28), (4.40). Hence, the properties of constant column sums of $\mathbf{W}_{nj}$ and $\mathbf{W}^{z}_{nj}$ as well as the properties of vanishing sums of the middle columns of $\mathbf{V}_{nk}$ and $\mathbf{V}^{z}_{nk}$ are used. Now, applying first the relations (4.122) and (4.124) to the above expressions (4.125)–(4.126) and second the latter net current equations to the (4.103), the following system of equations is finally derived to explicitly calculate the average neutron flux moments:

$$\begin{pmatrix} \overline{\widetilde{\Phi}}_0 \\ \overline{\widetilde{\Phi}}_2 \end{pmatrix} = \frac{1}{\alpha_{00}\alpha_{22} - \alpha_{02}\alpha_{20}} \begin{pmatrix} \alpha_{22} & -\alpha_{02} \\ -\alpha_{20} & \alpha_{00} \end{pmatrix} \begin{pmatrix} \kappa_0 \\ \kappa_2 \end{pmatrix} \tag{4.127}$$

with

$$\begin{aligned}
\kappa_0 :=\ & \overline{\widetilde{S}}_0 - \beta_{00}c_{03} - \beta_{02}c_{23} - \beta^z_{00}c^z_{02} - \beta^z_{02}c^z_{22} \\
& - \gamma_{00}\sum_{l=1}^{3} J^-_{0l} - \gamma_{02}\sum_{l=1}^{3} J^-_{2l} - \gamma^z_{00}(J^{z-}_{0+} + J^{z-}_{0-}) - \gamma^z_{02}(J^{z-}_{2+} + J^{z-}_{2-}), \\
\kappa_2 :=\ & -\frac{2}{5}\overline{\widetilde{S}}_0 - \beta_{20}c_{03} - \beta_{22}c_{23} - \beta^z_{20}c^z_{02} - \beta^z_{22}c^z_{22} \\
& - \gamma_{20}\sum_{l=1}^{3} J^-_{0l} - \gamma_{22}\sum_{l=1}^{3} J^-_{2l} - \gamma^z_{20}(J^{z-}_{0+} + J^{z-}_{0-}) - \gamma^z_{22}(J^{z-}_{2+} + J^{z-}_{2-})
\end{aligned}$$

as well as

$$\begin{aligned}
\alpha_{00} &:= \Sigma_{r0} + \frac{4\sqrt{3}}{3a}(g_{000}\hat{m}_{000} + g_{020}\hat{m}_{200}) + \frac{1}{a_z}(g^z_{000}\hat{m}^z_{000} + g^z_{020}\hat{m}^z_{200}), \\
\alpha_{02} &:= -2\Sigma_{r0} + \frac{4\sqrt{3}}{3a}(g_{000}\hat{m}_{020} + g_{020}\hat{m}_{220}) + \frac{1}{a_z}(g^z_{000}\hat{m}^z_{020} + g^z_{020}\hat{m}^z_{220}), \\
\alpha_{20} &:= -\frac{2}{5}\Sigma_{r0} + \frac{4\sqrt{3}}{3a}(g_{200}\hat{m}_{000} + g_{220}\hat{m}_{200}) + \frac{1}{a_z}(g^z_{200}\hat{m}^z_{000} + g^z_{220}\hat{m}^z_{200}), \\
\alpha_{22} &:= \frac{4}{5}\Sigma_{r0} + \Sigma_{r2} + \frac{4\sqrt{3}}{3a}(g_{200}\hat{m}_{020} + g_{220}\hat{m}_{220}) + \frac{1}{a_z}(g^z_{200}\hat{m}^z_{020} + g^z_{220}\hat{m}^z_{220}),
\end{aligned}$$

$$\begin{aligned}
\beta_{nk} &:= \frac{4\sqrt{3}}{3a}(g_{n00}\hat{m}_{0k3} + g_{n20}\hat{m}_{2k3} + g_{nk3}), \\
\beta^z_{nk} &:= \frac{1}{a_z}(g^z_{n00}\hat{m}^z_{0k2} + g^z_{n20}\hat{m}^z_{2k2} + g^z_{nk2}), \qquad n, k = 0, 2,
\end{aligned}$$

and

$$\gamma_{nk} := \frac{4\sqrt{3}}{3a}(g_{n00}\hat{h}_{0k} + g_{n20}\hat{h}_{2k} + \hat{w}_{nk}),$$
$$\gamma^z_{nk} := \frac{1}{a_z}(g^z_{n00}\hat{h}^z_{0k} + g^z_{n20}\hat{h}^z_{2k} + \hat{w}^z_{nk}), \qquad n,k = 0,2.$$

Diffusion method: Turning towards the diffusion theory approach, we substitute $\overline{\Phi}_0 = c^{(z)*}_{00}$ in the equations of (4.119) and obtain

$$\overline{\Phi}_0 = c_{00} + m_{01,0}\Big(- r_{00,0}c_{00} - r_{00,3}c_{03} + \hat{q}_{01}\sum_{l=1}^{3} J^-_{0l}\Big),$$
$$\overline{\Phi}_0 = c^z_{00} + m^z_{01,0}\Big(- r^z_{00,0}c^z_{00} - r^z_{00,2}c^z_{02} + \hat{q}^z_{01}\sum_{l=1}^{3} J^{z-}_{0l}\Big)$$

or, equivalently,

$$c_{00} = \hat{m}_{000}\overline{\Phi}_0 + \hat{m}_{003}c_{03} + \hat{h}_{00}\sum_{l=1}^{3} J^-_{0l}, \tag{4.128}$$
$$c^z_{00} = \hat{m}^z_{000}\overline{\Phi}_0 + \hat{m}^z_{002}c^z_{02} + \hat{h}^z_{00}(J^{z-}_{0+} + J^{z-}_{0-}) \tag{4.129}$$

with

$$\hat{q}_{01} := \check{q}_{01,1} + 2\check{q}_{01,2},$$
$$r_{00,0} := 3\hat{q}_{01}p_{00,0},$$
$$r_{nm,3} := 3\hat{q}_{01}p^-_{00,3},$$

$$\hat{q}^z_{01} := \check{q}^z_{01,1} + \check{q}^z_{01,2},$$
$$r^z_{00,0} := 2\hat{q}^z_{01}p^z_{00,0},$$
$$r^z_{nm,2} := 2\hat{q}^z_{01}p^{-z}_{00,2},$$

and

$$\hat{m}^{(z)}_{000} := \frac{1}{1 - m^{(z)}_{01,0}r^{(z)}_{00,0}},$$
$$\hat{m}_{003} := \hat{m}_{000}m_{01,0}r_{00,3},$$
$$\hat{m}^z_{002} := \hat{m}^z_{000}m^z_{01,0}r^z_{00,2},$$
$$\hat{h}^{(z)}_{00} := -\hat{m}^{(z)}_{000}m^{(z)}_{01,0}\hat{q}^{(z)}_{00},$$

where $p^{(z)}_{00,0}$, $p^{-}_{00,3}$, $p^{z-}_{00,2}$ and $\breve{q}^{(z)}_{01,1}$, $\breve{q}^{(z)}_{01,2}$ are entries of the matrices $\mathbf{P}^{(z)-}_{nm}$ of (4.28), (4.40) and $\mathbf{Q}^{(z)--1}_{0j}$ of (4.46), (4.47), respectively. Finally, equation (4.106) can be rewritten in the explicit form

$$\overline{\Phi}_0 = \frac{1}{\alpha_{00}} \left(\overline{S}_0 - \beta_{00} c_{03} - \beta^z_{00} c^z_{02} - \gamma_{00} \sum_{l=1}^{3} J^-_{0l} - \gamma^z_{00} (J^{z-}_{0+} + J^{z-}_{0-}) \right) \tag{4.130}$$

with

$$\begin{aligned}
\alpha_{00} &:= \Sigma_{r0} + \frac{4\sqrt{3}}{3a} g_{000} \hat{m}_{000} + \frac{1}{a_z} g^z_{000} \hat{m}^z_{000}, \\
\beta_{00} &:= \frac{4\sqrt{3}}{3a} (g_{000} \hat{m}_{003} + g_{003}), \\
\beta^z_{00} &:= \frac{1}{a_z} (g^z_{000} \hat{m}^z_{002} + g^z_{002}), \\
\gamma_{00} &:= \frac{4\sqrt{3}}{3a} (g_{000} \hat{h}_{00} + \hat{w}_{00}), \\
\gamma^z_{00} &:= \frac{1}{a_z} (g^z_{000} \hat{h}^z_{00} + \hat{w}^z_{00}).
\end{aligned}$$

Determining the average nodal neutron flux moments via (4.127) and (4.130), the first flux coefficients c_{n0} and c^z_{n0} can subsequently be calculated by the use of the relations (4.122), (4.124) and (4.128), (4.129). However, they serve only as auxiliary quantities.

4.7 Simplifying implementation assumptions

In the previous sections, the equations to solve the steady-state multi-group SP_3 transport and diffusion problem are derived. The differences between the SP_3 and the diffusion approaches are gradually presented.

In the SP_3 theory described in Section 2.4.3 and the subsequent mathematical processing, the second-moment removal cross sections $\Sigma^i_{r2,g}$ and diffusion coefficients $D^i_{2,g}$ are required in addition to the zeroth-moment quantities $\Sigma^i_{r0,g}$ and $D^i_{0,g}$ (cf. definitions (2.31) and (2.38), (2.50)). As shown in Table 4.1, $\Sigma^i_{r2,g}$ and $D^i_{2,g}$ comprise the higher within-group scattering cross sections $\Sigma^i_{s2,gg}$ and $\Sigma^i_{s3,gg}$. Linear anisotropic scattering is enclosed indirectly in consequence of the applied transport correction, i.e., the scattering cross section $\Sigma^i_{s1,gg}$ is eliminated. For the sake of simplicity, $\Sigma^i_{s2,gg}$ and $\Sigma^i_{s3,gg}$ are not included in the current SP_3 implementation. Hence, identical cross-section data are used in the DYN3D trigonal SP_3 and diffusion models, which benefits the general cross-section set input structure. In Table 4.2, the diffusion coefficients and removal cross sections implemented in DYN3D are summarized.

Zeroth-moment data according to SP_3 and diffusion theory				
$\Sigma^i_{r0,g}$	$=$	$\Sigma^i_{t,g} - \Sigma^i_{s0,gg}$		
$D^i_{0,g}$	$=$	$\frac{1}{3\Sigma^i_{r1,g}} = \frac{1}{3(\Sigma^i_{t,g}-\Sigma^i_{s1,gg})}$		(without transport correction)
$D^i_{0,g}$	$=$	$\frac{1}{3(\Sigma^i_{t,g}-\sum_{g'=1}^{G}\Sigma^i_{s1,g'g})}$	$= \frac{1}{3\Sigma^i_{tr,g}}$	(with transport correction)
Second-moment data for SP_3 theory				
$\Sigma^i_{r2,g}$	$=$	$\Sigma^i_{t,g} - \Sigma^i_{s2,gg}$		
$D^i_{2,g}$	$=$	$\frac{9}{35\Sigma^i_{r3,g}} = \frac{9}{35(\Sigma^i_{t,g}-\Sigma^i_{s3,gg})}$		

TABLE 4.1: Diffusion coefficients and removal cross sections of the within-group SP_3 transport and diffusion theory without and with transport correction.

Zeroth-moment data according to SP_3 and diffusion implementation				
$\Sigma^i_{r0,g}$	$=$	$\Sigma^i_{a,g} + \sum_{\substack{g'=1 \\ g'\neq g}}^{G}\Sigma^i_{s0,g'g}$	$\equiv$	$\Sigma^i_{t,g} - \Sigma^i_{s0,gg}$
$D^i_{0,g}$	$=$	$\frac{1}{3\Sigma^i_{tr,g}}$		
Second-moment data for SP_3 implementation				
$\Sigma^i_{r2,g}$	$=$	$\Sigma^i_{a,g} + \sum_{g'=1}^{G}\Sigma^i_{s0,g'g}$	$\equiv$	$\Sigma^i_{t,g}$
$D^i_{2,g}$	$=$	$\frac{9}{35(\Sigma^i_{a,g}+\sum_{g'=1}^{G}\Sigma^i_{s0,g'g})}$	$\equiv$	$\frac{9}{35\Sigma^i_{t,g}}$

TABLE 4.2: Diffusion coefficients and removal cross sections implemented in the DYN3D code.

In contrast to the diffusion equation (2.52), the SP_3 equations (2.45)–(2.46) contain the second flux moment $\widetilde{\Phi}_2$ in addition to the zeroth flux moment $\widetilde{\Phi}_0$, i.e., the neutron flux is dependent on the polar angle $\theta = \cos^{-1}\mu$ of the direction of neutron motion (see Figure 2.2 and equation (2.8)). In this manner, the trigonal DYN3D SP_3 calculation model can still reproduce anisotropy effects higher than linear even if $\Sigma^i_{sn,gg}$ are neglected for $n \geq 2$, while the diffusion model suffers from the limitation of capturing maximum linear anisotropic flux behavior based on the applied transport-corrected diffusion coefficient.

With the Cartesian DYN3D SP_3 model, significant improvements were obtained compared to the corresponding diffusion calculations [9, 11], notwithstanding the use of the reduced cross-section input set described above. This performance is shown and discussed in Chapter 5 for the trigonal-geometry DYN3D models.

4.8 Algorithmic summary

Sections 4.1–4.6 present a precise derivation of all relevant mathematical interrelations concerning the neutron currents, the neutron sources, the neutron transverse leakages, and the neutron flux moments as well as the respective interface and boundary conditions. In

Quantity	Initial value
k_{eff}^0	1
$\widetilde{\Phi}_{0,1}^{i\,0}$	1000
$\widetilde{\Phi}_{0,g}^{i\,0}$, $g > 1$	$\frac{1}{\Sigma_{r0,g}^i} \sum_{g'<g} \Sigma_{s0,gg'}^i \widetilde{\Phi}_{0,g'}^{i\,0}$
$\widetilde{\Phi}_{2,g}^{i\,0}$	0
$\mathbf{c}_{n,g}^{i\,0}$	0
$\mathbf{c}_{n,g}^{z,i\,0}$	0
$\widetilde{S}_f^{i\,0}$	$\sum_{g'=1}^{G} \nu\Sigma_{f,g'}^i \widetilde{\Phi}_{0,g'}^{i\,0}$
$\mathbf{s}_f^{i\,0}$	0
$\mathbf{s}_f^{z,i\,0}$	0
$\mathbf{J}_{n,g}^{+,i\,0}$	$\frac{1}{4}\widetilde{\Phi}_{n,g}^{i\,0}$
$\mathbf{J}_{n,g}^{z+,i\,0}$	$\frac{1}{4}\widetilde{\Phi}_{n,g}^{i\,0}$
$\mathbf{J}_{n,g}^{-,i\,0}$	from $\mathbf{J}_{n,g}^{+,i\,0}$ via (4.55), (4.56)
$\mathbf{J}_{n,g}^{z-,i\,0}$	from $\mathbf{J}_{n,g}^{z+,i\,0}$ via (4.58), (4.59)

TABLE 4.3: Initial values of the numerical SP_3 ($n = 0, 2$) and diffusion ($n = 0$) procedures.

this section, the sequences of implementation are summarized in a compact algorithmic form describing the inner and outer iteration schemes in detail (recall the overview block diagram of Figure 4.1 as a general guideline).

For all nodal volume elements V^i and all energy groups g, the geometrical dimensions a^i and a_z^i, the diffusion coefficients $D_{n,g}^i$ as well as the cross sections $\Sigma_{rn,g}^i$, $\Sigma_{s0,gg'}^i$, $\nu\Sigma_{f,g}^i$, $\kappa_g^i\Sigma_{f,g}^i$, the fission spectrum χ_g^i, and the albedos $\tau_{n,g}^i$ are given for $n = 0, 2$. In Table 4.3, the initial values of the numerical procedures are listed. For the diffusion method, naturally, only quantities for $n = 0$ are needed.

The inner iteration loop is interrupted after a fixed number of iterations $\max_{in}$ (typically there is no need for more than five). The outer iteration cycle stops as soon as the fission source term $\widetilde{S}_f$ and the multiplication factor k_{eff} meet some predefined tolerance criteria.

Algorithms 4.1 and 4.2 outline the iterative procedures for the DYN3D SP_3 transport method, while Algorithms 4.3 and 4.4 summarize the respective DYN3D diffusion method. In the course of the numerical procedure, every calculation step is performed for all nodes V^i.

Algorithm 4.1 Outer iteration scheme of the nodal neutron flux calculation using the steady-state SP_3 transport method

Require: a^i, a_z^i, $D_{n,g}^i$, $\Sigma_{rn,g}^i$, $\Sigma_{s0,gg'}^i$, $\nu\Sigma_{f,g}^i$, $\kappa_g^i\Sigma_{f,g}^i$, χ_g^i, ϵ_f, ϵ_k, $\forall i = 1,...,I$, $\forall g, g' = 1,...,G$, $n = 0,2$

Initialize $k_{\text{eff}}^{(0)} = k_{\text{eff}}^0$, $\widetilde{\overline{\Phi}}_{n,g}^{i(0)} = \widetilde{\overline{\Phi}}_{n,g}^{i\,0}$, $\mathbf{c}_{n,g}^{i(0)} = \mathbf{c}_{n,g}^{i\,0}$, $\mathbf{c}_{n,g}^{z,i(0)} = \mathbf{c}_{n,g}^{z,i\,0}$, $\widetilde{\overline{S}}_f^{i(0)} = \widetilde{\overline{S}}_f^{i\,0}$, $\mathbf{s}_f^{i(0)} = \mathbf{s}_f^{i\,0}$, $\mathbf{s}_f^{z,i(0)} = \mathbf{s}_f^{z,i\,0}$, $\mathbf{J}_{n,g}^{\pm,i(0)} = \mathbf{J}_{n,g}^{\pm,i\,0}$, $\mathbf{J}_{n,g}^{z\pm,i(0)} = \mathbf{J}_{n,g}^{z\pm,i\,0}$, $\forall i$, $\forall g$, $n = 0,2$.
$it = 1$
repeat
  Determine $l_{nk,g}^{i(it)}$ from $\mathbf{J}_{n,g}^{z\pm,i(it-1)}$ via (4.86), $\forall i$, $\forall g$, $k > 0$, $n = 0,2$.
  Determine $l_{nk,g}^{z,i(it)}$ from $\mathbf{J}_{n,g}^{\pm,i(it-1)}$ via (4.95), $\forall i$, $\forall g$, $k > 0$, $n = 0,2$.
  Determine $\widetilde{\overline{S}}_{su,g}^{i(it)}$ from $\widetilde{\overline{\Phi}}_{n,g'}^{i(it-1)}$ via (4.65), $\forall i$, $\forall g$, $g' > g$.
  Determine $s_{0k\,su,g}^{i(it)}$ from $c_{nk,g'}^{i(it-1)}$ via (4.69), $\forall i$, $\forall g$, $g' > g$, $k > 0$.
  Determine $s_{0k\,su,g}^{z,i(it)}$ from $c_{nk,g'}^{z,i(it-1)}$ via (4.73), $\forall i$, $\forall g$, $g' > g$, $k > 0$.
  for $g = 1$ to G **do**
    Determine $\widetilde{\overline{S}}_{sd,g}^{i(it)}$ from $\widetilde{\overline{\Phi}}_{n,g'}^{i(it-1)}$ via (4.64), $\forall i$, $g' < g$.
    Determine $s_{0k\,sd,g}^{i(it)}$ from $c_{nk,g'}^{i(it-1)}$ via (4.68), $\forall i$, $g' < g$, $k > 0$.
    Determine $s_{0k\,sd,g}^{z,i(it)}$ from $c_{nk,g'}^{z,i(it-1)}$ via (4.72), $\forall i$, $g' < g$, $k > 0$.
    Determine $\widetilde{\overline{S}}_{0,g}^{i(it)}$ from $\widetilde{\overline{S}}_{sd,g}^{i(it)}$, $\widetilde{\overline{S}}_{su,g}^{i(it)}$, $k_{\text{eff}}^{(it-1)}$, $\widetilde{\overline{S}}_f^{i(it-1)}$ via (4.63), $\forall i$.
    Determine $s_{0k,g}^{i(it)}$ from $s_{0k\,sd,g}^{i(it)}$, $s_{0k\,su,g}^{i(it)}$, $k_{\text{eff}}^{(it-1)}$, $s_{0k\,f}^{i(it-1)}$ via (4.67), $\forall i$, $k > 0$.
    Determine $s_{0k,g}^{z,i(it)}$ from $s_{0k\,sd,g}^{z,i(it)}$, $s_{0k\,su,g}^{z,i(it)}$, $k_{\text{eff}}^{(it-1)}$, $s_{0k\,f}^{z,i(it-1)}$ via (4.71), $\forall i$, $k > 0$.
    Determine $c_{nk,g}^{i(it)}$ from $s_{0k,g}^{i(it)}$, $l_{nk,g}^{i(it)}$ via (4.104), $\forall i$, $k > 0$, $n = 0,2$.
    Determine $c_{nk,g}^{z,i(it)}$ from $s_{0k,g}^{z,i(it)}$, $l_{nk,g}^{z,i(it)}$ via (4.105), $\forall i$, $k > 0$, $n = 0,2$.
    Inner iteration (Algorithm 4.2): Compute $\widetilde{\overline{\Phi}}_{n,g}^{i(it)}$, $c_{n0,g}^{i(it)}$, $c_{n0,g}^{z,i(it)}$, $\mathbf{J}_{n,g}^{\pm,i(it)}$, $\mathbf{J}_{n,g}^{z\pm,i(it)}$, $n = 0,2$.
    Update $c_{nk,g}^{i(it)}$ from $\mathbf{c}_{n,g}^{i(it)}$, $\mathbf{J}_{n,g}^{-,i(it)}$ via (4.110), $\forall i$, $k > 0$, $n = 0,2$.
    Update $c_{nk,g}^{z,i(it)}$ from $\mathbf{c}_{n,g}^{z,i(it)}$, $\mathbf{J}_{n,g}^{z-,i(it)}$ via (4.115), $\forall i$, $k > 0$, $n = 0,2$.
  end for
  Determine $\widetilde{\overline{S}}_f^{i(it)}$ from $\widetilde{\overline{\Phi}}_{n,g}^{i(it)}$ via (4.66), $\forall i$.
  Determine $s_{0k\,f}^{i(it)}$ from $c_{nk,g}^{i(it)}$ via (4.70), $\forall i$, $k > 0$.
  Determine $s_{0k\,f}^{z,i(it)}$ from $c_{nk,g}^{z,i(it)}$ via (4.74), $\forall i$, $k > 0$.
  Compute multiplication factor $k_{\text{eff}}^{(it)} = \dfrac{\sum_{i=1}^{I}\left(\widetilde{\overline{S}}_f^{i(it)}\right)^2}{\sum_{i=1}^{I}\widetilde{\overline{S}}_f^{i(it)}\widetilde{\overline{S}}_f^{i(it-1)}}$.
  $it = it + 1$
until $\sqrt{\frac{1}{I}\sum_{i=1}^{I}\left(\frac{\widetilde{\overline{S}}_f^{i(it)} - \widetilde{\overline{S}}_f^{i(it-1)}}{\widetilde{\overline{S}}_f^{i(it-1)}}\right)^2} \leq \epsilon_f$ and $\left|\frac{k_{\text{eff}}^{(it)} - k_{\text{eff}}^{(it-1)}}{k_{\text{eff}}^{(it-1)}}\right| \leq \epsilon_k$
Determine $\overline{\Phi}_{0,g}^i$ from $\widetilde{\overline{\Phi}}_{n,g}^i$ via (4.96), $\forall i$, $\forall g$.
Determine node-averaged thermal power densities P^i from $\overline{\Phi}_{0,g}^i$ via (4.1), $\forall i$.

Algorithm 4.2 Inner iteration scheme of the nodal neutron flux calculation using the steady-state SP_3 transport method

Require: a^i, a_z^i, $D_{n,g}^i$, $\Sigma_{rn,g}^i$, $\tau_{n,g}^i$, $\max_{in}$, $\forall i = 1, ..., I$, $\forall g = 1, ..., G$, $n = 0, 2$

1: Receive $c_{nk,g}^{i(it)}$, $c_{nk,g}^{z,i(it)}$, $\overline{\widetilde{S}}_{0,g}^{i(it)}$, $\mathbf{J}_{n,g}^{-,i(it-1)}$, $\mathbf{J}_{n,g}^{z-,i(it-1)}$, $\forall i$, $k > 0$, $n = 0, 2$, from outer iteration loop (Algorithm 4.1).
2: Initialize $c_{nk,g}^{i(1)} = c_{nk,g}^{i(it)}$, $c_{nk,g}^{z,i(1)} = c_{nk,g}^{z,i(it)}$, $\overline{\widetilde{S}}_{0,g}^{i(1)} = \overline{\widetilde{S}}_{0,g}^{i(it)}$, $\mathbf{J}_{n,g}^{-,i(0)} = \mathbf{J}_{n,g}^{-,i(it-1)}$, $\mathbf{J}_{n,g}^{z-,i(0)} = \mathbf{J}_{n,g}^{z-,i(it-1)}$, $\forall i$, $k > 0$, $n = 0, 2$.
3: $in = 1$
4: **while** $in \leq \max_{in}$ **do**
5: Determine $\overline{\widetilde{\Phi}}_{n,g}^{i(in)}$ from $c_{nk,g}^{i(in)}$, $c_{nk,g}^{z,i(in)}$, $\overline{\widetilde{S}}_{0,g}^{i(in)}$, $\mathbf{J}_{n,g}^{-,i(in-1)}$, $\mathbf{J}_{n,g}^{z-,i(in-1)}$ via (4.127), $\forall i$, $k > 0$, $n = 0, 2$.
6: Determine $c_{n0,g}^{i(in)}$ from $\overline{\widetilde{\Phi}}_{n,g}^{i(in)}$, $c_{nk,g}^{i(in)}$, $\mathbf{J}_{n,g}^{-,i(in-1)}$ via (4.122), $\forall i$, $k > 0$, $n = 0, 2$.
7: Determine $c_{n0,g}^{z,i(in)}$ from $\overline{\widetilde{\Phi}}_{n,g}^{i(in)}$, $c_{nk,g}^{z,i(in)}$, $\mathbf{J}_{n,g}^{z-,i(in-1)}$ via (4.124), $\forall i$, $k > 0$, $n = 0, 2$.
8: Determine $\mathbf{J}_{n,g}^{+,i(in)}$ from $\mathbf{c}_{n,g}^{i(in)}$, $\mathbf{J}_{n,g}^{-,i(in-1)}$ via (4.35), $\forall i$, $n = 0, 2$.
9: Determine $\mathbf{J}_{n,g}^{z+,i(in)}$ from $\mathbf{c}_{n,g}^{z,i(in)}$, $\mathbf{J}_{n,g}^{z-,i(in-1)}$ via (4.38), $\forall i$, $n = 0, 2$.
10: Obtain $\mathbf{J}_{n,g}^{-,i(in)}$ from $\mathbf{J}_{n,g}^{+,i(in)}$ via (4.55), (4.56), $\forall i$, $n = 0, 2$.
11: Obtain $\mathbf{J}_{n,g}^{z-,i(in)}$ from $\mathbf{J}_{n,g}^{z+,i(in)}$ via (4.58), (4.59), $\forall i$, $n = 0, 2$.
12: $in = in + 1$
13: **end while**
14: Return $\overline{\widetilde{\Phi}}_{n,g}^{i(it)} = \overline{\widetilde{\Phi}}_{n,g}^{i(in)}$, $c_{n0,g}^{i(it)} = c_{n0,g}^{i(in)}$, $c_{n0,g}^{z,i(it)} = c_{n0,g}^{z,i(in)}$, $\mathbf{J}_{n,g}^{\pm,i(it)} = \mathbf{J}_{n,g}^{\pm,i(in)}$, $\mathbf{J}_{n,g}^{z\pm,i(it)} = \mathbf{J}_{n,g}^{z\pm,i(in)}$, $\forall i$, $n = 0, 2$, to outer iteration loop.

Algorithm 4.3 Outer iteration scheme of the nodal neutron flux calculation using the steady-state diffusion theory method

Require: a^i, a_z^i, $D_{0,g}^i$, $\Sigma_{r0,g}^i$, $\Sigma_{s0,gg'}^i$, $\nu\Sigma_{f,g}^i$, $\kappa_g^i\Sigma_{f,g}^i$, χ_g^i, ϵ_f, ϵ_k, $\forall i = 1,...,I$, $\forall g, g' = 1,...,G$

1: Initialize $k_{\text{eff}}^{(0)} = k_{\text{eff}}^0$, $\overline{\widetilde{\Phi}}_{0,g}^{i(0)} = \overline{\widetilde{\Phi}}_{0,g}^{i\,0}$, $\mathbf{c}_{0,g}^{(z),i(0)} = \mathbf{c}_{0,g}^{(z),i\,0}$, $\overline{S}_f^{i(0)} = \overline{S}_f^{i\,0}$, $\mathbf{s}_f^{(z),i(0)} = \mathbf{s}_f^{(z),i\,0}$, $\mathbf{J}_{0,g}^{(z)\pm,i(0)} = \mathbf{J}_{0,g}^{(z)\pm,i\,0}$, $\forall i$, $\forall g$.
2: $it = 1$
3: **repeat**
4: Determine $l_{0k,g}^{(z),i(it)}$ from $\mathbf{J}_{0,g}^{(z)\pm,i(it-1)}$ via (4.86), (4.95), $\forall i$, $\forall g$, $k > 0$.
5: Determine $\overline{S}_{su,g}^{i(it)}$ from $\overline{\Phi}_{0,g'}^{i(it-1)}$ via (4.75), $\forall i$, $\forall g$, $g' > g$.
6: Determine $s_{0k\,su,g}^{(z),i(it)}$ from $c_{0k,g'}^{(z),i(it-1)}$ via (4.76), $\forall i$, $\forall g$, $g' > g$, $k > 0$.
7: **for** $g = 1$ to G **do**
8: Determine $\overline{S}_{sd,g}^{i(it)}$ from $\overline{\Phi}_{0,g'}^{i(it-1)}$ via (4.75), $\forall i$, $g' < g$.
9: Determine $s_{0k\,sd,g}^{(z),i(it)}$ from $c_{0k,g'}^{(z),i(it-1)}$ via (4.76), $\forall i$, $g' < g$, $k > 0$.
10: Determine $\overline{S}_{0,g}^{i(it)}$ from $\overline{S}_{sd,g}^{i(it)}$, $\overline{S}_{su,g}^{i(it)}$, $k_{\text{eff}}^{(it-1)}$, $\overline{S}_f^{i(it-1)}$ via (4.75), $\forall i$.
11: Determine $s_{0k,g}^{(z),i(it)}$ from $s_{0k\,sd,g}^{(z),i(it)}$, $s_{0k\,su,g}^{(z),i(it)}$, $k_{\text{eff}}^{(it-1)}$, $s_{0k\,f}^{(z),i(it-1)}$ via (4.76), $\forall i$, $k > 0$.
12: Determine $c_{0k,g}^{(z),i(it)}$ from $s_{0k,g}^{(z),i(it)}$, $l_{0k,g}^{(z),i(it)}$ via (4.107), (4.108), $\forall i$, $k > 0$.
13: Inner iteration (Algorithm 4.4): Compute $\overline{\Phi}_{0,g}^{i(it)}$, $c_{00,g}^{(z),i(it)}$, $\mathbf{J}_{0,g}^{(z)\pm,i(it)}$.
14: Update $c_{0k,g}^{(z),i(it)}$ from $\mathbf{c}_{0,g}^{(z),i(it)}$, $\mathbf{J}_{0,g}^{(z)-,i(it)}$ via (4.119), $\forall i$, $k > 0$.
15: **end for**
16: Determine $\overline{S}_f^{i(it)}$ from $\overline{\Phi}_{0,g}^{i(it)}$ via (4.75), $\forall i$.
17: Determine $s_{0k\,f}^{(z),i(it)}$ from $c_{0k,g}^{(z),i(it)}$ via (4.76), $\forall i$, $k > 0$.
18: Compute multiplication factor $k_{\text{eff}}^{(it)} = \dfrac{\sum_{i=1}^{I}\left(\overline{\widetilde{S}}_f^{i(it)}\right)^2}{\sum_{i=1}^{I}\overline{\widetilde{S}}_f^{i(it)}\overline{\widetilde{S}}_f^{i(it-1)}}$.
19: $it = it + 1$
20: **until** $\sqrt{\frac{1}{I}\sum_{i=1}^{I}\left(\frac{\overline{\widetilde{S}}_f^{i(it)} - \overline{\widetilde{S}}_f^{i(it-1)}}{\overline{\widetilde{S}}_f^{i(it-1)}}\right)^2} \leq \epsilon_f$ and $\left|\frac{k_{\text{eff}}^{(it)} - k_{\text{eff}}^{(it-1)}}{k_{\text{eff}}^{(it-1)}}\right| \leq \epsilon_k$
21: Determine node-averaged thermal power densities P^i from $\overline{\Phi}_{0,g}^i$ via (4.1), $\forall i$.

Algorithm 4.4 Inner iteration scheme of the nodal neutron flux calculation using the steady-state diffusion theory method

Require: a^i, a^i_z, $D^i_{0,g}$, $\Sigma^i_{r0,g}$, $\tau^i_{0,g}$, $\max_{in}$, $\forall i = 1, ..., I$, $\forall g = 1, ..., G$

1: Receive $c^{(z),i(it)}_{0k,g}$, $\overline{S}^{i(it)}_{0,g}$, $\mathbf{J}^{(z)-,i(it-1)}_{0,g}$, $\forall i$, $k > 0$, from outer iteration loop (Algorithm 4.3).
2: Initialize $c^{(z),i(1)}_{0k,g} = c^{(z),i(it)}_{0k,g}$, $\overline{S}^{i(1)}_{0,g} = \overline{S}^{i(it)}_{0,g}$, $\mathbf{J}^{(z)-,i(0)}_{0,g} = \mathbf{J}^{(z)-,i(it-1)}_{0,g}$, $\forall i$, $k > 0$.
3: $in = 1$
4: **while** $in \leq \max_{in}$ **do**
5: Determine $\overline{\Phi}^{i(in)}_{0,g}$ from $c^{(z),i(in)}_{0k,g}$, $\overline{S}^{i(in)}_{0,g}$, $\mathbf{J}^{(z)-,i(in-1)}_{0,g}$ via (4.130), $\forall i$, $k > 0$.
6: Determine $c^{(z),i(in)}_{00,g}$ from $\overline{\Phi}^{i(in)}_{0,g}$, $c^{(z),i(in)}_{0k,g}$, $\mathbf{J}^{(z)-,i(in-1)}_{0,g}$ via (4.128), (4.129), $\forall i$, $k > 0$.
7: Determine $\mathbf{J}^{(z)+,i(in)}_{0,g}$ from $\mathbf{c}^{(z),i(in)}_{0,g}$, $\mathbf{J}^{(z)-,i(in-1)}_{0,g}$ via (4.45), $\forall i$.
8: Obtain $\mathbf{J}^{(z)-,i(in)}_{0,g}$ from $\mathbf{J}^{(z)+,i(in)}_{0,g}$ via (4.58), (4.59), $\forall i$.
9: $in = in + 1$
10: **end while**
11: Return $\overline{\Phi}^{i(it)}_{0,g} = \overline{\Phi}^{i(in)}_{0,g}$, $c^{(z),i(it)}_{00,g} = c^{(z),i(in)}_{00,g}$, $\mathbf{J}^{(z)\pm,i(it)}_{0,g} = \mathbf{J}^{(z)\pm,i(in)}_{0,g}$, $\forall i$, to outer iteration loop.

5 Verification Analysis

This chapter focuses on the analysis of the performance of the trigonal SP_3 and diffusion models with particular regard to mesh refinement analyses. Diverse two-dimensional hexagonal test and benchmark problems with different material compositions are studied.

Section 5.1 gives an introductory overview of potential sources of errors in reactor calculations. In Section 5.2, the DYN3D diffusion method on trigonal geometry is verified using a fine-mesh diffusion reference solution. The respective verification of the trigonal DYN3D SP_3 method is presented by means of a fine-mesh SP_3 transport problem. Furthermore, the performances of both trigonal DYN3D models are compared against a higher transport solution using the latter benchmark problem to demonstrate the potential superiority of the DYN3D SP_3 method over the diffusion model. All test problems of this section are defined for the use of assembly-homogenized cross sections. The trigonal DYN3D SP_3 and diffusion methods are further verified against detailed-geometry full-transport references in Section 5.3. Three full-core and single-assembly test problems are considered involving, in each example, cases with weak and strong anisotropy effects. The few-group cross-section data sets are homogenized from assembly down to pin-size level. Section 5.4 evaluates the computation times with respect to solution approaches and nodal refinement levels.

The following facts will become evident by the end of this chapter:

- The verification analysis of both trigonal DYN3D models based on mathematical benchmarks provides proof of their methodological reliability.
- The superiority of the SP_3 transport over the diffusion model can be clearly demonstrated by means of an academic benchmark especially prepared to magnify transport effects.
- Considering physical test problems with detailed-geometry full-transport reference solutions, the superposition of errors complicates the analysis of the accuracy of

the methods. However, the trigonal SP_3 model achieves significantly better agreement with the reference solutions than the trigonal diffusion approach in cases with pronounced anisotropy effects.

5.1 Evaluation of error sources

Recalling the main steps of reactor calculations outlined in Section 1.1, the corresponding intrinsic simplifications and approximations naturally entail specific deficiencies. This in turn necessitates an examination of the contribution of each assumption to the total error. Of course, errors in measurement and nuclear-data evaluation of the microscopic cross sections compiled in data bases such as ENDF (cf. Figure 1.1) exist and, in case of deterministic lattice calculations, uncertainties resulting from the complicated resonance (self-shielding) treatment are present. These errors will affect the accuracy in modeling the behavior of a real reactor. However, all of these errors evidently must be present also in the benchmark reference solutions to be considered in this chapter, so that they are irrelevant for the subsequent analyses. Thus, only the following categories of error sources [43, 93, 120, 145] subsequent to the lattice calculation have to be discussed:

- the spatial-homogenization effect that results from the averaging, i.e., the flux-volume weighting of the macroscopic cross sections applying the fluxes calculated by the lattice code, and
- an error resulting from averaging macroscopic cross sections over energy intervals (groups), which produces few-group homogenized data from continuous-energy or multi-group cross sections ("group-collapsing").

For both items, it should be noted that the lattice calculations are usually carried out in an infinite lattice environment (zero-current boundary conditions) producing a certain space-dependent neutron spectrum. However, the few-group homogenized cross sections generated in this spectrum are later used with ambient core conditions, i.e., a different actual core spectrum. This can also lead to a relevant error contribution.

While the aforementioned types of error sources are merely cross-section related, the following items directly concern the methods developed in the present work:

- the transport effect emerging from the quality and reactor-specific validity of the diffusion or higher-order approximation to the transport equation, i.e., the ability to represent anisotropy effects, and

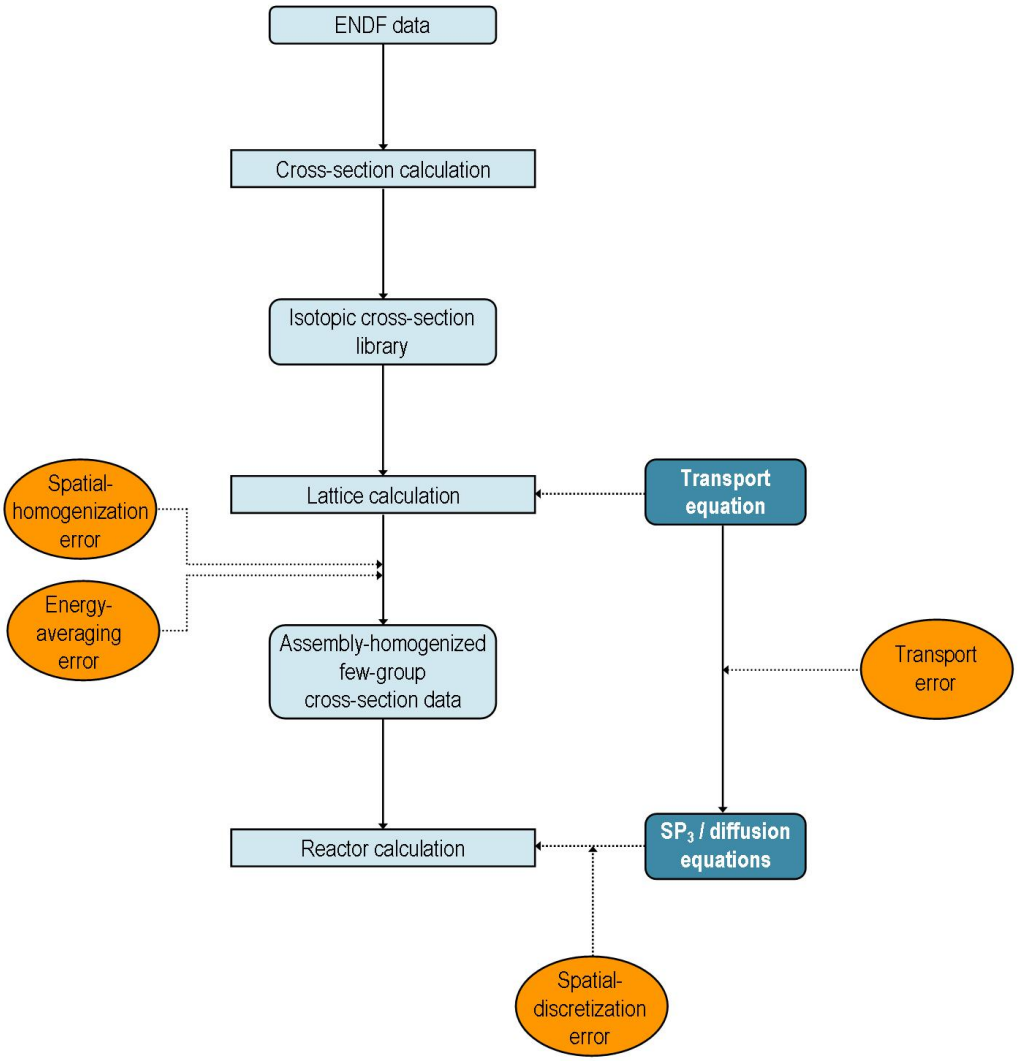

FIGURE 5.1: Error sources in the data flow of reactor physics calculations.

- the spatial-discretization effect in consequence of the employed nodal method, i.e., the methodological sophistication of the intra-nodal flux approximation, and the applied spatial mesh.

In Figure 5.1, an illustration of the errors in the reactor calculation data flow is provided.

As the phenomena described above can hardly be isolated in a reactor calculation, they all interfere with each other and complicate the analysis of the accuracy of the methods themselves.

Material	1	2	3	4	5
$D_{0,1}$	1.383200	1.382990	1.395220	1.394460	1.395060
$D_{0,2}$	0.386277	0.389403	0.386225	0.387723	0.384492
$\Sigma_{a,1} + \Sigma_{s0,21}$	2.48836e-2	2.62865e-2	2.45662e-2	2.60117e-2	2.46141e-2
$\Sigma_{a,2}$	6.73049e-2	8.10328e-2	8.44801e-2	9.89671e-2	8.93878e-2
$\Sigma_{s0,21}$	1.64977e-2	1.47315e-2	1.56219e-2	1.40185e-2	1.54981e-2
$\Sigma_{f,1}$	1.86139e-3	1.81560e-3	2.36371e-3	2.31026e-3	2.50773e-3
$\Sigma_{f,2}$	3.48111e-2	3.50622e-2	4.91322e-2	4.95721e-2	5.31856e-2
$\nu\Sigma_{f,1}$	4.81619e-3	4.66953e-3	6.04889e-3	5.91507e-3	6.40256e-3
$\nu\Sigma_{f,2}$	8.46154e-2	8.52264e-2	1.19428e-1	1.20497e-1	1.29281e-1

TABLE 5.1: Cross-section data for the VVER-1000 two-group benchmark [22].

5.2 VERIFICATION AGAINST MATHEMATICAL BENCHMARKS

The reliability of the trigonal DYN3D models is demonstrated by means of academical benchmarks in this section, applying reference solutions produced by other codes which use exactly the same assembly-homogenized cross sections as input to DYN3D.

Since identical cross-section data and exterior boundary conditions are used for both the DYN3D and the respective fine-mesh reference calculations, the occurrence of errors owing to spatial-homogenization and energy-averaging effects is eliminated. The mesh refinement studies of Sections 5.2.1 and 5.2.2 additionally exclude transport effects and, therefore, specifically identify spatial-discretization errors. In the limit of infinitely fine mesh spacing, the spatial-discretization error approaches zero.

5.2.1 FINE-MESH DIFFUSION BENCHMARK FOR VVER-1000

A VVER-1000-type core benchmark, provided in the work of Chao and Shatilla [22], is considered to verify the consistency of the implementation of the trigonal diffusion method DYN3D-TRIDIF. The core is loaded with 163 fuel assemblies having a typical VVER-1000 assembly pitch[1] of 23.6 cm. 25 assemblies have control-rod (CR) clusters inserted. In Table 5.1, the two-group assembly-homogenized cross-section data are given for the five fuel types, which were generated by Knight and Chao [21, 84, 85] using fuel configuration and material data based on an existing PWR benchmark specified by Koebke et al. [90]. The reflector region outside the fuel assemblies is not explicitly modeled. It can be represented by albedos at the core boundary. Chao and Shatilla provided solutions for the VVER-1000 benchmark applying two different albedos for the problems corresponding to vacuum ($\tau_0 = 0$) and more realistic ($\tau_0 = 0.6$) boundary conditions (cf. expression (4.57)). In this

[1] The distance between the centers of two adjacent fuel assemblies is called assembly pitch.

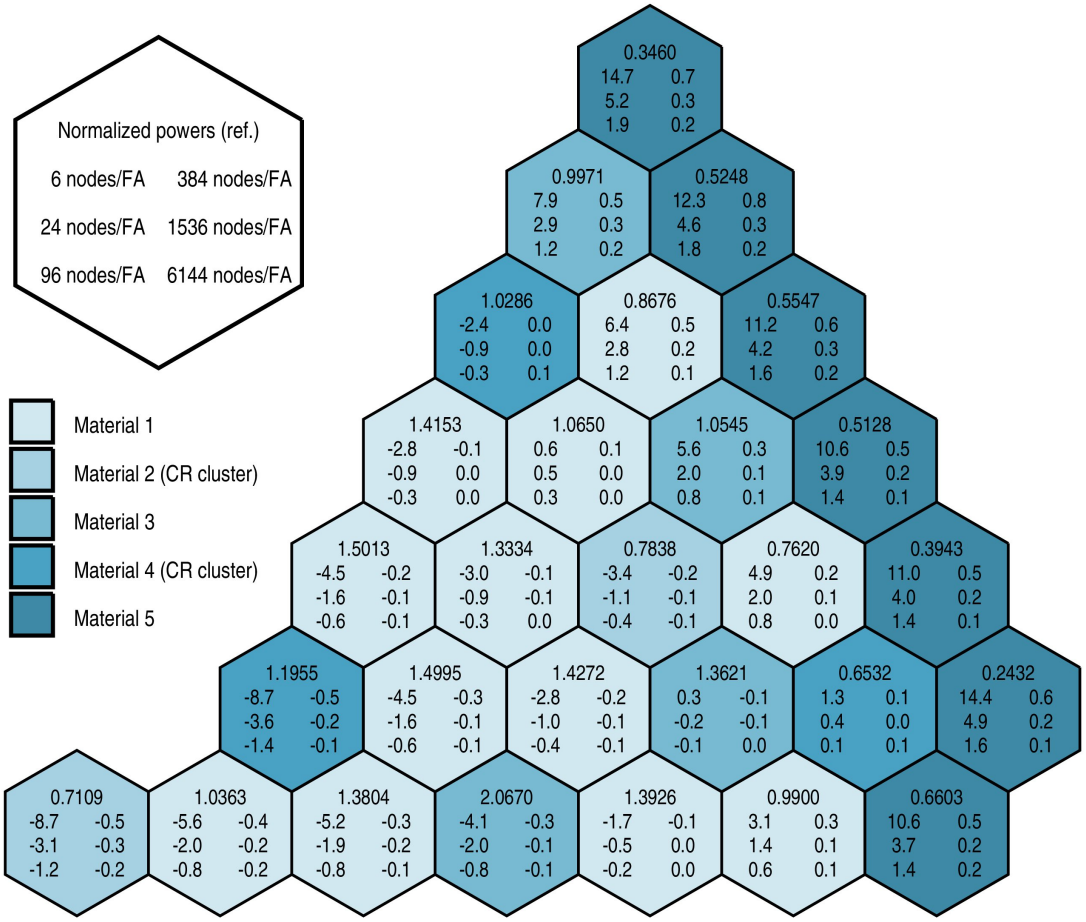

FIGURE 5.2: Core configuration of the VVER-1000 benchmark. Normalized power distribution obtained by DIF3D and relative errors (%) determined by DYN3D-TRIDIF for different mesh refinements.

work, the vacuum boundary case is exemplified to demonstrate the performance of DYN3D-TRIDIF by means of the more extreme example with higher flux gradients. The fine-mesh diffusion reference solution was generated by the finite-difference code DIF3D [40] applying the given coarse-mesh cross sections. Both power distribution and multiplication factor were extrapolated from DIF3D runs with the subdivisions of 384 and 486 triangles per hexagon.

A mesh refinement study is performed with DYN3D-TRIDIF. In Figure 5.2, the normalized power distribution of a 60° sector of the VVER-1000 core and the respective relative errors considering nodal refinements from 6 to 6144 triangles per fuel assembly (FA) are depicted. The corresponding effective multiplication factors obtained by DYN3D-TRIDIF and the respective deviations from the DIF3D reference multiplication factor[2], denoted by $\delta_{k_{\text{eff}}}$, as well as the maximum and root mean square (RMS)[3] power differences in comparison to the

[2]The difference in k_{eff} is calculated via $\delta_{k_{\text{eff}}} = \frac{k_{\text{eff}} - k_{\text{eff,ref}}}{k^2_{\text{eff,ref}}} \times 1\text{e}5\,\text{pcm}$.

[3]The RMS value of a set of I power differences $\{P_1 - P_{1,\text{ref}}, ..., P_I - P_{I,\text{ref}}\}$ is given by $\sqrt{\frac{1}{I}\sum_{i=1}^{I}(P_i - P_{i,\text{ref}})^2}$. This analogously applies to fluxes.

Method	No. of trigonal nodes per FA	k_{eff}	$\delta_{k_{\text{eff}}}$ (pcm)	Max. diff. (%)	RMS diff. (%)
DYN3D-TRIDIF	6	1.008968	245	14.7	7.4
	24	1.007461	96	5.2	2.7
	96	1.006887	40	1.9	1.0
	384	1.006650	16	0.8	0.4
	1536	1.006544	6	0.3	0.2
	6144	1.006493	1	0.2	0.1
DYN3D-HEXNEM1		1.007074	58	5.8	2.9
DYN3D-HEXNEM2		1.006540	5	1.3	0.6
DIF3D (ref.)		1.006485			

TABLE 5.2: VVER-1000 benchmark: Effective multiplication factors k_{eff}, maximum and RMS power differences – DYN3D-TRIDIF and DYN3D-HEXNEM1/2 in comparison to the DIF3D reference.

reference values are displayed in Table 5.2. High relative errors in the power distribution of more than 10 % in the subdivision case of 6 nodes per assembly can be observed in the outermost core region (material 5). On account of the vacuum boundary conditions and the fact that material 5 features the highest fission cross sections, the neutron flux suffers a strong gradient at the core boundary. The largest deviation occurs in the corner assemblies of the core, since three assembly sides face the vacuum boundary. Furthermore, it can be seen that the central zone, with 7 out of 19 fuel assemblies of the innermost three assembly rings of the core having control-rod clusters inserted, shows rather high power deviations in a coarse nodalization due to the accumulation of local flux minima resulting from the control absorbers. While the power distribution is overestimated by DYN3D-TRIDIF in the outer core assemblies, there is an underestimation in the core center. Such a convex deviation behavior is simply a compensation effect resulting from normalization and was also observed by other authors [28, 37, 63]. (A concave deviation shape is also possible. Curvature and magnitude of the effect depend on the particular core configuration.) With 6 trigonal nodes per assembly, DYN3D-TRIDIF only reasonably reproduces strong local flux gradients in this extreme example. Applying further mesh refinement, however, significantly reduces the spatial-discretization error. The mean power difference decreases by a factor of two to three with every higher level of refinement. Using a fine nodalization, very good agreement between DYN3D-TRIDIF and the reference solution is achieved. Both the eigenvalue and the power distribution spatially converge to the reference values.

Hence, the functional reliability of the trigonal DYN3D diffusion model is proven.

In Table 5.2, also the results obtained by the DYN3D hexagonal diffusion methods HEXNEM1 and HEXNEM2 are summarized. The discrepancies in k_{eff} and the nodal power

Material	1	2	3
$\Sigma_{t,1}$	0.025	0.025	0.075
$\Sigma_{s0,11}$	0.013	0.024	0.0
$\Sigma_{s1,11}$	0.0	0.006	0.0
$\nu\Sigma_{f,1}$	0.0155	0.0	0.0

TABLE 5.3: Cross-section data for the one-group benchmark by Hébert [73].

distributions between the models DYN3D-TRIDIF, DYN3D-HEXNEM1, and DYN3D-HEXNEM2 can be traced back to the fact that the hexagonal DYN3D flux expansion ansatzes differ from the trigonal approach in both the polynomial and exponential part (see Section 3.6.2). Due to only an incomplete set of polynomials and only three exponential terms, the trigonal method is weaker than its hexagonal analogon. HEXNEM2 features the most sophisticated approach. However, in the present case, DYN3D-TRIDIF outperforms the accuracy of HEXNEM1 already with a refinement of 24 nodes, HEXNEM2 with a refinement of 384 nodes. More detailed information concerning the behavior of DYN3D-HEXNEM2 relating to this VVER-1000 benchmark problem is provided in the work by Grundmann and Hollstein [63].

The author would like give the supplementary information that, applying realistic boundary conditions ($\tau_0 = 0.6$), the DYN3D-TRIDIF results agree significantly better with the reference solution already in case of coarse nodalization. The maximum power differences are by about a factor of two smaller than the values presented in this extreme example.

5.2.2 Fine-mesh SP_3 academic benchmark

For the verification of the trigonal SP_3 method DYN3D-TRISP3, a one-group benchmark with anisotropic scattering is considered, which was originally proposed by Hébert for various one-dimensional-geometry cases and two-dimensional Cartesian geometry [70] and further developed for hexagonal-geometry problems [73]. This benchmark does not represent a real-life problem. The 30° core sector consists of one type of hexagonal fuel assemblies and two types of reflector assemblies with an assembly pitch of 32.9 cm. The one-group coarse-mesh cross-section data are given in Table 5.3. Whereas material 2 allows solely scattering, material 3 features pure absorption. Thus, the neutron flux is dominated by a strong migration process in direction towards the absorber. In such a case, the importance of a method capable of representing anisotropic flux behavior becomes obvious. Using these cross sections and vacuum outer boundary conditions, the SP_3 transport reference solution has been obtained by the code TRIVAC [75] applying finite-element discretization and quadratic flux expansion. The TRIVAC results converged well already

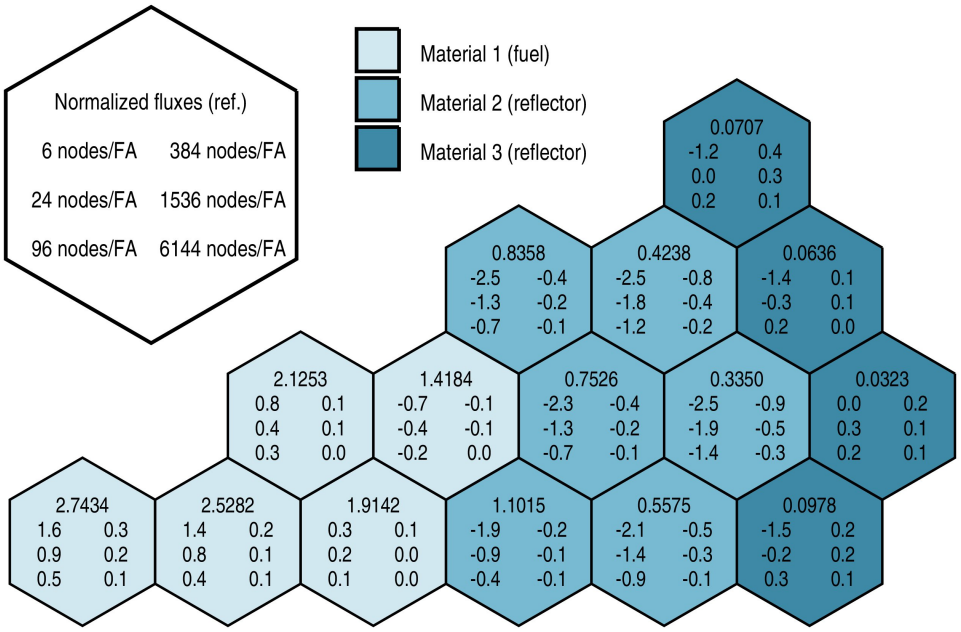

FIGURE 5.3: Core configuration of the Hébert benchmark. Normalized neutron flux distribution obtained by TRIVAC (SP_3 option) and relative errors (%) determined by DYN3D-TRISP3 for different mesh refinements.

Method	No. of trigonal nodes per FA	k_{eff}	$\delta_{k_{\text{eff}}}$ (pcm)	Max. diff. (%)	RMS diff. (%)
DYN3D-TRISP3	6	1.001100	77	2.5	1.7
	24	1.000085	-25	1.9	1.0
	96	0.999939	-39	1.4	0.7
	384	1.000039	-29	0.9	0.4
	1536	1.000156	-18	0.5	0.2
	6144	1.000238	-10	0.3	0.1
TRIVAC - SP_3 (ref.)		1.000330			

TABLE 5.4: Hébert benchmark: Effective multiplication factors k_{eff}, maximum and RMS flux differences – DYN3D-TRISP3 in comparison to the TRIVAC (SP_3) reference.

with a small number of lozenges per hexagon. The reference solution used here has been generated with 300 lozenges per assembly [124].

Similar to the study by Chiba [28], DYN3D-TRISP3 calculations have been run to evaluate and compare the neutron fluxes and effective multiplication factors. In Figure 5.3, the normalized flux distribution of the considered core sector and the respective relative errors are depicted. Also here, a mesh refinement study is performed. In Table 5.4, the effective multiplication factors obtained from the DYN3D-TRISP3 calculations with nodal refinements from 6 to 6144 triangles per fuel assembly are given and compared to the TRIVAC reference value. Furthermore, the maximum and RMS flux differences are evaluated. There

is an overestimation of the nodal flux distribution in the core center and a respective underestimation in the reflector regions due to compensation effects of the applied normalization. However, a general good agreement between DYN3D-TRISP3 and the reference solution is achieved.

By demonstrating spatial convergence of both the DYN3D-TRISP3 multiplication factors and the flux distributions to the fine-mesh TRIVAC SP_3 reference solution in this section, the methodological reliability of the trigonal DYN3D SP_3 model can be conceived as verified.

5.2.3 Fine-mesh SP_5 academic benchmark

In this section, the latter academic benchmark problem is used to compare the trigonal DYN3D SP_3 transport and diffusion models with a higher transport reference solution obtained by the TRIVAC code now using the SP_5 option (plus again a finite-element discretization of 300 lozenges per hexagon and quadratic flux expansion) [124]. Hébert [73] especially prepared the cross-section data given in Table 5.3 to magnify transport and anisotropic effects. The capability of diffusion theory to capture extreme anisotropic flux behavior is expected to be poor.

As already discussed in Section 2.3, the SP_N solution is generally not equivalent to the P_N solution and therefore increasing N does not in any case provide a more accurate result. However, it is common experience that the maximum potential accuracy is obtained around SP_5 or SP_7 [119]. On this account, the fine-mesh TRIVAC SP_5 solution is considered a reasonable reference solution.

The development of two methods based on different approximations of the transport equation but using identical underlying spatial discretization allows a comparative analysis of both methods with regard to transport effects. As very similar nodal flux expansions are applied to DYN3D-TRISP3 and DYN3D-TRIDIF (cf. Section 3.5), the spatial-discretization error becomes negligible when considering identical trigonal refinement levels. In any case, the spatial-discretization error approaches zero in the limit of infinitely fine mesh spacing.

DYN3D-TRISP3 and DYN3D-TRIDIF calculations have been run applying the refinements from 6 to 6144 trigonal nodes. In Figure 5.4, the normalized flux distribution of the considered core sector and the respective relative errors for the coarse nodalization of 6 and the fine nodalization of 6144 triangles per assembly are depicted. The effective multiplication factors and the deviations from the TRIVAC reference as well as the maximum and RMS flux differences for both trigonal models are summarized in Table 5.5 listing all refinement levels. For the hexagonal DYN3D methods, the results are also given. Especially

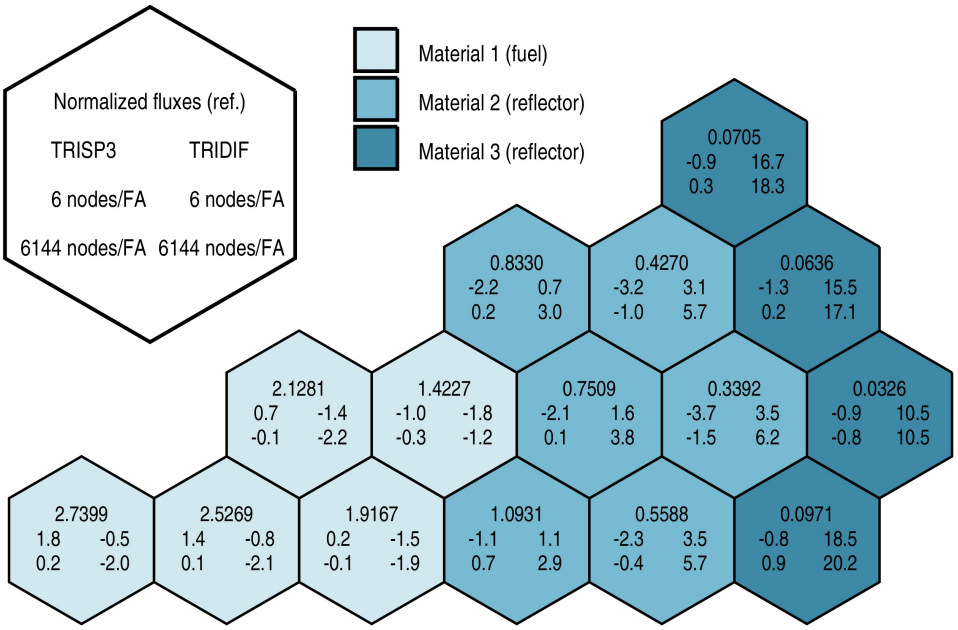

FIGURE 5.4: Core configuration of the Hébert benchmark. Normalized neutron flux distribution obtained by TRIVAC (SP_5 option) and relative errors (%) determined by DYN3D-TRISP3 and DYN3D-TRIDIF for the nodalizations 6 and 6144.

Method	No. of trigonal nodes per FA	k_{eff}	$\delta_{k_{\text{eff}}}$ (pcm)	Max. diff. (%)	RMS diff. (%)
DYN3D-TRISP3	6	1.001100	-17	3.7	1.8
	24	1.000085	-118	3.2	1.3
	96	0.999939	-133	2.7	1.0
	384	1.000039	-123	2.2	0.8
	1536	1.000156	-111	1.8	0.7
	6144	1.000238	-103	1.5	0.6
DYN3D-TRIDIF	6	0.973001	-2820	18.5	8.2
	24	0.971983	-2921	20.0	9.0
	96	0.971902	-2929	20.4	9.3
	384	0.972064	-2913	20.5	9.3
	1536	0.972220	-2898	20.4	9.3
	6144	0.972322	-2888	20.2	9.3
DYN3D-HEXNEM1		0.973931	-2727	20.0	9.3
DYN3D-HEXNEM2		0.972710	-2849	21.0	9.4
TRIVAC - SP_5 (ref.)		1.001271			

TABLE 5.5: Hébert benchmark: Effective multiplication factors k_{eff}, maximum and RMS flux differences – DYN3D-TRISP3, DYN3D-TRIDIF, and DYN3D-HEXNEM1/2 in comparison to the TRIVAC (SP_5) reference.

in the outer reflector region, DYN3D-TRISP3 superiorly represents the flux distribution in comparison to DYN3D-TRIDIF (and also DYN3D-HEXNEM1/2) by more than an order of magnitude. Recalling Section 1.3, diffusion theory requires the migration process to be scattering collision dominated. In material 3, this requirement is not fulfilled with the consequence that the DYN3D diffusion models fail with an error in flux of about 20 %. DYN3D-TRISP3 performs reasonably well in a coarse nodalization with a maximum flux deviation of 3.7 % in the inner reflector region. The maximum error is diminished to 1.5 % in a fine nodalization showing an overall good performance. The differences in k_{eff} are significantly reduced from almost 3000 pcm by the DYN3D diffusion methods to about 100 pcm by the DYN3D SP_3 approach.

Hence, the concluding statement of this section is: By means of the present academic benchmark, anisotropy effects are quantitatively identified and the superiority of the trigonal DYN3D SP_3 method over the respective diffusion model is clearly demonstrated.

A further remark shall be made on the assessment of trigonal nodalizations of differing size or hexagonal nodalizations with different underlying flux expansions. Here, the effect of the spatial-discretization error has to be considered in addition to the transport error. Such effects superpose and may impact the degree of agreement in different directions, e.g., accidental error compensation is possible [93]. The findings that DYN3D-TRIDIF shows results closer to the reference solution for 6 nodes per assembly than with a finer nodalization and that DYN3D-HEXNEM2 agrees less well with the reference than DYN3D-HEXNEM1, are examples of such phenomena.

5.3 Verification against detailed-geometry full-transport-theory problems

In this section, further comparison studies are performed to verify the trigonal DYN3D models. Realistic and detailed-geometry full-transport-theory problems are investigated. In contrast to the cases of Section 5.2, spatial-homogenization and energy-averaging effects occur in addition to spatial-discretization and transport effects.

The employed few-group cross-section data sets are homogenized from assembly level in Section 5.3.1 to one sixth of an assembly in Section 5.3.2 down to pin-size level in Section 5.3.3.

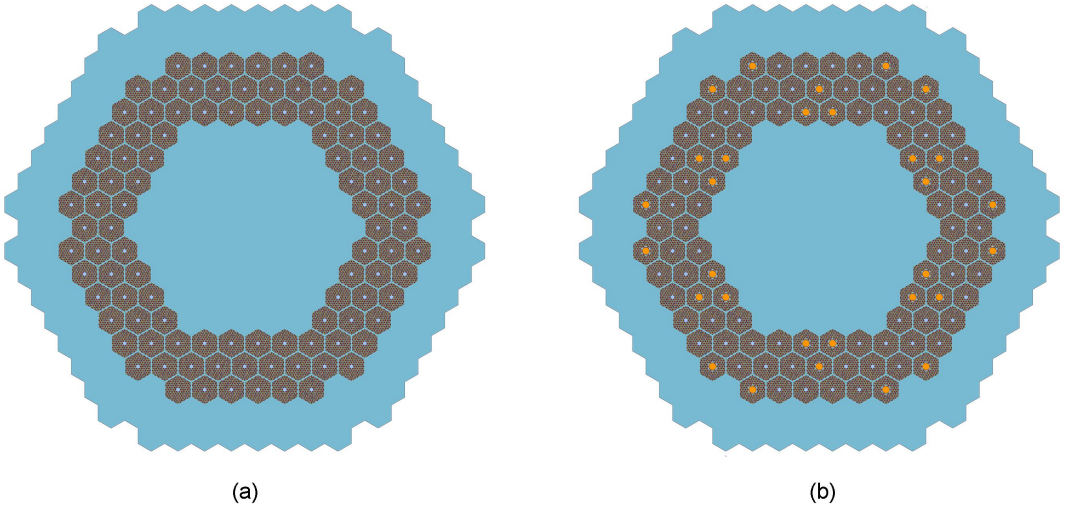

FIGURE 5.5: Simplified HTGR core models without (a) and with (b) control rods.

FIGURE 5.6: Geometry of the two-dimensional fuel-reflector model (30° core profile).

5.3.1 HTGR CORE

A two-dimensional simplified core of the prismatic-fuel-type high-temperature gas-cooled reactor (HTGR), which was developed by the Idaho National Engineering and Environmental Laboratory (INEEL) in the frame of the Next Generation Nuclear Plant (NGNP) project [118], is considered the reference. The core is loaded with 102 fuel assemblies embedded in an inner and outer graphite reflector occupying 61 and 102 assembly positions, respectively. The assembly pitch is 36 cm. Further core parameters are provided in the work of Rohde et al. [136].

Two core models – with and without inserted control rods – are analyzed. The NGNP core design comprises control rod channels which are asymmetrically aligned in several fuel and outer reflector elements. For the case study without inserted control rods, however, all assemblies are modeled without any control rod channels. In the case of inserted control rods, only fuel assembly rod channels are taken into account, reflector control rods are neglected. Instead of an asymmetrical composition, a central alignment of the control rods is furthermore assumed for the sake of simplicity. In Figure 5.5, the considered HTGR core geometries are illustrated. To model the reflector regions, a diagonal section of the core has been used as shown in Figure 5.6.

Considering a core temperature of 1200 K, the verification analysis has been performed as follows. First, full-core heterogeneous reference solutions have been obtained using the

Group	Upper group energy (MeV)
1	1.500e1
2	2.231
3	8.210e-1
4	5.530e-3
5	4.805e-5
6	4.000e-6
7	6.250e-7
8	3.500e-7
9	2.800e-7
10	1.400e-7
11	5.800e-8
12	3.000e-8

TABLE 5.6: 12-energy-group structure for the HTGR analysis.

continuous-energy Monte Carlo code Serpent [109, 110]. The Monte Carlo calculations have been performed with 500 inactive and 1000 active neutron cycles and 60,000 neutron histories per cycle (cf. Section 2.2.1). For the present test cases, this is considered sufficient. Second, homogenized cross-section sets required for the nodal analysis have been created also using the Serpent code. The cross sections have been generated for hexagonal assemblies in an infinite environment (reflective boundary conditions) in 12 energy groups [51]. The group structure shown in Table 5.6 is a predefined subset of the CASMO-4 [135] basic 70-group energy structure and consists of 3 fast, 2 resonance, and 7 thermal energy groups. A relatively large number of thermal groups is believed to be sufficient to properly account for thermal upscattering events. It should be noted, however, that an optimization of the energy group structure for HTGR applications has not been performed [52]. Finally, 30°-symmetry-sector DYN3D calculations with vacuum exterior boundary conditions have been run using the few-group constants generated by the Serpent code.

In Figure 5.7, the Serpent outputs of the thermal-flux distributions for both considered cases are presented.

CASE WITHOUT CONTROL RODS: In Figure 5.8, a 30° sector of the considered HTGR core without control rods is depicted exemplarily showing the relative errors in the radial power distribution obtained by DYN3D-TRISP3 and DYN3D-TRIDIF for the subdivisions of 6 and 96 nodes per hexagonal assembly. In Table 5.7, the effective multiplication factors and the differences from the Serpent reference value[4] as well as the maximum and RMS

[4]The standard deviation of k_{eff} in the Serpent calculations is about 0.0002.

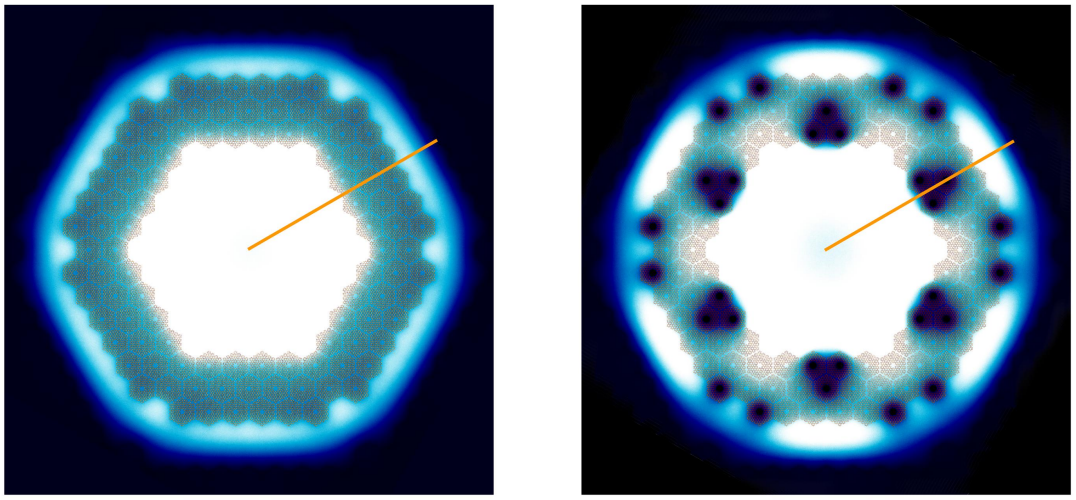

(a) (b)

FIGURE 5.7: Serpent thermal-flux distribution of the simplified HTGR core without (a) and with (b) inserted control rods. Indication of the 30° core radius.

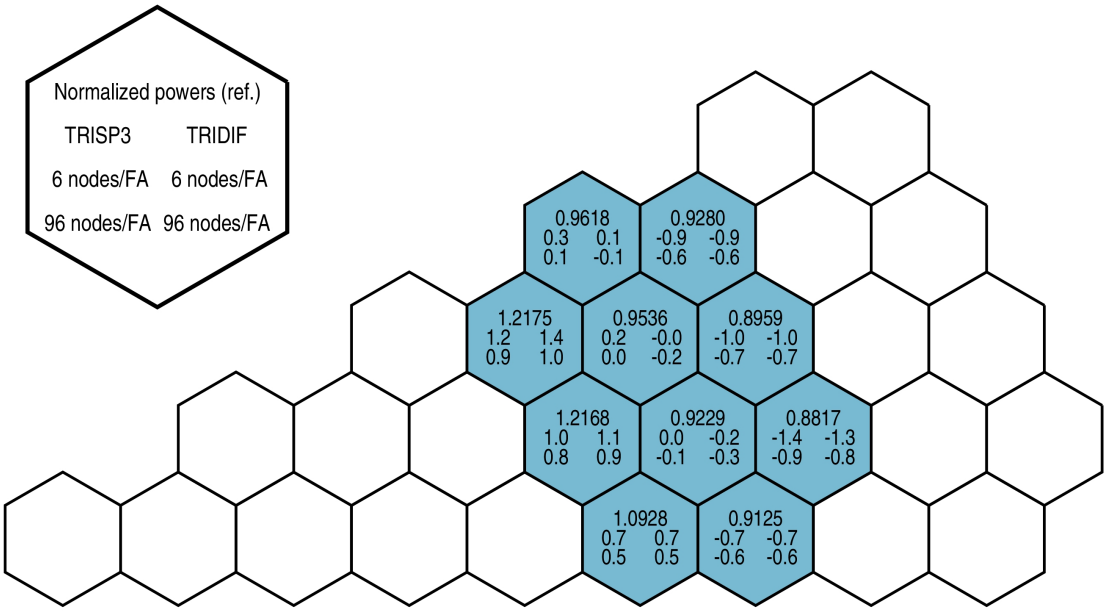

FIGURE 5.8: HTGR core without control rods: Normalized power distribution obtained by Serpent and relative errors (%) determined by DYN3D-TRISP3 and DYN3D-TRIDIF for the nodalizations 6 and 96.

Method	No. of trigonal nodes per FA	k_{eff}	$\delta_{k_{\text{eff}}}$ (pcm)	Max. diff. (%)	RMS diff. (%)
DYN3D-TRISP3	6	1.317994	115	1.4	0.9
	24	1.319332	192	1.1	0.7
	96	1.320052	233	0.9	0.6
	384	1.320375	252	0.9	0.6
DYN3D-TRIDIF	6	1.318244	129	1.4	0.9
	24	1.319642	210	1.2	0.8
	96	1.320383	252	1.0	0.7
	384	1.320707	271	0.9	0.6
DYN3D-HEXNEM1		1.321472	315	0.3	0.2
DYN3D-HEXNEM2		1.322347	366	0.7	0.4
Serpent (ref.)		1.316010			

TABLE 5.7: HTGR core without control rods: Effective multiplication factors k_{eff}, maximum and RMS power differences – DYN3D-TRISP3, DYN3D-TRIDIF, and DYN3D-HEXNEM1/2 in comparison to the Serpent reference.

power differences are summarized for the trigonal DYN3D SP_3 and diffusion models and additionally for the hexagonal DYN3D diffusion methods. Nodal refinements from 6 to 384 triangles per assembly are considered. Additionally, the graphs in Figure 5.9 represent the normalized shapes of the fast-, resonance-, and thermal-group neutron fluxes of DYN3D-TRISP3/TRIDIF and Serpent along the core radius at an angle of 30° (in Figure 5.7, an indication of this radius is given). For the fast and the resonance fluxes, the energy groups 1, 2, 3 and 4, 5 are collapsed, respectively. The flattening of these curves in the inner ($r < 145\,\text{cm}$) and outer ($r > 229\,\text{cm}$) reflector regions due to missing fission sources and dominant neutron downscattering into thermal energy groups is shown. Accordingly, pronounced peaks in the thermal flux, combining groups 6 to 12, are identified in the reflector zones adjacent to the fuel. For DYN3D, the trigonal discretization of 96 nodes per assembly has been chosen. In this manner, flux values at 113 mesh points have been extracted and interpolated along the radius. Only one curve per collapsed energy group, however, is displayed for DYN3D-TRISP3/TRIDIF, since no visible difference between the DYN3D SP_3 and diffusion fluxes can be perceived. Generally, a good agreement between the different DYN3D methods and the Monte Carlo reference is demonstrated. The deviations in k_{eff} are about 200 pcm for the trigonal approaches, the RMS difference in power is generally less than 1 %. Also the fast-, resonance-, and thermal-flux curves of DYN3D-TRISP3/TRIDIF agree very well with the Serpent flux reference shapes.

The trigonal DYN3D SP_3 method predicts the reference solution better than the trigonal DYN3D diffusion method. However, in this rather isotropic case, the degree of improvement is very marginal.

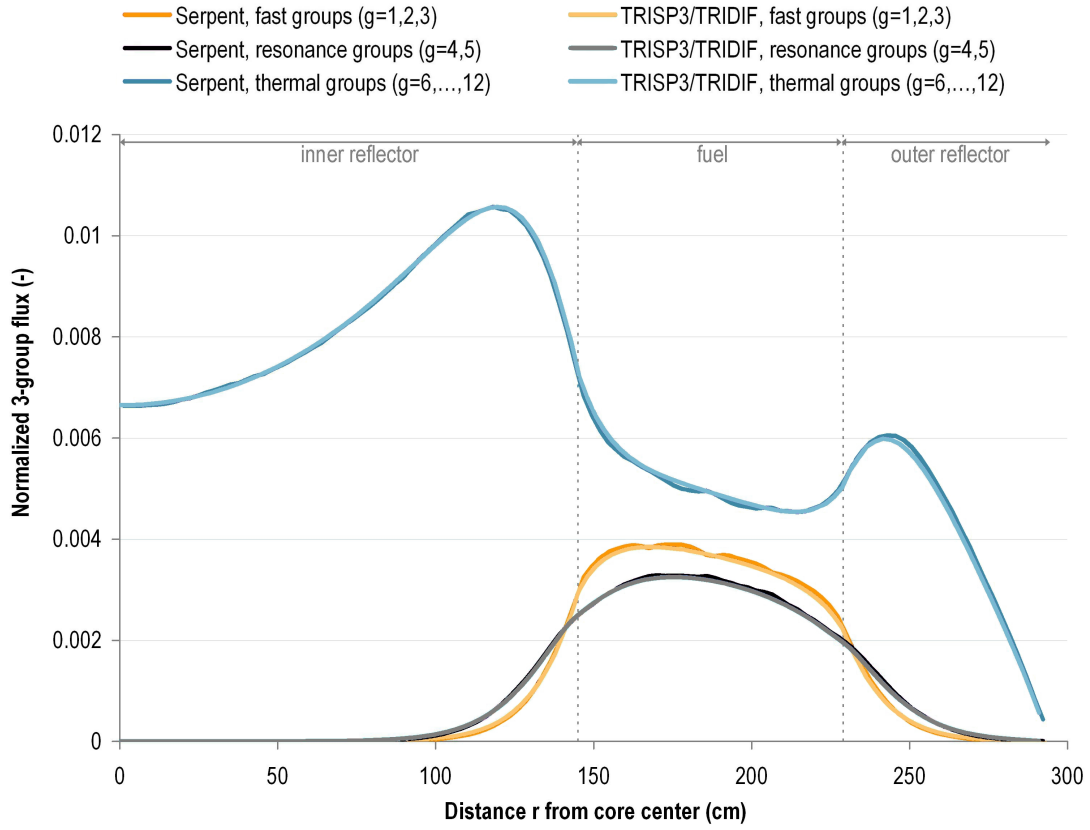

FIGURE 5.9: HTGR core without control rods: Normalized neutron flux distribution along the 30° core line obtained by Serpent and DYN3D-TRISP3/TRIDIF (96 nodes per assembly).

The hexagonal-geometry DYN3D diffusion models agree well with the reference power distribution in this example due to the intra-nodal flux ansatzes, which are more sophisticated in the hexagonal than in the trigonal approaches.

The phenomenon that a coarse trigonal nodalization gives better multiplication factors in this case than calculating with a higher nodal resolution can be traced back to coincidental error compensation. The same argumentation applies to the general results of DYN3D-HEXNEM1 and DYN3D-HEXNEM2.

CASE WITH CONTROL RODS: In Figure 5.10, a 30° symmetry sector of the HTGR core with inserted control rods is depicted. Also here, the relative errors in the radial power distribution obtained by DYN3D-TRISP3 and DYN3D-TRIDIF for the nodalizations of 6 and 96 triangles per assembly are shown. The effective multiplication factors and the maximum and RMS power differences from the Serpent Monte Carlo reference solution for the nodal subdivisions from 6 to 384 triangles per assembly are listed in Table 5.8. The graphs in Figure 5.11 show the normalized shapes of the fast-, resonance-, and thermal-group neutron fluxes of DYN3D-TRISP3/TRIDIF and Serpent along the core radius at an

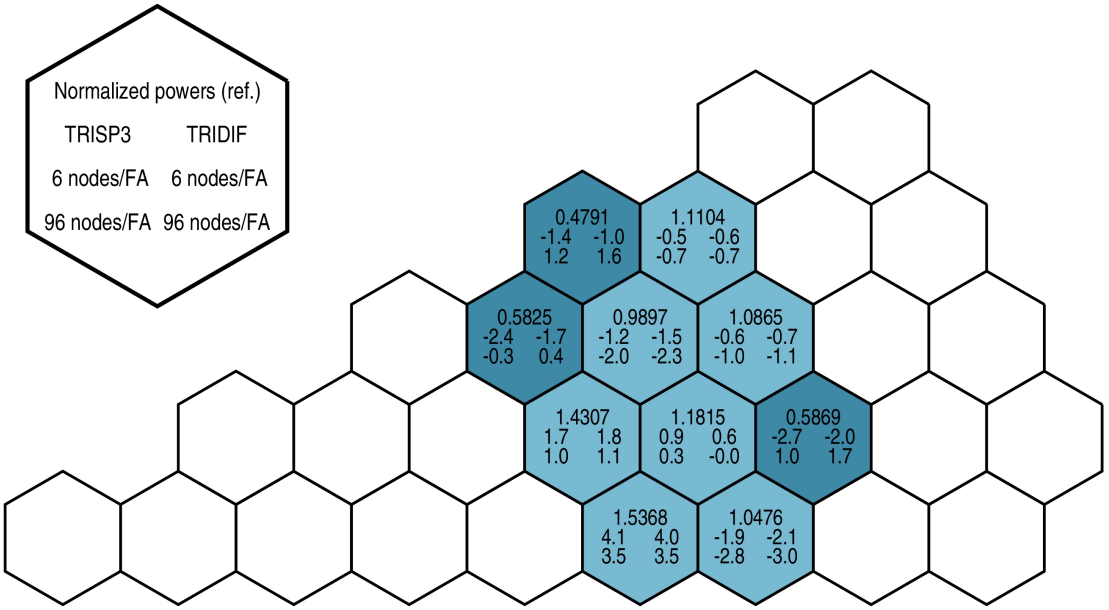

FIGURE 5.10: HTGR core with inserted control rods: Normalized power distribution obtained by Serpent and relative errors (%) determined by DYN3D-TRISP3 and DYN3D-TRIDIF for the nodalizations 6 and 96.

Method	No. of trigonal nodes per FA	k_{eff}	$\delta_{k_{\text{eff}}}$ (pcm)	Max. diff. (%)	RMS diff. (%)
DYN3D-TRISP3	6	0.997185	-1360	4.1	2.0
	24	0.992167	-1851	3.7	1.7
	96	0.990934	-1972	3.5	1.7
	384	0.990648	-2000	3.4	1.7
DYN3D-TRIDIF	6	0.995924	-1484	4.0	1.9
	24	0.990937	-1971	3.6	1.8
	96	0.989744	-2088	3.5	1.9
	384	0.989494	-2112	3.4	1.9
DYN3D-HEXNEM1		0.991483	-1918	3.2	1.7
DYN3D-HEXNEM2		0.989681	-2094	3.4	2.1
Serpent (ref.)		1.011090			

TABLE 5.8: HTGR core with inserted control rods: Effective multiplication factors k_{eff}, maximum and RMS power differences – DYN3D-TRISP3, DYN3D-TRIDIF, and DYN3D-HEXNEM1/2 in comparison to the Serpent reference.

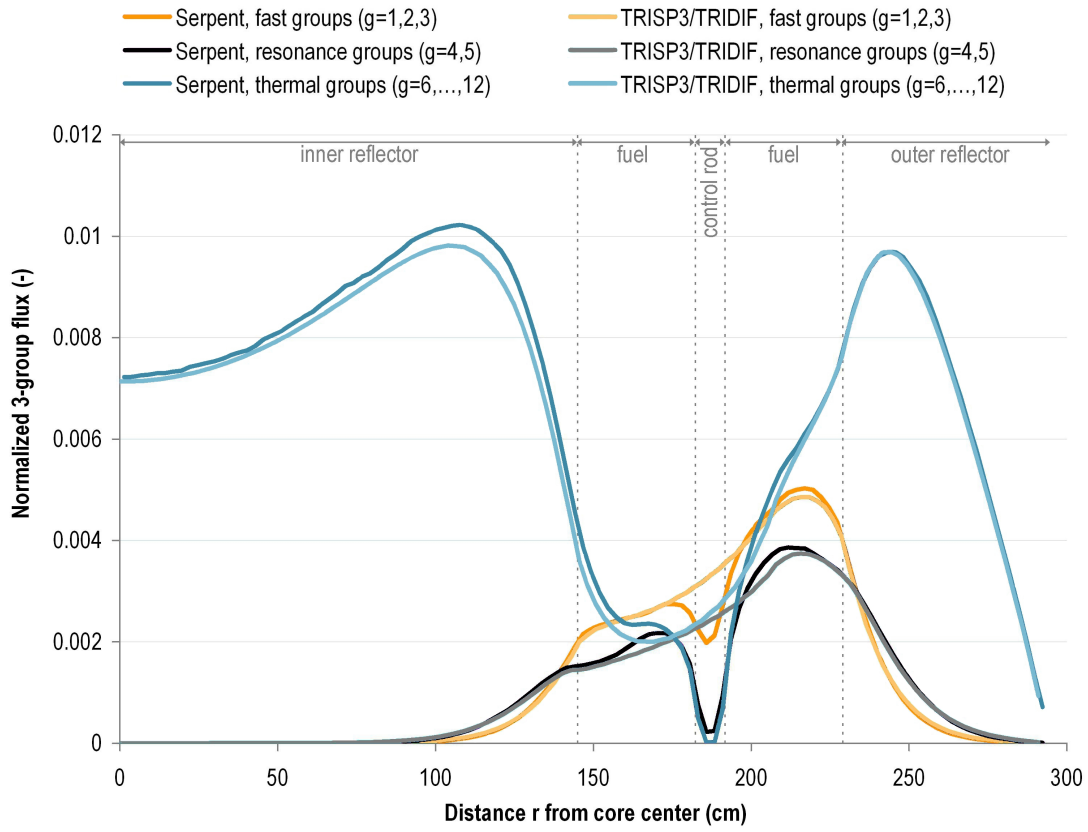

FIGURE 5.11: HTGR core with inserted control rods: Normalized neutron flux distribution along the 30° core line obtained by Serpent and DYN3D-TRISP3/TRIDIF (96 nodes per assembly).

angle of 30° (see Figure 5.7 (b)) considering a refinement of 96 nodes per assembly. In the reflector regions, naturally, the same physical effects are observed than in the case without control rods. The fuel region ($145 < r < 229$ cm), evidently, shows a different behavior and can be divided into the following three zones (cf. Figure 5.10 for clarification):

- zone 1: a symmetry boundary line between two fuel assemblies with inserted control rod ($145 < r < 166$ cm),
- zone 2: a line from corner to corner through the center of a fuel assembly with inserted control rod ($166 < r < 208$ cm), and
- zone 3: a symmetry boundary line between two fuel assemblies without control rod ($208 < r < 229$ cm).

Concerning zones 1 and 3, the considered radius is located on graphite material with fuel rods (and coolant channels) in the immediate vicinity. Hence, fission and scattering from fast to resonance energies lead to an increase of the fast and the resonance neutron flux. The thermal flux, naturally, decreases from the reflector to the fuel region caused by

absorption. Due to the presence of boron carbide (B_4C) in the close vicinity of zone 1, the fluxes in this zone are generally lower than in zone 3. However, in zone 2, one centrically modeled control rod is diagonally cut, which results in strong local flux minima in the middle of the region. Certainly, neither DYN3D-TRISP3 nor DYN3D-TRIDIF is capable of reproducing those narrow minima, caused by the absorber rod, especially in the thermal flux, as DYN3D uses cross sections that are homogenized over the much broader fuel assembly. Therefore, this discrepancy is not a shortcoming of the SP_3 transport or diffusion method but of the homogenization procedure. As a consequence, DYN3D underestimates the flux outside zone 2. This behavior is also reflected in the corresponding assembly powers. In a coarse nodalization, the nodal power distribution is generally underestimated in the 30° region as a result of the overestimation of the power in the inner corner assembly due to compensation effects of the applied normalization. The maximum power difference with about 4 % occurs in the assembly with the largest distance to the absorber assemblies. In this region, the highest power density occurs, which is connected to a strong thermal-flux gradient in direction to the inner reflector. The deviations in power and also the differences in k_{eff} of about 2000 pcm are generally rather high as a result of the significant flux gradients.

Discontinuity factors can remedy such a situation. However, the use of discontinuity factors is generally not considered in this work since the underlying theory has only been established for the diffusion method (cf. Section 3.1). In view of the precise comparison of the performance of the trigonal DYN3D SP_3 and diffusion models, simply applying diffusion-theory discontinuity factors to the SP_3 method may reproduce the SP_3 results inconsistently and generate an additional error source (although a general improvement of the results could be expected).

The conclusion which can be drawn from the full-core HTGR calculations is that DYN3D-TRISP3 produces better results compared to DYN3D-TRIDIF. However, the improvements are marginal when using assembly-homogenized cross sections in such a strongly heterogeneous material configuration. The anisotropy effect simply becomes unpronounced. With use of cross sections homogenized over smaller nodes, the SP_3 effect is expected to appear more emphasized.

5.3.2 HTGR fuel block with control rod

In this section, the cross-section data are homogenized for six regions within an assembly.

A simplified single HTGR control rod fuel block of the aforementioned prismatic NGNP design [118] is considered taking the real asymmetric rod channel position into account. In Figure 5.12, the single assembly HTGR model is depicted. We investigate the two cases

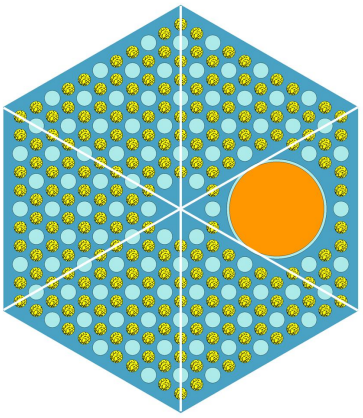

FIGURE 5.12: Simplified single HTGR control rod fuel assembly model with indication of six homogenized-cross-section regions.

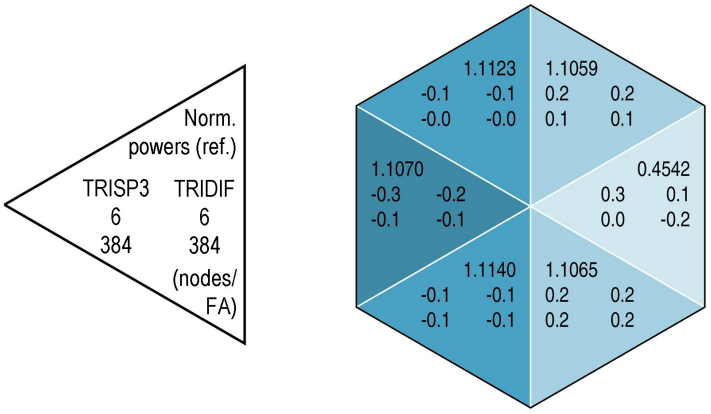

FIGURE 5.13: HTGR single assembly without inserted control rod: Normalized power distribution obtained by Serpent and relative errors (%) determined by DYN3D-TRISP3 and DYN3D-TRIDIF for the nodalizations 6 and 384.

with and without inserted control rod. Here, the advantage of a method based on trigonal geometry over a purely hexagonal method is obvious.

Considering a core temperature of 1200 K, the heterogeneous reference solutions as well as the homogenized cross-section sets have been generated again by the Monte Carlo code Serpent [109, 110]. The cross sections have been created on an infinite assembly level (reflective boundary conditions) in a 12-energy-group structure (cf. Table 5.6) and extracted for six congruent trigonal regions (see Figure 5.12) [51].

CASE WITHOUT CONTROL ROD INSERTED: The Monte Carlo normalized power distribution reference values for the case without inserted control rod as well as the relative errors obtained by the trigonal DYN3D SP_3 and diffusion models applying reflective boundary conditions are depicted in Figure 5.13. A refinement study is performed up to 1536 nodes per assembly, i.e., 256 nodes per homogenized trigonal region. However, only the nodalizations of 6 and 384 triangles per assembly are presented in this figure. Note that the

Method	No. of trigonal nodes per FA	k_{inf}	$\delta_{k_{inf}}$ (pcm)	Max. diff. (%)	RMS diff. (%)
DYN3D-TRISP3	6	1.418970	-4	0.3	0.2
	24	1.418985	-4	0.2	0.1
	96	1.418995	-3	0.2	0.1
	384	1.419001	-3	0.2	0.1
	1536	1.419006	-3	0.2	0.1
DYN3D-TRIDIF	6	1.418970	-4	0.2	0.2
	24	1.418984	-4	0.2	0.1
	96	1.418993	-3	0.2	0.1
	384	1.419000	-3	0.2	0.1
	1536	1.419004	-3	0.2	0.1
Serpent (ref.)		1.419060			

TABLE 5.9: HTGR single assembly without inserted control rod: Infinite multiplication factors k_{inf}, maximum and RMS power differences – DYN3D-TRISP3 and DYN3D-TRIDIF in comparison to the Serpent reference.

Serpent solutions are not absolutely symmetric owing to statistical imprecision. In addition, the infinite multiplication factors and their relative deviations from the reference value[5] as well as the maximum and RMS power differences for DYN3D-TRISP3 and DYN3D-TRIDIF are summarized in Table 5.9 for the full refinement study. In Figure 5.14, the graphs of the normalized shapes of the fast-, resonance-, and thermal-group neutron fluxes of DYN3D-TRISP3/TRIDIF and Serpent along the horizontal central assembly line are additionally depicted for the refinement level of 384 nodes, i.e., 16 triangles in the horizontal profile. The fluxes are collapsed in the same manner as presented in Section 5.3.1. As we consider a reflective environment, the flux shapes, naturally, are rather flat for this case. Due to a concentration of fuel on the left side, a moderate increase in the fast flux and a respective slight decrease in the thermal flux is observed. The helium filled control rod channel on the right hardly influences the neutron flux. The decrease in power in this region evidently results from the relatively small average fission cross sections. A very good agreement between the DYN3D methods and the Monte Carlo reference is obtained already for the coarsest nodalization with a difference in k_{inf} in the single-digit range and a maximum difference in power of 0.3 % and less. With increasing mesh refinement, the power minimum in the helium channel region is superiorly represented by the DYN3D SP_3 method (cf. Figure 5.13). However, this effect is rather marginal. The overall performance of DYN3D-TRISP3 and DYN3D-TRIDIF is very similar in this case as a consequence of the overall isotropic flux behavior.

[5]The standard deviation of k_{inf} in the Serpent calculations is about 0.0002.

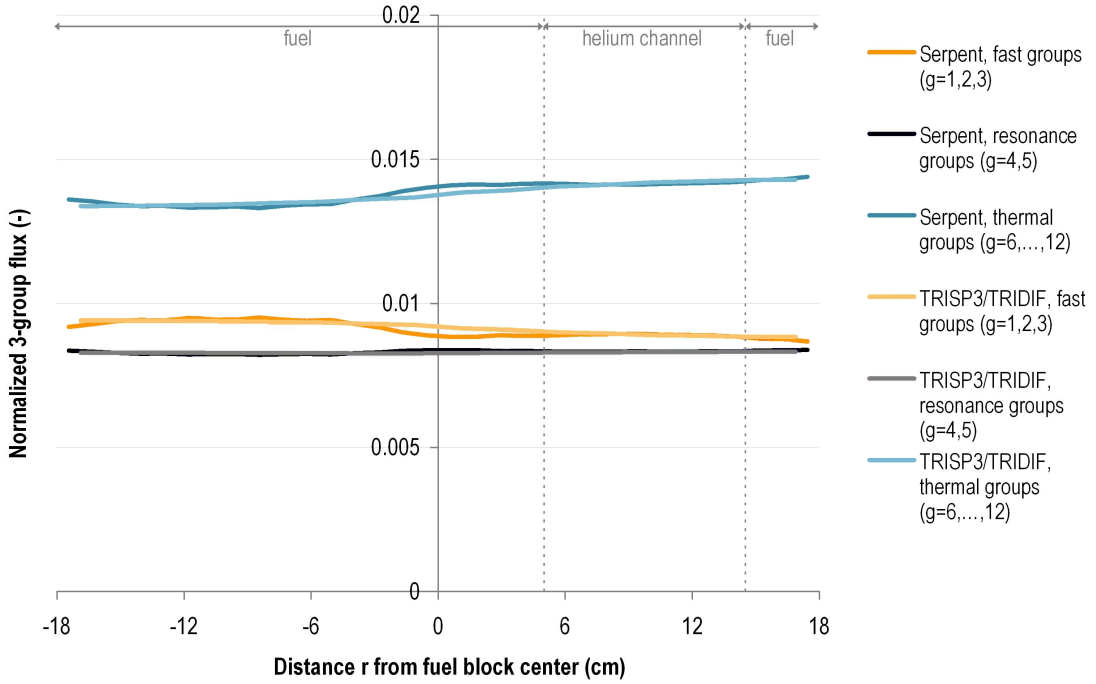

FIGURE 5.14: HTGR single assembly without inserted control rod: Normalized neutron flux distribution along the horizontal central assembly line obtained by Serpent and DYN3D-TRISP3/TRIDIF (384 nodes).

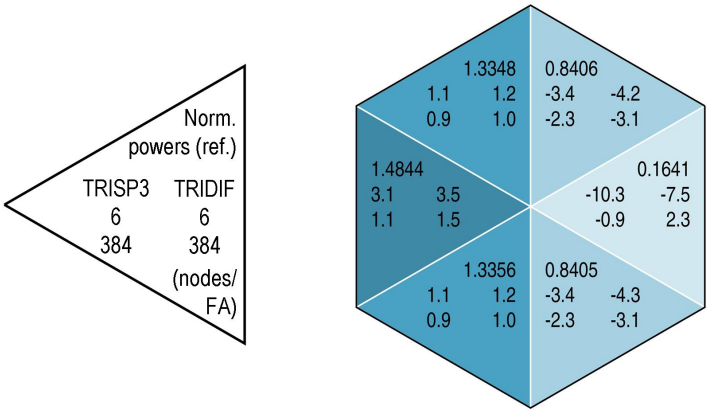

FIGURE 5.15: HTGR single assembly with inserted control rod: Normalized power distribution obtained by Serpent and relative errors (%) determined by DYN3D-TRISP3 and DYN3D-TRIDIF for the nodalizations 6 and 384.

CASE WITH INSERTED CONTROL ROD: In Figure 5.15, the Serpent reference normalized power distribution as well as the relative errors obtained by DYN3D-TRISP3 and DYN3D-TRIDIF are depicted for the inserted-control-rod case. In Table 5.10, the infinite multiplication factors and the relative deviations from the reference value as well as the maximum and RMS power differences for both trigonal DYN3D models are listed. The graphs of the normalized shapes of the fast-, resonance-, and thermal-group neutron fluxes of the

Method	No. of trigonal nodes per FA	k_{inf}	$\delta_{k_{\text{inf}}}$ (pcm)	Max. diff. (%)	RMS diff. (%)
DYN3D-TRISP3	6	0.565346	14108	10.3	4.9
	24	0.543393	6182	4.3	2.2
	96	0.534428	2945	2.1	1.5
	384	0.531467	1876	2.3	1.5
	1536	0.530908	1674	2.3	1.5
DYN3D-TRIDIF	6	0.553963	9998	7.5	4.2
	24	0.531493	1885	2.7	1.9
	96	0.522590	-1329	2.9	1.9
	384	0.519903	-2300	3.1	2.2
	1536	0.519599	-2409	3.1	2.2
Serpent (ref.)		0.526272			

TABLE 5.10: HTGR single assembly with inserted control rod: Infinite multiplication factors k_{inf}, maximum and RMS power differences – DYN3D-TRISP3 and DYN3D-TRIDIF in comparison to the Serpent reference.

trigonal DYN3D methods and Serpent along the horizontal central assembly line are displayed in Figure 5.16. Here, separate curves are shown for DYN3D-TRISP3 and DYN3D-TRIDIF as small differences can be perceived in this example. Due to the presence of boron carbide (B_4C), a so-called black absorber, there is a general decrease in the flux towards the absorber resulting in a vanishing thermal flux in the domain of the control rod ($5.0 < r < 14.5\,\text{cm}$). Using cross sections homogenized over regions of the size of one sixth of the considered assembly, the circular control-rod region (cf. Figure 5.12) is "artificially provided with some fuel" in the DYN3D calculation. Hence, DYN3D is not capable of reproducing the existent gradients in the resonance and thermal flux, which is not a shortcoming of the intrinsic method but of the homogenization procedure itself. However, the finer the spatial refinement is chosen, the less pronounced this effect becomes. This reflects in the power profile with an error of about 10 % in case the node size equals the size of the homogenized region. For a finer nodalization, DYN3D-TRISP3 reduces the error to less than 1 % in the control rod node and performs superior to DYN3D-TRIDIF.

In case of the coarsest nodalization, DYN3D-TRIDIF represents the reference solution closer than DYN3D-TRISP3 due to coincidental error cancellation.

Regarding the multiplication factors, a convergence of the DYN3D SP_3 results towards the Monte Carlo solution is clearly evident. However, the results are far away from the Serpent reference. The remaining deviation (about 1700 pcm) must be caused by a combination of the deficiencies of the SP_3 approach with spatial-homogenization/energy-averaging errors. Discontinuity or superhomogenization (SPH) factors can reduce such discrepancies. However, they have deliberately not been used in the present calculations (cf. Section 3.1).

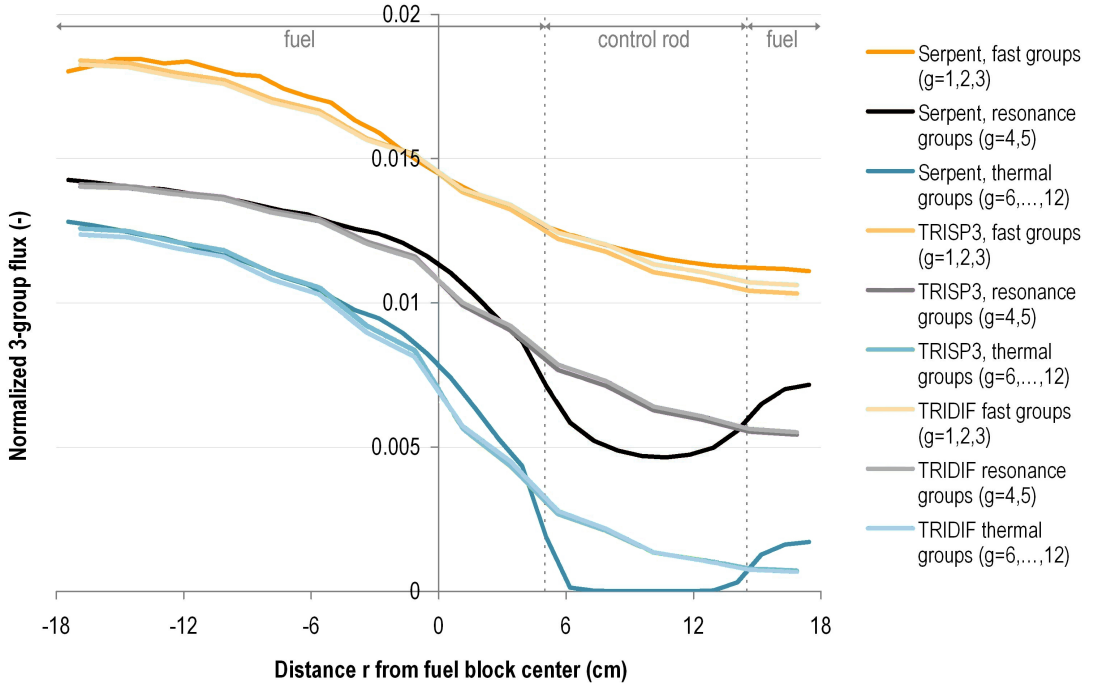

FIGURE 5.16: HTGR single assembly with inserted control rod: Normalized neutron flux distribution along the horizontal central assembly line obtained by Serpent, DYN3D-TRISP3, and DYN3D-TRIDIF (384 nodes).

The bottom line of this HTGR single-assembly study is that DYN3D-TRISP3 delivers a performance superior to DYN3D-TRIDIF in regions with extreme flux gradients, especially if applying fine nodalization. A refinement of the cross-section homogenization areas would emphasize this effect.

5.3.3 VVER-1000-LIKE FUEL ASSEMBLY

In the previous subsections, the performance of the trigonal DYN3D models is analyzed requiring cross sections homogenized on assembly or quasi-assembly size. Now, an example is investigated using cross sections homogenized on pin-cell level.

A single hexagonal fuel assembly with two different material compositions is chosen. Both fuel assembly types consist of 151 fuel pins and 18 guide tubes. In one case, 6 burnable-absorber pins are introduced. The used materials as well as the fuel rod geometry and the fuel pin pitch[6] are typical for a VVER-1000 fuel assembly (a detailed description is given in [115]). However, the diameter of the guide tubes is scaled down to fit the nodalization grid. The guide tubes and the space between the pins are filled with unborated water.

[6]The distance between the centers of two adjacent fuel pins is called fuel pin pitch.

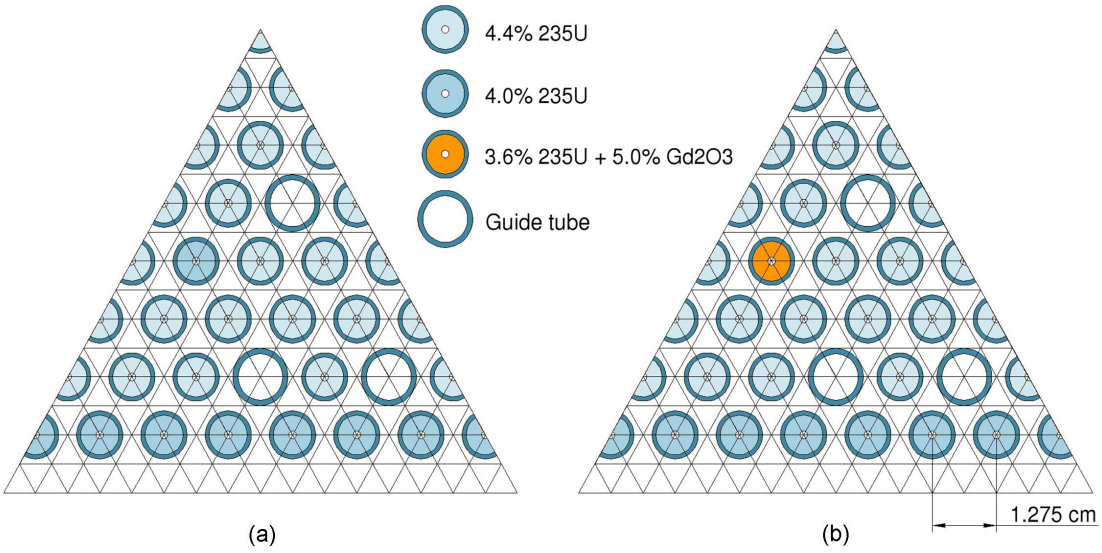

FIGURE 5.17: 60° sectors of a VVER-1000-like fuel assembly without (a) and with (b) a fuel/gadolinium pin.

In Figure 5.17, 60° symmetry sectors of the two test cases – without and with burnable-absorber (fuel/gadolinium) pin – are illustrated.

The two-dimensional heterogeneous reference solutions have been generated by the HELIOS 1.10 lattice transport code [18], which solves the transport equation by a method based on current coupling and collision probabilities. The transport calculations have been performed in 190 neutron energy groups. For the DYN3D pin-level calculations, a refinement of 1536 trigonal nodes has been chosen. With this nodalization, one fuel pin or guide tube is radially represented by six trigonal elements. We have the following regions:

- triangles containing one sixth of a higher enriched UO_2 fuel pin (4.4 % ^{235}U) and unborated water (H_2O),
- triangles containing one sixth of a lower enriched UO_2 fuel pin (4.0 % ^{235}U) and unborated water (H_2O),
- triangles containing one sixth of a fuel/gadolinium pin (3.6 % ^{235}U + 5.0 % Gd_2O_3) and unborated water (H_2O),
- triangles containing one sixth of a guide tube (Zr alloy) and unborated water (H_2O),
- inner triangles containing only unborated water (H_2O), and
- peripherical triangles containing only unborated water (H_2O).

The macroscopic cross sections required for DYN3D have also been generated by the HELIOS code, using reflective assembly boundary conditions and allowing for ambient

Group	Upper group energy (MeV)
1	2.0000e1
2	2.2313
3	8.2085e-1
4	9.1188e-3
5	1.3007e-4
6	3.9279e-6
7	6.2506e-7
8	1.4572e-7

TABLE 5.11: 8-energy-group structure for the VVER analysis.

Method	No. of trigonal nodes per FA	k_{inf}	$\delta_{k_{inf}}$ (pcm)	Max. diff. (%)	RMS diff. (%)
DYN3D-TRISP3	1536	1.421852	-43	2.4	0.9
DYN3D-TRIDIF	1536	1.422373	-18	2.0	0.8
HELIOS (ref.)		1.422729			

TABLE 5.12: VVER-1000-like fuel assembly without fuel/gadolinium pin: Infinite multiplication factors k_{inf}, maximum and RMS power differences – DYN3D-TRISP3 and DYN3D-TRIDIF in comparison to the HELIOS reference.

effects. They have been extracted for the aforementioned regions in the 8-energy-group structure shown in Table 5.11, which is considered appropriate for light-water reactors [13, 120]. Finally, the DYN3D calculations have been performed also using reflective exterior boundary conditions.

CASE WITHOUT BURNABLE-ABSORBER PINS: In Figure 5.18, the HELIOS reference normalized power distribution as well as the relative errors obtained by DYN3D-TRISP3 and DYN3D-TRIDIF are presented for the case without absorber pin. The infinite multiplication factors and the relative deviations from the reference value as well as the maximum and RMS power differences for both trigonal DYN3D models are summarized in Table 5.12. Due to the wide (and unrealistic) inter-assembly water gap of the present assembly model, the highest power values are located in the outermost area of the assembly with the power peak in the outer corner pins as a result of extensive moderation in the junction area of three adjacent assemblies. This maximum nodal power value is well predicted by DYN3D-TRISP3 with 0.0 % error, whereas DYN3D-TRIDIF shows a slight deviation of -0.4 %. However, the maximum error in power of the trigonal DYN3D methods occurs in the opposite node of the corner pin. Here, the DYN3D diffusion method shows a better local representation of the reference value with -2.0 % deviation in comparison to -2.4 % determined by DYN3D-TRISP3, which is simply a compensation effect. Globally, the trigonal DYN3D methods

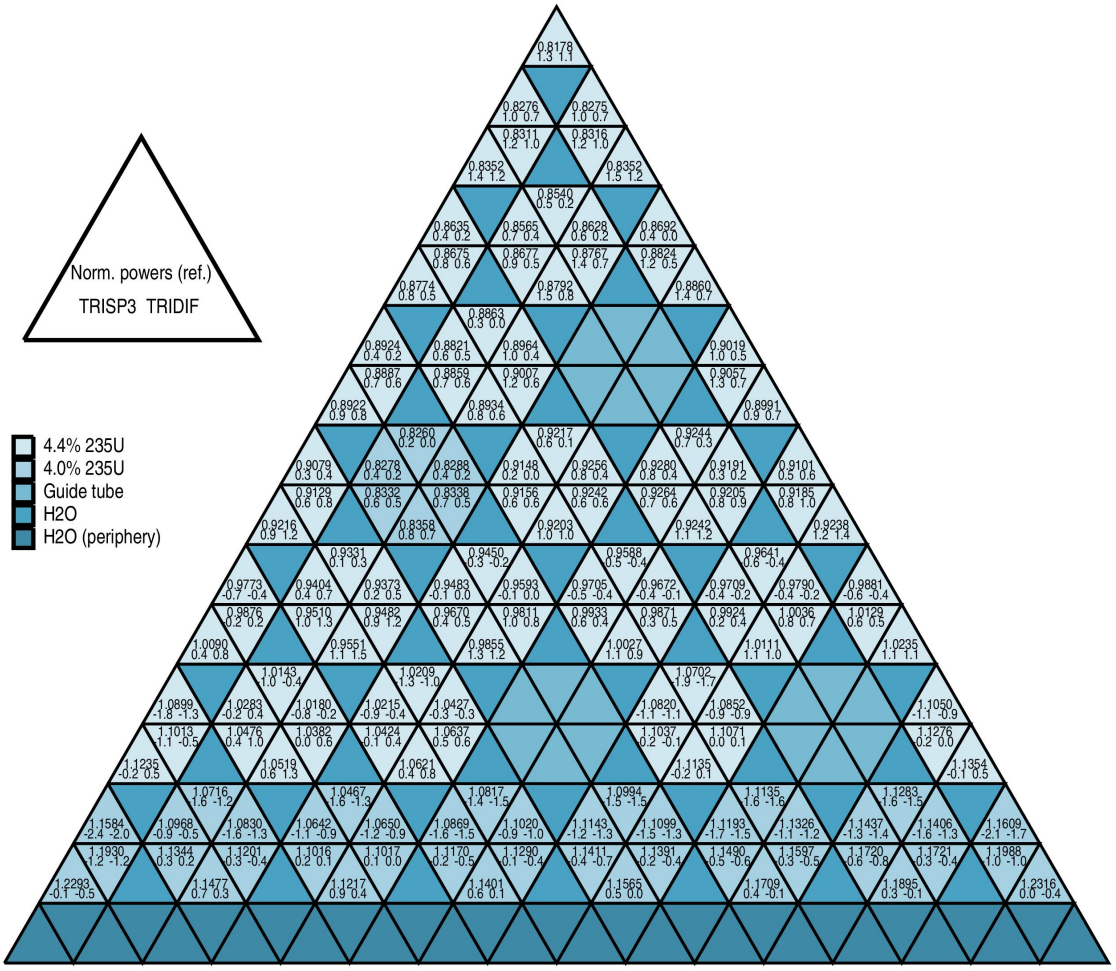

FIGURE 5.18: VVER-1000-like fuel assembly without fuel/gadolinium pin: Normalized power distribution obtained by HELIOS and relative errors (%) determined by DYN3D-TRISP3 and DYN3D-TRIDIF.

slightly overestimate the relatively low power values in the inner assembly region and underestimate the higher powers in the outer area. A general good agreement, however, between DYN3D and the HELIOS reference is achieved. Both trigonal DYN3D methods show similar results with $\delta_{k_{\text{inf}}}$ values in the lower double-digit range and an average deviation in power of less than 1 % as a consequence of the rather negligible anisotropic effects in the neutron flux.

CASE WITH BURNABLE-ABSORBER PINS: The HELIOS reference normalized power distribution as well as the relative errors obtained by the trigonal DYN3D SP_3 and diffusion models for the case with the strong absorbing fuel/gadolinium pin are shown in Figure 5.19. The infinite multiplication factors and the respective deviations from the reference value as well as the maximum and RMS power differences for DYN3D-TRISP3 and DYN3D-TRIDIF are summarized in Table 5.13. The DYN3D diffusion method reproduces the reference solution with an error of almost 9 % in the nodes containing gadolinium material (highlighted

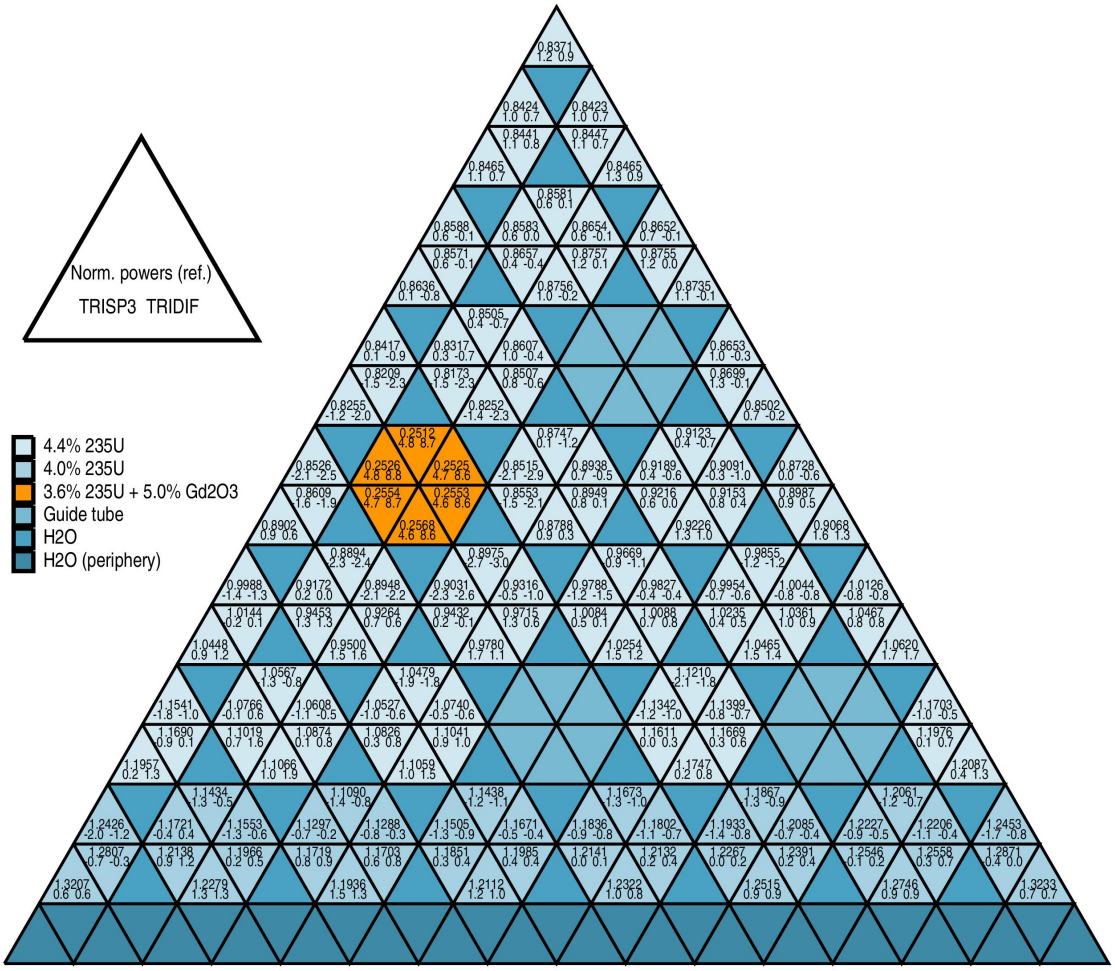

FIGURE 5.19: VVER-1000-like fuel assembly with fuel/gadolinium pin: Normalized power distribution obtained by HELIOS and relative errors (%) determined by DYN3D-TRISP3 and DYN3D-TRIDIF.

Method	No. of trigonal nodes per FA	k_{inf}	δk_{inf} (pcm)	Max. diff. (%)	RMS diff. (%)
DYN3D-TRISP3	1536	1.287081	-858	4.8	1.4
DYN3D-TRIDIF	1536	1.278561	-1361	8.8	2.0
HELIOS (ref.)		1.301624			

TABLE 5.13: VVER-1000-like fuel assembly with fuel/gadolinium pin: Infinite multiplication factors k_{inf}, maximum and RMS power differences – DYN3D-TRISP3 and DYN3D-TRIDIF in comparison to the HELIOS reference.

in orange), whereas, with the DYN3D SP_3 method, this error is reduced to less than 5 %. Also in the immediate vicinity of the absorber pin, DYN3D-TRISP3 superiorly predicts the power distribution. The global performance, however, is comparable to the aforementioned case. With regard to the multiplication factors, the DYN3D SP_3 approach reduces the difference in k_{inf} by 500 pcm.

The rather high deviations in k_{inf} can be reduced by the use of pin-cell discontinuity factors (CDFs) or superhomogenization (SPH) factors. However, this is generally abandoned in this work (cf. Section 3.1).

The fact that DYN3D-TRIDIF shows results in the inner assembly area slightly closer to the reference solution than DYN3D-TRISP3 can be explained by the superposition of the transport error with the spatial-homogenization and group-collapsing effects. Such a fortunate error cancellation in low-order methods was also observed by Kozlowski et al. [93].

The bottom line of this simplified VVER-1000 single-assembly study is that the performance of the DYN3D SP_3 method is superior to the respective diffusion method in regions with significantly pronounced flux gradients resulting in anisotropic neutron transport behavior.

5.4 Computation times

This section gives an overview of the computational effort of the test cases analyzed in this chapter.

As the computation times depend not only on the computer performance of the used processor but also on the DYN3D input requirements like the number of inner iterations and particular outer iteration stop criteria (cf. Section 4.8), the following review should be considered in a relative manner rather than absolutely.

In Tables 5.14–5.18, the DYN3D computation times are summarized for the VVER-1000 and the Hébert benchmarks considered in Section 5.2 as well as for the HTGR core and fuel-block examples and the VVER-1000-like single assembly of Section 5.3. Note that the respective cases with and without inserted absorber do not significantly differ from each other. All calculations have been run on a 2.8 GHz computer (Intel(R) Core(TM)2) using a maximum number of inner iterations $\max_{in}$ of 3 to 5 (cf. Algorithms 4.2 and 4.4) as well as outer iteration tolerance criteria ϵ_f and ϵ_k of 1e-7 or 1e-8 (cf. Algorithms 4.1 and 4.3).

The main conclusion of this overview is that the trigonal DYN3D SP_3 calculations are generally about four times more expensive than the respective diffusion runs. This can be

Method	No. of trigonal nodes per FA	Computation time
DYN3D-TRIDIF	6	< 1 s
	24	< 1 s
	96	6 s
	384	41 s
	1536	243 s
	6144	1359 s $\approx$ 22.7 min
DYN3D-HEXNEM1		< 1 s
DYN3D-HEXNEM2		< 1 s

Table 5.14: Computation times required for the VVER-1000 benchmark calculations.

Method	No. of trigonal nodes per FA	Computation time
DYN3D-TRISP3	6	< 1 s
	24	< 1 s
	96	2 s
	384	14 s
	1536	107 s
	6144	949 s $\approx$ 15.8 min
DYN3D-TRIDIF	6	< 1 s
	24	< 1 s
	96	< 1 s
	384	3 s
	1536	24 s
	6144	255 s $\approx$ 4.3 min
DYN3D-HEXNEM1		< 1 s
DYN3D-HEXNEM2		< 1 s

Table 5.15: Computation times required for the Hébert benchmark calculations.

Method	No. of trigonal nodes per FA	Computation time
DYN3D-TRISP3	6	29 s
	24	159 s
	96	899 s $\approx$ 15.0 min
	384	5662 s $\approx$ 94.4 min
DYN3D-TRIDIF	6	7 s
	24	37 s
	96	196 s $\approx$ 3.3 min
	384	1379 s $\approx$ 23.0 min
DYN3D-HEXNEM1		1 s
DYN3D-HEXNEM2		2 s

Table 5.16: Computation times required for the HTGR core calculations.

Method	No. of trigonal nodes per FA	Computation time
DYN3D-TRISP3	6	< 1 s
	24	1 s
	96	7 s
	384	48 s
	1536	386 s
DYN3D-TRIDIF	6	< 1 s
	24	< 1 s
	96	2 s
	384	12 s
	1536	86 s

TABLE 5.17: Computation times required for the HTGR single-assembly calculations.

Method	No. of trigonal nodes per FA	Computation time
DYN3D-TRISP3	1536	100 s
DYN3D-TRIDIF	1536	22 s

TABLE 5.18: Computation times required for the VVER-1000-like single-assembly calculations.

traced back to the fact that DYN3D-TRISP3 solves a 2×2 system of equations for the flux moments Φ_0 and Φ_2 in comparison to only a single equation for Φ_0 in the DYN3D-TRIDIF approach. It is further found that a mesh refinement step increases the calculation time by roughly a factor of seven. In addition to the quadrupling of the number of nodal elements with every higher level of refinement, the convergence behavior of the implemented solver deteriorates (cf. outer iteration schemes of Algorithms 4.1 and 4.3).

Depending on the core configuration to be calculated, one has to deliberate about whether the diffusion or SP_3 approximation to the transport equation is the appropriate choice considering both the potential gain in accuracy in a certain discretization and the spent computation time.

6 Conclusions

This thesis focuses on the simplified P_3 (or SP_3) and diffusion approximations to the neutron transport equation. The SP_3 transport and diffusion equations are solved in the scope of a nodal method based on trigonal geometry and are implemented in the reactor code DYN3D. Here, the main results are summarized and possible areas of future research are suggested.

6.1 Summary

The reliable safe operation of nuclear reactors is highly dependent on the ability to precisely determine the neutron flux, from which reactivity feedback coefficients as well as criticality, power, and temperature distributions are derived. A reactor, however, is a complex object in terms of its geometry, its composition, and the nuclear data involved. This renders a whole-core neutron transport calculation practically impossible. In Chapter 1, the main steps of reactor calculations are outlined and the three-dimensional nodal reactor dynamics code DYN3D is introduced.

The neutron flux in a reactor is governed by several mechanisms by which neutrons can be gained or lost from the system, such as streaming effects as well as scattering, absorption, and fission events. Balancing these mechanisms against the time rate of change in the neutron density yields the neutron transport equation, which is presented in Chapter 2. Distinguishing between Monte Carlo and deterministic methods, an overview of different solution approaches to the transport equation is given. It is shown that the simplified P_N method allows an efficient solution technique, which is applicable to full-core calculations. The simplified P_N equations are derived leading to both the SP_3 and diffusion equations and revealing the main difference between both methods: the inclusion of higher-order neutron flux moments in the SP_3 approach. This fact involves the capability of the SP_3

method to describe anisotropic neutron migration processes, while merely the zeroth flux moment is taken into account in diffusion theory and only linear anisotropy effects can be reproduced by using the transport-corrected diffusion coefficient. A further advantage of the SP_3 approach becomes evident in Chapter 2: The SP_3 equations in within-group representation form a pair of coupled diffusion-type equations, which enables the use of very similar solution strategies of both the SP_3 and diffusion approaches.

In Chapter 3, the nodal reactor analysis concept is introduced. Nodal methods provide a framework for determining the three-dimensional neutron flux distribution throughout the reactor core, which avoid high computational costs. For reactor cores with hexagonal fuel assemblies, the capability of mesh refinement is an obvious advantage of a nodal method based on trigonal geometry. Furthermore, this geometry is particularly relevant for the modeling of asymmetric fuel assemblies as they can be found in high-temperature reactor cores. Analyzing also the previously existing DYN3D models, it is shown that the nodal approaches implemented in DYN3D can be regarded as hybrid forms of two classes of common nodal methods encompassing the advantages of both approaches and, hence, providing a highly efficient code. The DYN3D nodal methods are based on the transverse-integration procedure and use a combination of polynomial and exponential ansatzes to expand the unknown functions of the neutron flux.

Chapter 4 of this thesis focuses on the rigorous analysis of the mathematical interrelations. In the context of the development of numerical solution procedures for the SP_3 transport and diffusion equations in trigonal geometry, the nodal face-averaged partial neutron currents are important quantities since they significantly contribute to the inter-nodal neutron balance by realizing the nodal coupling. The response-matrix equations are derived to calculate the moments of the node-interface outgoing partial currents leading to an iterative procedure involving inner and outer iteration cycles from which the nodal fluxes are determined. Although only node-averaged neutron fluxes are finally used to derive relevant reaction rates, the accuracy of these node-averaged fluxes is strongly impacted by the intra-nodal flux representation, which is known to be more sophisticated in the SP_3 transport than in the diffusion approach.

A compact verification analysis of the performance of the trigonal DYN3D SP_3 transport and diffusion models is presented in Chapter 5. With particular regard to mesh refinement studies, diverse hexagonal test and benchmark problems with different material compositions are investigated. By means of mathematical benchmarks defined for the use of assembly-homogenized cross sections, the spatial convergence of the DYN3D diffusion and SP_3 results to the corresponding fine-mesh reference solutions provides proof of their respective functional reliability. The superiority of the SP_3 over the diffusion model is

demonstrated by means of an academic benchmark especially prepared to magnify transport effects. To investigate examples related more closely to practical applications, test problems with detailed-geometry full-transport reference solutions are analyzed in addition. Due to various error sources, such as homogenization effects and the assumption of an infinitely periodic lattice during cross-section generation, deviations of the DYN3D results from the reference solutions are inevitable. In the frame of their methodological possibilities, however, the results of the trigonal DYN3D models developed in this work agree well with the considered reference solutions. The question to which degree an error should be minimized, e.g., by refining the nodal mesh, has to be posed in the context of each specific core configuration – considering the potential gain in accuracy subject to the computational costs.

It should be emphasized that, as yet, none of the worldwide well-established core analysis codes comprises a multi-group SP_3 transport theory model based on nodal triangular meshes, which combines the advantage of the capability to capture anisotropic transport effects with the possibility of mesh refinement for hexagonal fuel assembly geometries. Therefore, the present work constitutes a significant contribution to the nodal-code development from which benefits may be expected throughout the community and ensures that DYN3D remains a world-wide competitive reactor code.

To summarize and conclude this thesis: The development of two methods based on different approximations of the transport equation using identical underlying spatial discretization allows a profound comparative analysis of both methods with regard to their mathematical derivations, nodal expansion approaches, solution procedures, and most importantly their physical performance. From the latter aspect, the following main conclusion can be drawn: The trigonal DYN3D SP_3 model achieves significantly better agreement with the reference solutions than the trigonal DYN3D diffusion approach in cases with pronounced anisotropy effects. The gain in accuracy obtained by the SP_3 model increases with the use of cross sections homogenized over smaller nodes. The improvements provided in this thesis are particularly relevant to the modeling of reactor cores with fuel assemblies comprising absorber material such as inserted control rods or burnable absorbers.

6.2 Recommendations for future work

In addition to the application of the newly available code to further investigating practical problems in reactor physics like those mentioned above, areas for future development fall into the following groups:

- the reduction of the computational costs,
- the increase of flexibility of the discretization, and
- the enhancement of the physical and mathematical approaches.

Due to a considerable computational burden, nodal calculations on a very fine mesh are certainly not practical in the near term for full-core analyses. In addition to the possible application of acceleration methods, the computational costs could be simply but significantly reduced if it was possible to apply a refinement locally. In this manner, a fine resolution could be used in regions with strong anisotropy effects, whereas a coarse nodalization may be sufficient elsewhere. A hybrid use of the SP_3 transport and diffusion methods, similar to the work by Lee and Downar [106], could be added to the aforementioned approach.

With respect to the discretization, a more flexible mesh refinement could be implemented. The present trigonal models only allow the number of nodal rows within one trigonal node to be 2^m, $m \in \mathbb{N}$. A user-defined number of such rows would enable the representation of more realistic fuel assembly compositions. In this manner, e.g., the VVER-1000 fuel assembly of Figure 5.17 (page 117) could be modeled without the unrealistic peripherical water nodes.

Enhancement of the physical and mathematical approaches of the trigonal DYN3D diffusion and SP_3 models could be achieved, e.g., via the incorporation of higher-order anisotropic scattering beyond the first-moment within-group scattering cross section in the SP_3 implementation and the application of assembly and pin-cell discontinuity factors, while pointing out that, as yet, ADFs for the SP_3 theory have not been defined. Furthermore, an improved inter-nodal coupling by averaging the partial currents over subdivisions of the trigonal node faces could be derived and the flux expansion could be upgraded via higher-order polynomial and/or additional exponential basis functions, similar to the DYN3D-HEXNEM2 ansatz or the approach by Christoskov and Petkov [37].

Finally, this work should be extended to the applicability of time-dependent phenomena, since this is indispensable for reactor safety analysis.

Bibliography

[1] *Sodium-Cooled Fast Reactor (SFR),* Idaho National Laboratory. `http://www.inl.gov/research/sodium-cooled-fast-reactor/`, 2013.

[2] *Very High Temperature Reactor (VHTR),* Idaho National Laboratory. `http://www.inl.gov/research/very-high-temperature-reactor/`, 2013.

[3] R. E. Alcouffe and R. D. O'Dell, *CRC Handbook of Nuclear Reactors Calculations (Y. Ronen, ed.)*, vol. 1, CRC Press, Inc., 1986, ch. Transport Calculations for Nuclear Reactors, pp. 341–462.

[4] A. Ancona, M. Becker, D. R. Harris, A. D. Menezes, M. A. Robinson, and D. M. VerPlank, *Unified analysis of nodal methods*, Transactions of the American Nuclear Society, 24 (1976), pp. 444–445.

[5] J.-M. Aragonés and C. Ahnert, *A linear discontinuous finite difference formulation for synthetic coarse-mesh few-group diffusion calculations*, Nuclear Science and Engineering, 94 (1986), pp. 309–322.

[6] T. Bahadir and S.-Ö. Lindahl, *Evaluation of rodded BWR assembly pin powers with SIMULATE5*, in Proceedings of PHYSOR 2012 Advances in Reactor Physics, Knoxville, Tennessee, USA, April 15-20 2012.

[7] T. Bahadir, S.-Ö. Lindahl, and S. P. Palmtag, *SIMULATE-4 multigroup nodal code with microscopic depletion model*, in Proceedings of the International Topical Meeting on Mathematics and Computation, Supercomputing, Reactor Physics and Nuclear and Biological Applications (M&C 2005), Avignon, France, September 12-15 2005.

[8] C. Beckert and U. Grundmann, *A nodal expansion method for solving the multigroup SP_3 equations in the reactor code DYN3D*, in Proceedings of the Joint International

Topical Meeting on Mathematics & Computation and Supercomputing in Nuclear Applications (M&C + SNA 2007), Monterey, California, USA, April 15-19 2007.

[9] ——, *Development and verification of a nodal approach for solving the multigroup SP_3 equations*, Annals of Nuclear Energy, 35 (2008), pp. 75–86.

[10] ——, *Entwicklung einer Transportnäherung für das reaktordynamische Rechenprogramm DYN3D (Abschlussbericht)*, Tech. Report FZD-497, Forschungszentrum Dresden-Rossendorf, Institut für Sicherheitsforschung, 2008.

[11] C. Beckert, U. Grundmann, and S. Mittag, *Multigroup diffusion and SP_3 solutions for a PWR MOX/UO_2 benchmark with the code DYN3D*, Transactions of the American Nuclear Society and the European Nuclear Society, 97 (2007), pp. 701–702.

[12] G. I. Bell and S. Glasstone, *Nuclear Reactor Theory*, Van Nostrand Reinhold Company, 1970.

[13] Y. Bilodid. Generation of reference data, 2012.

[14] P. S. Brantley, *Spatial and Angular Moment Analysis of Continuous and Discretized Particle Transport Problems*, PhD thesis, University of Michigan, 1998.

[15] P. S. Brantley and E. W. Larsen, *Variational derivation of the simplified P_3 approximation*, in Proceedings of the Joint International Conference on Mathematical Methods and Supercomputing for Nuclear Applications (M&C '97), vol. 1, Saratoga Springs, New York, USA, October 5-9 1997.

[16] ——, *The simplified P_3 approximation*, Nuclear Science and Engineering, 134 (2000), pp. 1–21.

[17] O. Cabellos, J.-M. Aragonés, and C. Ahnert, *Generalized effects in two group cross sections and discontinuity factors in the DELFOS code for PWR cores*, in Proceedings of the International Conference on Mathematics and Computation, Reactor Physics and Environmental Analysis in Nuclear Applications (M&C '99), vol. 1, Madrid, Spain, September 27-30 1999.

[18] J. J. Casal, R. J. J. Stamm'ler, E. A. Villarino, and A. A. Ferri, *HELIOS: geometric capabilities of a new fuel assembly program*, in Proceedings of the International Topical Meeting on Advances in Mathematics, Computations and Reactor Physics, vol. 2, Pittsburgh, Pennsylvania, USA, April 28 - May 2 1991.

[19] Y.-A. Chao, *Comments on the treatment of transverse leakage in advanced nodel codes for hexagonal nodes*, Nuclear Science and Engineering, 109 (1991), pp. 423–424.

[20] ——, *A theoretical analysis of the coarse mesh finite difference representation in advanced nodal methods*, in Proceedings of the International Conference on Mathematics and Computation, Reactor Physics and Environmental Analysis in Nuclear Applications (M&C '99), Madrid, Spain, September 27-30 1999.

[21] ——. Personal communication, 2012.

[22] Y.-A. Chao and Y. A. Shatilla, *Conformal mapping and hexagonal nodal methods – II: Implementation in the ANC-H code*, Nuclear Science and Engineering, 121 (1995), pp. 210–225.

[23] Y.-A. Chao, C.-A. Suo, and J. A. Penkrot, *On the theory of interface flux nodal method*, in Proceedings of the International Conference on Numerical Methods in Nuclear Engineering, Montreal, Canada, September 6-9 1983.

[24] Y.-A. Chao and N. Tsoulfanidis, *Conformal mapping and hexagonal nodal methods – I: Mathematical foundation*, Nuclear Science and Engineering, 121 (1995), pp. 202–209.

[25] Y.-A. Chao and A. Yamamoto, *The explicit representation for the angular flux solution in the simplified P_N (SP_N) theory*, in Proceedings of PHYSOR 2012 Advances in Reactor Physics, Knoxville, Tennessee, USA, April 15-20 2012.

[26] C. Chauliac, J.-M. Aragonés, D. Bestion, D. G. Cacuci, N. Crouzet, F.-P. Weiss, and M. Zimmermann, *NURESIM – A European simulation platform for nuclear reactor safety: Multi-scale and multi-physics calculations, sensitivity and uncertainty analysis*, Nuclear Science and Engineering, 241 (2011), pp. 3416–3426.

[27] C. Chauliac, J.-M. Aragonés, D. Bestion, M. Zimmermann, D. G. Cacuci, and N. Crouzet, *NURESIM – Final Activity Report (FAR)*, Tech. Report FI6O-CT-2005-516560, European Commission, Euratom Research and Training Programme on Nuclear Energy within the Sixth Framework Programme, December 2009.

[28] G. Chiba, *Application of the hierarchical domain decomposition boundary element method to the simplified P_3 equation*, Annals of Nuclear Energy, 38 (2011), pp. 1033–1038.

[29] B. Cho, J. H. Won, and N. Z. Cho, *Analytic function expansion nodal (AFEN) method extended to multigroup simplified P_3 (SP_3) equations via partial current moment transformation*, Transactions of the American Nuclear Society, 103 (2010), pp. 714–717.

[30] J. Y. Cho, H. G. Joo, B.-O. Cho, and S. Q. Zee, *Hexagonal CMFD formulation employing triangle-based polynomial expansion nodal kernel*, in Proceedings of M&C 2001, Salt Lake City, Utah, USA, September 2001.

[31] J. Y. Cho and C. H. Kim, *Polynomial expansion nodal method for hexagonal core analysis*, Transactions of the American Nuclear Society, 73 (1995), pp. 179–180.

[32] ——, *Higher order polynomial expansion nodal method for hexagonal core neutronics analysis*, Annals of Nuclear Energy, 25 (1998), pp. 1021–1031.

[33] N. Z. Cho, Y. H. Kim, and K. W. Park, *Extension of analytic function expansion nodal method to multigroup problems in hexagonal-z geometry*, Nuclear Science and Engineering, 126 (1997), pp. 35–47.

[34] N. Z. Cho and J. Lee, *Analytic function expansion nodal (AFEN) method in hexagonal-z three-dimensional geometry for neutron diffusion calculation*, Journal of Nuclear Science and Technology, 43 (2006), pp. 1320–1326.

[35] ——, *Analytic function expansion nodal method for multigroup diffusion equations in cylindrical (r, θ, z) geometry*, Nuclear Science and Engineering, 159 (2008), pp. 229–241.

[36] B. Christensen, *Three-dimensional static and dynamic reactor calculations by the nodal expansion method*, Tech. Report Risø-R-496, Risø National Laboratory, Denmark, May 1985.

[37] I. Christoskov and P. T. Petkov, *A development of the HEXNEM nodal expansion method*, Annals of Nuclear Energy, 51 (2013), pp. 235–239.

[38] D. E. Cullen, *CRC Handbook of Nuclear Reactors Calculations (Y. Ronen, ed.)*, vol. 1, CRC Press, Inc., 1986, ch. Nuclear Cross Section Preparation, pp. 13–131.

[39] P. J. Davis, *Circulant Matrices*, John Wiley & Sons, Inc., 1979.

[40] K. L. Derstine, *DIF3D: A code to solve one-, two-, and three-dimensional finite-difference diffusion theory problems*, Tech. Report ANL-82-64, Argonne National Laboratory, 1984.

[41] T. J. Downar, D. A. Barber, R. M. Miller, C. Lee, T. Kozlowski, D. J. Lee, Y. Xu, J. Gan, H. G. Joo, J. Y. Cho, K. Lee, and A. P. Ulses, *PARCS: Purdue advanced reactor core simulator*, in Proceedings of PHYSOR 2002, Seoul, Korea, October 7-10 2002.

[42] T. J. Downar, H. G. Joo, and G. Jiang, *A hybrid ANM/NEM interface current technique for the nonlinear nodal calculation*, in Proceedings of the Joint International Conference on Mathematical Methods and Supercomputing for Nuclear Applications (M&C '97), vol. 1, Saratoga Springs, New York, USA, October 5-9 1997.

[43] T. J. Downar, C. H. Lee, and G. Jiang, *An assessment of advanced nodal methods for MOX fuel analysis in light water reactors*, in Proceedings of the 2000 ANS

International Topical Meeting on Advances in Reactor Physics and Mathematics and Computations into the Next Millennium (PHYSOR 2000), Pittsburgh, Pennsylvania, USA, May 7-11 2000.

[44] T. J. Downar, D. Lee, Y. Xu, T. Kozlowski, and J. Staudenmier, *PARCS v2.6 U.S. NRC Core Neutronics Simulator, Theory Manual (Draft)*, 2004.

[45] J. J. Duderstadt and L. J. Hamilton, *Nuclear Reactor Analysis*, John Wiley & Sons, Inc., 1976.

[46] S. Duerigen, S. Mittag, and E. Nikitin, *Verification of the trigonal-geometry diffusion and SP_3 models of the code DYN3D*, in Proceedings of the 22nd Symposium of AER on VVER Reactor Physics and Reactor Safety, Pruhonice, Czech Republic, October 1-5 2012.

[47] P. D. Esser and K. S. Smith, *A semianalytical two-group nodal model for SIMULATE-3*, Transactions of the American Nuclear Society, 68 (1993), pp. 220–222.

[48] H. Finnemann, F. Bennewitz, and M. R. Wagner, *Interface current techniques for multidimensional reactor calculations*, Atomkernenergie, 30 (1977), pp. 123–128.

[49] H. D. Fischer and H. Finnemann, *The nodal integration method – a diverse solver for neutron diffusion problems*, Atomkernenergie, 39 (1981), pp. 229–236.

[50] M. Frank, A. Klar, E. W. Larsen, and S. Yasuda, *Time-dependent simplified P_N approximation to the equations of radiative transfer*, Journal of Computational Physics, 226 (2007), pp. 2289–2305.

[51] E. Fridman. Generation of reference data, 2012.

[52] ——. Personal communication, 2012.

[53] E. Fridman and E. Shwageraus, *Modeling of SFR cores with Serpent–DYN3D codes sequence*, Annals of Nuclear Energy, 53 (2013), pp. 354–363.

[54] E. M. Gelbard, *Application of spherical harmonics method to reactor problems*, Tech. Report WAPD-BT-20, Bettis Atomic Power Laboratory, 1960.

[55] ——, *Simplified spherical harmonics equations and their use in shielding problems*, Tech. Report WAPD-T-1182, Bettis Atomic Power Laboratory, 1961.

[56] ——, *Applications in the simplified spherical harmonics equations in spherical geometry*, Tech. Report WAPD-TM-294, Bettis Atomic Power Laboratory, 1962.

[57] ——, *Spherical Harmonics Methods: P_L and Double-P_L Approximations*, Gordon and Breach Science Publishers, New York, 1968, ch. 4, pp. 271–358.

[58] S. González-Pintor, D. Ginestar, and G. Verdú, *High order finite element method for the Lambda modes problem on hexagonal geometry*, Annals of Nuclear Energy, 36 (2009), pp. 1450–1462.

[59] S. González-Pintor, G. Verdú, and D. Ginestar, *Spectral element method for the neutron diffusion equation on a triangular mesh*, in Proceedings of the International Conference on Mathematics, Computational Methods & Reactor Physics (M&C 2009), Saratoga Springs, New York, May 3-7 2009.

[60] U. Grundmann, *HEXNEM – a nodal method for the solution of the neutron diffusion equation in hexagonal geometry*, in Proceedings of the International Conference on Mathematics and Computation, Reactor Physics and Environmental Analysis in Nuclear Applications (M&C '99), Madrid, Spain, September 27-30 1999.

[61] ——, *Calculations of a steady state of the OECD/NRC PWR MOX/UO2 transient benchmark with DYN3D*, in Proceedings of the Annual Meeting on Nuclear Technology (Jahrestagung Kerntechnik), Aachen, Germany, May 16-18 2006.

[62] ——. Personal communication, 2012.

[63] U. Grundmann and F. Hollstein, *A two-dimensional intranodal flux expansion method for hexagonal geometry*, Nuclear Science and Engineering, 133 (1999), pp. 201–212.

[64] U. Grundmann and S. Mittag, *Super-homogenisation factors in pinwise calculations by the reactor dynamics code DYN3D*, Annals of Nuclear Energy, 38 (2011), pp. 2111–2119.

[65] U. Grundmann and U. Rohde, *DYN3D/M2 – a code for calculation of reactivity transients in cores with hexagonal geometry*, Tech. Report FZR 93 - 01, Forschungszentrum Rossendorf e.V., January 1993.

[66] ——, *DYN3D – a 3-dimensional core model for steady state and transient analysis in thermal reactors*, in Proceedings of the International Conference on the Physics of Reactors (PHYSOR '96), Mito, Japan, September 16-20 1996.

[67] U. Grundmann, U. Rohde, and S. Mittag, *DYN3D – three-dimensional core model for steady-state and transient analysis of thermal reactors*, in Proceedings of the 2000 ANS International Topical Meeting on Advances in Reactor Physics and Mathematics and Computations into the Next Millennium (PHYSOR 2000), Pittsburgh, Pennsylvania, USA, May 7-11 2000.

[68] U. Grundmann, U. Rohde, S. Mittag, and S. Kliem, *DYN3D version 3.2 – code for calculation of transients light water reactors (LWR) with hexagonal or quadratic fuel elements – description of models and methods*, Tech. Report FZR-434, Forschungszentrum Rossendorf (FZR), August 2005.

[69] N. Guessous and M. Akhmouch, *Higher order analytical nodal methods in response-matrix formulation for the multigroup neutron diffusion equations*, Annals of Nuclear Energy, 29 (2002), pp. 1765–1778.

[70] A. Hébert, *The search for superconvergence in spherical harmonics approximations*, Nuclear Science and Engineering, 154 (2006), pp. 134–173.

[71] ——, *A simplified presentation of the multigroup analytic nodal method in 2-D Cartesian geometry*, Annals of Nuclear Energy, 35 (2008), pp. 2142–2149.

[72] ——, *Applied Reactor Physics*, Presses internationales Polytechnique, 2009.

[73] ——, *Mixed-dual implementations of the simplified P_n method*, Annals of Nuclear Energy, 37 (2010), pp. 498–511.

[74] ——, *A raviart-thomas-schneider implementation of the simplified P_n method in 3-D hexagonal geometry*, in Proceedings of PHYSOR 2010 – Advances in Reactor Physics to Power the Nuclear Renaissance, Pittsburgh, Pennsylvania, USA, May 9-14 2010.

[75] ——, *A user guide for TRIVAC version 4*, Tech. Report IGE-293, École Polytechnique de Montréal, Canada, 2012.

[76] A. Hébert and P. Benoist, *A consistent technique for the global homogenization of a pressurized water reactor assembly*, Nuclear Science and Engineering, 109 (1991), pp. 360–372.

[77] A. Hébert and A. Kavenoky, *Development of the SPH homogenization method*, in Proceedings of the International Topical Meeting on Advances in Mathematical Methods for the Solution of Nuclear Engineering Problems, Munich, Germany, April 27-29 1981.

[78] A. F. Henry, *Refinements in accuracy of coarse-mesh finite-difference solution of the group-diffusion equations*, in Proceedings of the Seminar on Numerical Reactor Calculations, International Atomic Energy Agency (IAEA), Vienna, Austria, January 17-21 1972.

[79] M. Herman and A. Trkov, *ENDF-6 Formats Manual – Data formats and procedures for the Evaluated Nuclear Data File ENDF/B-VI and ENDF/B-VII (Document ENDF-102)*, Tech. Report BNL-XXXXX-2009, National Nuclear Data Center, Brookhaven National Library, Upton, New York, USA, June 2009.

[80] J. J. Herrero, N. García-Herranz, D. Cuervo, and C. Ahnert, *Neighborhood-corrected interface discontinuity factors for multi-group pin-by-pin diffusion calculations for LWR*, Annals of Nuclear Energy, 46 (2012), pp. 106–115.

[81] S. G. Hong, N. Z. Cho, and J. M. Noh, *A three-dimensional nodal diffusion code based on the AFEN methodology*, Journal of the Korean Nuclear Society, 27 (1995), pp. 870–876.

[82] A. Kavenoky, *The SPH homogenization method*, in Proceedings of the Specialists' Meeting on Homgenization Methods in Reactor Physics, Lugano, Switzerland, November 13-15 1978. IAEA-TECDOC-231 (1980).

[83] Y. Kim, J. Yoo, D. Hahn, and C. H. Kim, *A conformal mapped nodal SP_3 method for hexagonal core analysis*, Annals of Nuclear Energy, 36 (2009), pp. 498–504.

[84] M. P. Knight. Personal communication, 2012.

[85] M. P. Knight, P. K. Hutt, and I. Lewis, *Comparison of PANTHER nodal solutions in hexagonal-z geometry*, Nuclear Science and Engineering, 121 (1995), pp. 254–263.

[86] B. Kochunas, Y. Xu, and T. J. Downar, *Development of the triangular nodal method TRIPEN for prismatic HTR analysis*, in Proceedings of PHYSOR 2010 – Advances in Reactor Physics to Power the Nuclear Renaissance, Pittsburgh, Pennsylvania, USA, May 9-14 2010.

[87] K. Koebke, *A new approach to homogenization and group condensation*, in Proceedings of the Specialists' Meeting on Homgenization Methods in Reactor Physics, Lugano, Switzerland, November 13-15 1978. IAEA-TECDOC-231 (1980).

[88] ——, *Advances in homogenization and dehomogenization*, in Proceedings of the International Topical Meeting on Advances in Mathematical Methods for the Solution of Nuclear Engineering Problems, Munich, Germany, April 27-29 1981.

[89] K. Koebke, L. Hetzelt, M. R. Wagner, and H.-J. Winter, *Principles and application of advanced nodal reactor analysis methods*, in Proceedings of the Topical Meeting on Reactor Physics and Shielding, Chicago, Illinois, USA, September 17-19 1984.

[90] K. Koebke, M. R. Wagner, H.-J. Winter, and A. Wörner, *Benchmark 19 – Two-dimensional PWR-burnup problem (with fuel management)*, Tech. Report ANL-7416 Supplement 3, Argonne National Laboratory, December 1985.

[91] P. Kotiluoto, *Fast tree multigrid transport application for the simplified P_3 approximation*, Nuclear Science and Engineering, 138 (2001), pp. 269–278.

[92] T. Kozlowski, *Spatial Homogenization Methods for Pin-by-Pin Neutron Transport Calculations*, PhD thesis, Purdue University, 2005.

[93] T. Kozlowski and D. Lee, *Cell homogenization method for pin-by-pin neutron transport calculations*, Nuclear Science and Engineering, 169 (2011), pp. 1–18.

[94] J. Krepel, U. Rohde, U. Grundmann, and F.-P. Weiss, *DYN3D-MSR spatial dynamics code for molten salt reactors*, Annals of Nuclear Energy, 34 (2007), pp. 449–462.

[95] K. Küfner and R. Heger, *DIAMANT2 – Ein Multigruppen Neutronentransportprogramm für Dreiecks- und Hexagonalgeometrie*, Tech. Report KfK 3033, Kernforschungszentrum Karlsruhe, September 1980.

[96] S. Langenbuch, *Ein neues Grobgitterverfahren zur Lösung der orts- und zeitabhängigen Neutronendiffusionsgleichungen*, PhD thesis, Technische Universität München, Fachbereich Elektrotechnik, 1976.

[97] S. Langenbuch, W. Maurer, and W. Werner, *Coarse-mesh flux-expansion method for the analysis of space-time effects in large light water reactor cores*, Nuclear Science and Engineering, 63 (1977), pp. 437–456.

[98] ——, *High-order schemes for neutron kinetics calculations, based on a local polynomial approximation*, Nuclear Science and Engineering, 64 (1977), pp. 508–516.

[99] E. W. Larsen, *Asymptotic diffusion and simplified P_N approximations for diffusive and deep penetration problems. Part 1: Theory*, Transport Theory and Statistical Physics, 39 (2011), pp. 110–163.

[100] E. W. Larsen, J. E. Morel, and J. M. McGhee, *Asymptotic derivation of the simplified P_N equations*, in Proceedings of the Joint International Conference on Mathematical Methods and Supercomputing in Nuclear Applications (M&C + SNA '93), Karlsruhe, Germany, April 19-23 1993.

[101] ——, *Asymptotic derivation of the multigroup P_1 and simplified P_N equations with anisotropic scattering*, Nuclear Science and Engineering, 123 (1996), pp. 328–342.

[102] E. W. Larsen, G. Thömmes, A. Klar, M. Seaïd, and T. Götz, *Simplified P_N approximations to the equations of radiative heat transfer and applications*, Journal of Computational Physics, 183 (2002), pp. 652–675.

[103] J.-J. Lautard and T. Flumiani, *Extension of the mixed dual finite element method to the solution of the SP_N transport equation in 2D unstructured geometries composed by arbitrary quadrilaterals*, in Proceedings of the 18th International Conference on Transport Theory (18 ICTT), Rio de Janeiro, Brazil, July 20-25 2003.

[104] R. D. Lawrence, *Progress in nodal methods for the solution of the neutron diffusion and transport equations*, Progress in Nuclear Energy, 17 (1986), pp. 271–301.

[105] R. D. Lawrence and J. J. Dorning, *A nodal Green's function method for multidimensional neutron diffusion calculations*, Nuclear Science and Engineering, 76 (1980), pp. 218–231.

[106] C.-H. Lee and T. J. Downar, *A hybrid nodal diffusion/SP_3 method using one-node coarse-mesh finite difference formulation*, Nuclear Science and Engineering, 146 (2004), pp. 176–187.

[107] D. Lee, T. Kozlowski, T. J. Downar, C. Lee, and H. C. Lee, *Application of SP_3 approximation to MOX transient analysis in PARCS*, Transactions of the American Nuclear Society, 91 (2004), pp. 252–256.

[108] J. Lee and N. Z. Cho, *AFEN method and its solutions of the hexagonal three-dimensional VVER-1000 benchmark problem*, Progress in Nuclear Energy, 48 (2006), pp. 880–890.

[109] J. Leppänen, *Development of a New Monte Carlo Reactor Physics Code*, PhD thesis, Helsinki University of Technology, 2007.

[110] ——, *Serpent – a Continuous-energy Monte Carlo Reactor Physics Burnup Calculation Code, User's Manual*, VTT Technical Research Centre of Finland, August 2012.

[111] E. E. Lewis and W. F. Miller, Jr., *Computational Methods of Neutron Transport*, John Wiley & Sons, Inc., 1984.

[112] E. E. Lewis and G. Palmiotti, *Simplified spherical harmonics in the variational nodal method*, Nuclear Science and Engineering, 126 (1997), pp. 48–58.

[113] Y. Li, H. Wu, L. Cao, and Q. Chen, *A 2D triangular nodal-SP3 method for solving neutron transport equation*, in Proceedings of PHYSOR 2010 – Advances in Reactor Physics to Power the Nuclear Renaissance, Pittsburgh, Pennsylvania, USA, May 9-14 2010.

[114] Y.-W. H. Liu and E. M. Gelbard, *Accuracy of nodal transport and simplified P_3 fluxes in benchmark tests*, Transactions of the American Nuclear Society, 52 (1986), pp. 430–432.

[115] T. Loetsch, V. Khalimonchuk, and A. Kuchin, *Proposal of a benchmark for core burnup calculations for a VVER-1000 reactor core*, in Proceedings of the 19th Symposium of AER on VVER Reactor Physics and Reactor Safety, Varna, Bulgaria, September 21-25 2009.

[116] J. A. Lozano, J. Jimenez, N. García-Herranz, and J.-M. Aragonés, *Development and performance of the ANDES/COBRA-III coupled system in hexagonal-z geometry*, in Proceedings of the International Conference on Mathematics, Computational Methods & Reactor Physics (M&C 2009), Saratoga Springs, New York, May 3-7 2009.

[117] H. Lu, H. Wu, L. Cao, Y. Zhou, C. Xian, and D. Yao, *Two-dimensional nodal transport method for triangular geometry*, Annals of Nuclear Energy, 34 (2007), pp. 424–432.

[118] P. E. MacDonald, J. W. Sterbentz, R. L. Sant, P. D. Bayless, R. R. Schultz, H. D. Gougar, R. L. Moore, A. M. Ougouag, and W. K. Terry, *NGNP preliminary point design – results of the initial neutronics and thermal-hydraulic assessments*, Tech. Report INEEL/EXT-03-00870 Revision 1, Idaho National Engineering and Environmental Laboratory, September 2003.

[119] R. G. McClarren, *Theoretical aspects of the simplified P_n equations*, Transport Theory and Statistical Physics, 39 (2011), pp. 73–109.

[120] S. Mittag. Personal communication, 2012.

[121] S. Mittag, P. T. Petkov, and U. Grundmann, *Discontinuity factors for non-multiplying material in two-dimensional hexagonal reactor geometry*, Annals of Nuclear Energy, 30 (2003), pp. 1347–1364.

[122] J. E. Morel, A. Gonzalez-Aller, and J. S. Warsa, *A lumped linear-discontinuous spatial discretization scheme for triangular-mesh S_n calculations in r-z geometry*, Nuclear Science and Engineering, 155 (2007), pp. 168–178.

[123] J. E. Morel, J. M. McGhee, and E. W. Larsen, *A three-dimensional time-dependent unstructured tetrahedral-mesh SP_N method*, Nuclear Science and Engineering, 123 (1996), pp. 319–327.

[124] E. Nikitin. Generation of reference data, 2012.

[125] J. M. Noh and N. Z. Cho, *A new approach of analytic basis function expansion to neutron diffusion nodal calculation*, Nuclear Science and Engineering, 116 (1994), pp. 165–180.

[126] K. W. Park, C. J. Park, K. T. Lee, N. Z. Cho, and Y. H. Kim, *Pin-cell homogenization via generalized equivalence theory and embedding assembly calculation*, Transactions of the American Nuclear Society, 85 (2001), pp. 334–336.

[127] I. Pataki and A. Keresztúri, *Calculation of the second AER kinetic benchmark problem by using a new nodal method*, in Proceedings of the 22nd Symposium of AER on VVER Reactor Physics and Reactor Safety, Pruhonice, Czech Republic, October 1-5 2012.

[128] R. R. Paternoster and W. F. Walters, *The nodal transport method for general triangular meshes in* (x, y) *geometry*, Progress in Nuclear Energy, 18 (1986), pp. 153–160.

[129] A. Pautz, H.-W. Bolloni, K.-A. Breith, R. van Geemert, J. Heinecke, G. Hobson, S. Merk, B. Pothet, and F. Curca-Tivig, *The ARTEMIS core simulator: A central component in AREVA NP's code convergence project*, in Proceedings of the Joint International Topical Meeting on Mathematics & Computation and Supercomputing in Nuclear Applications (M&C + SNA 2007), Monterey, California, USA, April 15-19 2007.

[130] G. C. Pomraning, *Asymptotic and variational derivations of the simplified* P_N *equations*, Annals of Nuclear Energy, 20 (1993), pp. 623–637.

[131] R. H. Prinsloo and D. I. Tomašević, *The analytic nodal method in cylindrical geometry*, Nuclear Engineering and Design, 238 (2008), pp. 2898–2907.

[132] J. M. Putney, *A hexagonal geometry nodal expansion method for fast reactor calculations*, Progress in Nuclear Energy, 18 (1986), pp. 113–121.

[133] R. Rachamin, C. Wemple, and E. Fridman, *Neutronic analysis of SFR core with HELIOS-2, SERPENT, and DYN3D codes*, Annals of Nuclear Energy, 55 (2013), pp. 194–204.

[134] P. Reuss, *Neutron Physics*, EDP Sciences, 2008.

[135] J. Rhodes and M. Edenius, *CASMO-4. A fuel assembly burnup program, User's Manual*, Tech. Report SSP-01/400 Revision 4, Studsvik Scandpower, 2004.

[136] U. Rohde, S. Baier, S. Duerigen, E. Fridman, S. Kliem, and B. Merk, *Development and verification of the coupled 3D neutron kinetics/thermal-hydraulics code DYN3D-HTR for the simulation of transients in block-type HTGR*, Nuclear Engineering and Design, 251 (2012), pp. 412–422.

[137] U. Rohde, S. Mittag, U. Grundmann, P. Petkov, and J. Hadek, *Application of a stepwise verification and validation procedure to the 3D neutron kinetics code DYN3D within the European NURESIM project*, in Proceedings of the 17th International Conference on Nuclear Engineering (ICONE17), Brussels, Belgium, July 12-16 2009.

[138] W. Rothenstein and M. Segev, *CRC Handbook of Nuclear Reactors Calculations (Y. Ronen, ed.)*, vol. 1, CRC Press, Inc., 1986, ch. Unit Cell Calculations, pp. 133–203.

[139] R. Sanchez and N. J. McCormick, *A review of neutron transport approximations*, Nuclear Science and Engineering, 80 (1982), pp. 481–535.

[140] E. Schneider, M. Seaïd, J. Janicka, and A. Klar, *Validation of simplified P_N models for radiative transfer in combustion systems*, Communications in Numerical Methods in Engineering, 24 (2008), pp. 85–96.

[141] W. Shen and M. Dahmani, *Review of worldwide reactor-physics codes and their applicability to the current and next-generation CANDU® reactors*, in Proceedings of PHYSOR 2010 – Advances in Reactor Physics to Power the Nuclear Renaissance, Pittsburgh, Pennsylvania, USA, May 9-14 2010.

[142] R. A. Shober, R. N. Sims, and A. F. Henry, *Two nodal methods for solving time-dependent group diffusion equations*, Nuclear Science and Engineering, 64 (1977), pp. 582–592.

[143] R. N. Sims, *A Coarse-Mesh Nodal Diffusion Method Based on Response Matrix Condensations*, PhD thesis, Massachusetts Institute of Technology, 1977.

[144] K. S. Smith, *An analytic nodal method for solving the two-group, multidimensional, static and transient neutron diffusion equations*, master's thesis, Massachusetts Institute of Technology, 1979.

[145] ——, *Assembly homogenization techniques for light water reactor analysis*, Progress in Nuclear Energy, 17 (1986), pp. 303–335.

[146] W. M. Stacey, *Nuclear Reactor Physics*, Wiley-VCH Verlag GmbH & Co. KGaA, 2004.

[147] R. J. J. Stamm'ler and M. J. Abbate, *Methods of Steady-State Reactor Physics in Nuclear Design*, Academic Press Inc., 1983.

[148] N. Sugimura, T. Ushio, A. Yamamoto, and M. Tatsumi, *Calculation models of AEGIS/SCOPE2, a core calculation system of next generation*, in Proceedings of PHYSOR 2006, ANS Topical Meeting on Reactor Physics, Vancouver, Canada, September 10-14 2006.

[149] K. Tada, A. Yamamoto, S. Kosaka, G. Hirano, and Y. Yamane, *Development of a prototype pin-by-pin fine mesh calculation code for BWR core analysis*, in Proceedings of the International Conference on the Physics of Reactors (PHYSOR '08), Interlaken, Switzerland, September 14-19 2008.

[150] K. Tada, A. Yamamoto, Y. Yamane, S. Kosaka, and G. Hirano, *Validation of neutron current formulations for the response matrix method based on the SP_3 theory*, Annals of Nuclear Energy, 37 (2010), pp. 22–27.

[151] K. Tada, Y. Yamamoto, Y. Yamane, S. Kosaka, and G. Hirano, *Application of the SP3 nodal method with second order source and leakage approximations in axial direction for BWR pin-by-pin core analysis*, in Proceedings of the International Congress on Advances in National Power Plants (ICAPP '09), Tokyo, Japan, May 10-14 2009.

[152] Y. Tahara, T. Kanagawa, and H. Sekimoto, *Two-dimensional baffle/reflector constants for nodal code in PWR core design*, Journal of Nuclear Science and Technology, 37 (2000), pp. 986–995.

[153] M. Tatsumi, H. Hyoudou, N. Sugimura, and A. Yamamoto, *AEGIS/SCOPE2, a next-generation in-core fuel management system – (2) core calculation code, SCOPE2*, Transactions of the American Nuclear Society, 97 (2007), pp. 562–564.

[154] M. Tatsumi and A. Yamamoto, *Advanced PWR core calculation based on multi-group nodal-transport method in three-dimensional pin-by-pin geometry*, Journal of Nuclear Science and Technology, 40 (2003), pp. 376–387.

[155] D. I. Tomašević, *Variational Derivation of the Simplified P_2 Nodal Approximation*, PhD thesis, University of Michigan, 1994.

[156] ——, *An extension of the multigroup analytic nodal method (MANM) to problems in hexagonal-z geometry*, in Proceedings of the International Conference on Mathematics, Computational Methods & Reactor Physics (M&C 2009), Saratoga Springs, New York, May 3-7 2009.

[157] D. I. Tomašević and E. W. Larsen, *Variational derivation of simplified P_2 equations with boundary conditions*, Transactions of the American Nuclear Society, 70 (1994), pp. 159–161.

[158] R. van Geemert, *Development and verification of a high performance multi-group SP_3 transport capability in the ARTEMIS core simulator*, in Proceedings of the International Conference on the Physics of Reactors (PHYSOR '08), Interlaken, Switzerland, September 14-19 2008.

[159] D. R. Vondy, *CRC Handbook of Nuclear Reactors Calculations (Y. Ronen, ed.)*, vol. 1, CRC Press, Inc., 1986, ch. Diffusion Theory, pp. 205–340.

[160] M. R. Wagner, *Three-dimensional nodal diffusion and transport theory methods for hexagonal-z geometry*, Nuclear Science and Engineering, 103 (1989), pp. 377–391.

[161] W. F. Walters, *The TLC scheme for numerical solution of the transport equation on equilateral triangular meshes*, in Proceedings of the Topical Meeting on Advances in Reactor Computations, Salt Lake City, Utah, USA, March 28-30 1983.

[162] W. F. Walters, F. W. Brinkley, and D. R. Marr, *User's guide for TWOHEX: A code package for two-dimensional, neutral-particle transport in equilateral triangular meshes*, Tech. Report LA-10258-M, Los Alamos National Laboratory, October 1984.

[163] B. Xia and Z. Xie, *Flux expansion nodal method for solving multigroup neutron diffusion equations in hexagonal-z geometry*, Annals of Nuclear Energy, 33 (2006), pp. 370–376.

[164] A. Yamamoto, Y. Kitamura, and Y. Yamane, *Cell homogenization methods for pin-by-pin core calculations tested in slab geometry*, Annals of Nuclear Energy, 31 (2004), pp. 825–847.

[165] A. Yamamoto and M. Tatsumi, *Improvement of spatial discretization error on semi-analytic nodal method using the scattered source substraction method*, Journal of Nuclear Science and Technology, 43 (2006), pp. 1481–1489.

[166] V. Zimin and D. Baturin, *Polynomial nodal method for solving neutron diffusion equations in hexagonal-z geometry*, Annals of Nuclear Energy, 29 (2002), pp. 1105–1117.